University of Crete
Department of Physics

The X-ray Source Population of the Small Magellanic Cloud

by

Valsamo Antoniou

Thesis

submitted for the Degree of Doctor of Philosophy in Physics

Heraklion, Crete
April 2008

To my husband Yannis,
for his endless love and support
all these years...

PhD Thesis

The X-ray Source Population of the Small Magellanic Cloud

Thesis Author : V. Antoniou

Thesis Supervisor : D. Hatzidimitriou

Thesis Committee :

V. Charmandaris
Member

D. Hatzidimitriou
Thesis supervisor

N. Kylafis
Member

I. Papadakis
Member

I. Papamastorakis
Member

T. Tomaras
Member

I.M. Vardavas
Member

A. Zezas
External supervisor

ACKNOWLEDGEMENTS

First of all, I would like to thank my supervisor, Assoc. Prof. Despina Hatzidimitriou for her guidance and support during my PhD thesis. We had fruitful and long discussions together, even by the phone across the ocean! She was the one who believed in me more than anybody else, even during my undergraduate studies, giving me the opportunity to make part of my PhD thesis at the Center of Astrophysics in Cambridge, MA under the supervision of Dr. Andreas Zezas. I will always be grateful to her for this opportunity and her support through the years.

This thesis would not be in your hands if it was not for the help of Dr. Andreas Zezas. During the past 4 years, Andreas was both a teacher and a very good friend of mine at the same time. I used to call him boss and I will do it even after the completion of this thesis! His support, transfer of knowledge and high expectations provided me the confidence I needed in my first "scientific" steps. He was always patient, available, ready to give a solution to a problem that came up the last minute, and with a simple explanation to everything. I really enjoyed working with him all these years. I am also glad that very soon he will be a professor at the University of Crete. A university that I loved to be part of it all these years because of its great environment to study and work.

Furthermore, I would like to thank the director of Skinakas Observatory, Prof. I. Papamastorakis, and Prof. N. Kylafis for their support in the progress of my work. I also thank Prof. N. Kylafis for managing to pull funding for me until the last minute.

I would also like to thank the great team of Skinakas Observatory. Tasos, Giorgos, Makis, and mostly Anna were at all times there for me. I will always remember and acknowledge their help. Many thanks should go to all my friends for their understanding on why I could not always follow them.

Moreover, I thank Steve Beikman for his support as a system administrator at the High Energy Astrophysics Division of CfA in really intense moments following hardware problems, Silas Laycock for long discussions on the analysis of the IMACS Magellan data, and Ewan O' Sullivan for advice with the *XMM-Newton* data analysis. In addition, I thank Ewan for providing his computers to run some intensive and time-consuming simulations.

Since the very first day at the university, but even before that, and until the last one, I received the greatest of love, support, and understanding from my family. My parents always insisted that I should keep going on and never give up, no matter how difficult is something if I really wanted it, while for my young brother I was always the older successful sister. I wish some day I will be able to give them back the support they offered me. I also thank Yannis' family for being close to me these last 6 months.

Last but not least, from the deepest of my heart I thank my husband Yannis. He was always there for me, and this thesis is as much his success as it is mine. We made it through almost everything together, from the simplest to the most difficult. Even now, this very last moment, he is next to me every single minute, even from across the ocean. I will do my best to be always there for you too!

ABSTRACT

The X-ray Source Population of the Small Magellanic Cloud

by
Valsamo Antoniou

In this work we study the X-ray source population of the Small Magellanic Cloud (SMC). The SMC is our second nearest star-forming galaxy, which allows us to identify the optical counterparts of the X-ray binary population (XRB) and therefore directly study their link with star-formation (SF). Using *Chandra*, *XMM-Newton* and optical photometric catalogs we study the young XRB population of this galaxy, down to luminosity levels of quiescent X-ray source populations. The *Chandra* observations in particular cover the central, densest and most active region of the SMC, while the *XMM-Newton* survey is designed to probe regions of different stellar populations ($10-500$Myr). Based on the comparison of these observations with comprehensive stellar catalogs of the SMC, we propose for the first time 25 candidate High Mass X-ray Binaries, of which 16 are candidate Be X-ray binaries (Be-XRBs; 9 new candidates in the *Chandra* survey and 7 in the *XMM-Newton* fields). Moreover, we confirm previous classification of Be-XRBs for 19 sources (18 in *Chandra*, and 1 in the *XMM-Newton* survey). We also examine the "overabudance" of Be-XRBs in the SMC fields with respect to the Milky Way. In luminosities down to $\sim 10^{34}$ erg s^{-1} , we find that Be-XRBs are ~ 2 times more common in the SMC when compared to the Milky Way even after taking into account the difference in the formation rates of OB stars. This residual excess can be attributed to the lower metallicity of the SMC. Finally, we find that the mixing of Be-XRBs with other than their natal stellar population is not an issue in our comparisons of Be-XRBs and stellar populations in the SMC. Instead we find indication for variation of the XRB populations of the SMC on kiloparsec scales, related to local variations of the formation rate of OB stars and slight variation of their age, which results in different relative numbers of Be stars and therefore XRBs. Comparison of the Be-XRB populations with their local star-formation history shows that they are observed in regions with SF rate bursts $\sim 30-70$ Myr ago. The age range coincides with the age of maximum Be-star formation, based on independent studies of Galactic and SMC Be stars. We also find a strong correlation between the number of Be-XRBs and the strength of the SF at the age of maximum Be-star formation (i.e. ~ 40 Myr ago), while regions with strong but more recent SF (e.g. the Wing) are deficient in Be-XRBs. Regions that host HMXBs, which however have not been proved yet to be Be-XRBs, show a similar SF history (with a significant burst at ~ 40 Myr ago). We thus conclude that the majority of the optically unidentified SMC HMXBs have a Be nature. The very strong correlation of the young X-ray sources with the stellar population in scales of a few arcminutes (~ 0.5kpc) provides strong evidence for relatively small supernova kicks during the formation of the compact object. Finally, we have used the 2dF (Two-degree Field) spectrograph on the 3.9m Anglo-Australian Telescope (AAT) to confirm the classification of candidate Be-XRBs as emission line stars and identify their spectral type and luminosity class when possible. Our sample is selected from the *Chandra* survey and existing *XMM-Newton* observations

of the SMC. These observations show that the distribution of spectral types of Be-XRBs in the SMC agrees with that of the LMC, while it is in contrast to the population of Be-XRBs in the Milky Way. In addition we confirmed the different distributions of spectral type of Be stars in XRB systems and individual Be stars. With these spectra we also discover the second supergiant X-ray binary in the SMC. Overall this study demonstrates the importance of the Be-XRBs as a dominant component of young XRB populations, and shows evidence for strong evolution of the X-ray source populations of ages < 100Myr and different metallicities.

Contents

1 Introduction **1**

1.1 The Small Magellanic Cloud galaxy 1

1.1.1 The star-formation history of the SMC 4

1.2 X-ray Binaries 6

1.3 High-Mass X-ray Binaries 7

1.3.1 Accretion processes in HMXBs 9

1.3.2 Be/X-ray Binaries 14

1.3.3 Supergiant X-ray Binaries 17

1.4 Low-Mass X-ray Binaries 18

1.5 The SMC observed in X-rays 18

1.6 Goals and thesis outline 19

2 The *Chandra* survey of the SMC "Bar": X-ray source catalog and the Luminosity Function of High-Mass X-ray Binaries **24**

2.1 Introduction 26

2.2 Description of the survey 28

2.3 Data analysis 29

2.3.1 Source Detection 31

2.3.2 Source Parameters . . . 32
2.4 X-ray Luminosity Function of point sources . . . 36
2.4.1 Incompleteness correction . . . 36
2.4.2 Background and foreground sources . . . 37
2.4.3 The XLF of High-Mass X-ray Binaries . . . 39
2.5 Discussion . . . 42
2.5.1 The HMXB population of the SMC as seen with *Chandra* . . . 43
2.5.2 The faint-end of the XLF of young XRBs and the "propeller effect" . . . 45
2.6 Conclusions . . . 48

3 The *Chandra* Survey of the SMC "Bar": Optical counterparts of X-ray sources 52
3.1 Introduction . . . 54
3.1.1 The *Chandra* survey of the SMC . . . 55
3.2 Optical data . . . 58
3.2.1 OGLE-II catalog . . . 59
3.2.2 MCPS catalog . . . 60
3.3 Cross-correlation analysis . . . 61
3.3.1 OGLE-II and MCPS . . . 61
3.3.2 Other bibliographic sources . . . 65
3.4 Finding charts . . . 66
3.5 Photometric data . . . 66
3.6 Color-Magnitude Diagram . . . 67
3.7 Chance coincidence probability . . . 70
3.8 Discussion . . . 73
3.8.1 Classification criteria . . . 74

3.8.2 Sources with multiple optical matches 79

3.8.3 Properties of the optical counterparts and implications for the nature of the X-ray sources 79

3.8.4 Comparison with the Galactic and LMC Be-XRBs 83

3.8.5 Local variations of the Be-XRB populations 86

3.9 Conclusions 88

4 An *XMM-Newton* survey of the Small Magellanic Cloud 96

4.1 Observations and data analysis 96

4.2 Candidate Be-XRBs from the *XMM-Newton* survey 103

4.3 Be-XRBs in the *Chandra* and *XMM-Newton* surveys of the SMC 108

5 Small Magellanic Cloud: Star-formation history and X-ray binary populations 112

5.1 Introduction 113

5.2 Observations and data analysis 114

5.2.1 X-ray observations 114

5.2.2 Identification of candidate optical counterparts 115

5.3 Star-formation history and XRB populations 115

5.3.1 SF history of observed fields 116

5.3.2 Observed fields with known Be-XRBs and pulsars 116

5.4 Discussion 119

6 Optical spectroscopy of High-Mass X-ray Binaries in the Small Magellanic Cloud 124

6.1 Introduction 124

6.2 Observations and data reduction . . . 125
6.3 Determination of spectral types . . . 132
6.4 Discussion . . . 136
6.4.1 Distribution of spectral types . . . 136
6.4.2 Optical and near-infrared photometry of the Be-XRB 2dF sample . . . 138
6.4.3 Optical variability . . . 144
6.4.4 The second supergiant X-ray binary discovered in the SMC . . . 146
6.4.5 The peculiar optical spectrum of X-ray source AX J0051-722 . . . 147
6.5 Conclusions . . . 148

7 Conclusions and future work **154**
7.1 An overview of the presented work . . . 154
7.2 Relevant Future work . . . 158
7.2.1 Analysis of high quality optical photometric data . . . 158
7.2.2 Investigate the Be nature of currently candidate SMC Be-XRBs . . . 159
7.2.3 Optical identification of X-ray sources in the *Chandra* deep fields . . . 159

Appendices **161**

A Properties of *Chandra* X-ray sources **161**

B Notes on individual *Chandra* sources **182**
B.1 Sources with uncertain nature . . . 182
B.2 Sources with Be candidate counterparts from Mennickent et al. 2002 . . . 183
B.3 Sources identified with OGLE variable stars . . . 184
B.4 Sources with available spectral classification for their counterparts . . . 185

B.5 *Chandra* sources with bright optical counterparts ($M_{V_o} \leq -0.25$) only between the 1σ and 2σ search radii 186

B.6 *Chandra* sources with optical counterparts in the locus of OB stars and hard or possibly hard spectrum between the 1σ and 2σ search radii 187

C SMC HMXBs observed with 2dF **226**

C.1 2dF spectra of 20 HMXBs in the SMC 226

D Light curves of HMXBs with 2dF spectra **231**

List of Figures

1.1 A view of the Small Magellanic Cloud in H_α, L, R, V, and B filters that also includes two foreground globular star clusters NGC 362 (top) and 47 Tucanae (right). North is up and East to the left (Credit & Copyright: Stéphane Guisard). 2

1.2 This early morning picture was taken from Australia. The SMC appears on the upper right while the LMC is seen on the bottom left of this image (Credit & Copyright: Chris Schur). 3

1.3 "Snapshots" of SMC star formation activity for a particular age bin (adapted Fig.6 from Harris & Zaritsky 2004). Each pixel represents one of the 351 SMC studied subregions ($\sim 12' \times 12'$), with a pixel value that is proportional to the subregion's SFR. 4

1.4 Global SFH of the SMC (adapted Fig.7 from Harris & Zaritsky 2004). Notice the different scalings of the time axis because the age bins become logarithmically narrower for younger ages. The displayed error bars represent the 1σ confidence interval for each age bin. The times at which the SMC had a perigalactic passage are indicated by the rows of short vertical lines: encounters with the LMC (top), encounters with the Milky Way (bottom). These lines fade out at older ages as a representation of the uncertainty of the encounter times with increasing age. . . . 5

1.5 The main classes of X-ray binaries based on different compact objects and companion stars. 7

1.6 Sketch representing the formation of a HMXB (adapted Fig.16.15 from Tauris & van den Heuvel 2006). 8

1.7 Geometry of stellar-wind accretion onto a compact object orbiting its massive companion. The amount of mass that is not accreted but its flow is perturbed forms an accretion wake beyond the compact object (adapted Fig.7.B3 from Charles & Seward 1995). 10

1.8 Illustration of an X-ray pulsar and its magnetosphere (adapted Fig.7.8 from Charles & Seward 1995). 13

1.9 The distribution of the X-ray pulse periods of SMC pulsars (using data from the online census of Coe; for details refer to the text). 14

1.10 X-ray outbursts are related to the passage of the neutron star through the circumstellar disk of the Be star (adapted Fig.7.22 from Charles & Seward 1995). . 15

2.1 A DSS image of the SMC with overlaid the footprints of the ACIS-I arrays of the 5 *Chandra* fields. 28

2.2 An adaptively smoothed full-band (0.5-7.0 keV) mosaic of the observed fields. . . 31

2.3 Full band, adaptively smoothed, exposure corrected, images of the five SMC fields (their orientation is not the same). The detected sources are shown with circles and their numbers correspond to the naming convention in Tables A.1–A.5. . . . 33

2.4 X-ray color-color diagram of the detected sources in all fields, using the X-ray colors estimated with the BEHR algorithm (see text). The grid shows the expected X-ray colors for an absorbed power-law model. The horizontal lines correspond to different values of photon index Γ, while the vertical lines correspond to different valus of HI column density (in units of 10^{22} cm^{-2}). Sources associated with early-types stars are marked with red circles. 35

2.5 Plot of the source detection probability curves for different background levels: from left to right (in each plot) 0.0005, 0.005, 0.03, 0.08, 0.3, 0.5, 0.8, 1.0, 1.6, 2.1 cnts/pix and different off axis angles (different panels): from left to right and top to bottom : on-axis, 2, 4, 6, 8′off-axis. Notice the x-axis scale difference in the last three panels. 38

2.6 Plot of the local source background surface brightness versus net source number of counts for sources detected in the 5 Fields. The solid and dashed lines show the 50% and 75% completeness limits for sources at a given background level and source intensity (black, red, green and blue lines are for off-axis angles of $0'$, $2'$, $4'$, $6'$, respectively). Sources to the left and top of these curves have lower detection probability. 39

2.7 Plot of the completeness-corrected (solid line) and uncorrected (dashed line) cumulative XLFs of the sources with early-type counterparts in all fields. The hatched area shows the 1σ uncertainty of the XLF taking into account uncertainties of the number of sources as well as of their luminosity (including Poisson noise on the number of observed source counts and spectral uncertainties). . . . 41

2.8 A plot of Col1 (Top; a) and Col2 (Bottom; b) against the X-ray luminosity (0.1-10.0 keV band) of the X-ray sources, with the Be/X-ray binaries marked with circles. 44

3.1 A DSS optical image of the center of the SMC (outline of the 5 observed *Chandra* fields ($16' \times 16'$) and the 5 overlapping OGLE-II fields). 56

3.2 CMD of all single and the brightest of multiple matches of our *Chandra* sources . 69

3.3 Chance coincidence probability as a function of the search radius around the X-ray source The estimated chance coincidence probability for each *Chandra* source is shown in black (asterisks) for the OGLE-II data and in grey (open triangles) for data from the MCPS catalog (for reasons of clarity between the OGLE-II and MCPS data, the latter are shown with a small shift in the search radius). The thick lines represent the estimated probability of detecting by chance one source for a single match, while the thin lines indicate the probability of detecting one or more spurious matches for a source with one or more associations (i.e. total number of matches). 72

3.4 **(a)** *Lower panel*: The star-formation rate at the age of $\sim$ 42 Myr versus the number of Be-XBRs in each *Chandra* field. **(b)** *Upper panel*: The star-formation rate at the age of $\sim$ 42 Myr versus the ratio of the number of Be-XBRs to the number of OB spectral type stars in each field (Be-XRB systems are shown in black, while the overall population of HMXBs is shown in gray). The error bars in the x-axis were derived assuming Poisson statistics. In the y-axis error bars indicate lower and upper limits of the mean SF rate in each *Chandra* field. 87

4.1 The observed fields of the *Chandra* and *XMM-Newton* surveys, which sample different stellar populations, are overlaid on an optical image (© Photo by D. Malin, Anglo-Australian Observatory/Royal Observatory, Edinburgh). The squares are $16' \times 16'$, while the circles have a diameter of $\sim 30'$. 97

4.2 The age of various SMC fields observed with *Chandra* and *XMM-Newton*. Open triangles indicate archival observations, while filled squares show the fields used in the *XMM-Newton* study, which sample stellar populations in a wide range of ages. 98

4.3 A full band (0.2-12.0keV) exposure-corrected mosaic image of the 3 EPIC cameras (PN, MOS1, MOS2) for *XMM-Newton* field 2. The detected sources are shown with circles of $5''$ radius. 100

4.4 Hardness ratios plots used in this study. In order of appearance (from top to bottom) for *XMM-Newton* fields 1, 2, 3, and 6, respectively). Overlaid is a grid for different values of Γ (horizontal lines) and N_H (diagonal lines with N_H given in units of $10^{22}\mathrm{cm}^{-2}$) derived by estimating the expected number of counts in each band for an absorbed power-law model, and assuming the effective area on the detector's aimpoint. 101

4.5 CMD of all multiple matches of our *XMM-Newton* sources. 106

4.6 Part of the previous CMD (Figure 4.5) showing all optical matches of our *XMM-Newton* sources in greater detail. 107

5.1 (*upper panel*) The black points show the average SF history for the MCPS regions (using data from Harris & Zaritsky 2004) which overlap with our *Chandra* and *XMM-Newton* fields and host one or more detected (candidate and confirmed) Be-XRBs. The SF history of MCPS regions which overlap with the same fields but they do not host any Be-XRBs is shown with gray points. (*middle panel*) The same plot as above but for MCPS regions with and without X-ray pulsars, and (*bottom panel*) with and without Be-XRBs from the *Chandra* Wing survey (P.I. Coe, AO6). For clarity a small offset of log(age[Myr]) ~ 0.025 has been applied in the distributions of areas without Be-XRBs and/or pulsars. Notice the difference in the y-axis of the bottom panel plot with respect to the other panels. 117

5.2 The number of observed Be-XRBs in the different studied fields versus the SF rate at the age of $\sim$ 42 Myr. For the point labeled as Wing refer to the text (§5.3.2). 119

6.1 Distribution of Hα equivalent widths. Our 2dF Be-XRB sample is indicated with a red solid line, Be-XRBs from the sample of Coe et al. 2005 are shown with a blue solid line, while EWs for isolated Be stars (data are taken from Ashok et al. 1984) are presented with a dotted green line. 130

6.2 Hα emission line profiles normalized by the local continuum. From bottom to top in each panel we show the following sources: *(Left-Top)* 3_3 (XMM_33), 4_1, 4_5 (XMM_9), 4_8, 5_16, *(Right-Top)* 5_2, 5_4, 5_7 (XMM_30), 6_1, 6_2, *(Left-Bottom)* 6_4, XMM_14, XMM_15, XMM_17, XMM_3, *(Right-Bottom)* XMM_39, XMM_47, XMM_5, XMM_7, 5_12. For clarity we applied a y-axis offset to the different spectra of each panel. 131

6.3 Sample normalized spectra in the 3800Å-5000Å wavelength range are shown, with characteristic spectral features marked. 135

6.4 Comparison of the B spectral subtype distributions of Be-XRBs to isolated Be stars. Negative spectral subtypes correspond to O-type stars. *(Top panel)* The spectral distribution of Be-XRBs in the SMC (solid bars), the LMC (solid line), and the Milky Way (dashed line) is shown. The SMC and LMC data are taken from Liu et al. (2005), while in the SMC sample we have added our classification using the 2dF spectrograph. Data for the Milky Way are taken from Liu et al. (2006). *(Bottom panel)* The spectral distribution of isolated Be stars from the Bright Star Catalog (using data from Porter et al. 1996). 137

6.5 CMD of optical counterparts of X-ray sources with 2dF spectra 141

6.6 Histogram of (J-K)o values of the Be-XRBs from this sample. 142

6.7 A (J-K) color versus EW(Hα) plot for the 2dF Be-XRB sample. 144

6.8 Estimated variability from the OGLE-II and MACHO light curves for our 2dF sample against the Hα equivalent width. 145

B.1 OGLE *I* band images for Chandra sources in field 3 *This is an electronic Figure.* 208

B.2 OGLE *I* band images for Chandra sources in field 4 *This is an electronic Figure.* 209

B.3 OGLE *I* band images for Chandra sources in field 5 *This is an electronic Figure.* 215

B.4 OGLE *I* band images for Chandra sources in field 6 *This is an electronic Figure.* 217

B.5 OGLE *I* band images for Chandra sources in field 7 *This is an electronic Figure.* 222

C.1 2dF spectra of 20 HMXBs in the SMC. 227

D.1 I band OGLE-II light curves for sources with 2dF spectra. The x-axis gives the time (Julian Date - 2450000) in years, and the y-axis the I band magnitude. . . . 232

D.2 MACHO light curves for sources with 2dF spectra. The x-axis gives the time (Julian Date - 2400000.5), and the y-axis the "blue" instrumental magnitude. . . 235

List of Tables

1.1 Observational data of the Small Magellanic Cloud 2

2.1 Summary of observations 29

2.2 XLF fits 42

3.1 *Chandra* source data statistics 57

3.2 Optical counterparts of X-ray sources in *Chandra* field 3 63

3.3 Total number of counterparts 64

3.4 Chance associations between the X-ray sources and the stars in the OGLE-II catalog 73

3.5 Chance associations between the X-ray sources and the stars in the MCPS catalog 74

3.6 Summary of optical and X-ray properties 77

3.6 Summary of optical and X-ray properties 78

4.1 Log of *XMM-Newton* observations 99

4.2 X-ray properties of *XMM-Newton* sources with hard X-ray spectra 104

4.3 Optical properties of candidate Be-XRBs detected with *XMM-Newton* 105

6.1 The Be-XRB sample observed with 2dF 128

6.2 Measurements of the Hα emission in the Be-XRBs sample 129

6.3 Spectral classification 134

6.4 Optical counterparts of selected X-ray sources with 2dF spectra from this study . 139

6.4 Optical counterparts of selected X-ray sources with 2dF spectra from this study . 140

6.5 Infrared counterparts of our 2dF Be-XRB sample 143

A.1 FIELD 3: Master Source List 162

A.1 FIELD 3: Master Source List *continued* 163

A.2 FIELD 4: Master Source List 164

A.2 FIELD 4: Master Source List *continued* 165

A.3 FIELD 5: Master Source List 166

A.3 FIELD 5: Master Source List *continued* 167

A.4 FIELD 6: Master Source List 168

A.4 FIELD 6: Master Source List *continued* 169

A.5 FIELD 7: Master Source List 170

A.5 FIELD 7: Master Source List *continued* 171

A.6 FIELD 3: Source Photometry and X-ray Colors 172

A.6 FIELD 3: Source Photometry and X-ray Colors 173

A.7 FIELD 4: Source Photometry and X-ray Colors 174

A.7 FIELD 4: Source Photometry and X-ray Colors 175

A.8 FIELD 5: Source Photometry and X-ray Colors 176

A.8 FIELD 5: Source Photometry and X-ray Colors 177

A.9 FIELD 6: Source Photometry and X-ray Colors 178

A.9 FIELD 4: Source Photometry and X-ray Colors 179

A.10 FIELD 7: Source Photometry and X-ray Colors 180

A.10 FIELD 7: Source Photometry and X-ray Colors 181

B.1 Bright optical counterparts ($M_{V_o} \leq -0.25$) of X-ray sources within the 2σ search radius (no match(es) found in the 1σ search radius) 187

B.2 Summary of optical and X-ray properties of sources presented in Table B.1 . . . 188

B.3 Optical counterparts of X-ray sources in *Chandra* field 4 190

B.3 Optical counterparts of X-ray sources in *Chandra* field 4 191

B.3 Optical counterparts of X-ray sources in *Chandra* field 4 192

B.3 Optical counterparts of X-ray sources in *Chandra* field 4 193

B.4 Optical counterparts of X-ray sources in *Chandra* field 5 194

B.4 Optical counterparts of X-ray sources in *Chandra* field 5 195

B.4 Optical counterparts of X-ray sources in *Chandra* field 5 196

B.5 Optical counterparts of X-ray sources in *Chandra* field 6 197

B.5 Optical counterparts of X-ray sources in *Chandra* field 6 198

B.5 Optical counterparts of X-ray sources in *Chandra* field 6 199

B.6 Optical counterparts of X-ray sources in *Chandra* field 7 200

B.6 Optical counterparts of X-ray sources in *Chandra* field 7 201

B.6 Optical counterparts of X-ray sources in *Chandra* field 7 202

B.7 Additional optical info 203

B.7 Additional optical info 204

B.7 Additional optical info 205

B.7 Additional optical info 206

B.7 Additional optical info 207

Chapter 1

Introduction

1.1 The Small Magellanic Cloud galaxy

The Small Magellanic Cloud (SMC) is an irregular dwarf galaxy, gravitationally bound to our own Milky Way galaxy. It was discovered by the Portuguese explorer Fernando de Magellan in 1519 during the first circumnavigation of planet Earth, and it is located to the East of the Galactic foreground globular cluster 47 Tucanae (Figure 1.1). The SMC appears to the naked eye as a misty spot in the Southern night sky (Figure 1.2)[1] . It is a member of the Local Group of galaxies, together with the Large Magellanic Cloud (LMC). The SMC is our second nearest star-forming galaxy (after the LMC) located at $\sim$ 60 kpc (e.g. Hilditch, Howarth & Harries 2005). The main observational data for the SMC are presented in Table 1.1 (Van den Bergh 2000; unless otherwise stated).

The main observational feature of the SMC (seen in Figure 1.1) is its "Bar", although it bears no relation to a dynamical bar (van den Bergh 2000). It extends from North-East to South-West with a size of $\sim 2.5^\circ \times 1^\circ$. In the Eastern part of the SMC, and facing the LMC, there is the so-called "Wing", with a size of $\sim 6^\circ \times 1^\circ$. Both the SMC "Bar" and "Wing" regions host young populations: OB associations, young clusters, supergiants, and HII regions. In larger distances from the center of the SMC intermediate age populations dominate, while a fairly

[1] http://www.schursastrophotography.com/10dastro/aus06/lmcsmc1.html

Table 1.1. Observational data of the Small Magellanic Cloud

Right ascension (J2000)	$00^{h}52^{m}44.8^{s}$
Declination (J2000)	$-72°49'43''$
Type	Irr
Total mass	$2 \times 10^{9}\,M_{\odot}$ (1)
Distance	60 ± 1 kpc (2)
Apparent dimensions	$5°20' \times 3°5'$
Total star-formation rate	$0.05\,M_{\odot}$/yr (3)

References. — (1) Westerlund (1997), (2) Hilditch, Howarth & Harries (2005), (3) Wilke et al. (2004)

Figure 1.1 A view of the Small Magellanic Cloud in H_{α}, L, R, V, and B filters that also includes two foreground globular star clusters NGC 362 (top) and 47 Tucanae (right). North is up and East to the left (Credit & Copyright: Stéphane Guisard).

Figure 1.2 This early morning picture was taken from Australia. The SMC appears on the upper right while the LMC is seen on the bottom left of this image (Credit & Copyright: Chris Schur).

regular spheroid extends to its outer regions (a halo roughly extending to $\sim 7^{\circ}$ from its center). The spheroid hosts older populations, including old clusters, red-giant stars, carbon stars, and planetary nebulae. A more detailed description of the structure of the SMC can be found in Westerlund (1997), and van den Bergh (2000).

The SMC has been extensively studied in all wavelengths over the years allowing us to obtain a very good picture of its properties. Its proximity, well mapped extinction (Zaritsky et al. 2002), moderate Galactic foreground absorption ($N_H \simeq 6 \times 10^{20} cm^{-2}$; Dickey & Lockman 1990), small line-of-sight depth of its central young stellar populations (<10 kpc; e.g. Crowl et al. 2001; Harries, Hilditch & Howarth 2003), and its well-determined recent star-formation history (SFH; Harris & Zaritsky 2004) make the SMC an excellent laboratory to study the population of young (< 500 Myr) X-ray binaries.

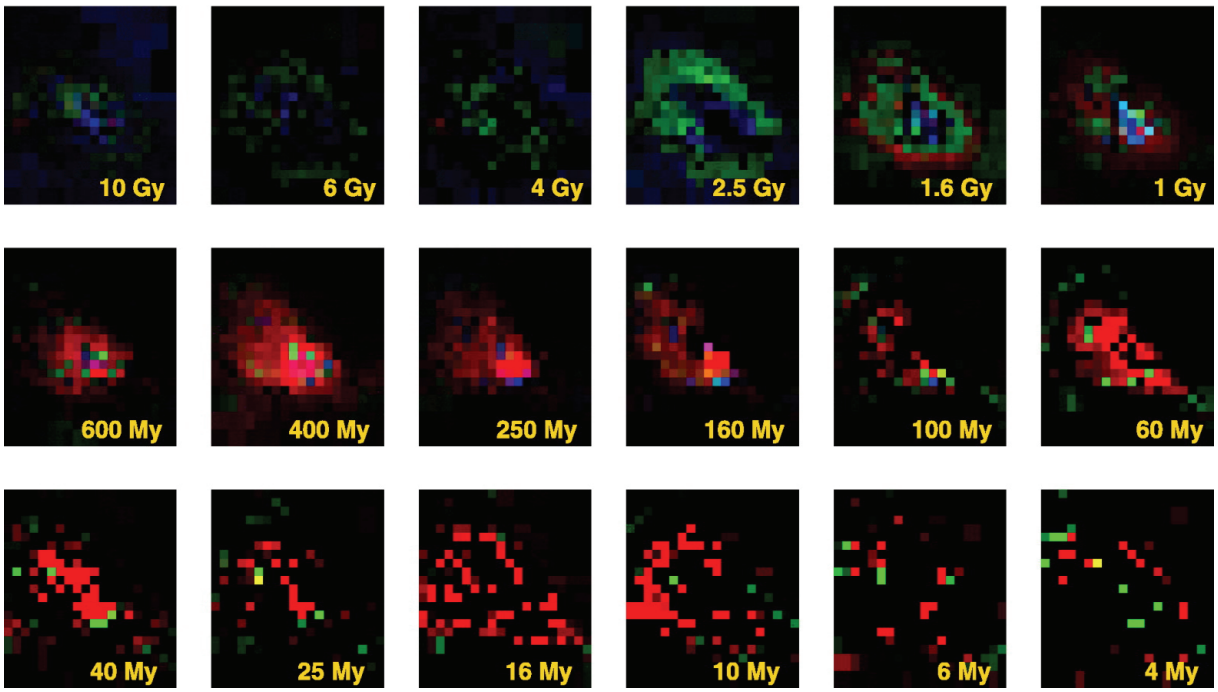

Figure 1.3 "Snapshots" of SMC star formation activity for a particular age bin (adapted Fig.6 from Harris & Zaritsky 2004). Each pixel represents one of the 351 SMC studied subregions ($\sim 12' \times 12'$), with a pixel value that is proportional to the subregion's SFR.

1.1.1 The star-formation history of the SMC

There have been several studies of the SMC star-fomation history. The most comprehensive is that of Harris & Zaritsky (2004), who presented the spatially resolved SFH of the SMC across the entire central $4° \times 4.5°$ area of the main body, based on $UBVI$ photometry from their Magellanic Clouds Photometric Survey (MCPS; Zaritsky et al. 2002), and using the StarFISH package (Harris & Zaritsky 2001). StarFISH performs a χ^2 minimization between the observed and model photometry based on theoretical isochrones. To derive a spatially resolved SFH, they divided the SMC survey in a grid of 351 subregions ($\sim 12' \times 12'$ each). The best SFH solutions for these regions are presented in Figure 1.3 (adapted from Harris & Zaritsky 2004) as "pixels" of variable size whose brightness is proportional to the local star formation rate (SFR). Each panel in this figure represents a "snapshot" of the star formation activity at a particular age bin. Red corresponds to Z = 0.008, green corresponds to Z = 0.004, and blue corresponds to Z = 0.001[2].

[2][Fe/H] $\equiv \log(Z/Z_\odot)$, with $Z_\odot$=0.02 for the solar metallicity of [Fe/H] = 0; Russell & Dopita (1992).

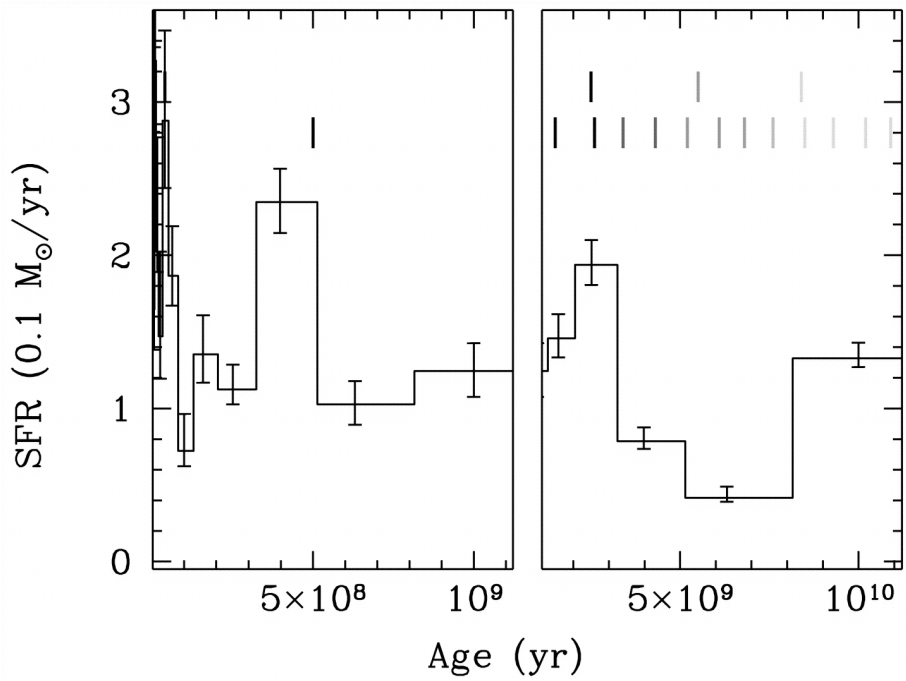

Figure 1.4 Global SFH of the SMC (adapted Fig.7 from Harris & Zaritsky 2004). Notice the different scalings of the time axis because the age bins become logarithmically narrower for younger ages. The displayed error bars represent the 1σ confidence interval for each age bin. The times at which the SMC had a perigalactic passage are indicated by the rows of short vertical lines: encounters with the LMC (top), encounters with the Milky Way (bottom). These lines fade out at older ages as a representation of the uncertainty of the encounter times with increasing age.

The SMC experienced a burst of star-formation $\sim 30 - 60$ Myr ago (Harris & Zaritsky 2004), along with an older star-formation event (~ 400 Myr ago) and widespread star-formation a few Gyr ago which led to the formation of a smooth stellar spheroid (e.g. Gardiner & Hatzidimitriou 1992, Hatzidimitriou 1999). The most prominent recent star-forming activity took place in the central part of the SMC along its North-East South-West axis, and partly in the Wing, giving it its bar-like appearance in optical wavelengths. Enhanced star-formation during the past $\sim 10 - 20$ Myr is also present in the region between the Small and the Large Magellanic Clouds (the SMC bridge region; Harris & Zaritsky 2004).

The global SFH of the SMC is shown in Figure 1.4 (Harris & Zaritsky 2004), after summing the SFRs for all individual studied subregions and metallicity (Z = 0.001, 0.004, and 0.008,

corresponding to [Fe/H] = -1.3, -0.7, and -0.4). An increase is observed in the mean SFR during the most recent 3 Gyr punctuated by bursts at ages of 2.5, 0.4, and 0.06 Gyr. The bursts at 2.5 and 0.4 Gyr are temporally coincident with past perigalactic passages of the SMC with the Milky Way (Harris & Zaritsky 2004).

1.2 X-ray Binaries

The X-ray Binaries (XRBs) are accreting systems containing a compact object (either a neutron star or a black hole) and a companion star. These systems are among the brightest X-ray sources, and since their discovery in the 1960s (Giacconi et al. 1962) they have been extensively studied in all wavelengths. Nowadays, more than 400 such systems are known (confirmed and candidate) in the Milky Way and the Magellanic Clouds (Liu, van Paradijs & van den Heuvel 2005, 2006 & 2007). Many XRBs are transient in X-rays appearing as bright sources in the sky for a few weeks and then fading away. The recurrent time scales vary from days to tenth of years. The transient behavior is related (a) to the orbital motion of the system, and (b) to the episodic nature of high accretion rate events.

The identification of the optical counterpart of the XRBs has been proved very important in order to determine the nature of an XRB. Based on the mass of the companion star there are two main classes of XRBs: the High-Mass XRBs (HMXBs) with $M \geq 10\,M_{\odot}$, and the Low-Mass XRBs with $M \leq 1\,M_{\odot}$. Systems with intermediate mass of the companion star are less frequent and they are referred to as Intermediate Mass XRBs. In Figure 1.5 we present the main classes of XRBs. If the compact object is a black-hole, then the binary is generally referred as a black-hole X-ray binary (BH-XRB), with either an early or a late type companion. Neutron stars with low magnetic fields ($\sim 10^{9} - 10^{10}$G) and late-type companions (of spectral type A or later) form the class of neutron star LMXBs (NS-LMXBs). In cases of neutron stars with high magnetic fields ($\sim 10^{12}$G) and an early-type companion (O or B) we have the so-called Be X-ray binaries (Be-XRBs) or the supergiant X-ray binaries (SG-XRBs). Be-XRBs have Oe or Be stars as companions, while SG-XRBs have an O or B type supergiant. In the following, we will focus in the study of HMXBs, and in particular in Be-XRB systems, and in some extend in SG-XRBs. For completeness the most basic characteristics of a LMXB system are also presented below.

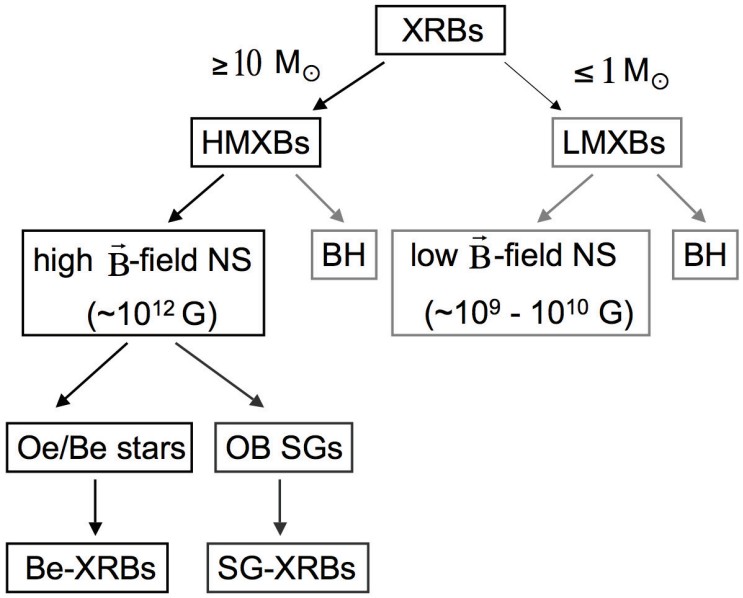

Figure 1.5 The main classes of X-ray binaries based on different compact objects and companion stars.

1.3 High-Mass X-ray Binaries

In order to describe the different components of a HMXB (especially during its evolution), we adopt the following convention: *(a)* We will refer to the *donor* as the massive star which is passing mass to the *compact* object. *(b)* In the original binary, before the gravitational collapse, we will refer to the *original primary* as the progenitor component of the compact object and as the *original secondary* to the progenitor component of the donor.

The HMXBs are the result of the evolution of a massive binary. They are believed to be formed via a standard evolutionary channel[3]. In most evolutionary models the progenitor of a HMXB is a massive close binary with moderate mass ratio ($q \geq 0.5$). The original primary evolves rapidly through hydrogen burning, generates a helium core and after few Myr expands to fill its Roche lobe. Matter from its envelope (unburnt hydrogen) will be transfered onto the original secondary with further expansion. The first stage of mass transfer begins. In few thousand years a significant amount of mass has been transfered to the original secondary, making it now heavier than the original primary, that is now a helium star of $\sim 2-4\,M_\odot$. Conservation of mass

[3]Their formation and evolution is best described in the recent review of Tauris & van den Heuvel (2006).

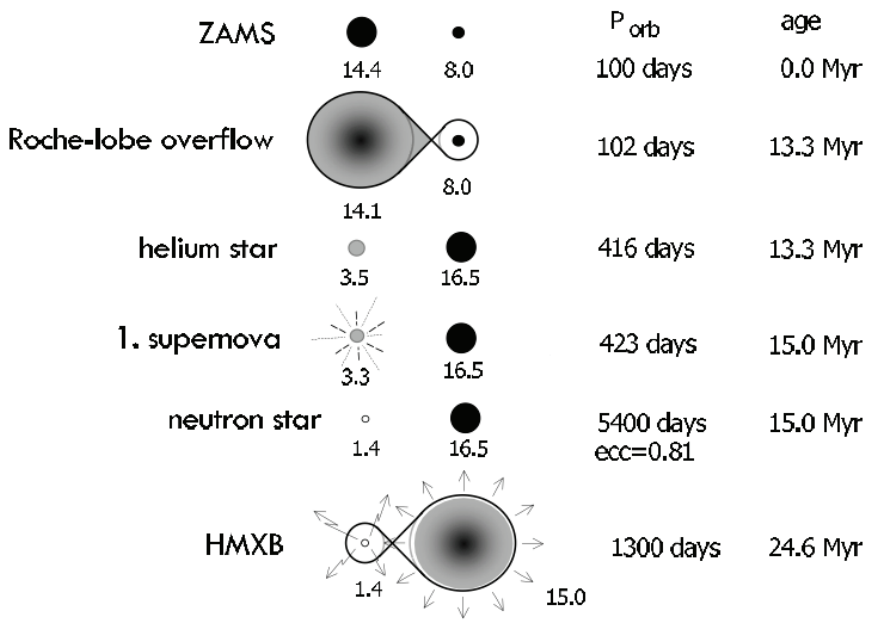

Figure 1.6 Sketch representing the formation of a HMXB (adapted Fig.16.15 from Tauris & van den Heuvel 2006).

and angular momentum widens the binary orbit and leaves a disk around the newly massive star because it is rotating rapidly. The helium star evolves rapidly (helium fusion to form a carbon core) and within a couple Myr it expands again filling its Roche lobe and therefore starting a second mass-transfer stage. This stage will last only a few thousand years and only a small fraction of mass (mostly helium) will be transfered onto the original secondary, leaving behind a carbon core. Within few decades this carbon star will undergo a supernova explosion (because of gravitational collapse) and it will become a neutron star in even wider orbits about the donor. If the binary is not disrupted from the kicks imparted to the compact object during the supernova explosion, then it becomes a HMXB. A sketch representing its formation is shown in Figure1.6 (adapted Fig.16.15 from Tauris & van den Heuvel 2006). In order for a neutron star to be formed, all the above models assume masses for the original primary of $\geq 12\,M_{\odot}$. In addition, in these models it is assumed that due to accretion of high-angular momentum material from the original primary, the original secondary will have a Be nature, though no attempt has been made to describe the exact physical processes.

1.3.1 Accretion processes in HMXBs

Many binaries transfer matter at some stage during their evolution. There are two main processes that account for the mass-transfer (Frank, King & Raine 2002):
(i) Roche-lobe overflow: One of the components of the binary system increases its radius during its evolution, or the binary separation decreases to the point that the gravitational pull can remove the outer layers of its envelope. Mass is transferred from the Roche lobe of the secondary to that of the primary through the inner Lagrangian point L_1. In Roche-lobe overflow almost all the mass lost by one component is accreted by the other.
(ii) Stellar-wind accretion: Massive star suffer significant mass-loss during their early evolution via strong almost spherical winds. These winds are manifested as outflows of plasma from the stellar surface into the interstellar medium. In these cases, some of the material of the donor's wind will be gravitationally captured by the compact companion.

In general, HMXBs are systems that accrete matter from an early (O or B) spectral-type companion. The OB donor has a strong stellar wind, with typical mass-transfer rates of $10^{-6} - 10^{-10}\,M_\odot$/yr. In systems with close orbits, mass is captured through the substantial stellar wind and powers the X-ray source. Roche-lobe (critical gravitational potential lobe) overflow can also be a supplement to the mass transfer rate in HMXBs, though on rare occasions (Charles & Coe 2005).

Stellar wind accretion

If the angular momentum of the outflowing material is low, then the gas can fall directly onto the compact object. This is the case in low density flows such as stellar winds. Stellar wind accretion is mostly seen in close binary systems that involve a compact object (neutron star or black hole) orbiting closely an early-type (O or B) star. Mass-loss rates as high as $10^{-5}\,M_\odot$/yr are observed from these luminous stars. One can imagine the compact object to be embedded in an outflowing stellar wind. One of the fundamental questions related to stellar wind accretion in XRBs is whether the amount of mass captured by the compact object is sufficient to power the X-ray source. Bondi & Hoyle (1944) calculated the amount of material accreted by a compact object traveling through a uniform medium. Using this result, we can then estimate the produced

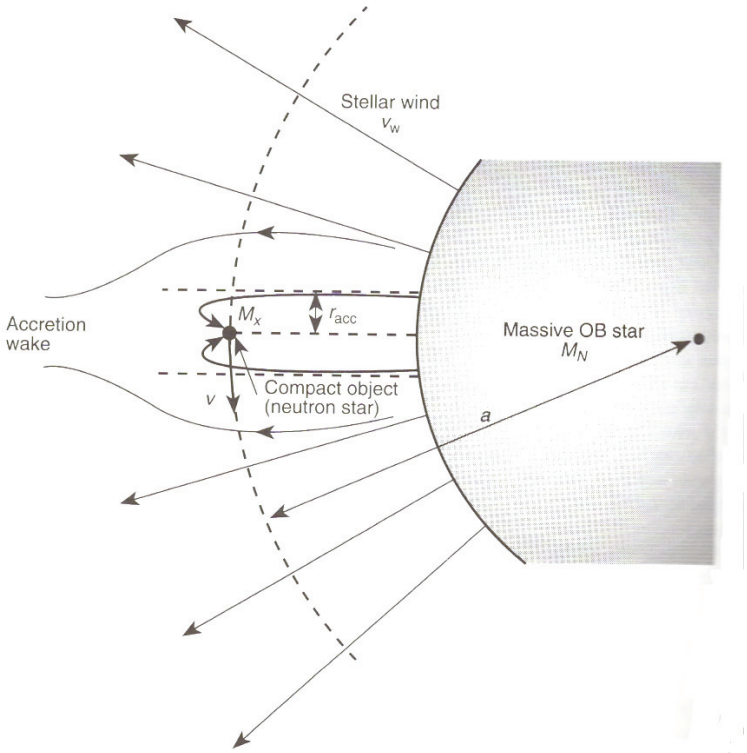

Figure 1.7 Geometry of stellar-wind accretion onto a compact object orbiting its massive companion. The amount of mass that is not accreted but its flow is perturbed forms an accretion wake beyond the compact object (adapted Fig.7.B3 from Charles & Seward 1995).

X-ray luminosity for a compact object of mass M_x orbiting with velocity v_x a star (of mass M_{OB}) at a distance α from its center. The star (in this case an early-type) is losing mass through an intense wind of velocity v_w (Figure 1.7).

The velocity of the wind relative to the star will be

$$v_{rel}^2 = v_x^2 + v_w^2 \tag{1.1}$$

where

$$v_x^2 = GM_{OB}/\alpha \tag{1.2}$$

Material within a cylinder of radius r_{acc} will be captured by the compact object, while mass outside this cylinder will escape. This critical radius is also known as the *capture radius*. Material can only be accreted in cases where its potential energy near the compact object is in magnitude larger than its kinetic energy. So, for a particle of mass m this translates to

$$r_{acc} = 2GM_x/v_{rel}^2 \tag{1.3}$$

The accreted by the compact object mass per unit time is then given by the mass supply through the accretion cylinder, which is

$$\dot{\mathrm{M}} = \pi \mathrm{r}_{\mathrm{acc}}^2 \mathrm{v}_{\mathrm{rel}} \rho \tag{1.4}$$

For a uniform stellar wind the density ρ is equal to

$$\rho = \dot{\mathrm{M}}_{\mathrm{w}} / 4\pi\alpha^2 \mathrm{v}_{\mathrm{w}} \tag{1.5}$$

Solving the above system of equations we get the fraction of the wind captured by the compact object:

$$\frac{\dot{\mathrm{M}}}{\dot{\mathrm{M}}_{\mathrm{w}}} = \frac{1}{4} (\frac{\mathrm{r}_{\mathrm{acc}}}{\alpha})^2 \frac{\mathrm{v}_{\mathrm{rel}}}{\mathrm{v}_{\mathrm{w}}} \tag{1.6}$$

From the above we get accretion rates of order $10^{-4} - 10^{-3}$ of the mass-loss rate $\dot{\mathrm{M}}_{\mathrm{w}}$, thus the stellar-wind accretion is an inefficient process when compared to Roche-lobe overflow. However, sources accreting via stellar winds are observable because of the high mass-loss rates (typically $\sim 10^{-6} - 10^{-5}\,\mathrm{M}_{\odot}/\mathrm{yr}$).

If a mass m is accreted onto the surface of a star with mass M and radius R, then the gravitational potential energy released by the accretion is $\Delta \mathrm{E}_{\mathrm{acc}} = \mathrm{GMm/R}$. For a neutron star $\Delta \mathrm{E}_{\mathrm{acc}} \sim 10^{20}$erg/s with typical values R $\sim$ 10km and M $\sim$ $\mathrm{M}_{\odot}$. If all the kinetic energy of the infalling matter is transformed to radiation at the stellar surface, then the *accretion luminosity* is $\mathrm{L}_{\mathrm{acc}} = \mathrm{GM}\dot{\mathrm{M}}/\mathrm{R}$. By including appropriate units the above formula can be written as:

$$\mathrm{L}_{\mathrm{acc}} = 1.3 \times 10^{36} \dot{\mathrm{M}}_{16} (\mathrm{M}/\,\mathrm{M}_{\odot}) (10\mathrm{km/R}) \mathrm{erg/s}, \tag{1.7}$$

where $\dot{\mathrm{M}} = 10^{16} \dot{\mathrm{M}}_{16}$g/s (Frank, King & Raine 2005). For typical values of accretion rates in HMXBs ($\sim 1.5 \times 10^{-10}\,\mathrm{M}_{\odot}/\mathrm{yr} \sim 10^{16}$g/s) we estimate a luminosity of 10^{36}erg/s for a neutron star accreting from a stellar wind, emitted mainly as X-rays. For comparison, main sequence late O and B stars have luminosities of the order of $\sim 5\,\mathrm{L}_{\odot} \sim 10^{34}$erg/s (Binney & Merrifield 1998).

We can also derive the X-ray luminosity as a function of the mass-loss rate. If we introduce the Schwarzschild radius of a star, $r = 2GM/c^2$, the accretion luminosity can be written as:

$$\mathrm{L}_{\mathrm{acc}} = \frac{1}{2} \dot{\mathrm{M}} \mathrm{c}^2 \frac{\mathrm{r}}{\mathrm{R}} = \eta \dot{\mathrm{M}} \mathrm{c}^2, \tag{1.8}$$

where $\eta = 1/2 \times (\mathrm{r/R})$ is the efficiency of conversion of the rest mass energy of the accreted matter into radiation. For typical values of mass and radius for neutron stars it is $\eta = 0.1$. Thus

accretion onto neutron stars is a very powerful source of energy, especially when compared to the energy release from the conversion of hydrogen to helium ($\eta = 0.007$). Combining equations (1.6) and (1.8), and assuming that the wind velocity v_w is much larger than the orbital velocity v_x, we get:

$$L_x \sim \eta \frac{\dot{M}_w c^2}{4} (\frac{2GM_x}{\alpha})^2 {v_w}^{-4} \tag{1.9}$$

Thus, the L_x is proportional to the mass-loss rate $\dot{M}$ and very sensitive to the wind velocity v_w.

Accretion disk formation

The transfered material has in many cases rather high specific angular momentum, so it cannot be accreted directly onto the compact object. The gas tends to follow a circular orbit because this is the orbit of lowest energy for a given angular momentum. We thus expect, in cases of Roche-lobe overflow, the gas initially to orbit the primary in the binary plane at a radius R_{circ}, such that the Keplerian orbit at R_{circ} has the same angular momentum as the transferring gas had on passing through L_1. However, within such a ring there are dissipative processes (e.g. collisions of gas elements, shocks, viscous dissipation, etc.) which convert some of the energy of the orbital motion about the primary into internal (i.e. heat) energy. Eventually, some of this energy is radiated and therefore lost from the gas. In order to overcome this energy loss, the gas sinks deeper into the gravitational potential of the primary by orbiting closer to it. This in turn results in more angular momentum losses. In such cases we might expect most of the gas to spiral slowly inwards towards the primary through a series of approximately circular orbits in the binary orbital plane, a configuration known as an *accretion disk*. This spiralling-in process results in a loss of angular momentum, and since there are no external torques, this can only occur by transfer of angular momentum outwards through the disk by internal torques. Now, the outer parts of the disk gain angular momentum and spiral outwards (Frank, King & Raine 2002).

X-ray Pulsars

Neutron stars with strong magnetic fields ($\sim 10^{12}$G) and misaligned magnetic and rotation axes exhibit X-ray pulsations. In this case (as is the case for Be/XRBs), regardless if there

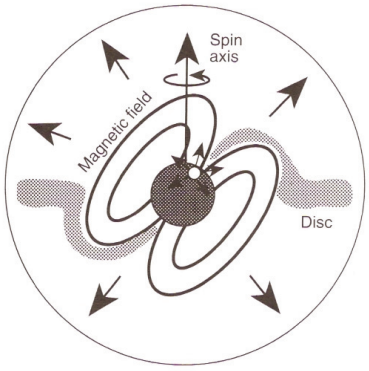

Figure 1.8 Illustration of an X-ray pulsar and its magnetosphere (adapted Fig.7.8 from Charles & Seward 1995).

is a disk or not, the gas will eventually reach a point where its motion will be controlled by the magnetosphere of the compact object. At this magnetospheric radius, the gas will move along the magnetic field lines (Field 1.8) and will fall to the magnetic polar caps of the neutron star. The material will hit its surface, and X-rays will be produced. Because of the existence of material just above the poles, the X-ray emission is shadowed. The X-ray pulsars are observable whenever the beamed emission from the magnetic poles crosses the line-of-sight.

Corbet (1984) found a strong correlation between the orbital periods (P_{orb}) of Be/neutron star binaries and the spin period (P_s) of the neutron star. Since then many authors have presented an updated version of the so-called "Corbet" diagram (e.g. Schmidtke & Cowley 2005 for SMC X-ray pulsars). The strong correlation between these two quantities implies that the Be-XRBs all have similar neutron star characteristics and average circumstellar density profiles. The $P_{orb} - P_s$ correlation is a result of the slow equatorial Be winds, which affect the equilibrium spin period of the pulsar (Waters & van Kerkwijk 1989). In the SMC they have been found 51 X-ray pulsars so far (listed in the online census of Malcolm Coe[4]), with pulse periods in the range 0.09s to 1323s. However, the majority of SMC X-ray pulsars have relatively short pulse periods (< 200s; Figure 1.9).

[4]http://www.astro.soton.ac.uk/∼mjc/ as of 13/02/2008.

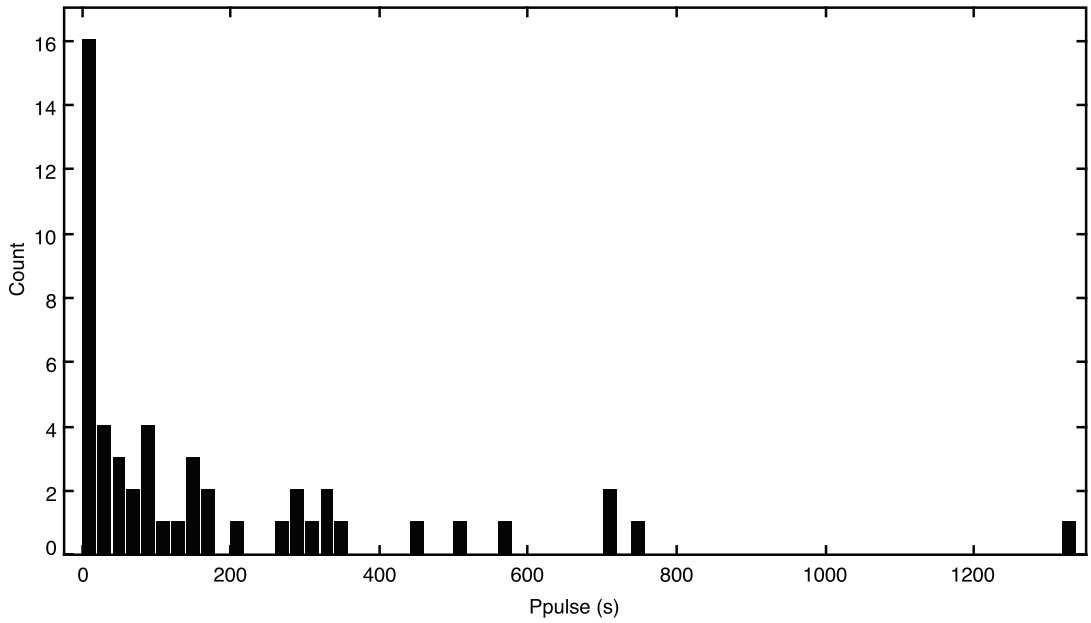

Figure 1.9 The distribution of the X-ray pulse periods of SMC pulsars (using data from the online census of Coe; for details refer to the text).

1.3.2 Be/X-ray Binaries

Be-XRBs are the most numerous sub-class of HMXBs. In the census of Liu et al. (2005) there are 53 and 10 confirmed Be-XRBs out of the 92 and 36 HMXBs in the SMC and the LMC, respectively (i.e. 57% for the SMC and 28% for the LMC). In the Milky Way, out of the 114 HMXB candidates, $\sim$ 60% are known or suspected Be-XRBs, while 32% are supergiant/X-ray binaries (SG-XRBs; Liu et al. 2006). However, some sources in both catalogs are only tentatively identified as HMXBs on the basis of their X-ray properties similar to the known HMXBs (transient character and/or a hard X-ray spectrum; Liu et al. 2005), while one third of the HMXBs remains optically unidentified because of the large uncertainty in the X-ray source position of historically known X-ray sources (for example, detected with Einstein or ASCA).

The orbit of the Be-XRBs is generally wide and eccentric (e $\sim$ 0.3). Persistent Be-XRB systems have orbital periods of several hundred days, while they show low X-ray luminosity ($L_X < 10^{36}$ erg/s). The bright pulsating transient Be-XRBs have orbital periods of a few tens of days.

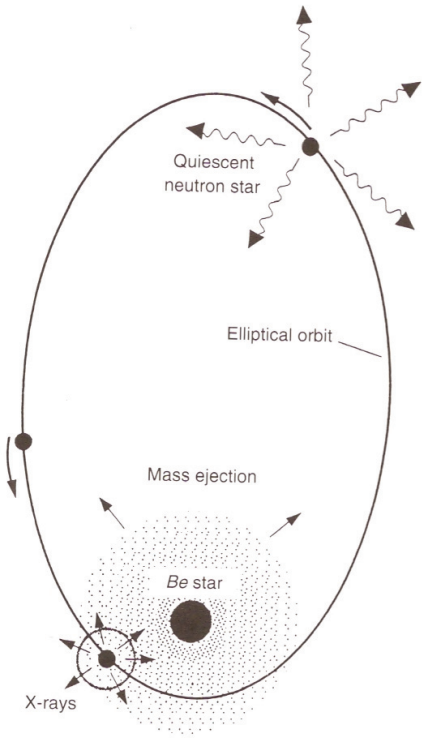

Figure 1.10 X-ray outbursts are related to the passage of the neutron star through the circumstellar disk of the Be star (adapted Fig.7.22 from Charles & Seward 1995).

Systems in quiescence have even lower luminosities ($L_X < 10^{34}$ erg/s). X-ray outbursts are related to the passage of the neutron star through the circumstellar disk (Figure 1.10). This disk around the Be stars is often referred to as a decretion disk, while it forms from a high density equatorial outflow (currently believed to be due to the high velocities of Be stars; Meynet 2008). The Be-XRBs accrete directly from the decretion disk, thus these systems are very variable. In particular, the main behavior of Be-XRB systems can be summarized to the following (from the review of Charles & Coe 2006):

1. *Type-I outbursts:* regular periodic outbursts during periastron passage characterised by moderate increases of the X-ray luminosity (typically $L_X < 10^{37}$ erg/s) lasting a few days
2. *Type-II outbursts:* giant outbursts at any phase with the X-ray luminosity reaching near Eddington values ($L_X \sim 10^{38}$ erg/s for a neutron star), probably arising from a sudden expansion of the circumstellar disk, lasting several tens of days
3. *Non-detected (i.e. looked for but not found) outbursts:* related to low H_α emission, thus a

small disk, or to other unknown reasons

General properties of Be stars

A Be star is defined as "a non-supergiant B star whose spectrum has, or had at some time, one or more Balmer lines in emission" (Collins 1987). Nowadays, this wide definition excludes Herbig AeBe stars, Algol systems, etc. The circumstellar line emission in Be stars forms in the equatorial decretion disk, while Be stars rotate fast at $> 70\% - 80\%$ of their critical velocity (Porter 1996). Martayan et al. (2006) showed that the initial velocities of the Be stars are significantly higher than the initial velocities of the normal B stars, giving some support to the view that only stars with a sufficiently high initial velocity can go through a Be episode. The reason that makes Be stars fast rotators is still a subject of debate, however, Langer & Heger (1998) discuss the evolution of surface parameters of rotating massive stars during the main sequence and find that the outer layers may spin up as a result of the evolution of the angular momentum distribution.

The most common lines in emission are those of H_I, He_I, Fe_{II}, and sometimes also Si_{II} and Mg_{II} (Porter & Rivinius 2003). Their strength can vary significantly, ranging from total absence (thus classifying them as normal B-type stars during this period) to re-appearance even after decades. In the Bright Star Catalog the mean frequency of Be stars is 17%, though it doubles for early-type Be stars (B1e stars; Zorec & Briot 1997). Maeder, Grebel & Mermilliod (1999) studying 1 cluster in the SMC and 9 in the LMC (in the same age interval) found a relative fraction of Be stars to all B stars of 39% and 23%, respectively. We mention here that the above numbers should to be considered as lower limits because of the episodic nature of the "Be phenomenon". The Hα line strength varies significantly, following the disappearance and reappearance of the decretion disk. McSwain et al. (2008) estimate that 25-50% of the Be stars may go undetected in a single spectroscopic observation, and photometric snapshots are even less likely to discern such weak emitters. Despite the limited sample in the study of Maeder, Grebel & Mermilliod (1999), they found that there are more fast rotators among massive stars at lower metallicity. Moreover, Ekström et al. (2008) found that the transfer of angular momentum to the outer layers of the star, thus its spin up, becomes more efficient for stars of higher initial mass and/or higher initial metallicity. However, they note that at high metallicity, mass loss becomes more

and more important and can prevent the stars from reaching the breakup limit.

Another characteristic of Be stars is their observed infrared excess. The circumstellar disk around a Be star can contribute to its luminosity. However, the disk contribution to the continuum emission is significant only at relatively long wavelengths (near- and mid-IR), since the disks have relatively low temperatures compared to the central stars (typically $T_{disk} \approx 1/2 T_{eff}$; Negueruela & Coe 2002). The observed infrared excess of Be stars is usually interpreted as free-free and free-bound emission from a hot gas envelope around the Be star, while it tends to increase as the spectral type of the central star becomes early, most probably because of the increased number of stellar photons short of the Lyman limit (Gehrz, Hackwell & Jones 1974).

The long-term (multiyear) optical light curves of Be stars show high variability. Multiyear optical light curves for SMC, LMC, and Milky Way sources can be found in the OGLE-II[5] (Udalski, Kubiak & Szymański 1997; Zebruń et al. 2001) and MACHO[6] database (Alcock et al. 1999). Some show clear periodic outbursts, others exhibit a slow change in mean brightness, and some show extreme variability with swoops and dips that may last months or years: in such studies, the challenge is to find any underlying periodic behavior that persists even through the long-term changes (Schmidtke et al. 2004).

1.3.3 Supergiant X-ray Binaries

Supergiant XRBs form the second subclass of HMXBs. In SG-XRBs, the mass donor is a massive star of luminosity class I or II. The compact object accretes material from a highly supersonic wind (radially outflowing), thus these systems are persistent X-ray sources (in contrast to Be-XRBs that accrete directly from the decretion disk of the Be star; Charles & Coe 2005). Because of the much steadier wind outflow, the X-ray emission tends to be at a regular low-level. Outbursts may occur rarely, but there will not be observed regular periodic outbursts at periastron (Type I outbursts; §1.3.2). The shorter orbital period systems have circular orbits, whereas the longer period systems show some eccentricity.

[5] http://ogle.astrouw.edu.pl/

[6] http://wwwmacho.mcmaster.ca/Data/MachoData.html

In the SMC there is only one known source of this type, SMC X-1 (Webster et al. 1972), located in the Wing. Nagase (1989) discovered SMC X-1 as an X-ray pulsar with 0.72s pulse period, 3.89d orbital period, while it has been identified as a B0Ib supergiant (optical companion source Sk 160; Sanduleak 1968). Bradt & McClintock (1983) found an L_x of $\sim 6 \times 10^{38}$ergs^1 in the 2-11keV band (derived from the maximum observed flux density).

1.4 Low-Mass X-ray Binaries

In Low-Mass X-ray Binaries (LMXBs) the companion star is of late (later than A) spectral type or it can even be a white dwarf in more evolved systems. These companions do not have strong stellar winds to power the X-ray source, and the mass transfer occurs when the companion fills its Roche lobe. The optical counterparts of LMXBs are intrinsically faint objects. A few characteristic emission lines (broad H and He emission lines) superposed on a rather flat continuum are observed in their optical spectra. The optical continuum of LMXBs is dominated by the emission from an accretion disk around the compact object as a result of the reprocessing of a fraction of the X-rays into optical photons in the disk, while the contribution from the secondary is generally negligible (Liu et al. 2007). Thus the companion stars of LMXBs are continuously hidden from view in the glare of the X-ray illuminated disk. Evidence on the nature of the compact object in most bright LMXBs is indirect (Charles & Coe 2006), for example from X-ray bursting behavior for neutron stars (as few of them are X-ray pulsars) or fast variability as first seen in Cygnus X-1 (the latter is also used as a diagnostic tool for black-hole candidates). The typical L_X of low X-ray luminosity systems, which are predominantly X-ray burst sources, is $\sim 10^{36} - 10^{37}$erg/s.

1.5 The SMC observed in X-rays

The proximity of the SMC, its relatively small size compared to the LMC and the detailed knowledge of its stellar content make it an excellent laboratory to study the young X-ray binary populations (HMXBs). Such studies in our own Galaxy are hampered by interstellar extinction and distance uncertainties. The first X-ray survey of the SMC with the *Einstein* satellite revealed

a large number of discrete X-ray sources, several of which were found to be Be/X-ray binary pulsars (Wang et al. 1992). The first systematic study of these populations was performed with the Röntgen Satellite (ROSAT; Trümper 1993) in the soft (0.1-2.5 keV band) and with the Advanced Satellite for Cosmology and Astrophysics (ASCA; Tanaka, Inoue & Holt 1994) in the hard (0.5-10.0 keV) bands. Both surveys showed a wealth of X-ray binary pulsars, several of which were identified with Be stars, and a large number of X-ray emitting supernova remnants (SNRs; Yokogawa et al. 2002; Haberl et al. 2000; Sasaki et al. 2000; Sasaki et al. 2002). More recently, a 10-year long monitoring campaign of selected fields with the Rossi-X-ray Timing Explorer (Rossi-XTE; Bradt, Rothschild & Swan 1993) has added several more transient X-ray binary sources in our recording of X-ray binaries in this galaxy (Laycock et al. 2005; Galache et al. 2008). Essentially every new X-ray observation of the SMC reveals a few more Be-XRBs. This has been also demonstrated by the recent *XMM-Newton* observations of selected fields in the SMC, which identified a few more X-ray binaries (Haberl & Pietsch 2004).

Overall, the majority of the X-ray binaries (92 in total; Liu et al. 2005) are located at the SMC "Bar" and the "Wing" regions, which are the regions of the most recent star-formation. So far 55 X-ray sources have been confirmed as X-ray binary pulsars based on the detection of X-ray pulsations. Twenty-eight of them are identified with Be stars, indicating that they are Be-X-ray binaries, while 26 additional X-ray sources, without detected X-ray pulsations, are identified with Be-stars also suggesting that they are Be-X-ray binaries (Liu et al. 2005). There are also 39 additional sources classified as HMXBs, based either on their association with an early-type star (lacking any more detailed spectroscopic classification) or the measurement of a hard X-ray spectrum.

1.6 Goals and thesis outline

In the present work we address the main open questions regarding the X-ray source population of the Small Magellanic Cloud:

1. Why the SMC hosts such a large number of known Be-XRBs (in comparison to the LMC and the Milky Way)?

2. How is this large number of Be-XRBs related to its star-formation history?

3. What are the properties of the Be-XRBs as a population?

In order to approach the above open questions, we observed the Small Magellanic Cloud both in X-rays and in optical. The results from the analysis of shallow ($\sim$ 10 ksec) *Chandra* observations of the central part of the SMC, along with the X-ray Luminosity Function of the sources associated with early-type stars, are presented in Chapter 2. The identification of new HMXB and candidate Be-XRBs from the *Chandra* survey is described in Chapter 3. The analysis of *XMM-Newton* observations of the outer parts of the SMC, which sample older stellar populations, and the identification of new candidate Be-XRBs are given in Chapter 4. The connection of star-formation history and HMXB populations is analyzed in Chapter 5, while the results of the optical spectroscopic follow-up of candidate Be-XRBs in the SMC with the 2dF spectrograph at the Anglo-Australian Telescope are given in Chapter 6. Finally, the main conclusions from this study and the future plans of this project are given in Chapter 7.

Bibliography

[1] Alcock, C., et al. 1999, Pub. Astr. Soc. Pacific., 111, 1539

[2] Binney, J., & Merrifield, M. 1998, Galactic astronomy / James Binney and Michael Merrifield. Princeton, NJ : Princeton University Press, 1998. (Princeton series in astrophysics) QB857 .B522 1998

[3] Bondi, H., & Hoyle, F. 1944, Mon. Not. R. Astr. Soc., 104, 273

[4] Bradt, H. V. D., & McClintock, J. E. 1983, Ann. Rev. Astron. Astrophys., 21, 13

[5] Charles, P. A., & Coe, M. J. 2006, Compact stellar X-ray sources, 215

[6] Charles, P. A., & Seward, F. D. 1995, Cambridge, New York: Cambridge University Press, —c1995, ISBN 0521261821

[7] Corbet, R. H. D. 1984, Astr. Astrophys., 141, 91

[8] Crowl, H. H., Sarajedini, A., Piatti, A. E., Geisler, D., Bica, E., Clariá, J. J., & Santos, J. F. C., Jr. 2001, Astron. Journ., 122, 220

[9] Dickey, J. M., & Lockman, F. J. 1990, Ann. Rev. Astron. Astrophys., 28, 215

[10] Frank, J., King, A., & Raine, D. J. 2002, Accretion Power in Astrophysics, by Juhan Frank and Andrew King and Derek Raine, pp. 398. ISBN 0521620538. Cambridge, UK: Cambridge University Press, February 2002.

[11] Giacconi, R., Gursky, H., Paolini, F. R., & Rossi, B. B. 1962, Physical Review Letters, 9, 439

[12] Gehrz, R. D., Hackwell, J. A., & Jones, T. W. 1974, Astrophys. J., 191, 675

[13] Harries, T. J., Hilditch, R. W., & Howarth, I. D. 2003, Mon. Not. R. Astr. Soc., 339, 157

[14] Harris, J., & Zaritsky, D. 2001, Astrophys. J. Suppl., 136, 25

[15] Harris, J., & Zaritsky, D. 2004, Astron. Journ., 127, 1531

[16] Hilditch, R. W., Howarth, I. D., & Harries, T. J. 2005, Mon. Not. R. Astr. Soc., 357, 304

[17] Langer, N., & Heger, A. 1998, Properties of Hot Luminous Stars, 131, 76

[18] Liu, Q. Z., van Paradijs, J., & van den Heuvel, E. P. J. 2005, Astr. Astrophys., 442, 1135

[19] Liu, Q. Z., van Paradijs, J., & van den Heuvel, E. P. J. 2006, Astr. Astrophys., 455, 1165

[20] Liu, Q. Z., van Paradijs, J., & van den Heuvel, E. P. J. 2007, Astr. Astrophys., 469, 807

[21] Lorimer, D. R., & Kramer, M. 2004, Handbook of pulsar astronomy, by D.R. Lorimer and M. Kramer. Cambridge observing handbooks for research astronomers, Vol. 4. Cambridge, UK: Cambridge University Press, 2004

[22] Maeder, A., Grebel, E. K., & Mermilliod, J.-C. 1999, Astr. Astrophys., 346, 459

[23] Martayan, C., Frémat, Y., Hubert, A.-M., Floquet, M., Zorec, J., & Neiner, C. 2006, Astr. Astrophys., 452, 273

[24] McSwain, M. V., Huang, W., Gies, D. R., Grundstrom, E. D., & Townsend, R. H. D. 2008, Astrophys. J., 672, 590

[25] Nagase, F. 1989, Pub. Astr. Soc. Japan., 41, 1

[26] Negueruela, I., & Coe, M. J. 2002, Astr. Astrophys., 385, 517

[27] Porter, J. M. 1996, Mon. Not. R. Astr. Soc., 280, L31

[28] Porter, J. M., & Rivinius, T. 2003, Pub. Astr. Soc. Pacific., 115, 1153

[29] Russell, S. C., & Dopita, M. A. 1992, Astrophys. J., 384, 508

[30] Sanduleak, N. 1968, Astron. Journ., 73, 246

[31] Schmidtke, P. C., Cowley, A. P., Levenson, L., & Sweet, K. 2004, Astron. Journ., 127, 3388

[32] Schmidtke, P. C., & Cowley, A. P. 2005, Astron. Journ., 130, 2220

[33] Tauris, T. M., & van den Heuvel, E. P. J. 2006, Compact stellar X-ray sources, 623

[34] Udalski, A., Kubiak, M., & Szymanski, M. 1997, Acta Astronomica, 47, 319

[35] van den Bergh, S. 2000, The galaxies of the Local Group, by Sidney Van den Bergh. Published by Cambridge, UK: Cambridge University Press, 2000 Cambridge Astrophysics Series Series, vol no: 35

[36] van den Heuvel, E. P. J., & van Paradijs, J. 1997, Astrophys. J., 483, 399

[37] Webster, B. L., Martin, W. L., Feast, M. W., & Andrews, P. J. 1972, Nature, 240, 183

[38] Westerlund, B. E. 1997, Cambridge Astrophysics Series, 29

[39] Wilke, K., Klaas, U., Lemke, D., Mattila, K., Stickel, M., & Haas, M. 2004, Astr. Astrophys., 414, 69

[40] Zaritsky, D., Harris, J., Thompson, I. B., Grebel, E. K., & Massey, P. 2002, Astron. Journ., 123, 855

[41] Zebrun, K., et al. 2001, Acta Astronomica, 51, 317

[42] Zorec, J., & Briot, D. 1997, Astr. Astrophys., 318, 443

Chapter 2

The *Chandra* survey of the SMC "Bar": X-ray source catalog and the Luminosity Function of High-Mass X-ray Binaries

We present results from the analysis of shallow ($\sim$ 10 ksec) *Chandra* observations of the central part of the SMC. We detect a total of 158 discrete X-ray sources down to a limiting luminosity of $\sim 4 \times 10^{33}$ erg s^{-1}. For those sources we calculate their X-ray intensities and X-ray colors. In order to avoid the large number of expected interlopers we focus on the X-ray sources associated with early-type stars. The spectral characteristics of these sources indicate that they have hard X-ray spectra with spectral indices typical of pulsar X-ray binaries. In addition we find a trend for lower-luminosity sources to have softer spectra, which we interpret in terms of a weaker accretion component and a stronger relative contribution of thermal emission from the surface of the neutron star. The X-ray luminosity function (XLF) of the sources associated with early-type stars is represented by a flat power-law with a cumulative slope of ($0.35^{+0.12}_{-0.11}$). In addition there is an indication for a break at $\sim 10^{35}$ erg s^{-1}, with high and low luminosity cumulative slopes of ~ 0.6 and ~ 0.18, respectively. The high end of the XLF is consistent with the XLFs observed in other star-forming galaxies. The flattening of the XLF can be explained in

terms of the standard Be/X-ray binary model, where the pulsar undergoes intermittent accretion episodes during its passage through the decretion disk of the donor. The transition between the accretion and quiescent phase can be quite sharp resulting in a "desert range" on their XLF. Finally, we see indication for a steepening of the XLF at low luminosities ($< 10^{34}$ erg s^{-1}), which in combination with the softer spectra of these sources indicates that we are beginning to detect the brightest quiescent High-Mass X-ray Binaries.

Subject headings: galaxies: irregular — galaxies: individual — X-rays: galaxies

2.1 Introduction

The Small Magellanic Cloud (SMC) at a distance of ∼60 Kpc (Hildich et al. 2005) is our second nearest star-forming galaxy. It has been extensively studied in virtually every wavelength (see e.g. van den Bergh 2000). Detailed studies of its star-formation history show that it experienced a burst of star-formation $\sim 30-60$ Myr ago (Harris & Zaritsky 2004), along with an older star-formation event ($\sim$ 400 Myr ago) and widespread star-formation a few Gyr ago which led to the formation of a smooth stellar spheroid (e.g. Gardiner & Hatzidimitriou 1992, Hatzidimitriou 1999). The most prominent recent star-forming activity took place in the central part of the SMC along its North-East South-West axis, giving it its bar-like appearance in optical wavelengths. Enhanced star-formation during the past $\sim$ 15 Myr is also present at the interface between the Small and the Large Magellanic Clouds (the SMC Wing region; Harris & Zaritsky 2004).

The proximity of the SMC, its relatively small size compared to the LMC and the detailed knowledge of its stellar content make it an excellent laboratory to study the young X-ray binary populations (High-Mass X-ray Binaries; HMXBs). Such studies in our own Galaxy are hampered by interstellar extinction and distance uncertainties. The first X-ray survey of the SMC with the *Einstein* satellite revealed a large number of discrete X-ray sources, several of which were found to be Be/X-ray binary pulsars (Wang et al. 1992). The first systematic study of these populations was performed with the Röntgen Satellite (ROSAT; Trümper 1993) in the soft (0.1-2.5 keV band) and with the Advanced Satellite for Cosmology and Astrophysics (ASCA; Tanaka, Inoue & Holt 1994) in the hard (0.5-10.0 keV) bands. Both surveys showed a wealth of X-ray binary pulsars, several of which were identified with Be stars, and a large number of X-ray emitting supernova remnants (SNRs; Yokogawa et al. 2002; Haberl et al. 2000; Sasaki et al. 2000; Sasaki et al. 2002). More recently a 10-year long monitoring campaign of selected fields with the Rossi-X-ray Timing Explorer (Rossi-XTE; Bradt, Rothschild & Swan 1993) has added several more transient X-ray binary sources in our tally of X-ray binaries in this galaxy (Laycock et al. 2005; Galache et al. 2008). Essentially every new X-ray observation of the SMC reveals a few more Be X-ray binaries. This has been also demonstrated by the recent XMM-Newton observations of selected fields in the SMC, which identified a few more X-ray binaries (Haberl & Pietsch 2004). Overall the majority of the X-ray binaries are located at the SMC "Bar" and the "Wing" regions, which are the regions of the most recent star-formation. So far

55 X-ray sources have been confirmed as X-ray binary pulsars based on the detection of X-ray pulsations. Twenty-eight of them are identified with Be stars, indicating that they are Be-X-ray binaries, while 26 additional X-ray sources, without detected X-ray pulsations, are identified with Be-stars also suggesting that they are Be-X-ray binaries (Liu et al. 2005). There are also 39 additional sources classified as HMXBs, based either on their association with an early-type star (lacking any more detailed spectroscopic classification) or the measurement of a hard X-ray spectrum.

In terms of the overall populations Shtykovskiy & Gilfanov (2005), derived the X-ray luminosity function (XLF) of the X-ray sources with early-type optical counterparts detected in several publicly available *XMM-Newton* observations of the SMC and the LMC. The find that the XLF of young X-ray sources in both galaxies are similar to those of other more distant star-forming galaxies. However, they find an indication for a flattening of the XLF in low fluxes (below $\sim 2 \times 10^{35}$ erg s^{-1}). They show that the "propeller effect" starts to become important only at luminosities below $\sim 10^{33}$ erg s^{-1}. This effect refers to the inhibition of the accretion flow in low accretion rates, due to the increased strength of the magnetic pressure compared to the inflowing gas pressure (e.g. Illarionov & Sunyaev 1975).

From these results it is clear that the SMC offers a unique environment to study the populations of young X-ray binaries and in particular the faint end of their X-ray luminosity distribution. This led us to initiate a shallow wide-area X-ray survey of the central part of the SMC with *Chandra* and XMM-Newton. This survey is complemented by two longer *Chandra* pointings, which provide a 10-fold increase in our detection limit. In this paper we describe the wide-area *Chandra* survey of the SMC "Bar", the analysis of the data and the the properties of the detected X-ray source populations. The identification of the optical counterparts, the optical spectroscopic observations of the brightest of them, and the detailed X-ray analysis of the bright X-ray sources are presented in three companion papers (Antoniou et al. 2008a; Antoniou et al. 2008b; Taylor et al. 2008, in prep.). In Section 2 of this paper we describe the parameters of the *Chandra* survey; in Section 3 we present the data analysis procedures and the X-ray source catalog; in Section 4 we describe the calculation of incompleteness corrections for different off-axis angles and the derivation of the X-ray luminosity function of the detected sources; and in Section 5 we discuss these results and their implications for the understanding of the young X-ray binary populations.

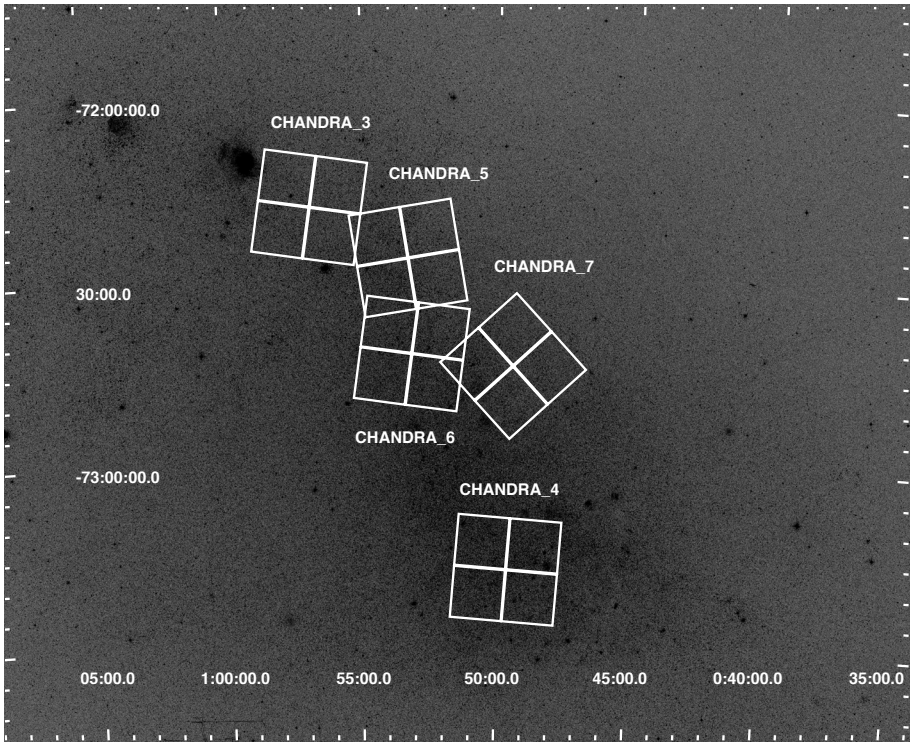

Figure 2.1 A DSS image of the SMC with overlaid the footprints of the ACIS-I arrays of the 5 *Chandra* fields.

2.2 Description of the survey

The *Chandra* survey consists of 5 fields along the SMC "Bar" observed with the Advanced Camera and Imaging Spectrometer (ACIS; Garmire et al. 2003). The surveyed regions were chosen to be on the SMC-"bar", on the basis of its high star-forming activity and the large number of known X-ray binaries from previous X-ray surveys, which ensures the detection of large populations of new sources and allows us to study the already known sources in lower activity states. In Fig. 2.1 we present the footprints of the observed fields on a Digitized Sky Survey (DSS) image of the SMC.

We opted to use the ACIS-I array because of its large field of view ($16' \times 16'$). In addition to the 4 ACIS-I chips (0,1,2,3) we also used chips 6 and 7 of the ACIS-S array in order to increase the area coverage (albeit with lower sensitivity because of the large off-axis angle). The exposure time of each field was adjusted in order to reach an absorption-corrected luminosity of 5×10^{33} erg s^{-1}, given the average HI column density from the maps of Stanimirovic et

Table 2.1. Summary of observations

Field	RA (J2000)	Dec (J2000)	Exposure	N_H	Conv. factors[1]
	h m s	° ′ ″	ksec	10^{20} cm^{-2}	Obs. (corrected)
(1)	(2)	(3)	(4)	(5)	(6)
3	00 56 46.14	-72 18 10.78	9.28	5.94	9.16 (9.86)
4	00 49 30.74	-73 16 52.34	11.59	4.96	9.16 (9.72)
5	00 53 11.45	-72 26 29.92	7.66	6.33	9.18 (9.93)
6	00 53 04.40	-72 42 18.22	9.32	6.33	9.18 (9.92)
7	00 49 25.00	-72 44 22.80	8.83	6.19	9.16 (9.88)

[1]Counts to flux conversion factor in units of 10^{-12}erg/cm^2/count in the 0.5-7.0 keV band, assuming a power-law spectrum ($\Gamma = 1.7$) with Galactic-line-of-sight absorption (Column 5).

al. (1999). The observations were performed between May and October 2002, in FAINT mode because of telemetry limitations (POG). The coordinates of the pointings and the parameters of each exposure are presented in Table 2.1. In Column (1) we give the Field ID; in Columns (2) and (3) we give the RA and Dec (J2000) of the field center (aimpoint of the ACIS-I array), in Column (4) we give the exposure time; in Column (5) we give the average HI column density for each field, in Column (6) we give the observed (and absorption corrected) count rate to flux conversion factor for the aimpoint of each field, assuming a power-law model ($\Gamma = 1.7$) and the HI column density from Column (5).

2.3 Data analysis

The data analysis was performed with the CIAO tool suite v3.4, and CALDB v3.4. We analyzed the 5 datasets following the standard *Chandra* data analysis threads [1]. First the type-1 events files were reprocessed with the *acis_process_events* task in order to correct for the time dependent gain shift[2] and Charge-Transfer Inefficiency effects (Townsley et al. 2000), reject cosmic ray afterglows and apply the latest calibration data. We then created type-2 event files by applying the standard screening criteria (event ASCA grades 0,1,2,3,4,7) and in-flight Good-Time Inter-

[1]http://asc.harvard.edu/ciao/threads/index.html

[2]http://asc.harvard.edu/ciao/why/acistgain.html

vals (GTIs). In order to search for background flares we created lightcurves from the detector area excluding any bright sources in each field. Inspection of these lightcurves showed no strong flares in any of the five observations.

The absolute astrometric accuracy of *Chandra* is $\sim 0.5''$[3]. Because of the very high spatial density of optical sources in the central part of the SMC it is not possible to correct for any residual astrometric offsets by cross-correlating the positions of bright X-ray sources with optical or infrared catalogs (e.g. SDSS and 2MASS). Instead, we used the few X-ray sources in each field with known optical counterparts (see Antoniou et al. 2008a) in order to check the absolute astrometry of these observations. We found that all X-ray sources had offsets smaller than $0.5''$ from their optical counterparts, which are consistent with the nominal pointing accuracy of *Chandra*. From our analysis we excluded the ACIS-S array CCDs because of their large off-axis angles which results in heavily degraded Point Spread Functions (PSFs) and therefore hampers the detection and localization of faint sources.

For each field we created images and exposure maps in four bands: soft (S; 0.3-1.0 keV), medium (M; 1.0-2.5 keV), hard (H; 2.5-7.0 keV) and full band (F; 0.3-7.0 keV), based on the event energies assigned by *acis_process_events*. We also created broad band exposure maps in the same bands by combining monochromatic exposure maps representing narrower bands defined so the effective area within each one does not vary by more than 20%. The narrow band maps were weighted only for their different energy range, which is equivalent to a flat energy spectrum or no spectral weighting (see Zezas et al. 2007). The latest release of CIAO (v3.4) and CALDB (v3.4) allow us to include in the exposure maps the spatial variations of the ACIS sensitivity due to the contaminant on the detector window.

We also created adaptively smoothed images using the *csmooth* task of the CIAO package. In order to avoid oversmoothing faint sources the minimum and maximum smoothing scales were set at 1 and 5 pixels, which correspond to an average significance of 2σ and 5σ respectively. In order to minimize chromatic aberration (resulting from larger smoothing scales in the bands with fewer counts), we used for each band the smoothing scales calculated for the full band image. In order to correct for sensitivity variations across the detector area, the smoothed images were exposure corrected by dividing them with exposure maps smoothed with the same scales as

[3]http://asc.harvard.edu/cal/ASPECT/celmon/

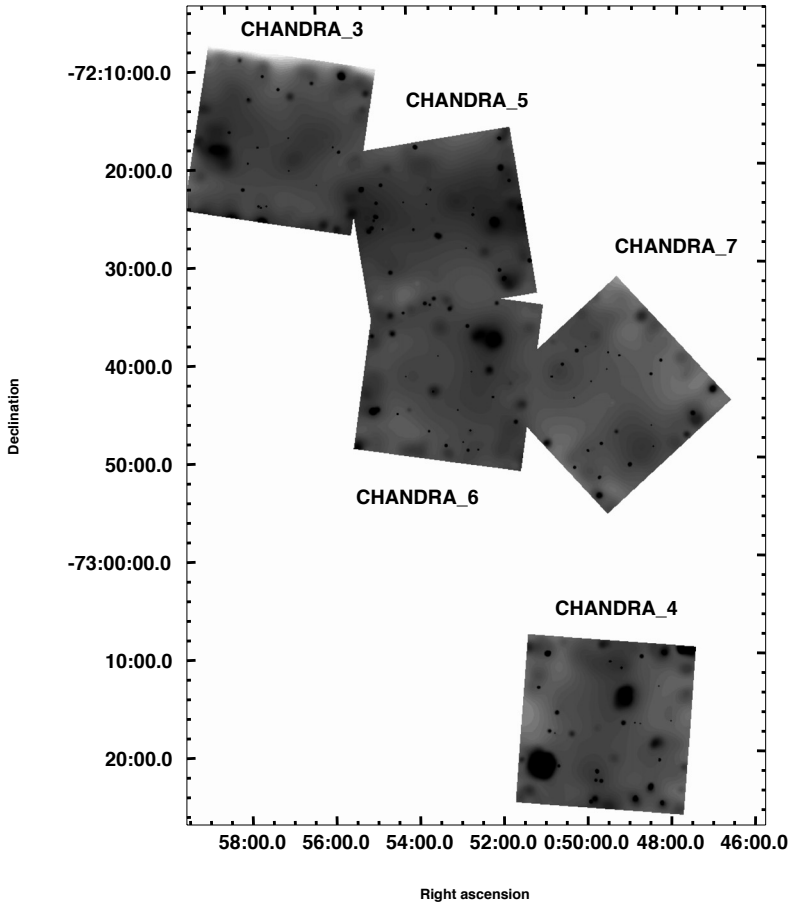

Figure 2.2 An adaptively smoothed full-band (0.5-7.0 keV) mosaic of the observed fields.

the images (in order to compensate for non-conservation of flux by the multiscale smoothing process). In Figure 2.2 we present an adaptively smoothed full-band mosaic of the 5 fields.

2.3.1 Source Detection

We searched each dataset for sources in each of the four bands. The source detection was performed with the *wavdetect* tool which employs a wavelet-based source detection algorithm. This algorithm is more reliable than sliding-cell algorithms in cases of very faint sources and sources of different sizes (Freeman et al. 2002). The latter is particularly important in the case of these ACIS-I observations because of the large variations of the PSF over the observed field. The source search was performed in wavelet scales (radii of the Mexican Hat wavelet function) of 1, 2, 4, 8, 16 and 32 pixels. In order to minimize the number of false detections on the CCD

gaps, for each *wavdetect* run we used the appropriate exposure map. The detection significance threshold was set to 2×10^{-7}, which corresponds to one false detection over the ACIS-I array.

The results from the *wavdetect* runs in each of the four energy bands (F, S, M, H) for a given field, were combined in order to create the final list of detected sources. The results of the source detection were visually inspected to ensure that all individual sources were included in the final source list.

In total we detect 158 sources in all 5 fields, and between 27 and 38 sources in each individual exposure. Our detection limit is $\sim 4 \times 10^{33}$ erg s^{-1} for on-axis sources (distance from optical axis $< 2.5'$). In Fig. 2.3 we present the full band, adaptively smoothed, exposure corrected, images of the five SMC fields. On these images the detected discrete sources are marked by circles, and named using the numbering in Tables A.1–A.5 (see §2.3.2).

2.3.2 Source Parameters

In order to determine the parameters of the detected X-ray sources, we defined source apertures on a case by case basis, including as many of the full-band source counts as possible, but at the same time minimizing contamination from nearby sources and background (see also Zezas et al. 2002). In order to ensure that each extraction aperture includes at least 90% of the counts for each source, the minimum source aperture was fixed to the 90% encircled energy radius, estimated from PSF models at different positions on the detector. The model PSFs were calculated for an energy of 1.5 keV, since most of the counts of each source are in the 1-2.5keV range. We note that the regions produced by *wavdetect* cannot be used for photometry, because they are based on a spatial fit of the distribution of the source counts and they may include other nearby sources or instrumental artifacts. We did not perform any correction for the finite aperture size since even our smallest aperture after the manual adjustments encompasses more than 99% of the encircled energy of a point source at each off-axis angle. Similarly, local background was estimated from circular or elliptical annuli around each source, excluding any encompassed sources. The inner radius of the annulus was set to be slightly larger than the source aperture in order to exclude any emission from the wings of the source PSF. The background regions were chosen to be large enough to provide a good determination of the background,

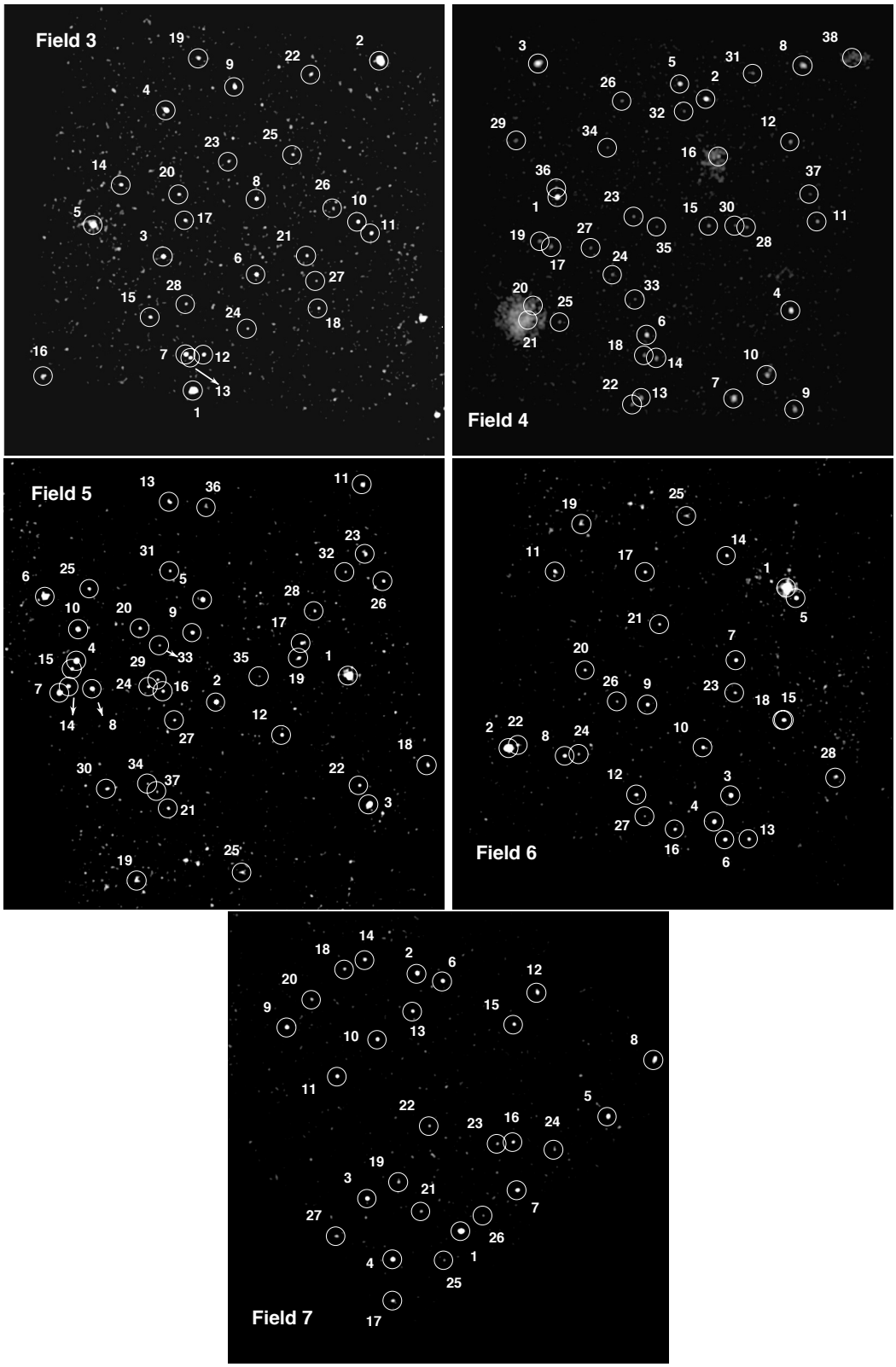

Figure 2.3 Full band, adaptively smoothed, exposure corrected, images of the five SMC fields (their orientation is not the same). The detected sources are shown with circles and their numbers correspond to the naming convention in Tables A.1–A.5.

while at the same time avoiding strong gradients of the detector sensitivity.

Using these extraction apertures we measured the number of counts for every source in each field and in each of the S, M, H and F bands. In order to perform direct comparisons of the intensities and hardness ratios between sources in the same field, we converted the measured counts to equivalent counts at the aimpoint of each field. The effective areas of these reference points are very similar (less that 5% difference), also allowing direct comparisons between sources in different fields (see Zezas et al. 2007 for a discussion of the effect of this normalization method on the measured source parameters). Fluxes for each source are calculated assuming a power-law model ($\Gamma = 1.7$) absorbed by the average Galactic column density along the line-of-sight to each field (Table 2.1). Since the measured source intensities were normalized to the aimpoint of each observation, we used count-rate-to-flux conversion factors calculated for the effective area at this position. The factors to convert count rates in the 0.3-7.0 keV band in each observation to observed flux in the 0.1-10.0 keV band are presented in Table 2.1. In parenthesis we also give the conversion factors to absorption corrected flux.

For each source we also calculated X-ray colors (Col1 = log(S/M), Col2 = log(M/H), Col3 = log(S/H), where S, M, H are the source counts in the soft medium and hard bands, respectively) using the Bayessian Estimation of Hardness Ratios (BEHR; Park et al. 2006). This method estimates the X-ray colors by taking into account the Poisson nature of the event detection process, and allowing for variations of the effective area. Because is it based on a Poisson model of the source intensity it provides accurate estimates of the uncertainties, and upper limits on the colors in the case of non detection in one of the two bands. Following Park et al. 2006, we use the mode of the color distribution, since it gives a more appropriate representation of the most likely color than the mean in the case of faint sources.

The source lists for each field are presented in Tables A.1–A.5. These tables give the source parameters from the detected sources in order of source intensity: Column (1) gives the source identifier used throughout this series of papers, Column (2) gives the CXC name of each source, and Columns (3) and (4) give the RA and Dec (J2000) of the source centroids. Columns (5)–(7) give the source parameters in the full band: number of observed (uncorrected for background and exposure effects) source counts, the ratio of the effective area at the position of each source with respect to the aimpoint of each observation, the number of background counts within

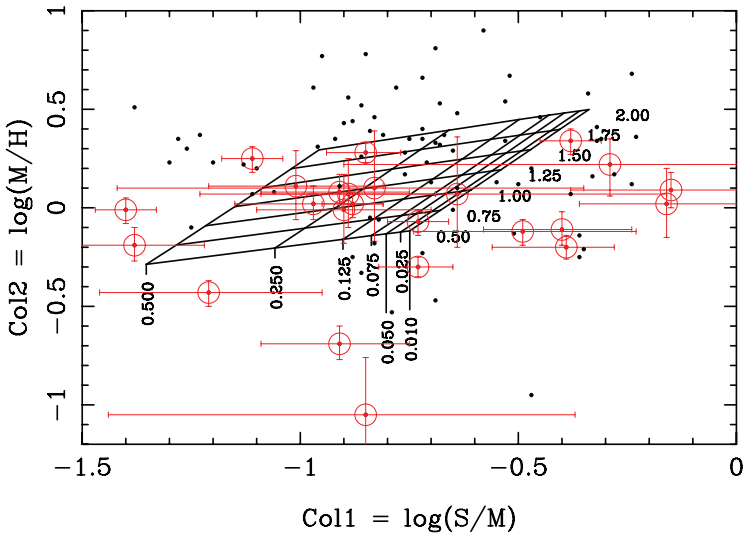

Figure 2.4 X-ray color-color diagram of the detected sources in all fields, using the X-ray colors estimated with the BEHR algorithm (see text). The grid shows the expected X-ray colors for an absorbed power-law model. The horizontal lines correspond to different values of photon index Γ, while the vertical lines correspond to different valus of HI column density (in units of 10^{22} cm^{-2}). Sources associated with early-types stars are marked with red circles.

the background aperture, the ratio of the source and background apertures, the number of net counts using BEHR (which accounts for background contamination, effective area variations and the Poisson nature of the observed counts detection probability), the source significance in σ assuming the Gehrels approximation (Gehrels 1986), the off-axis angle of each source, and the logarithm of the absorption corrected source luminosity in the 0.1–10.0 keV band assuming a power-law spectrum ($\Gamma = 1.7$) and Galactic line-of-sight HI column density for each field.

In Tables A.6–A.10, we present the photometric measurements in each of the soft, medium and hard bands, and the calculated X-ray colors. In Column (1) we give the source ID, in Columns (2)–(5), (6)–(9), and (10)–(13) we give the observed, background and net, effective area corrected counts (also calculated using BEHR), and the normalized effective area in the soft, medium and hard bands respectively. In Columns (14)–(16) we give the three X-ray colors (Col1 = log(S/M), Col2 = log(M/H), Col3 = log(S/H)).

In Figure 2.4 we present a Color-Color diagram for the detected sources. On this diagram we overlay grids which correspond to power-law and thermal (APEC; Smith et al. 2001) spectra of varying photon index, temperature and HI column density. We also mark the locus of $\Gamma =$

$0.6 - 1.5$ which is the typical photon index range for X-ray binary pulsars (e.g. Yokogawa et al. 2003). From these plots we see that there is large scatter in the spectral parameters of the detected sources. We find a number of sources within the locus of the X-ray binary pulsars, several of which are associated with Be stars (Antoniou et al. 2008a). We also find a number of sources to the right of the spectral grids (i.e. in regions of very low column density). Inspection of the X-ray spectra of these sources shows that they have a strong thermal component, resulting in a low inferred column density when compared to a simple absrorbed power-law model (see Taylor et al. 2008; in prep.).

2.4 X-ray Luminosity Function of point sources

X-ray luminosity functions are a powerful tool for the study of the X-ray source populations, and allow us to compare the overall source luminosity distribution between different galaxies or different populations within the same galaxy. From the measured source luminosities in the full band we constructed the X-ray luminosity functions (XLFs) for the sources detected in each individual field, as well as the combined XLF of sources detected in all 5 fields. Each exposure provides an independent snapshot of the dynamic X-ray source population (Zezas et al. 2007), and since the observations are taken at random time intervals, and different positions, we can safely combine the XLFs from the individual fields. In the case of multiple detections of the same source in the overlapping regions of Fields 3-5, 5-6, and 6-7 we include in the combined XLFs only the detection which is closer to the optical axis. In order to avoid complications due to source variability, different energy bands and the incompleteness of the ROSAT and ASCA surveys we defer an XLF study including data from these surveys to a future publication.

2.4.1 Incompleteness correction

In order to estimate the source detection probability we followed the same approach as in Zezas et al. (2007), by performing detailed simulations for sources of different intensities observed at different background levels. Because of the large variations of the PSF across the field of view, the detection efficiency is a strong function of position (in addition to source intensity and local background). Therefore, in the present study we extend this incompleteness correction

by measuring the effect of observing sources at different off-axis and azimuthal angles. The simulations were performed with the MARX v3.0 simulator for *Chandra* observations, and the source detection was performed with *wavedetect* using the same parameters as for the actual data. For each combination of source intensity, background level, off-axis and azimuthal angle, we performed 25 simulations in order to account for statistical variations. The fraction of the input sources which were detected for each case gives the detection probability. We find that there is no dependence of the detection probability on the azimuthal angle for a given off-axis angle. Therefore we calculate the incompleteness correction by averaging the incompleteness curves at all azimuthal positions for a given off-axis angle. In Figure 2.5 we present the incompleteness correction as a function of source intensity for different off-axis angles and background levels (in counts/pixel). As discussed in Zezas et al. (2007), since the completeness functions are measured in terms of the source intensity in counts, these results are applicable to any other study using the same detection method, regardless of the source spectrum, detector or detection band.

From the incompleteness function we can calculate the overall detection probability for sources of different intensities over the area of each field. In Fig. 2.6 we plot the background surface brightness (in cnts/pixel) against the observed number of counts for each source. In the same plot we overlay contours of the 50% and 75% completeness level for different off-axis angles. It is clear that sources with as few as 7 observed counts, equivalent to a luminosity of 4.0×10^{33} erg s^{-1} in the 0.5-7.0keV band (assuming an average count-rate to luminosity conversion factor for all fields, and an average exposure of 10 ksec), have a detection probability higher than 75%. This is a result of the very low background of *Chandra*. We note that we do not impose a S/N ratio limit; a source at this level would correspond to a significance of 2σ. We consider this limit as the nominal completeness limit of our survey. In the calculation of the XLF we only include sources down to this limit because fainter sources are severely affected by the Malmquist bias, which is not accounted for in our analysis.

2.4.2 Background and foreground sources

Because of the relatively large area of the survey and the low stellar density of the SMC, a large number of the detected sources are expected not to be associated with the SMC. In order to estimate the number of these sources we use the broad-band LogN-LogS fits of Kim et al. (2007),

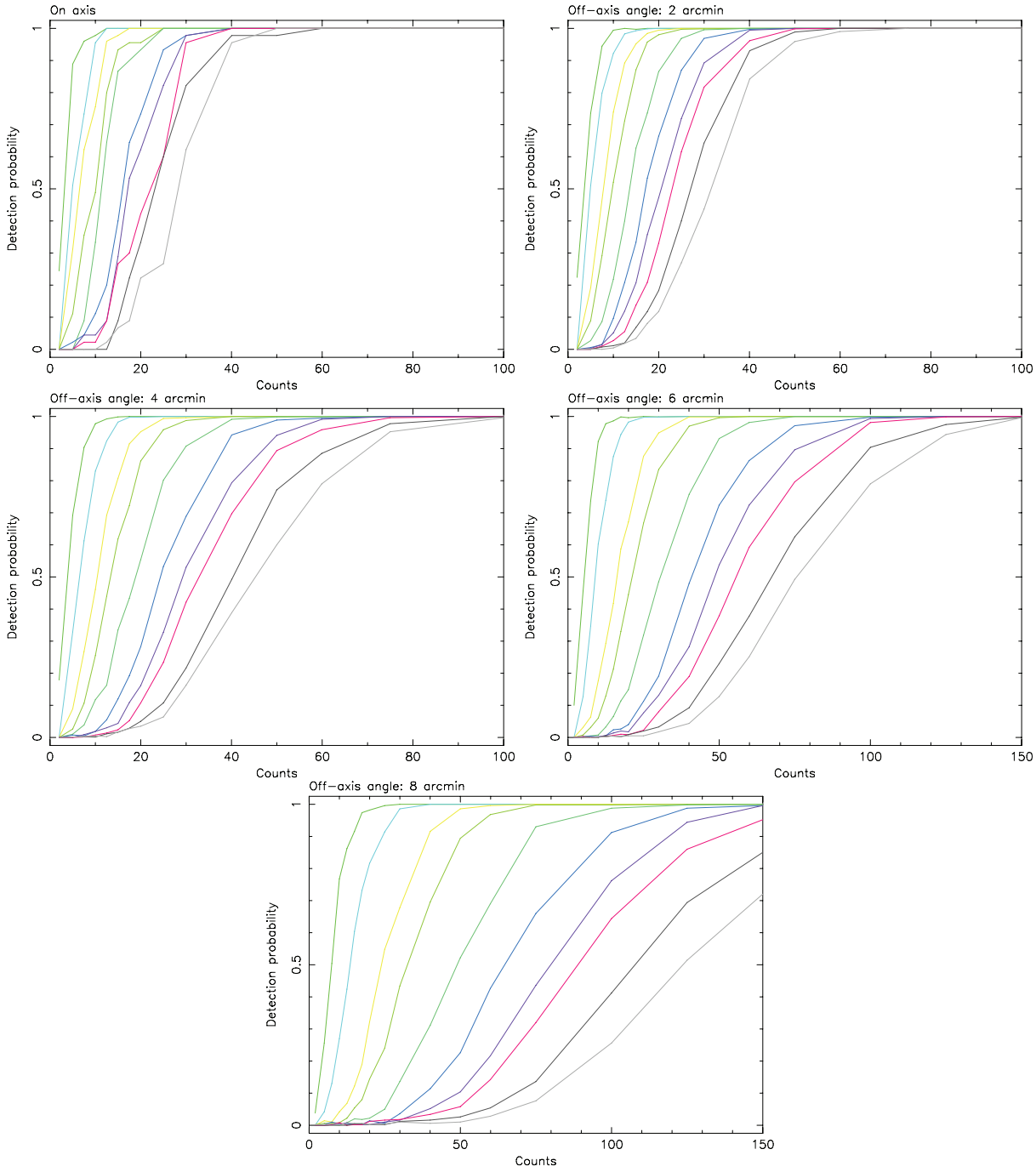

Figure 2.5 Plot of the source detection probability curves for different background levels: from left to right (in each plot) 0.0005, 0.005, 0.03, 0.08, 0.3, 0.5, 0.8, 1.0, 1.6, 2.1 cnts/pix and different off axis angles (different panels): from left to right and top to bottom : on-axis, 2, 4, 6, 8′off-axis. Notice the x-axis scale difference in the last three panels.

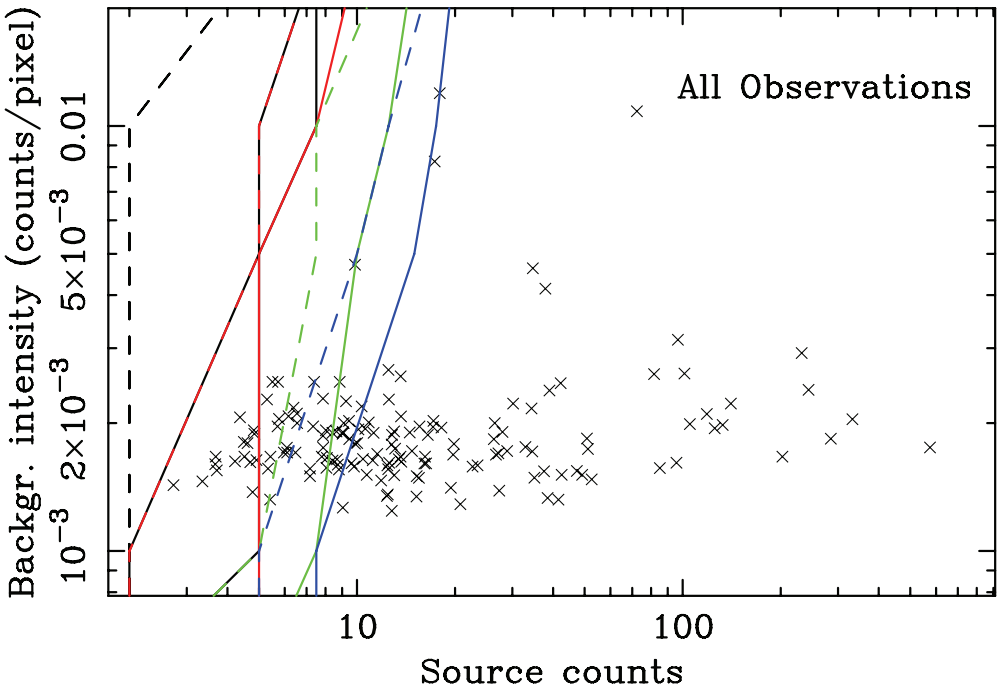

Figure 2.6 Plot of the local source background surface brightness versus net source number of counts for sources detected in the 5 Fields. The solid and dashed lines show the 50% and 75% completeness limits for sources at a given background level and source intensity (black, red, green and blue lines are for off-axis angles of $0'$, $2'$, $4'$, $6'$, respectively). Sources to the left and top of these curves have lower detection probability.

normalized for the area of the ACIS-I detector. Based on this LogN-LogS we estimate an average of 30-35 interlopers per ACIS-I field. Although this number is highly uncertain because of the cosmic variance (e.g. Kim et al. 2004 find a factor of 3 variation between the normalization of the LogN-LogS in different *ChaMP* fields), it clearly shows that the number of sources associated with the SMC in each field is too small to allow for any XLF fits.

2.4.3 The XLF of High-Mass X-ray Binaries

In order to overcome the problem of background contamination we focus on the XLF of HMXBs by selecting sources associated with early-type stars (O and B spectral types) based on the photometric and spectroscopic properties of their optical counterparts (Antoniou et al. 2008a, 2008c). These properties indicate that the majority of these sources are Be-XRBs, i.e. X-ray binaries accreting from an emission line early-type star. The accreted material in these objects

comes from a decretion disk around the donor star (which is also responsible for the emission lines; e.g. Coe & Charles 2006). This selection criterion gives a total of 29 (28 of which are above the 7 counts limit) in a narrow range of ages (30-70 Myr; Antoniou et al. 2008b).

Because of the relatively small number of sources and in order to obtain the maximum information from our data, we fitted their unbinned luminosity function. We performed the fit using the *Sherpa* fitting package following the same approach as in Zezas et al. (2007). First we bin the list of source intensities in counts space, in ascending order and with a bin size of one count. This "natural" binning scheme gives the maximum resolution, without artificially increasing the number of bins. We take into account incompleteness effects by calculating an ancillary response function (ARF) on the same grid as the XLF. In the case of a sample with a uniform background this ARF is effectively the detection probability as a function of source intensity. However, in our case, where the sources have very different backgrounds and are observed in different off-axis angles, the ARF consists of the detection probability of each source in each bin based on its observed background, off-axis angle, number of counts, and the incompleteness function discussed in § 2.4.1. For bins which include more than one source, the value of the ARF is their average detection probability, while for bins with no source we estimate the value of the ARF by interpolation. Because of the small number of counts the fit was performed using the Cash statistic (Cash 1979).

The observed and incompleteness corrected XLFs are presented in Fig.2.7 with the dashed and solid lines, respectively. The hatched area shows the 90% confidence bounds based on Monte Carlo simulations of the unbinned XLF (see e.g. Zezas & Fabbiano 2002): for each source we obtained 1000 samples of its intensity assuming a Poisson distribution with a mean equal to the observed number of counts. Each of these simulated XLFs was binned to the "natural" binning grid of the observed XLF, and the standard deviation of the number of sources in each bin is a measure of the uncertainty of the observed XLF due to the uncertainty of the intensity of each source. To this uncertainty we add in quadrature the uncertainty of the number of sources in each bin of the observed XLF, following the Gehrels approximation (Gehrels 1986). Finally we plot these errors on the cumulative XLF. We note that this method is only used for illustrative purposes; all fits are performed on the differential XLFs as described in the previous paragraph. For comparison, in the right panel of the same plot we show the XLF of the overall X-ray source population. Based on the above methods we find that the XLFs of the HMXB population in

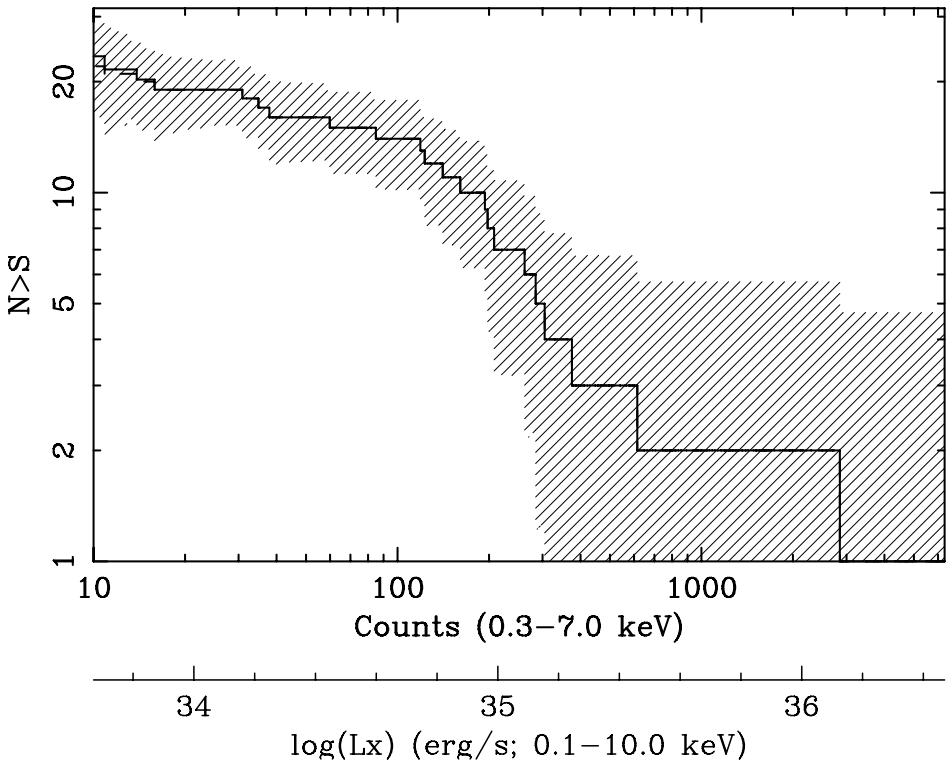

Figure 2.7 Plot of the completeness-corrected (solid line) and uncorrected (dashed line) cumulative XLFs of the sources with early-type counterparts in all fields. The hatched area shows the 1σ uncertainty of the XLF taking into account uncertainties of the number of sources as well as of their luminosity (including Poisson noise on the number of observed source counts and spectral uncertainties).

the SMC "Bar" is fitted with a power law with a cumulative slope of $0.35^{+0.12}_{-0.11}$. The results of the XLF fits are presented in Table 2.2.

In order to assess the significance of a low-luminosity turnover, we also fit the combined XLF with a broken power law of the form:

$$N(L) = \begin{cases} A(\frac{L}{L_{ref}})^{-\alpha_l} & \text{for } L \leq L_b \\ A\prime(\frac{L}{L_{ref}})^{-\alpha_h} & \text{for } L \geq L_b \end{cases}$$

where $A' = A(\frac{L_b}{L_{ref}})^{\alpha_2-\alpha_1}$ Here, α_1 and α_2 are the slopes below and above the break point, respectively, A is the number of sources at the reference luminosity L_{ref}, and L_b is the luminosity of the break-point. This fit gives low and high-luminosity cumulative slopes of $\alpha_l = 0.6$ and $\alpha_h = 0.18 \pm 0.22$ and a break-point at 1.2×10^{35} erg s^{-1}. Unfortunately, because of the small number of sources the parameters of the break-point and the low-luminosity slope are poorly constrained, while the fit statistic is only slightly improved. Because of the very small number of

Table 2.2. XLF fits

Model	Norm† Sources	L_b erg s^{-1}	α_h	α_l
(1)	(2)	(3)	(4)	(5)
power law	$1.13^{+0.40}_{-0.31}$	...	$0.35^{+0.12}_{0.11}$	...
broken power-law	$0.92^{+0.42}_{-0.31}$	1.2×10^{35} *b*	0.65 *b*	$0.19^{+0.20}_{-0.23}$

Note. — † Normalization of the XLF at 4.67×10^{33} erg s^{-1} (10 counts).
b Unconstrained parameter.

sources in each bin (less than 5, and typically 0) as well as because the position of the break-point has a fixed low bound (zero), it is not legitimate to use the F-test to compare the broken and the single power-law fits (e.g. Protassov et al. 2002). Instead, we perform extensive simulations for the simple and broken power-law models in order to calibrate the likelihood ratio test (LRT; e.g. Cowan 1998), in a similar way as in Zezas et al. (2007). We find that the broken power law provides a marginally improved fit over the simple power law at the 90% confidence level for the combined dataset.

2.5 Discussion

In the previous section we presented the results from our analysis of the *Chandra* observations of 5 fields along the central part of the SMC. These observations provide a detailed view of the low luminosity young X-ray source populations. We detect 158 sources down to a typical detection limit of 4.0×10^{33} erg s^{-1} (0.5-7.0keV). From the *Champ* LogN-LogS curve we find that the majority of these sources are not associated with the SMC. However, based on their optical identifications we find 27 sources associated with early type stars, most of which are Be stars (Antoniou et al. 2008a). We find that the XLF of these High Mass X-ray Binaries can be described by a flat power-law with a cumulative slope of ~ 0.4, somewhat flatter but consistent to that seen in other star-forming galaxies. Its shape shows an indication for a flattening at $\sim 10^{35}$ erg s^{-1}, although a fit with a broken power-law provides only a marginal statistically significant improvement. Next we discuss these results in the context of the Be/X-ray binary

phenomenology.

2.5.1 The HMXB population of the SMC as seen with *Chandra*

The X-ray colors of the X-ray binaries (Fig. 2.4) indicate that they have photon indices in the typical ranges of X-ray binary pulsars ($\Gamma = 0.6 - 1.5$; e.g. Yokogawa et al. 2003). In contrast to the narrow range of their X-ray colors above 1.0 keV (Col2 is sensitive to the power-law slope), Fig.2.4 shows a wide range of soft X-ray spectra, manifested by the spread of their Col1. This reflects a wide range of absorbing column densities and/or an additional thermal component. The population of Be-XRBs in the left of the diagram does not fall in a region of high HI column density (based on the maps of Staminirowich et al. 1999), indicating that the enhanced absorption is not due to foreground material but instead due to the immediate environment of the binary (e.g. material from the donor's wind).

In addition there is a population with very high values of Col1, indicative of very low absorption or more realistically an additional soft spectral component below 1.0 keV. Such a component could be due either to diffuse emission around the binary, or thermal emission from the surface of the pulsar. However, only a couple sources are close to regions of diffuse emission (which in any case is accounted for in the estimated source counts for each band). In Fig. 2.8a we plot Col1 against the X-ray luminosity of the X-ray sources, with the HMXBs (most of which are consistent with Be-XRBs) marked with red circles. We see a systematic effect for lower luminosity X-ray binaries to have softer spectra, which favors the pulsar thermal emission scenario, and indicates that at lower accretion rates (i.e. closer to apastron) we observe an increasing contribution from the neutron star thermal emission (i.e. decreasing contribution of the pulsed flux from the accretion flow). The fact that all these systems fall in a similar range of Col2 values as the overal population of Be X-ray binaries (Fig.2.8b) indicates that the softening of the spectrum is unlikely to be the result of the small number of counts, and a hard component (possibly from the accretion flow or the hotspot on the pulsar surface) is present even in very low luminosities. However, we note the gap between the soft/low-luminosity and the harder/higher-luminosity sources in the Col1-L_X plot. This gap could be due to the "propeler effect" (see below), since outbursting (hard) sources are above a luminosity cutoff, and low-accretion or quiescent (stronger soft component) sources are in much lower luminosities.

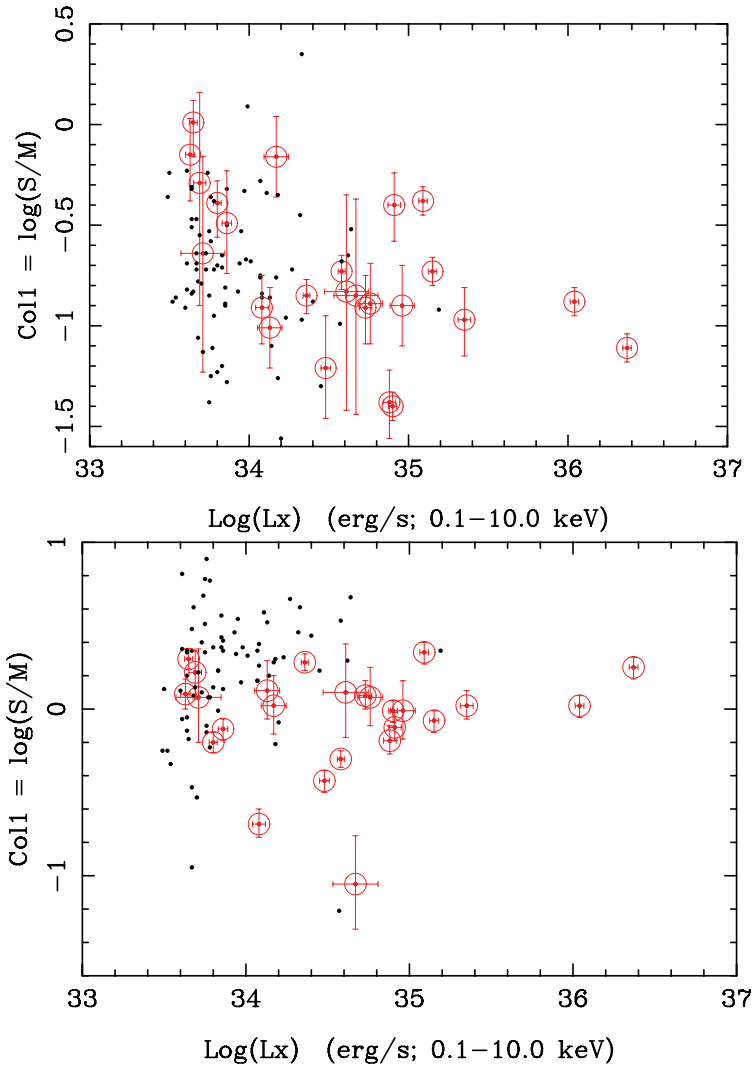

Figure 2.8 A plot of Col1 (Top; a) and Col2 (Bottom; b) against the X-ray luminosity (0.1-10.0 keV band) of the X-ray sources, with the Be/X-ray binaries marked with circles.

Comparison of this survey with previous surveys of the same area with ROSAT and ASCA, shows that we detect most of the previously known sources, but with typically lower luminosities. This suggests that we observe these sources in a low state of activity, while the small number of outbursting sources is consistent with the long periods and high eccentricities expected for Be/X-ray binaries. This in combination with the small number of sources observed in outburst (defined as sources with luminosities above 10^{37} erg s^{-1}, and close to the Eddington limit of a neutron star) also shows that they spend a very small fraction of their orbit accreting at high rates. This is in agreement with the very sharp and narrow peaks of the orbital-period folded lightcurves of X-ray binary pulsars detected with Rossi-XTE (Laycock et al. 2005).

2.5.2 The faint-end of the XLF of young XRBs and the "propeller effect"

The shape of the X-ray luminosity function is consistent to that reported by Shtykovskiy & Gilfanov (2005) based on archival *XMM-Newton* observations of the SMC. The overall slope (cumulative slope of $\alpha = 0.35^{+0.12}_{-0.11}$) is similar (but somewhat flatter) to that observed in other star-forming galaxies ($\alpha \sim 0.5$). We also confirm the flattening at luminosities below $\sim 10^{35}$ erg s^{-1} reported by Shtykovskiy & Gilfanov (2005). We note that this is not due to incompleteness effects since the sources at that range have $\sim 100 - 200$ counts.

In order to explain this flattening we revisit the standard model of Be/X-ray binaries (Stella et al. 1986; Negueruela 1998). According to this model we expect three main accretion phases depending on the orbital phase and orbital parameters of the system:

1. *Outburst phase* This occurs during the passage of the pulsar through the deccretion disk of the donor star (periastron). The high gas density and the low velocity of the equatorial circumstellar disk results to the accretion of gas onto the pulsar through the magnetic field lines. If the gas density is high enough an accretion disk may form. During this phase we observe the periodic Type-I bursts and the stronger and more random Type-II bursts (Negueruela 1998). This phase is expected to be short and its duration to be limited by the density profile of the decretion disk ($\rho = \rho_0(r/R)^{-n}$, where n is the density parameter and takes typical values between 2.0-3.0; Stevens et al. 1991; Waters et al. 1988).

2. *Low level accretion phase* While the pulsar is within the viscinity of the donor it accrets gas from the fast stellar wind rather than the more dense circumstellar disk. This phase occurs before and after the periastron passage. At the second occurence of this phase (while the pulsar is moving towards apoastron) we may also have accretion from any residual material left after the outburst phase. This would result in an asymmetry in the orbital-period folded lightcurves of Be X-ray binaries. Such an asymmetry is indeed seen in the lightcurves presented by Laycock et al. (2005).

3. *Quiescent phase* In the case of binaries with eccentric orbits (which is the case for most Be/X-ray binaries; e.g. Bilsden et al. 1997), the pulsar is expected to spend a significant part of the orbit outside the equatorial decretion flow. Since the radial dependence of this flow can be approximated by a power-law form $\rho = \rho_0(r/R)^{-n}$ (where r is the distance

from a star of radius R, ρ_0 is the central wind density and n is the density parameter which takes typical values between 2.0-3.0; Stevens et al. 1991; Waters et al. 1988), the gas density outside the decretion disk is expected to be quite low (and dominated by the much faster, more tenuous spherical wind). In this case, we would expect the transition to magnetospheric accretion (which occurs if the Alfvén radius is within the co-rotation radius), where the accretion flow is inhibited due to the magnetic pressure of the pulsar ("propeler effect"; Illarionov & Sunyaev 1975), and the emitted luminosity changes abruptly (e.g. Stella et al. 1986), by a factor $f = (\frac{GMP^2}{4\pi^2 R^3})$=$170 M_{1.4}^{1/3} R_6^{-1} P^{2/3}$, where G is the gravitational constant, R_6 is the radius of the neutron star in units of 10^6cm, P is its period in seconds, and $M_{1.4}$ is its mass in units of $1.4\,\mathrm{M}_\odot$ (Corbet et al. 2006). Therefore, the "propeler effect" is expected to dominate in this "accretion-starved" regime, and any X-ray emission would be produced by the heated surface of the pulsar.

The duration of these three phases depends on the concentration of the wind (described by the slope of its radial density distribution), the eccentricity, inclination and size of the orbit. Raguzova & Lipunov (1998) find that more eccentric, longer period systems have stronger and sharper outbursts. Their simulated lightcurves show large scale and often abrupt transitions in the X-ray luminosity of the pulsar as it orbits the donor (the so-called "luminosity gap"; see also Corbet 2006). This behaviour is in agreement with the orbital-phase folded lightcurves of SMC Be-XRBs monitered by XTE (Laycock et al. 2005). Therefore it is possible that: (a) Be/X-ray binary pulsars spend a significant fraction of their orbit in quiescence or a low-accretion rate regime, and (b) depending on their orbital parameters, there can be a sharp change in their luminosity as they move from the outburst to the quiescence phase. The critical luminosity where this happens depends on the spin period and the magnetic field strength (which control the "propeller effect"), but also the decretion disk parameters (which control the accretion flow).

This simple scheme would result in a small number of sources in outburst (X-ray luminosities in excess of 10^{37} erg s^{-1}), a larger number of sources in lower luminosities, down to the critical luminosity for the onset of the "propeller effect" and, depending on the distribution of orbital periods and eccentricities, a number of quiescent low luminosity sources. Between the last two regimes we expect a "desert range" of luminosities, with a very small number of sources and therefore a turnover in their luminosity function. In lower luminosities where we start seeing the heated surface of the pulsar, we would expect a rise in the number of sources, with the

slope depending on the duty cycle and therefore the orbital characteristics of the X-ray binaries. There is indeed a hint for an up-turn in low luminosities ($L_X \sim 1034$ erg s^{-1}) in the XLF presented in Fig. **??**. As discussed in §2.5.1 the detection of a stronger soft component in the lowest-luminosity sources provides further support for this idea.

Shtykovskiy & Gilfanov (2005) calculate the result of the "propeller effect" on the X-ray luminosity function of the HMXBs in the LMC, and they find that it should produce a flattening between $10^{32} - 10^{33}$ erg s^{-1} depending on the strength of the magnetic field. However, both the XLF and spectral properties of the detected sources show evidence for the onset of the propeller effect at higher luminosities ($\sim 10^{35}$ erg s^{-1}). The discrepancy with the theoretical calculation could be due to either stronger magnetic fields for the SMC pulsars, or more likely the eccentric orbits of HMXBs. In this case, as described earlier, the combination of the propeller effect and the low gas density outside the decretion disk can result in an abrupt change from the outburst state to the quiescent state, with a few sources being in the "low accretion rate regime". Given the luminosity range of the sources observed in our survey, we only have a couple sources which can be classified as outbursting, while the majority of the sources in the $10^{35} - 10^{36}$ erg s^{-1} range would be in the "low accretion rate regime". Because of the very small number of outbursting sources it is not possible to obtain a reliable measurement of their XLF during outburst (which would reflect the distribution of accretion rates during the passage through the donor's deccretion disk). Adopting the standard HMXB XLF from Galactic and extragalactic young X-ray binary populations (which includes several different types of sources) may result in an overestimation of the distribution of accretion rates in Be X-ray binaries which is the dominant population in the SMC, and in turn underestimation of the critical luminosity for the onset of the propeller effect. Moreover, in the 3-phase model described earlier the accretion rates in the "low-accretion" regime, where the propeller effect is becoming important, are much lower than during outburst which would result in a higher-cutoff luminosity and therefore a higher luminosity break than predicted by Shtykovskiy & Gilfanov (2005).

2.6 Conclusions

We presented the analysis of shallow ($\sim$ 10 ksec) *Chandra* observations of the central part of the SMC. We detect a total of 158 discrete X-ray sources down to a detection limit of 4×10^{33} erg s^{-1}. Of those only 27 sources are found to be associated with early-type stars in the SMC (Antoniou et al. 2008a). From the spectral characteristics and luminosity function of the X-ray sources associated with early-type stars we found that:

- They have hard-ray spectra typical of pulsar X-ray binaries.
- There is a trend for lower-luminosity sources to have softer spectra, which is consistent with a weaker accretion component and a stronger relative contribution of thermal emission from the surface of the neutron star.
- Their X-ray luminosity function can be represented by a flat power-law with a cumulative slope of $(0.35^{+0.12}_{-0.11})$. There is also an indication for a break at $\sim 10^{35}$ erg s^{-1}, with low and high luminosity cumulative slopes of ~ 0.6 and ~ 0.18, respectively.
- The high end of the XLF is consistent with the XLFs observed in other star-forming galaxies.
- The flattening of the XLF can be explained in terms of the standard Be-XRB model, where the pulsar undergoes intermittent accretion episodes during its passage through the decretion disk of the donor. The transition between the accretion and quiescent phase can be quite sharp resulting in a "desert range" on their XLF.
- There is indication for a steepening of the XLF in low luminosities ($< 10^{34}$ erg s^{-1}) which, in combination with the softer spectra of the low-luminisity sources, indicates that we are observing the brightest quiescent X-ray binaries.

This work was supported by NASA contract NAS 8–39073 (CXC) and *Chandra* Grant G02-3117X. AZ and VA acknowledge support from NASA LTSA grant NAG5-13056. PT acknowledges support through the CfA REU program which is funded by the NSF. We would like to thank Silas Laycock and Jose Galache for useful discussions on the properties and variability of Be/X-ray binaries.

Bibliography

[1] Antoniou, V., Zezas, A., Hatzidimitriou, D., & McDowell, J. 2008a, Astrophys. J., submitted

[2] Antoniou, V., Zezas, A., Hatzidimitriou, D., & Kalogera, V. 2008b, Astrophys. J. Lett., submitted

[3] Bildsten, L., et al. 1997, Astrophys. J. Suppl., 113, 367

[4] Bradt, H. V., Rothschild, R. E., & Swank, J. H. 1993, Astr. Astrophys. Suppl., 97, 355

[5] Cash, W. 1979, Astrophys. J., 228, 939

[6] Charles, P. & Coe M., 2005, in "Compact Stellar X-ray Sources," eds. W.H.G. Lewin and M. van der Klis, Cambridge University Press

[7] Cowan G., Statistical Data Analysis, 1998, Clarendon Press, Oxford

[8] Freeman, P. E., Kashyap, V., Rosner, R., & Lamb, D. Q. 2002, Astrophys. J. Suppl., 138, 185

[9] Galache, J. L., Corbet, R. H. D., Coe, M. J., Laycock, S., Schurch, M. P. E., Markwardt, C., Marshall, F. E., & Lochner, J. 2008, ArXiv e-prints, 802, arXiv:0802.2118, Astrophys. J. Suppl., in press

[10] Garmire, G. P., Bautz, M. W., Ford, P. G., Nousek, J. A., & Ricker, G. R. 2003, Proc. SPIE, 4851, 28

[11] Gardiner, L. T., & Hatzidimitriou, D. 1992, Mon. Not. R. Astr. Soc., 257, 195

[12] Gehrels, N. 1986, Astrophys. J., 303, 336

[13] Haberl, F., Filipović, M. D., Pietsch, W., & Kahabka, P. 2000, Astr. Astrophys. Suppl., 142, 41

[14] Haberl, F., & Pietsch, W. 2004, Astr. Astrophys., 414, 667

[15] Hatzidimitriou, D. 1999, New Views of the Magellanic Clouds, 190, 299

[16] Harris, J., & Zaritsky, D. 2004, Astron. Journ., 127, 1531

[17] Hilditch, R. W., Howarth, I. D., & Harries, T. J. 2005, Mon. Not. R. Astr. Soc., 357, 304

[18] Illarionov, A. F., & Sunyaev, R. A. 1975, Astr. Astrophys., 39, 185

[19] Laycock, S., Corbet, R. H. D., Coe, M. J., Marshall, F. E., Markwardt, C., & Lochner, J. 2005, Astrophys. J. Suppl., 161, 96

[20] Liu, Q. Z., van Paradijs, J., & van den Heuvel, E. P. J. 2005, Astr. Astrophys., 442, 1135

[21] Negueruela, I. 1998, Astr. Astrophys., 338, 505

[22] Park, T., Kashyap, V. L., Siemiginowska, A., van Dyk, D. A., Zezas, A., Heinke, C., & Wargelin, B. J. 2006, ApJ, in press, (arXiv:astro-ph/0606247)

[23] Sasaki, M., Haberl, F., & Pietsch, W. 2000, Astr. Astrophys. Suppl., 147, 75

[24] Sasaki, M., Haberl, F., & Pietsch, W. 2002, Astr. Astrophys., 392, 103

[25] Shtykovskiy, P., & Gilfanov, M. 2005, Mon. Not. R. Astr. Soc., 362, 879

[26] Smith, R. K., Brickhouse, N. S., Liedahl, D. A., & Raymond, J. C. 2001, Astrophys. J. Lett., 556, L91

[27] Stanimirovic, S., Staveley-Smith, L., Dickey, J. M., Sault, R. J., & Snowden, S. L. 1999, Mon. Not. R. Astr. Soc., 302, 417

[28] Stella, L., White, N. E., & Rosner, R. 1986, Astrophys. J., 308, 669

[29] Stevens, I. R. 1991, Astrophys. J., 379, 310

[30] Tanaka, Y., Inoue, H., & Holt, S. S. 1994, Pub. Astr. Soc. Japan., 46, L37

[31] Townsley, L. K., Broos, P. S., Garmire, G. P., & Nousek, J. A. 2000, Astrophys. J. Lett., 534, L139

[32] Trüemper, J. 1993, Science, 260, 1769

[33] van den Bergh, S. 2000, The galaxies of the Local Group, by Sidney Van den Bergh. Published by Cambridge, UK: Cambridge University Press, 2000 Cambridge Astrophysics Series Series, vol no: 35

[34] Wang, Q., & Wu, X. 1992, Astrophys. J. Suppl., 78, 391

[35] Waters, L. B. F. M., van den Heuvel, E. P. J., Taylor, A. R., Habets, G. M. H. J., & Persi, P. 1988, Astr. Astrophys., 198, 200

[36] Yokogawa, J., Imanishi, K., Tsujimoto, M., Koyama, K., & Nishiuchi, M. 2003, Pub. Astr. Soc. Japan., 55, 161

[37] Zezas, A. & Fabbiano 2002, Astrophys. J., 577, 726

[38] Zezas, A., Fabbiano, G., Baldi, A., Schweizer, F., King, A. R., Rots, A. H., & Ponman, T. J. 2007, Astrophys. J., 661, 135

Chapter 3

The *Chandra* Survey of the SMC "Bar": Optical counterparts of X-ray sources

We present the candidate optical counterparts of the X-ray sources detected in our *Chandra* survey of the central region of the Small Magellanic Cloud (SMC) based on the OGLE-II and MCPS (Zaritsky et al. 2002) catalogs. In total, we present the most likely counterpart for 113 X-ray sources (52 of which have single matches). We estimate that the foreground contamination and chance coincidence probability are minimal for the bright counterparts (reddening corrected absolute V magnitude ≤ -0.25, corresponding to OB type stars). In particular, we identify 32 sources with early type counterparts (of OB spectral type). We propose here for the first time 11 candidate High Mass X-ray Binaries, of which 9 are candidate Be X-ray binaries (Be-XRBs). Moreover, we confirm previous classification of Be-XRBs for 18 sources. We estimate that the new candidate Be-XRBs have an age of $\sim 15 - 85$ Myr, consistent with the age of Be stars. We also examine the "overabudance" of Be-XRBs in the SMC fields covered by *Chandra*, in comparison with the Milky Way. In luminosities down to $\sim 10^{34}$ erg s^{-1} , we find that Be-XRBs are ~ 2 times more common in the SMC when compared to the Milky Way even after taking into account the difference in the formation rates of OB stars. This residual excess can be attributed to the lower metallicity of the SMC. Finally, we find that the mixing of Be-XRBs with other

than their natal stellar population is not an issue in our comparisons of Be-XRBs and stellar populations in the SMC. Instead we find indication for variation of the XRB populations of the SMC on kiloparsec scales, related to local variations of the formation rate of OB stars and slight variation of their age, which results in different relative numbers of Be stars and therefore XRBs.

Subject headings: Magellanic Clouds—stars: early-type—stars: emission-line, Be—stars: formation—pulsars: general—X-rays: binaries

3.1 Introduction

X-ray binaries (XRBs) are stellar systems consisting of a compact object (neutron star, black hole, white dwarf) accreting material from a close companion star. They are the end points of stellar evolution, and thus by studying them we can set constraints on stellar evolution and compact object formation models. They constitute a numerous class of X-ray bright objects, with typical luminosities of $\sim 10^{36} - 10^{38}$ erg s^{-1} when in outburst. They are divided into two classes depending on the mass of the donor star, with M $\leq$ 1 M$_{\odot}$ for the Low Mass XRBs (LMXBs), and M $\geq$ 10 M$_{\odot}$ for the High Mass X-ray Binaries (HMXBs).

The companion star in HMXBs is of O or B spectral type, with optical bolometric luminosity usually exceeding that of the accretion disk (e.g. van Paradijs & McClintock 1995). HMXBs can further be divided into two groups, the supergiant X-ray binaries (hereafter SG/XRBs), and the Be X-ray binaries (hereafter Be-XRBs). In the SG/XRBs the primary is a supergiant of spectral type earlier than B2, or an Of star, and it has evolved away from the main sequence (MS), while in the Be-XRBs, the primary is an Oe or Be star lying close to the MS. The optical spectra of Be-XRBs are characterized by emission lines (mostly of the Balmer series of hydrogen; for a review of HMXBs and their properties see, e.g. van Paradijs & McClintock 1995).

Different mechanisms are believed to be responsible for the mass transfer in these two groups of HMXBs. The most luminous SG/XRBs usually have an accretion disk fueled via Roche lobe overflow, while the less luminous systems may be fed by a supersonic stellar wind. In the Be-XRBs, Be stars are characterized by a low velocity, high density equatorial wind, resulting in periodic accretion episodes during the passage of the compact object through the decretion disk of the donor.

Be-XRBs show pulsations and have hard 1-10 keV spectra (i.e. with a power-law energy index of $\Gamma \sim 0-1$; e.g. White, Nagase & Parmar 1995, Yokogawa et al. 2003), which are signatures of accretion onto strongly magnetized neutron stars. In contrast, SG/XRBs have generally softer spectra, and do not always have a pulsar as the compact object.

Be-XRBs are the most numerous sub-class of HMXBs. In the Milky Way as well as in the Large Magellanic Cloud (LMC), they constitute 60-70% of all HMXBs (Sasaki, Pietsch & Haberl 2003),

while in the Small Magellanic Cloud (SMC) only two out of 92 known or probable HMXBs (Liu, van Paradijs & van den Heuvel 2005) are supergiant systems.

The SMC is an excellent laboratory to study the populations of Be-XRBs. It is the second nearest galaxy, and it has a large number of Be-XRBs seen through moderate Galactic foreground absorption ($N_H \simeq 6{\times}10^{20} cm^{-2}$; Dickey & Lockman 1990), and well mapped extinction (Zaritsky et al. 2002). In addition, its well measured distance (60 kpc; e.g. van den Bergh 2000, Hilditch, Howarth & Harries 2005), small line-of-sight depth of the young populations at its main body (<10 kpc; e.g. Crowl et al. 2001; Harries, Hilditch & Howarth 2003), well studied recent star-formation (SF) history (Harris & Zaritsky 2004), and generally uniform metallicity of the young populations facilitate the interpretation of the results. Therefore, one can study in great detail and in an homogeneous way the faint end of the X-ray binary populations.

Several studies of the optical characteristics of the XRB systems in the SMC, have been published in the last few years. Haberl & Sasaki (2000), based on the ROSAT surveys of the SMC, identified 25 X-ray sources as new Be-XRBs. Haberl & Pietsch (2004) extended this work presenting 65 SMC HMXBs, of which 45 are associated with an emission-line object indicating that they are Be-XRBs. In the latest census of HMXBs by Liu et al. (2005) 62 Be-XRBs are listed (for 92 confirmed or proposed HMXBs). In addition out of the 38 currently known X-ray pulsars in the SMC, 34 have identified optical counerparts (Coe et al. 2005a).

In this paper we study in a systematic way the young SMC XRB populations. The SMC ROSAT survey reached a non-uniform detection limit of $\sim 5{\times}10^{34}{-}10^{35}$ erg s^{-1} (e.g. Kahabka & Pietsch 1996, Haberl et al. 2000, Sasaki et al. 2000). Here we are using data down to $\sim 4 \times 10^{33}$ erg s^{-1} from the *Chandra* survey of the SMC (Zezas et al. 2003) that allow to investigate the faintest of the HMXB populations.

3.1.1 The *Chandra* survey of the SMC

The SMC as a prime target to study the faint end of the XRB populations (with typical $L_X < 10^{34}$ erg s^{-1}), overcoming in this way the inherent problems of observations in the Milky Way (e.g. distance determination, and obscuration). For this reason we initiated a *Chandra* survey, consisting of five observations of the central part of the SMC performed between

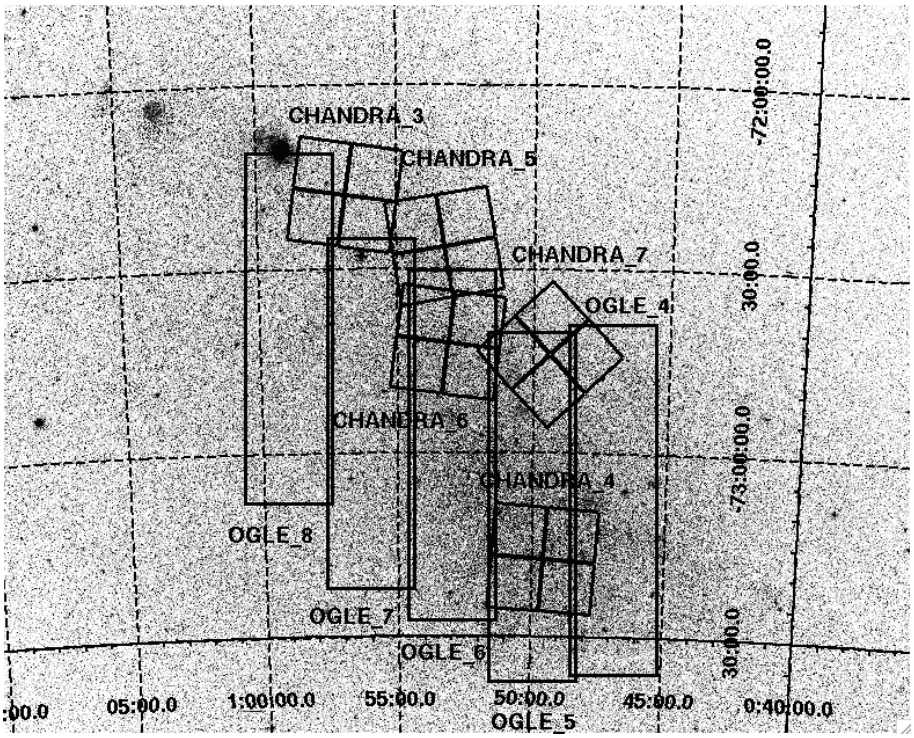

Figure 3.1 A DSS optical image of the center of the SMC (outline of the 5 observed *Chandra* fields ($16' \times 16'$) and the 5 overlapping OGLE-II fields).

May and October 2002 with the *Chandra* ACIS-I detector (Advanced CCD Imaging Spectrometer; Garmire et al. 2003). The survey covers an area of $1280\,arcmin^2$ along the central, most actively star forming, region of the SMC (also referred to as the SMC "bar", although it bears no relation to a dynamical bar; van den Bergh, 2000). In Figure 3.1 we plot the footprints of the *Chandra* and OGLE-II fields (for the latter see §3.2) overlaid on a Digitized Sky Survey (DSS) optical image of the main body of the SMC.

The survey yielded a total of 158 sources, detected on the ACIS-I CCDs, down to a limiting luminosity of $\sim 4 \times 10^{33}$ erg s^{-1}, which is within the luminosity range of quiescent HMXBs (typical $L_X \sim 10^{32} - 10^{34}$ erg s^{-1}; van Paradijs & McClintock 1995). Each of the 5 fields contained between 21 and 32 sources with fluxes at least of 3σ significance (assuming Gehrels statistics; Gehrels 1986) above their local background. A brief description of the survey and the first results are presented in Zezas et al. (2003). The final source-list (including the X-ray luminosity functions) will be presented in Zezas et al. (2008, in preparation), while the spectral and timing properties of the bright sources will be presented in Taylor et al. (2008, in

Table 3.1. *Chandra* source data statistics

Chandra field	Right Ascension (J2000.0) (h m s)	Declination (J2000.0) (° ′ ″)	Detected sources	Sources with $D_{off-axis} < 10'$
[1]	[2]	[3]	[4]	[5]
3	00 56 46.14	-72 18 10.78	28 (21)	27 (20)
4	00 49 30.74	-73 16 52.34	38 (32)	36 (31)
5	00 53 11.45	-72 26 29.91	37 (26)	36 (25)
6	00 53 04.40	-72 42 18.22	28 (22)	28 (22)
7	00 49 25.09	-72 44 22.80	27 (21)	26 (20)

preparation). Because of the large off-axis angle (and therefore large positional uncertainty) of sources on the ACIS-S3 and ACIS-S4 CCDs we do not include them in the present work.

The absolute astrometric accuracy of on-axis sources is dominated by the boresight error of *Chandra* ($< 0.6''$ at the 90% confidence level[1]). However, at larger off-axis angles the Point Spread Function (PSF) becomes broader and asymmetric, resulting in larger positional uncertainties (see *Chandra* POG, 2005). To estimate the positional errors of the off-axis sources, we used the empirical formula of Kim et al. (2004), which gives positional uncertainties for sources with 20 and 100 counts as a function of their off-axis angle (up to a maximum of $10'$). For sources with net number of counts within the range we linearly interpolated between these two estimates, while for sources with less than 20 or more than 100 counts we used the appropriate branch of the equation.

Five sources out of the 158, which were at large off-axis angles ($D_{off-axis} > 10'$), yielded high positional errors and were discarded from further consideration in this paper. The *Chandra* field IDs, and the coordinates of their centers are listed in Table 3.1 (Columns (1)-(3)). In Column (4) we present the number of all detected X-ray sources in each *Chandra* field, while in parenthesis we give the number of sources with 3σ level above their local background. In Column (5) we give the number of *Chandra* sources for which we searched for counterparts (i.e. detected in $D_{off-axis} < 10'$).

The identification and classification of the optical counterpart of an X-ray source allow us to

[1]http://cxc.harvard.edu/cal/docs/cal_present_status.html#abs_spat_pos

identify the interlopers, while it is the only way to confirm the type of XRBs (e.g. Be-XRBs, SG/XRBs, LMXBs). Although the classification of the counterparts is only secure via optical spectroscopic observations, color-magnitude and/or color-color diagrams (hereafter CMDs and 2-CDs, respectively) can be used to obtain rough classifications for the optical counterparts, and at least identify HMXBs. Also from the appropriate isochrones and the stellar tracks we can obtain a feel for the mass and the age of the donor star, if it dominates the optical emission of the X-ray sources.

In this paper we have used the *Chandra* survey of the SMC (Zezas et al. 2003), and searched for optical counterparts of the X-ray sources included in this survey. In particular, we confirm or suggest new counterparts of the above X-ray sources, based on their optical properties, and when possible we give a tentative classification. In Section 3.2 we present the optical catalogs used in this study, and in Section 5.2.2 the counterparts of the X-ray sources. We also present their finding charts (Section 3.4), and we examine the photometry of the optical data (Section 3.5). In Section 3.6 we describe the data used in the construction of the V, $B-V$ CMD for the classification of the sources, and we estimate the expected contamination by foreground stars, while in Section 3.7 we estimate the chance coincidence probability. In the discussion (Section 3.8) we present the criteria used to classify the X-ray sources, and distinguish among multiple matches the most likely counterpart. We also discuss the properties of the optical countertparts, and the relative numbers of Be-XRBs in the SMC, LMC and Milky way. In the Appendix we present notes on individual sources.

3.2 Optical data

The SMC has been surveyed extensively in the optical and in the near infrared. In the past decade, several photometric catalogs have become available, with varying photometric and astrometric accuracy, limiting magnitudes, completeness and spatial coverage. The most extensive of these are the US Naval Observatory USNO-B1.0 (Monet et al. 2003), the USNO CCD Astrograph Catalog (UCAC2, 2nd release; Zacharias et al. 2004), the Massive Compact Halo Objects database (MACHO, Alcock et al. 1997), the Optical Gravitational Lensing Experiment survey

(OGLE-II; Udalski et al. 1998a)[2], the $UBVR$ CCD Survey by Massey (2002), and the Magellanic Cloud Photometric Survey (MCPS; Zaritsky et al. 2002). We also mention, for completeness, the Two Micron All Sky Survey (2MASS; Skrutskie et al. 2006), which is sensitive to red stars, and thus it is not used in the present study (see §3.8.2).

Taking into consideration the photometric and astrometric accuracy of each of these surveys, and their spatial coverage of the *Chandra* fields, we selected the OGLE-II and MCPS surveys, as the main optical catalogs for the present study. We also looked for additional possible counterparts of the X-ray sources within the SIMBAD Astronomical Database[3], and for previously identified optical counterparts of known X-ray sources within the NASA's Astrophysics Data System[4](ADS) (for more details see §3.3.2).

3.2.1 OGLE-II catalog

The second release of the OGLE survey (hereafter OGLE-II) is a BVI survey of the SMC, carried out with the 1.3m Warsaw telescope at the Las Campanas Observatory (Udalski et al. 1998a). The survey provides photometric (in B, V and I band) and astrometric data for about 2.2 million stars in the dense central regions of the SMC "bar", down to $B \sim 20.0$ mag, $V \sim 20.5$ mag, and $I \sim 20.0$ mag, with typical completeness $\sim 75\%$, 80% and 85%, respectively, down to these limits. In the densest fields (e.g. corresponding to *Chandra* field 6), the completeness is reduced almost by half. The vast majority of observations was performed in the I band (because of the microlensing observing strategy of this survey). However meticulous photometry was also performed in both B and V bands (Udalski et al., 1998a). For these reasons, and because of its small astrometric error ($\sim 0.7''$), matching well the positional uncertainty of the *Chandra* detections (see §3.1.1), the small pixel size ($0.417''$), and the good average seeing (as good as $0.8''$ with typical median value of $1.25''$) during the survey, we opted to use the OGLE-II catalog in order to identify optical counterparts for the X-ray sources detected in our *Chandra* fields. However, due to incomplete coverage of our *Chandra* fields by the OGLE-II survey ($\sim 72\%$ of the area of our *Chandra* survey), we were able to search for optical counterparts for only 102 ($\sim 66.7\%$) of our sources. Four of our fields are partially covered by OGLE-II, and

[2]http://ogle.astrouw.edu.pl/ogle2/smc_maps.html

[3]http://simbad.u-strasbg.fr/Simbad/

[4]http://www.adsabs.harvard.edu

only field 4 is fully covered. However, due to the distribution of the X-ray sources in our *Chandra* fields, we were able to search for counterparts for all our sources also in field 6. For the remaining fields we searched for counterparts in the OGLE-II catalog for $\sim 22\%$, $\sim 28\%$ and $\sim 86\%$ of the detected sources in *Chandra* fields 3, 5 and 7, respectively.

3.2.2 MCPS catalog

Because of the incomplete coverage of the *Chandra* fields by the OGLE-II survey, we supplemented the optical data with the MCPS catalog (Zaritsky et al. 2002). The MCPS survey is based on drift-scan images of the SMC in the Johnson U, B and V and Gunn I filters obtained with the Las Campanas Swope telescope (1m). The MCPS catalog contains stellar photometry for more than 5 million stars in the central 18 deg^2 area of the SMC, which fully covers our *Chandra* survey. Only for one of our X-ray sources we were not able to look for counterparts in the MCPS catalog, because it falls in the gap between the different subscans of this survey. The final MCPS catalog includes only stars with both B and V detections, while there are not always measurements in the U band. The incompleteness is significant below $V \sim 20$ mag, while the typical seeing for this survey is $\sim 1.5''$, and the pixel size $0.7''$.

In general the two catalogs have consistent photometry: Evans et al. (2004) reported a difference of $\delta B_{(\mathrm{MCPS-OGLEII})} = +0.02$ mag for stars in their 2dF spectroscopic sample. Zaritsky et al. (2002), in their comparison between MCPS and OGLE-II magnitudes, found mean photometric offsets of $\delta B = 0.011$, $\delta V = 0.038$, and $\delta I = 0.002$ mags. However, in crowded fields, actual photometric (as well astrometric) uncertainties can be larger, due to source confusion (see also Zaritsky et al. 2002), which we consider to be more severe than in the OGLE-II catalog, due to the larger pixel size, and worse overall seeing. In addition, observations were not repeated in the MCPS survey, which makes it more likely to contain a higher percentage of stars with less reliable photometry, especially in the faint end, and crowded regions.

3.3 Cross-correlation analysis

3.3.1 OGLE-II and MCPS

In order to identify the optical counterparts of the *Chandra* sources we have first cross-correlated their coordinates with the OGLE-II, and the MCPS catalogs. The search radius for each X-ray source was calculated from the combination, in quadrature, of the astrometric uncertainty of the corresponding optical catalog, and the positional uncertainty for each X-ray source (including the absolute astrometric uncertainty of *Chandra*). When the resulting search radius was less than $1.5''$ we enforced a conservative minimum of $1.5''$ ($\sim 48\%$ of our sources). The maximum resulting radius was $5.29''$ with the average search radius being $1.99''$.

The optical counterparts of the X-ray sources are presented in Tables 3.2-B.6 (one for each *Chandra* field).[5] In Columns (1) and (2) we give the *Chandra* source ID and the search radius (in arcseconds), respectively. The X-ray sources (Column (1)) are named as F_NN, where F is the *Chandra* field number, and NN is the source ID in this field (from Zezas et al. 2008, in preparation). In Column (3) we give the proposed counterparts, following a similar notation: OGLE-II sources are named as O_F_NNNNNN, where F and NNNNNN are the field and optical source number, respectively (from Udalski et al., 1998a), and MCPS sources are named as Z_NNNNNN where NNNNNN is the line number of the source in Table 1 of Zaritsky et al. (2002). In Columns (4) and (5) we present the right ascension and declination (J2000.0) of the counterparts from their respective catalogs. The distance (in arcseconds) of the counterpart to the *Chandra* source is given in Column (6). The photometric data of the sources are presented in Columns (7) to (12) (these data are taken directly from the original catalogs without applying any reddening or zero-point correction): apparent magnitude in the V band (Column (7)), the B - V and U - B colors (Columns (9) and (11)), and their errors (Columns (8), (10) and (12), respectively). Non detections in a band are indicated by 99.99, while three dots indicate that an entry was not available at the original catalog. In Column (13) we give notes on individual sources: "n" indicates a new candidate counterpart for the X-ray source, "c" denotes that there are additional comments for this source in Table B.7 (appendix §B), while "u" indicates sources

[5]Here we only present Table 3.2 as an example, while the remaining Tables B.3-B.6 can be found in the appendix (§B).

for which we were not able to uniquely identify an optical counterpart.

Matched sources between the OGLE-II and MCPS catalogs are grouped together, with different source groups separated by blank lines. Single horizontal lines separate the counterparts of different X-ray sources, while double horizontal lines separate X-ray sources above and below the 3σ significance limit (see §3.1.1). When we were not able to uniquely identify a MCPS source with an OGLE-II source, we list all possible matches (in several cases, because of source confusion, two or more OGLE-II sources are detected as a single brighter source in MCPS). In cases of unclear matches between the two catalogs, we show the MCPS sources in parenthesis. The matched pairs are based on positional coincidence, visual inspection of the OGLE-II I band images, and comparison of the magnitudes and colors of the sources. MCPS sources that may be associated with OGLE-II sources but lie just outside the search radius of each X-ray source are marked with an "o" (e.g. Z_2132222 for X-ray source 4_36).

We indicate in bold face the most likely counterpart. In all but one case (*Chandra* source 3_19, which is discussed in §3.8.3), this is the brightest OGLE-II match, or, when there is no OGLE-II match the brightest MCPS source. For sources with more than one stars with the same or very similar magnitudes we indicate all of them in bold face. There are 3 such cases (*Chandra* sources 4_6, 7_16, and 7_17), for which even if we apply additional criteria (see §3.8.2) we cannot identify the true counterpart, and classify the sources.

From the total of 102 X-ray sources covered by the OGLE-II fields, we found that 34% have a unique candidate optical counterpart, 23% have two, and 29% have three or more matches. In total, we identified 229 optical matches for 87 X-ray sources.

Since the MCPS survey covers the entire area of the *Chandra* survey, we were able to search for counterparts for all X-ray sources apart from source 7_12, which falls on the gap between two scans of the MCPS survey (we identified a unique counterpart for this source from the OGLE-II survey). We found that 45% of the 152 X-ray sources have a unique candidate optical counterpart, 13% have two and 6% have three or more, resulting in a total of 138 matches. Fifty five X-ray sources do not have any match in the MCPS catalog; from them, 22 have match(es) in the deeper OGLE-II catalog.

In Table 3.3 we summarize the above results. In Column (1) we give the field ID, while in

Table 3.2. Optical counterparts of X-ray sources in *Chandra* field 3

X-ray			Optical counterpart									Notes
Src	Rad.	Src ID	Position (J2000.0)		Offset	V	δV	B-V	δ(B − V)	U-B	δ(U − B)	
			R.A.	Decl.								
	($''$)				($''$)							
[1]	[2]	[3]	[4]	[5]	[6]	[7]	[8]	[9]	[10]	[11]	[12]	[13]
3_1	1.58	**O_7_267132**	00 57 19.80	-72 25 34.0	0.13	19.76	0.30	99.99	99.99	···	···	u, c
		O_7_267163	00 57 19.84	-72 25 33.5	0.54	19.54	0.33	99.99	99.99	···	···	
		(Z_3066294)[!]	00 57 19.87	-72 25 34.0	0.21	18.66	0.06	0.78	0.08	-0.63	0.09	
		O_7_269933	00 57 19.77	-72 25 35.4	1.39	21.51	0.55	99.99	99.99	···	···	
3_2	2.18	**Z_2804383**	00 55 27.52	-72 11 00.5	2.01	20.30	0.07	-0.38	0.14	-0.33	0.16	u, c
		Z_2804939	00 55 27.75	-72 10 58.7	0.28	20.30	0.08	1.17	0.20	-1.85	0.22	
3_3	1.50	**O_8_49531**	00 57 36.01	-72 19 33.8	0.14	16.01	0.02	-0.02	0.04	···	···	c
		Z_3103982	00 57 36.09	-72 19 33.6	0.53	15.99	0.03	0.01	0.17	-1.05	0.17	
3_4	1.50	**O_8_56601**	00 57 32.76	-72 13 01.9	0.54	18.19	0.02	0.37	0.04	···	···	n, c
		Z_3096372	00 57 32.79	-72 13 01.9	0.62	18.28	0.04	0.20	0.05	-0.60	0.06	
3_7	1.50	**Z_3075967**[!]	00 57 24.02	-72 23 56.4	1.30	14.71	0.03	-0.07	0.03	-1.04	0.04	n
3_9	1.50	**Z_3003005**	00 56 52.62	-72 12 03.7	0.67	21.21	0.10	-0.55	0.12	99.99	99.99	n
3_12	1.80	**Z_3051372**	00 57 13.57	-72 23 59.1	1.41	21.14	0.11	0.51	0.21	99.99	99.99	n
3_15	1.73	**O_8_49051**	00 57 44.04	-72 22 15.6	1.69	20.89	0.12	0.47	0.27	···	···	n
		Z_3122823	00 57 44.06	-72 22 15.7	1.61	20.91	0.10	0.33	0.18	0.11	0.35	
3_17	1.50	**Z_3072898**	00 57 22.72	-72 17 57.8	1.05	21.85	0.24	0.04	0.43	-0.35	0.58	n
3_18	1.50	**Z_2893439**[!]	00 56 05.56	-72 21 59.0	0.72	15.88	0.03	-0.04	0.03	-1.09	0.04	c
3_19	2.88	**Z_3049033**	00 57 12.56	-72 10 45.6	2.71	17.95	0.04	-0.07	0.04	-0.80	0.27	u
		Z_3050592	00 57 13.23	-72 10 45.7	0.60	16.99	0.03	0.61	0.04	-0.08	0.05	
3_22	2.50	**Z_2899335**	00 56 08.08	-72 11 32.9	1.44	20.31	0.08	0.12	0.12	0.21	0.24	n
3_26	1.50	**Z_2871193**	00 55 56.04	-72 17 32.3	0.41	20.45	0.20	-0.35	0.22	99.99	99.99	n

[!]The fit with stellar atmosphere models was unsuccesful (quality flag +20, see Zaritsky et al. (2002) for more details).

Table 3.3. Total number of counterparts

Chandra field ID	Overlap by OGLE-II survey	Catalog used	X-ray sources with total number of counterparts 0	1	2	> 2
[1]	[2]	[3]	[4]	[5]	[6]	[7]
3	partial	O	2	3	0	1
		Z	14	11	2	0
		combined	14	10	2	1
4	full	O	3	14	8	11
		Z	14	16	3	3
		combined	3	12	11	10
5	partial	O	1	3	3	4
		Z	7	19	6	4
		combined	6	13	9	8
6	full	O	5	9	8	6
		Z	11	13	3	1
		combined	5	9	8	6
7	partial	O	4	6	4	8
		Z	9	10	5	1
		combined	5	8	3	10

Column (2) we indicate fields for which we have complete coverage by the OGLE-II survey. In Column (3) we specify the optical catalog used for the cross correlation (O for OGLE-II, Z for MCPS and "combined" for the results of the matched lists of OGLE-II and MCPS sources presented in Tables 3.2-B.6). In Columns (4), (5), (6) and (7) we give the number of sources with no counterparts, and with 1, 2 or more matches, respectively. Only in four cases (sources 4_23, 4_36, 5_34 and 7_5) we found two separate OGLE-II and MCPS matches within the *Chandra* search radius. The coordinates and photometry of these stars indicate that they are distinct objects, and thus we consider them as two individual sources. Because, in many cases, the MCPS sources are resolved into two or more OGLE-II stars, and because of the cases of non-matched associations just mentioned, the number of counterparts in the "combined" entry is always smaller than the numbers corresponding to individual catalogs.

In total, out of the 153 X-ray sources, 34% have unique candidate optical counterparts, 22% have two, and 23% have three or more optical matches. There are also 33 X-ray sources with

no matches.

3.3.2 Other bibliographic sources

For all detected sources we performed an extensive (but by no means complete) literature search for previously published identification and classifications. In Table B.7 (appendix §B) we present (when available) information on the X-ray sources and/or the optical sources detected within $1.5''$, based on a search of the ADS and SIMBAD Astronomical Databases (see also §3.2). In particular, in Column (1) we give the X-ray source ID (same as in Tables 3.2-B.6). In columns (2) and (4) we give any reported classification for the X-ray source and previously identified optical counterparts (the relevant references are given in Columns (3) and (5); comparison with previously published X-ray catalogs is based on positional coincidence and the spectral and timing properties of the sources will be presented in Zezas et al. (2008, in preparation) and Taylor et al. (2008, in preparation)). In the last 2 columns we present any other sources encompassed by the minimum search radius ($1.5''$) around the X-ray source. In Column (6) we present the source ID, and in Column (7) its reference.

We note that we have made no attempt to match the sources given in Columns (2), (4), and (6) since they are produced from several different surveys, with different areal coverage and positional accuracy. However, for completeness we present them all.

Summarizing the above results, we found, within the search radius, 2 AGNs (Dobrzycki et al. 2003a, 2003b; [DMS03] and [DSM03], respectively), 1 foreground star (Sasaki et al. 2000; [SHP00]), 14 pulsars (e.g. Edge et al. 2004, [EHI04]; Haberl et al. 2004, [HPS04]), 4 candidate HMXBs (e.g Haberl & Sasaki 2000; [HS00]), 12 confirmed Be-XRBs (e.g. [HS00]; Coe et al. 2005a, [CEG05]), 1 eclipsing binary (Wyrzykowski et al. 2004; [WUK04]), 1 planetary nebula (Murphy & Bessell 2000; [MB00]), 4 variable stars from the OGLE-II survey (one of which is also a candidate HMXB; Ita et al. 2004, Zebrun et al. 2001), 3 stars with spectral classification from 2dF (Evans et al. 2004), 1 B[e] star (Massey & Duffy 2001; reported here for the first time as single counterpart of an XRB), 11 optical matches within OB stellar associations (Oey et al. 2004), and 10 candidate Be stars (Mennickent et al. 2002; see §3.8.3 for more details).

3.4 Finding charts

For the *Chandra* sources which are covered by the OGLE-II survey, we created optical finding charts[6] presented in Figures B.1 - B.5 in the appendix (§B). These charts are created from the I band OGLE-II fields (Udalski et al. 1998a), they are $\sim 15'' \times 13''$ in size and they are centered on the position of the X-ray source, which is indicated by a cross-hair (each bar of the cross-hair is $0.8''$ long). The positional uncertainty of the finding charts is $\sim 0.7''$, based on the astrometry of the OGLE-II images. The search radius used in the cross-correlation is shown by a circle centered on the X-ray source, and is also given (in arcseconds) at the bottom right corner of each chart. All optical sources from the OGLE-II survey are indicated with an X symbol, while those from the MCPS survey are indicated with a cross. In addition, we present with a diamond the eclipsing binary star identified for *Chandra* source 4_1 (source No.550 in Udalski et al. 1998b). For the X-ray sources which fall on two neighboring OGLE-II fields we only show the finding chart with the largest coverage. We note here that we present finding charts only for those sources with OGLE-II coverage, as the MCPS images are not publicly available.

3.5 Photometric data

The photometric parameters of the optical matches of the X-ray sources in the OGLE-II and MCPS catalogs are from the second OGLE release (Udalski et al. 1998a), and the catalog of Zaritsky et al. (2002), respectively. These parameters are presented in Columns (7) to (12) of Tables 3.2-B.6 (see §5.2.2).

Although there are no known significant photometric offsets between the OGLE-II and MCPS catalogs (see §3.2.2), we look for photometric discrepancies specific to the objects found in our cross correlation by comparing the V and B band magnitudes, and B-V colors of the 18 stars identified as unique counterparts in both OGLE-II and MCPS. We find $\delta V_{(\mathrm{OGLEII-MCPS})} = 0.00 \pm 0.30$ mag, $\delta B_{(\mathrm{OGLEII-MCPS})} = -0.06 \pm 0.30$ mag and $\delta BV_{(\mathrm{OGLEII-MCPS})} = -0.06 \pm 0.27$ mag (error is the standard deviation). The zero-point differences are comparable to the corresponding errors quoted in the two catalogs. The relatively large scatter (0.30) is mainly

[6]These figures will be available online.

caused by the large photometric errors of faint sources, close to the detection limit (particularly of the MCPS catalog), and partly, by actual source variability.

3.6 Color-Magnitude Diagram

CMDs and 2-CDs are a standard tool for the characterization of stars (e.g. Johnson 1966). In this study, we use the V, $B-V$ CMD in order to classify the X-ray sources. An important parameter in CMD studies is the extinction correction. Several, different values have been proposed for the SMC reddening. For this work, we will use reddening values based on the red clump stars (Udalski et al. 1999) in regions as close as possible to the *Chandra* fields. The mean color excess is $E(B-V) = 0.09 \pm 0.02$ mag. Similar results ($E(B-V) \sim 0.09 \pm 0.07$) have been obtained by the spectroscopic study of Massey et al. (1995). Larsen et al. (2000) derived somewhat higher values of ($E(B-V) \sim 0.21 \pm 0.10$ intrinsic to the SMC and $\sim 0.07 \pm 0.02$ due to the foreground dust), although generally compatible with the previously mentioned values, within the combined errors. In conclusion, we adopt the value of $E(B-V) = 0.09$ for the entire area covered by the *Chandra* fields.

To derive the reddening correction for V, A_V ($= R_V E(B-V)$), we use the standard Galactic value of $R_V = 3.24$ (Schlegel et al. 1998), which was also used in previous published photometric catalogs of the SMC. A lower value of $R_V = 2.74 \pm 0.13$, which has been recently proposed for the SMC (Gordon et al. 2003), would result in a negligible difference of 0.04 mag in A_V. The adopted $R_V = 3.24$, gives a mean reddening value for the 5 OGLE-II fields of $A_V = 0.29$ mag. Based on the extinction curve of Cardelli et al. (1989), we estimate A_B and A_U of 0.39 mag and 0.46 mag, respectively. We correct the original data presented in Tables 3.2-B.6 for the extiction to the SMC ($E(B-V) = 0.09$ and A_V=0.29) and we use these corrected numbers for all the plots described below.

Throughout this study we adopt a distance modulus of $(m-M)_V = 18.89 \pm 0.11$ mag (derived from eclipsing O, B-type binaries in the SMC; Harries et al. 2003). The small depth of the young populations (<10 kpc; e.g. Crowl et al. 2001, Harries et al. 2003) results in a difference in the above distance modulus of only ~ 0.18 mag, while the corresponding difference in X-ray luminosity is $\sim 5.9 \times 10^{34}$ erg s^{-1}.

In Figure 3.2 we present the extinction corrected M_{V_o} vs. $(B-V)_o$ CMD diagram (absolute V magnitude vs. $B-V$ color) for all single and the brightest of multiple matches of our sources (which are indicated in bold face in Tables 3.2-B.6). Whenever both OGLE-II and MCPS photometric data exist we use the OGLE-II data. The identifier of each point is the X-ray source number (see §3.3.1), while we plot in the same color sources from the same *Chandra* field. On the same diagram we overlay with small dots the stars from the OGLE-II catalog in the area common with the *Chandra* field 4 (after having corrected the magnitudes and colors for reddening and distance as described above).

In order to identify on the CMD the locus of stars of different spectral types, we use data from the 2dF spectroscopic survey of SMC stars (the most extended such catalog available; Evans et al. 2004). This survey provides spectroscopic classification for 4161 stars in the SMC[7], covering spectral types from O to FG, and sampling the main sequence to ∼mid-B. However, the Be stars are generally redder than B type stars (e.g. McSwain & Gies 2005). Mennickent et al. (2002), studying the light curves of the OGLE-II data for the SMC, identified $\sim$ 1000 candidate Be stars. We have identified 10 of our proposed counterparts with their type-4 stars (objects with light curves similar to Galactic Be stars) from this catalog (shown in Figure 3.2 as black squares). For the classification of the *Chandra* sources we used the combined locus (blue curve) of early type stars (O, B) identified in the 2dF spectroscopic survey of Evans et al. (2004) and the candidate Be stars of Mennickent et al. (2002). This choice is in agreement with the range of the $B-V$ color of O and B spectral type stars from Massey (2002), and is confirmed by follow-up spectroscopy of selected targets from our survey (Antoniou et al. 2008, in preparation).

For stars brighter than $M_{V_o} \sim -0.25$ the majority of the candidate optical counterparts (either single or brightest of the multiple) lie within the loci of OB and Be stars, while fainter objects populate the high density regions of the CMD (lower main sequence and red clump), clearly indicating high incidence of chance coincidences in these dense regions. This issue is discussed in detail in §3.7.

Isochrones and stellar evolutionary tracks can give further insight on the properties of the com-

[7]In this paper we only utilized photometric catalogs, as we found only 3 matches of our *Chandra* sources with the 2dF catalog; see Table B.7 in the appendix (§B).

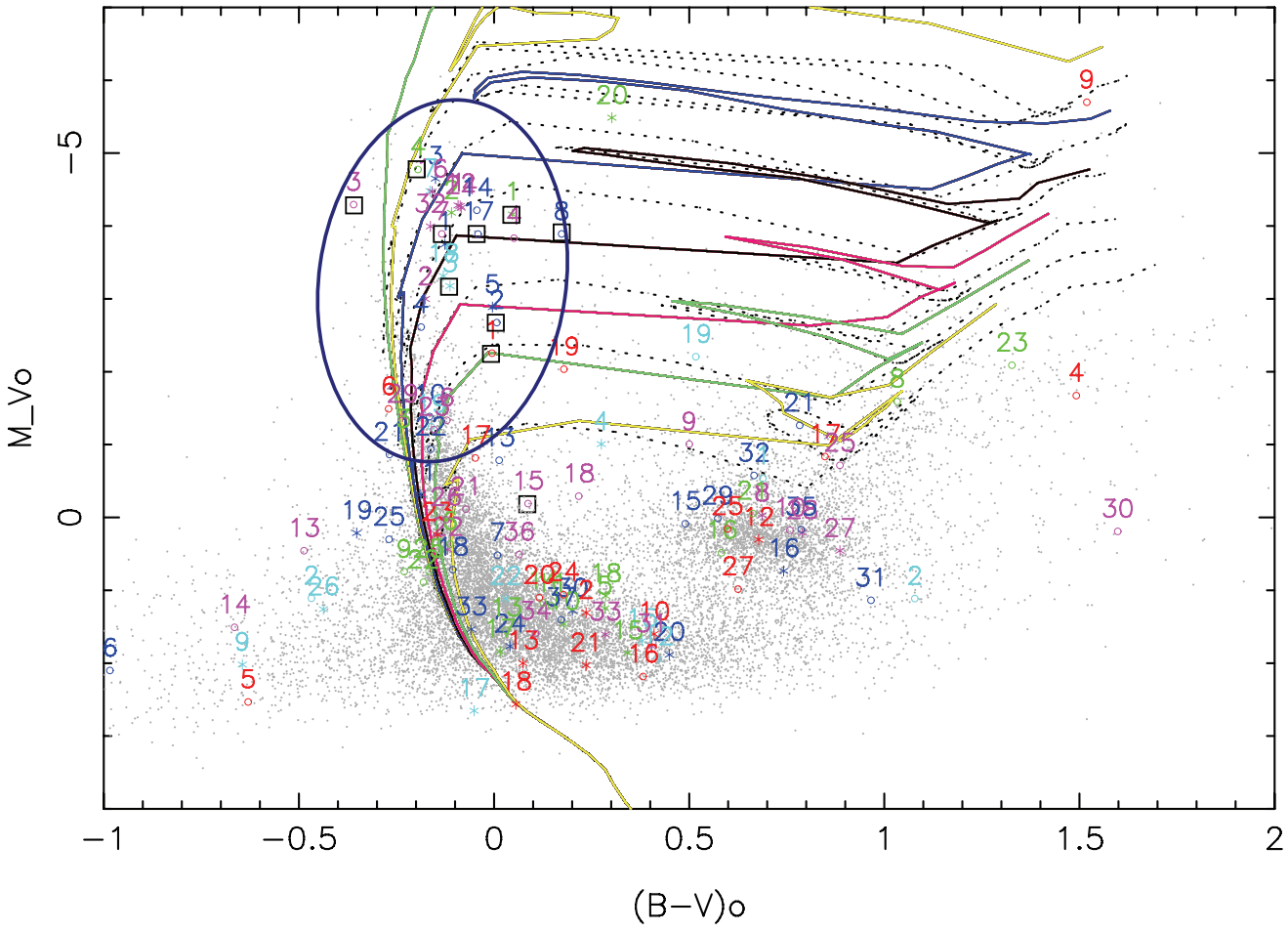

Figure 3.2 CMD of all single and the brightest of multiple matches of our *Chandra* sources

We present the M_{V_o} vs. $(B-V)_o$ CMD of all single matches (asterisk) and the brightest source of those with multiple matches (open circle) of our *Chandra* sources (which are indicated in bold face in Tables 3.2-B.6). The optical sources are color coded as, *Chandra* field 3: cyan; 4: blue; 5: magenta; 6: green; 7: red; while the OGLE-II stars that lie in our *Chandra* field 4 are indicated in grey small dots. The MS, the red giant branch and the red clump loci are clearly shown. With black squares we present the 10 candidate Be stars of Mennickent et al. (2002) that we have identified as optical counterparts. Overlaid are the isochrones (solid lines) and stellar evolutionary tracks (dotted lines) from Geneva database (Lejeune & Schaerer 2001) for ages of 8.7 Myr, 15.5 Myr, 27.5 Myr, 49.0 Myr, 87.1 Myr, 154.9 Myr and 275.4 Myr and initial stellar masses of 12 $M_\odot$, 9 $M_\odot$, 7 $M_\odot$, 5 $M_\odot$, 4 $M_\odot$ and 3 $M_\odot$ stars (from top to bottom).

panion star. In Figure 3.2, we overplot the isochrones from the Geneva database (Lejeune & Schaerer 2001) for the metallicity of the young stars in the SMC ([Fe/H] $= -0.68 \pm 0.13$ dex, equivalent to Z $= 0.004$[8]; Luck et al. 1998), for ages of 8.7 Myrs to 275.4 Myrs and initial stellar masses from 12 $M_\odot$ to 3 $M_\odot$, respectively. The age of the OB stars, discussed in the previous paragraph, ranges from 15.5 to $\sim$ 85 Myr.

Given the large area covered by the *Chandra* survey, we expect a significant contamination by Galactic foreground stars. Based on the tables of Ratnatunga & Bahcall (1985), the fraction of Galactic stars at the locus of early type stars is very small ($< 3.6\%$), and thus, the foreground contamination can be safely considered negligible. Exception to the above is the region of the CMD between $-6 < M_{V_o} < -4$ and $(B-V)_o > 0.75$, in which the contamination is more significant ($\sim$11%). However, there are no counterparts identified in this range (see Figure 3.2), except for *Chandra* source 7_9 that has been previously identified as a foreground star (Sasaki et al. 2000). These estimates are consistent with those of Massey (2002), although direct comparison is difficult because of the different detection limits of the two surveys.

3.7 Chance coincidence probability

To estimate the number of possible chance associations between the X-ray sources and the stars in the OGLE-II and MCPS catalogs, we followed a Monte-Carlo procedure similar to that in Zezas et al. (2002). We simulated 1000 random samples of X-ray sources by applying to the position of each source a random offset in R.A. and Dec.. The offsets were drawn from a uniform distribution, taking care that the new position is outside the search radius of each source but within the boundaries of the OGLE-II fields (the latter constraint does not apply to the MCPS catalog since in that case the overlap is complete). However the maximum offset was restricted so a source does not fall in a region of different stellar density. Each of these samples was cross-correlated with the optical catalogs in the same way as the observed data.

We calculated the chance coincidence probability for detecting *(a)* unique, and *(b)* any number of multiple optical matches (one or more), in the cases of search radii of $1.5''$ (our minimum

[8]For the conversion, we use the relation [Fe/H] $\equiv \log(Z/Z_\odot)$, with $Z_\odot$=0.02 for the solar metallicity of [Fe/H] = 0; Russell & Dopita 1992

search radius; see §3.3.1) and 2.5″ (only 20% of the *Chandra* sources have search radii larger than this). In addition, we estimated the expected chance coincidence probability for matches with optical sources of different spectral types (O, B, and later, following Binney & Merrifield, 1998) depending on their position on the CMD:

(i) MS and post-MS O type stars ($(B-V)_{\rm o} \leq -0.31$ and $(B-V)_{\rm o} > -0.31$, respectively, for $M_{V_o} \leq -4.5$)

(ii) MS and post-MS B type stars ($(B-V)_{\rm o} \leq -0.11$ and $(B-V)_{\rm o} > -0.11$, respectively, for $-4.5 < M_{V_o} \leq -0.25$)

(iii) later type stars ($M_{V_o} > -0.25$, with no restriction in the color range),

where M_{V_o} denotes the absolute V magnitude. The photometric data used here (both in B and V band) are corrected for extinction (see §3.6).

In Figure 3.3, we plot the expected chance coincidence probability per X-ray source as a function of the search radius for the cases of single, and multiple matches. The errors are estimated from the variance of the combined simulations of the 5 fields, and reflect field to field stellar density variations. These values are the average for all the *Chandra* fields (weighted by the number of sources in each field; a quantile-quantile plot of the distribution of the simulated chance associations shows that they follow approximately a Gaussian distribution). It is clear from Figure 3.3 that for the same search radius the OGLE-II data result in fewer spurious matches for single associations than the data from the MCPS catalog. This is mainly due to the smaller pixel size and better overall seeing of the OGLE-II catalog resulting in better positions, especially in crowded fields. On the other hand, we find no difference between the two catalogs for the case of one or more (multiple) matches.

The chance coincidence probability for OGLE-II and MCPS sources of different spectral types is presented in Tables 3.4 and 3.5, respectively. In Column (1) we give the magnitude range (M_{V_o}) of the stars in the optical catalog, and in Column (2) their color range ($(B-V)_o$). In Columns (3) and (4) we present the estimated chance coincidence probability for the single counterparts for 1.5″ and 2.5″ search radius, respectively, while in Columns (5) and (6) we present the corresponding results for sources with one or more matches.

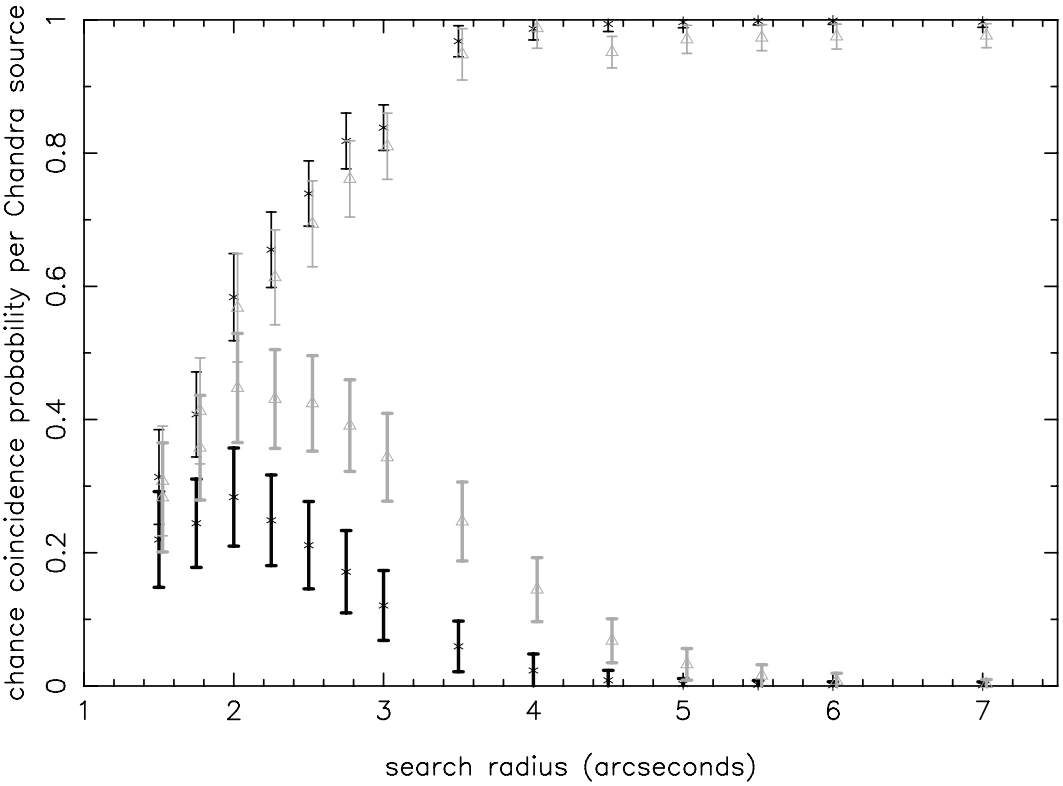

Figure 3.3 Chance coincidence probability as a function of the search radius around the X-ray source The estimated chance coincidence probability for each *Chandra* source is shown in black (asterisks) for the OGLE-II data and in grey (open triangles) for data from the MCPS catalog (for reasons of clarity between the OGLE-II and MCPS data, the latter are shown with a small shift in the search radius). The thick lines represent the estimated probability of detecting by chance one source for a single match, while the thin lines indicate the probability of detecting one or more spurious matches for a source with one or more associations (i.e. total number of matches).

These results indicate that only a relatively small fraction ($\leq 19\%$) of the bright blue ($M_{V_o} \leq -0.25$ and $(B-V)_o \leq -0.11$) counterparts can be considered spurious matches. Therefore for the sources with multiple matches, we can assume that if one of them is an early type star, this is the most likely counterpart. However, the high chance coincidence probability for the fainter optical sources does not allow us to securely identify an optical counterpart.

Table 3.4. Chance associations between the X-ray sources and the stars in the OGLE-II catalog

Magnitude range	Color range	Chance coincidence probability: single matches r=1.5″	single matches r=2.5″	multiple matches r=1.5″	multiple matches r=2.5″
[1]	[2]	[3]	[4]	[5]	[6]
$M_{V_o} \leq -4.5$	all	0.01 ± 0.16	0.02 ± 0.14	0.01 ± 0.16	0.02 ± 0.12
	$(B-V)_o \leq -0.31$[†]	...	...	...	...
	$(B-V)_o > -0.31$	0.01 ± 0.15	0.02 ± 0.14	0.01 ± 0.15	0.02 ± 0.12
$-4.5 < M_{V_o} \leq -0.25$	all	0.47 ± 0.35	0.82 ± 0.17	0.24 ± 0.23	0.65 ± 0.24
	$(B-V)_o \leq -0.11$	0.19 ± 0.30	0.70 ± 0.28	0.19 ± 0.32	0.52 ± 0.33
	$(B-V)_o > -0.11$	0.31 ± 0.34	$0.81 (> 0.61)$	0.24 ± 0.28	0.67 ± 0.31
$M_{V_o} > -0.25$	all	0.73 ± 0.17	0.35 ± 0.09	0.78 ± 0.20	$0.94 (> 0.87)$

[†]In the range $M_{V_o} \leq -4.5$ and $(B-V)_o \leq -0.31$ there are not stars, thus we cannot estimate there the chance coincidence probability

3.8 Discussion

In the previous sections we described the results from the cross-correlation of the sources detected in our *Chandra* survey of the SMC with the OGLE-II and MCPS optical catalogs. We find 52 sources with a single counterpart, 68 sources with two or more matches, while for 33 sources we do not find any matches, within an average search radius of 1.99″ (see §3.3.1). We also find that the chance coincidence probability and foreground contamination are minimal for early type (O, B) stars. Here, we will use the optical photometric data (discussed in §3.5 and §3.6), and the X-ray properties of the *Chandra* sources with early type optical counterparts (from Taylor et al. 2008, in preparation and Zezas et al. 2008, in preparation) in order to set constraints on their nature. We do not attempt to classify X-ray sources with faint optical matches ($M_{V_o} > -0.25$), because of their large photometric errors and high chance coincidence probability.

Table 3.5. Chance associations between the X-ray sources and the stars in the MCPS catalog

Magnitude range	Color range	Chance coincidence probability single matches r=1.5″	single matches r=2.5″	multiple matches r=1.5″	multiple matches r=2.5″
[1]	[2]	[3]	[4]	[5]	[6]
$M_{V_o} \leq -4.5$	all	0.01 ± 0.15	0.05 ± 0.16	0.01 ± 0.15	0.04 ± 0.13
	$(B-V)_o \leq -0.31^{\dagger}$	...	...	...	...
	$(B-V)_o > -0.31$	0.01 ± 0.15	0.05 ± 0.15	0.01 ± 0.15	0.04 ± 0.13
$-4.5 < M_{V_o} \leq -0.25$	all	$0.72(> 0.41)$	$0.89(> 0.78)$	0.25 ± 0.17	0.57 ± 0.17
	$(B-V)_o \leq -0.11$	0.14 ± 0.26	0.56 ± 0.35	0.11 ± 0.19	0.39 ± 0.30
	$(B-V)_o > -0.11$	0.67 ± 0.32	$0.89(> 0.76)$	0.33 ± 0.24	0.59 ± 0.19
$M_{V_o} > -0.25$	all	$0.92(> 0.80)$	0.70 ± 0.09	$1.00(> 0.66)$	$1.00(> 0.85)$

†In the range $M_{V_o} \leq -4.5$ and $(B-V)_o \leq -0.31$ there are not stars, thus we cannot estimate there the chance coincidence probability

3.8.1 Classification criteria

In order to classify the X-ray sources we use a scheme involving the position of the counterparts on the CMD and their spectral and timing X-ray properties:

(i) The broad spectral types of the optical counterparts of the X-ray sources are determined on the basis of their position on the CMD. In this work we focus on OB stars (see §3.6). It should be noted that the contribution of the accretion disk in the optical band is not expected to be significant for early type stars, while it becomes dominant for the later spectral types (van Paradijs & McClintock 1995).

(ii) A hard ($\Gamma < 1.6$) X-ray spectrum or hardness ratio is indicative of a pulsar binary (e.g. Yokogawa et al. 2003). Sources with softer spectra could be either background AGNs, black-hole binaries or neutron stars with weak magnetic fields. Although a subset of AGNs have hard X-ray spectra (Compton thick AGNs; e.g. Matt et al. 2000), the identification of a hard X-ray

source with an early type star would strongly suggest that it is a HMXB.

(iii) The X-ray to optical "color index", $\xi = B_o + 2.5log(F_X)$ (where B_o is the reddening corrected apparent B magnitude, and F_X is the 2.0-10.0 keV X-ray flux in μJy) introduced by van Paradijs & McClintock (1995), is another standard means of classifying X-ray sources, as HMXBs have lower values of ξ than the LMXBs. Since many of our optical counterparts do not have B band photometry, we define ξ in terms of the extinction corrected V band magnitude, and we calibrate it for different types of XRBs based on the HMXBs and LMXBs catalogs of Liu et al. (2005 for the SMC and LMC HMXBs, 2006 for the Galactic HMXBs, and 2001 for the Galactic and LMC LMXBs). For the Galactic HMXBs and LMXBs we only use data for objects which have X-ray fluxes in the 2.0-10.0 keV band, V band photometry, and reported $E(B-V)$ reddening correction (used to calculate V_o, assuming $R_V = 3.24$). For the SMC and LMC HMXBs, we opted to use all the available sources presented in the census of Liu et al. (2005) and we converted their flux densities from the various energy bands to the 2.0-10.0 keV band using a flat power-law spectrum (Γ=1, and $N_H = 6.0 \times 10^{21} cm^{-2}$ for the SMC HMXBs; $N_H = 6.0 \times 10^{20} cm^{-2}$ for the LMC HMXBs), since this catalog contains several sources detected in many different energy bands. In addition, for the SMC and LMC HMXBs we included even sources without reported $E(B-V)$, since we opted to correct all of them for extinction of $A_V = 0.29$ mag and $A_V \sim 0.55$ mag (mean value for the hot populations, Zaritsky et al. 2004), respectively. We find that the distributions of ξ are approximately Gaussian for all the samples. In particular, the SMC and LMC HMXBs have a mean value of 13.06 ± 3.37, and 12.72 ± 3.90, respectively (based on 55 and 20 sources for each sample), while the distribution of ξ for 35 Galactic HMXBs has a mean value of 10.93 ± 3.74. For the LMXBs we find a much higher value of $\xi = 20.82 \pm 2.07$ (from 44 Galactic sources). The errors given here are the standard deviation. So far, no LMXBs have been detected in the SMC, while for the LMC there is only one source listed in Liu et al. (2001) with $\xi = 21.73$. The sample of Liu et al. (2005) includes Magellanic Clouds HMXBs to a limiting luminosity of $L_x \sim 2 \times 10^{34}$ erg s^{-1} (2.0-10.0 keV), while the Galactic HMXBs sample (Liu et al. 2006) has a limiting luminosity of $L_x \sim 1.5 \times 10^{36}$ erg s^{-1} (2-10 keV). The sample of the Galactic LMXBs (Liu et al. 2006) has a limiting luminosity of $L_x \sim 3 \times 10^{37}$ erg s^{-1}. These numbers indicate that the SMC and LMC HMXBs tend to be X-ray louder than Galactic binaries. Since the vast majority of sources in our sample have luminosities in the $10^{33} - 10^{35}$ erg s^{-1} range, the expected values of ξ will be closer to those of quiescent Magellanic

Clouds HMXBs, well separated from the LMXB range.

Given the large area covered by the Chandra survey, we expect a significant number of background AGNs. However, we cannot use the f_X/f_{opt} ratio in order to identify them, since its range ($0.1 \leq f_X/f_{opt} \leq 10$; e.g. Silverman et al. 2005) also covers the bona fide Be-XRBs. Therefore, we do not attempt to identify any AGNs, but we note that the majority of the unclassified *Chandra* sources (see below Table 3.6) could be background AGNs.

For the classification of an X-ray source, the ξ parameter is not as sensitive as the position of the optical counterparts on the CMD and the X-ray spectral properties. Nevertheless, we can use this criterion to confirm the classification derived using the first two criteria and as a way to distinguish between outbursting and less active HMXBs.

A more detailed presentation of these classification criteria will be presented in a forthcoming paper.

Table 3.6. Summary of optical and X-ray properties

X-ray	Optical properties			X-ray properties			ξ	Classification	
src. ID	M_{V_o}	$(B-V)_o$	Offset ($''$)	spectrum*	pulsations	observed flux†		this work	previous°
[1]	[2]	[3]	[4]	[5]	[6]	[7]	[8]	[9]	[10]
3_1	0.58	99.99	0.13	soft (S)	no[(1)]	8.20 ± 0.45	14.62	unclassified	AGN (type I)?
	0.36	99.99	0.54				14.40		
3_2‡	1.11	-0.47	2.01	hard (S)	yes[(2)]	7.04 ± 0.44	14.77	Be-XRB?◇	Be-XRB, P
	1.11	1.08	0.28				14.77		
3_3	-3.17	-0.11	0.14	hard (S)	yes[(3)]	2.58 ± 0.24	9.40	Be-XRB?	Be-XRB, P
3_4	-1.00	0.28	0.54	soft (S)	···	2.32 ± 0.24	11.46	unclassified	···
3_7	-4.48	-0.16	1.30	hard? (HR)	no[(4)]	0.77 ± 0.14	6.77	Be-XRB?	HMXB?
3_18	-3.31	-0.13	0.72	···	yes[(5)]	0.19 ± 0.07	6.42	Be-XRB?	Be-XRB, P
3_19‡	-1.24	-0.16	2.71	hard? (HR)	···	0.18 ± 0.07	8.42	new Be-XRB?	···
	-2.20	0.52	0.60				7.46		
4_1	-3.75	-0.13	0.55	hard (S)	yes[(6)]	7.82 ± 0.40	10.05	Be-XRB?	Be-XRB, P
4_2	-2.67	0.01	0.47	hard (S)	yes[(7)]	4.31 ± 0.30	10.48	Be-XRB?	Be-XRB, P
4_3	-4.65	-0.15	0.28	hard (S)	no[(8),(9)]	5.56 ± 0.36	8.78	Be-XRB?	Be-XRB?
4_4	-2.61	-0.19	0.54	hard (S)	no[(4)]	2.60 ± 0.23	9.99	new Be-XRB?	unclassified△
4_5	-2.89	0.00	0.61	hard? (HR)	no[(8),(9)]	4.58 ± 0.45	10.33	Be-XRB?	Be-XRB?
4_8	-3.44	-0.09	0.63	hard? (HR)	no[(4)]	1.78 ± 0.20	8.74	new Be-XRB?	unclassified△
4_10	-1.38	-0.16	1.36	soft (HR)	no[(4)]	0.64 ± 0.12	9.69	unclassified	unclassified△
4_11	-0.31	-0.19	1.05	hard? (HR)	no[(4)]	0.31 ± 0.08	10.00	unclassified	unclassified△
4_14	-4.21	-0.04	1.93	hard? (HR)	yes[(10)]	0.53 ± 0.15	6.67	Be-XRB?	Be-XRB, P
4_17	-3.89	-0.04	0.99	hard? (HR)	···	0.27 ± 0.08	6.26	new Be-XRB?	···
4_19	-1.03	-0.17	2.27	hard? (HR)	···	0.21 ± 0.07	8.87	new Be-XRB?	···
4_22	-0.93	-0.16	2.32	···	···	0.29 ± 0.09	9.26	new HMXB?	···
4_32	-0.57	0.67	1.34	···	···	0.14 ± 0.06	8.87	unclassified	···
5_1	-4.28	-0.09	0.55	hard (S)	yes[(2)]	51.60 ± 1.16	11.52	Be-XRB?	Be-XRB, P
5_2	-3.00	-0.18	0.24	hard (S)	yes[(2)]	3.63 ± 0.30	9.92	Be-XRB?	Be-XRB, P
5_3	-4.29	-0.36	0.54	hard (S)	yes[(11)]	2.85 ± 0.28	8.36	Be-XRB?	Be-XRB, P
5_4	-3.83	0.05	0.79	hard (HR)	···	1.98 ± 0.24	8.65	new Be-XRB?	···
5_6	-1.33	-0.12	3.60	soft (HR)	···	1.91 ± 0.24	10.89	unclassified	···
5_7	-3.89	-0.13	1.19	hard? (HR)	yes[(12)]	1.11 ± 0.08	7.74	Be-XRB?	Be-XRB, P
5_9	-1.00	0.50	1.33	soft? (HR)	···	0.38 ± 0.10	9.48	unclassified	···
5_12	-4.27	-0.09	0.35	hard? (HR)	···	0.33 ± 0.09	6.04	new Be-XRB?	···
5_15	-0.19	0.09	0.50	soft? (HR)	no[(13)]	0.26 ± 0.09	9.87	unclassified	Quasar
5_16	-4.47	-0.16	0.83	hard? (HR)	yes[(14)]	0.44 ± 0.16	6.16	Be-XRB?	Be-XRB, P
5_18	-0.29	0.22	2.74	···	···	0.29 ± 0.10	9.90	unclassified	···
5_23	-1.20	-0.15	2.57	···	···	0.21 ± 0.08	8.59	new HMXB?	···
5_24	-4.24	-0.08	0.78	soft? (HR)	···	0.16 ± 0.07	5.34	unclassified	···

Table 3.6—Continued

X-ray	Optical properties			X-ray properties			ξ	Classification	
src. ID	M_{V_o}	$(B-V)_o$	Offset ($''$)	spectrum*	pulsations	observed flux†		this work	previous°
[1]	[2]	[3]	[4]	[5]	[6]	[7]	[8]	[9]	[10]
5_25	-0.71	0.89	1.81	···	···	0.18 ± 0.07	8.95	unclassified	···
5_29	-1.38	-0.23	0.78	hard? (HR)	···	0.14 ± 0.06	7.97	new Be-XRB?	···
5_32	-3.99	-0.16	2.22	soft? (HR)	···	0.13 ± 0.06	5.26	unclassified	···
6_1	-4.16	0.05	0.58	hard (S)	yes(15)	121.46 ± 1.71	12.60	Be-XRB?	Be-XRB, P
6_2	-4.18	-0.11	0.40	hard (S)	yes(2)	11.70 ± 0.54	10.03	Be-XRB?	Be-XRB, P
6_3	-1.04	-0.23	1.38	soft? (HR)	···	1.06 ± 0.16	10.57	unclassified	···
6_4	-4.77	-0.20	0.27	hard? (HR)	···	0.75 ± 0.14	6.46	Be-XRB?	Be-XRB
6_8	-1.59	1.03	2.02	soft? (HR)	···	0.37 ± 0.10	8.89	unclassified	···
6_20	-5.48	0.30	0.62	···	···	0.18 ± 0.07	4.18	unclassified	···
6_23	-2.09	1.33	0.56	···	···	0.13 ± 0.05	7.16	unclassified	···
7_1	-2.25	0.00	0.45	hard (S)	yes(16)	4.51 ± 0.35	10.94	Be-XRB?	Be-XRB, P
7_4	-1.67	1.49	2.10	···	···	0.93 ± 0.16	9.80	unclassified	···
	-1.34	0.14	0.76				10.13		
7_6	-1.49	-0.27	1.45	hard? (HR)	···	0.63 ± 0.13	9.57	new Be-XRB?	···
7_9	-5.70	1.52	0.77	hard? (HR)	no(17)	0.61 ± 0.13	5.32	unclassified	foreground star
7_17‡	-0.83	0.85	4.47	soft? (HR)	···	0.30 ± 0.10	9.44	unclassified	···
	-0.81	-0.05	1.28				9.46		
7_19	-2.03	0.18	1.36	···	···	0.19 ± 0.07	7.70	unclassified	···

†Calculated from net counts, in units of 10^{-13} erg cm^{-2} s^{-1} for the full energy band ($0.7 - 10.0$ keV; Zezas et al. 2008, in preparation).

°The references for the previously classified sources are given in Column [3] of Table B.7 (appendix §B).

△unclassified: sources of uncertain nature (Shtykovskiy & Gilfanov 2005).

‡For these sources, we present two optical matches, as their magnitudes and/or X-ray spectral properies do not allow us to propose the most likely counterpart (these cases are discussed in §3.8.3).

*A "?" following the hard or soft X-ray spectrum indicates a possibly hard or soft spectrum, respectively (due to the small number of X-ray counts).

◇Although this source with the hard X-ray spectrum remains unclassified in the 1σ search radius, there is a likely bright optical counterpart between the 1σ and 2σ search radii suggestive of the Be-XRB nature of this source (in agreement with Edge et al. 2004). For more details see §B.6 in the Appendix.

Note. — new Be-XRB?: candidate new Be-XRB (early type counterpart and hard or possibly hard X-ray spectrum); new HMXB?: candidate new HMXB (early type counterpart but no information about the X-ray spectrum); unclassified: sources with a soft X-ray spectrum or unavailable spectral information or without an early type optical counterpart - cannot be classified without further information (e.g. optical spectroscopy, X-ray timing or spectral analysis); P: pulsar.

References. — (1) Dobrzycki et al. 2003b, (2) Edge et al. 2004, (3) Macomb et al. 2003, (4) Shtykovskiy & Gilfanov 2005, (5) Sasaki et al. 2003, (6) Yokogawa et al. 2003, (7) Coe et al. 2005a, (8) Haberl & Sasaki 2000, (9) Haberl & Pietsch 2004, (10) Edge & Coe 2003, (11) Israel et al. (1995, (12) Marshall et al. (1998, (13) Dobrzycki et al. 2003a, (14) Buckley et al. 2001, (15) Corbet et al. 2002, (16) Corbet et al. (1998, (17) Sasaki et al. 2000.

3.8.2 Sources with multiple optical matches

For 61 X-ray sources in our survey with more than one optical match (out of the 68 in total), we tentatively identify them with the brightest optical source in the region of low chance coincidence within their error circle (§3.7). Whenever possible, we confirm this identification with the spectral properties of the X-ray source: a hard ($\Gamma < 1.6$) spectrum and/or detection of pulsations are tell-tale signatures of pulsar binaries. For example, we suggest that the counterpart of *Chandra* source 5_7 is the early type star O_7_70829 from the OGLE-II catalog, and not one of the three fainter stars within its error circle, which do not lie on the locus of OB stars, in agreement with the same identification by Sasaki et al. (2003), and also supported by its optical variability (Zebrun et al. 2001). We also classify this X-ray source as Be-XRB pulsar (in agreement with Haberl & Sasaki 2000), due to its possibly hard spectrum (for details see below §3.8.3), and its detected pulsations (Marshall et al. 1998). For the few (**4** out of the 68) X-ray sources which do not have optical counterparts in the region of low chance coincidence, we cannot propose a likely counterpart (discussed in §3.8.3).

3.8.3 Properties of the optical counterparts and implications for the nature of the X-ray sources

Following the above approach, out of the 120 X-ray sources with optical matches, we were able to identify 32 with early type counterparts (of O or B spectral type). In Table 3.6 we summarize the optical and X-ray properties of the *Chandra* sources with optical counterparts brighter than $M_{V_o} \leq -0.25$. We also present sources with counterparts fainter than $M_{V_o} > -0.25$, only in cases of reliable public classification (*Chandra* sources 3_1, 3_2, and 5_15). In total there are 50 *Chandra* sources for which we present their optical and X-ray properties in Table 3.6. In Column (1) we give the *Chandra* source ID, in Columns (2) and (3) the M_{V_o} magnitude and $(B-V)_{\rm o}$ color of their proposed counterparts (corrected for A_V= 0.29 mag and *E(B-V)*= 0.09), and in Column (4) its offset from the X-ray source (in arcseconds). In Column (5) we indicate if the X-ray source has a hard ($\Gamma < 1.6$) or soft ($\Gamma > 1.6$) spectrum, and whether this is based on spectral fits (S) (Taylor et al. 2008, in preparation) or X-ray colors (HR; calculated using the Bayesian method of Park et al. 2006). The X-ray color derived parameters are based on color-color diagrams involving X-ray colors defined as Col1=log(S/M) and Col2=log(M/H), where S,

M and H correspond to the soft (0.5-1.0 keV), medium (1.0-2.5 keV), and hard (2.5-7.0 keV) band, respectively. In Column (6) we present if the X-ray source has detected pulsations or not and its reference, while in Column (7) we give its observed flux in the full band ($0.7-10.0$ keV; Zezas et al. 2008, in preparation). In Column (8) we give the value of the ξ parameter. Finally, in Column (9) we present a tentative classification for the X-ray sources derived in this study. New candidate Be-XRBs are proposed on the basis of early type counterparts and hard (or possibly hard) spectrum of the *Chandra* sources (listed as "new Be-XRBs ?" in Table 3.6), while as new candidate HMXBs (listed as "new HMXBs ?") we consider those with early type counterparts but no spectral information available (due to their small number of X-ray counts). Sources with a soft X-ray spectrum, unavailable X-ray spectral information and/or sources without an early type optical counterpart cannot be classified without further information (e.g. optical spectroscopy, X-ray timing or spectroscopic analysis). In Column (10) we present any previous classification of *Chandra* sources (including those with fainter than $M_{V_o} \sim -0.25$ counterparts).

In this paper we present classifications for 30 sources of which 12 are previously unclassified. Our results are consistent with previous classifications in all cases of overlap (18 sources in total all of which are Be-XRBs). There are 20 additional sources that remain unclassified: 5 with OB spectral type counterparts and soft X-ray spectra (discussed below), and 15 sources with bright optical counterparts ($M_{V_o} \leq -0.25$), but not within the locus of OB stars. For 3 sources (out of the 50 in total presented in Table 3.6), we cannot confirm the previously published classification based on the data we used (1 possibly AGN, 1 Quasar, and 1 foreground star). The 12 sources with new classification have a mean value of $\xi = 8.14 \pm 1.28$ (assuming as above a flat power-law spectrum with Γ=1, and $N_H = 6.0 \times 10^{21} cm^{-2}$), which is in the range of quiescent HMXBs (as discussed in §3.8.1). In addition, these 12 X-ray sources have low luminosities ($L_x \sim 5 \times 10^{33} - 10^{35}$ erg s^{-1}), and all but 2 (for which we cannot derive spectral information) have hard or possibly hard X-ray spectra, which together with the intermediate value of the ξ parameter are indicative of residual accretion. Therefore, these 12 sources can be considered as HMXBs being in an intermediate state, e.g. soon after outburst.

In particular, we find 5 *Chandra* sources (sources 4_10, 5_6, 5_24, 5_32, 6_3) which have optical matches within the locus of OB stars, but have a soft or possibly soft X-ray spectrum. These sources could be XRB pulsars (hereafter XBPs) with a weak accretion component (e.g. XBPs close to quiescence), possibly as a result of the propeller effect (Illarionov & Sunyaev 1975).

This interpretation is consistent with their typical low X-ray luminosity ($L_{\rm x} \sim 10^{34}$ erg s^{-1}), and mean value of the ξ parameter (8.35 ± 2.82) characteristic of intermediate state XRBs.

There are 6 additional cases with more than one optical match for which it is not possible to select the most likely counterpart. The optical matches of *Chandra* sources 3_1, 4_6 and 7_16 are very faint, and because of their large photometric errors and high chance coincidence probability, we cannot select one of the two counterparts (*Chandra* source 3_1 is discussed in §B.3). This is also the case for *Chandra* source 4_23, for which we find two optical matches, one from each of the studied optical catalogs. The O_5_101577 source has only been detected in the I band (i.e. no B, V photometric data available for it), while the Z_2029266 source is also faint ($V > 19$ mag). Likewise, for *Chandra* sources 7_4 and 7_17 we cannot choose a likely counterpart without optical spectroscopic or variability information, as the 2 brightest sources within the search radius have similar V magnitudes. In particular, for *Chandra* source 7_4 we do not have spectral information, while source 7_17 has possibly a soft spectrum (also discussed in the Appendix, §B.1).

In the case of *Chandra* source 3_19 the brightest counterpart (source Z_3050592) is not an OB star, but it lies in the area between the red giant branch and the MS. Instead, we find that a fainter source (Z_3049033) is located in the OB star locus. For completeness, we present the optical properties of both sources in Table 3.6. However, the low X-ray luminosity of source 3_19 indicates that the compact object does not accrete via Roche-lobe overflow as would be expected in the case of an evolved donor (most probably this is a wind-fed system). Furthermore, the hard X-ray spectrum of this source, that is indicative of a pulsar, suggests a younger system, possibly a Be-XRB. Thus, we propose the OB star candidate Z_3049033 as the most likely counterpart of *Chandra* source 3_19.

In total, we identify 32 sources with early type counterparts, 24 of which have hard X-ray spectra, strongly suggesting that they are XBPs. All but one pulsars (i.e. 13) that have been identified as X-ray sources within our *Chandra* fields have hard spectra and early type counterparts (for completeness in our *Chandra* fields lie 19 pulsars[9], however only 14 have been detected in our survey). The one exception is *Chandra* source 3_18 (XBP, e.g. Sasaki et al. 2003, Haberl & Pietsch 2004): although its optical counterpart is an OB spectral type star, its small number of

[9]http://www.astro.soton.ac.uk/∼mjc/ as of 06/05/2007.

counts does not provide us the necessary spectral information.

Ten of the candidate Be stars of Mennickent et al. (2002) have been identified as counterparts to our *Chandra* sources. Three of those are proposed as counterparts to *Chandra* sources 4_8, 4_17, and 7_1 for the first time, while for seven X-ray sources (3_3, 4_2, 5_3, 5_7, 5_15, 6_1, and 6_4) there is a known counterpart in the literature (see Table B.7, §B in the appendix for more details). An extensive presentation of these 10 sources is given in §B.2. Eight type-4 stars (out of the 685 in total) from the above catalog have been previously identified as Be stars or Be-XRBs (Mennickent et al. 2002). This supports our classification of the aforementioned 3 sources as new candidate Be-XRBs. In addition, Mennickent et al. (2002) suggest that all the type-4 stars might be related to Be stars in some way, an assumption based also on the morphology of their light curves.

From the finding charts we see that a few sources have brighter counterparts that fall outside the 1σ search radius. Thus, we extended the search radius to twice the one used in the original search and we cross-correlated again the coordinates of the *Chandra* sources with the OGLE-II and MCPS catalogs. We find that out of the 33 X-ray sources without an optical counterpart identified in the 1σ search radius, there are 7 X-ray sources with bright optical matches ($M_{V_o} \leq -0.25$ mag) between the 1σ and 2σ search radii (see §B in the appendix). None of these matches lie in the locus of OB stars, while we ignore fainter matches. In addition there are 33 *Chandra* sources with optical matches between the 1σ and 2σ search radii, which are brighter than those found within the 1σ search radius. In particular, for 10 of these *Chandra* sources their optical matches lie in the locus of OB stars, and 3 of them have hard or possibly hard X-ray spectrum (sources 3_2, 4_13, 4_19). *Chandra* source 3_2 is a known pulsar, possibly Be-XRB (Edge et al. 2004), while sources 4_13 and 4_19 have not been previously identified. The hard spectrum of these sources and the early type counterpart make them candidate XBPs (see §B.6 in the Appendix). We note that although the chance coincidence probability for the bright optical matches within the 2σ search radius is very high ($\sim$70%; see Tables 3.4 and 3.5 for more details), the identification of a hard X-ray source with an optical source within the locus of OB stars makes it a candidate Be-XRB (these additional 3 sources are included in Table 3.6 and in our census of Be-XRBs in the SMC). For the remaining sources we do not propose any of their optical matches as a counterpart, and we only present them for completeness (Tables B.1 and B.2 in the Appendix, §B.5).

3.8.4 Comparison with the Galactic and LMC Be-XRBs

In order to understand the HMXB population of the SMC, several studies have compared the number of Be-XRBs in the Magellanic Clouds and the Milky Way (e.g. Haberl & Sasaki 2000, Majid, Lamb & Macomb 2004, Coe et al. 2005a, Haberl & Pietsch 2004; hereafter [HP04]). One approach is to compare the ratios of Be-XRBs to normal (i.e. non-emission line) OB stars. By studying the Be-XRB population with respect to their related stellar populations, we minimize age effects or variations due to SF rate differences for populations of different ages, allowing us to probe for intrinsic differences in the XRB formation efficiency. For the same reason, we do not compare the ratio of Be-XRBs to SG/XRBs, since this is sensitive to the age of these systems, and therefore to variations of the SF rate over these time scales. We note that because of the transient nature of the Be-XRBs, their numbers can be considered only as lower limits. This has been demonstrated by the increasing number of Be-XRBs detected in long term monitoring surveys of the SMC (e.g. Laycock et al. 2005). So far, various studies have confirmed 21 Be-XRBs in the SMC ([HP04], Raguzova & Popov 2005; hereafter [RP05]) and only 1 supergiant, which is located in the eastern wing of the SMC (SMC X-1, Webster et al. 1972). In the compilation of [HP04], 17 (out of the 21) Be-XRBs are X-ray pulsars, while for another 8 pulsars the identification with a Be star is suggested (see [HP04] and references therein). There are also 23 proposed Be-XRBs without detected pulsations, and one suggested Be-XRB with uncertain pulse period ([HP04]). Since the detection of pulsations requires high S/N X-ray data, in our study, we include all Be-XRBs, and not only those with detected X-ray pulsations. To these we add the Be-XRBs (and Be-XRBs candidates) identified in our study, raising the total number of known Be-XRBs in the SMC *Chandra* fields to 29 sources.

At this point, we revisit the relation between Be-XRBs and OB stars, taking into account the latest census of XRBs, and comparing it with the corresponding ratios for the LMC and Milky Way. The numbers of Be-XRBs in the 3 galaxies are based on the compilations of Liu et al. (2005, 2006). Since these compilations consist of different samples of sources detected in various surveys with different sensitivities, we use a subset of Be-XRBs down to the same detection limit of 10^{34} erg s^{-1} (in the 2.0-10.0 keV band; equivalent to $\sim 1.1 \times 10^{34}$ erg s^{-1} in the 0.7-10.0 keV band). This cut-off X-ray luminosity was chosen in order to assemble uniform samples of sources detected in surveys of the SMC and the Milky Way. From those catalogs we

used all sources with available spectral types for their counterparts. We also converted their flux densities from the various energy bands to the 2.0-10.0 keV band, assuming a flat power-law spectrum of $\Gamma = 1$.

In the catalog of Liu et al. (2006) we find 31 Galactic Be-XRBs located within 10 kpc from the Sun (based on distances from [RP05][10]) with $L_X \geq 10^{34}$ erg s^{-1} (Liu et al. 2006) and 17 Be-XRBs in the SMC area covered by our *Chandra* survey (including confirmed as well as candidate Be-XRBs; Liu et al. 2005). Including the 7 new candidate Be-XRBs from this work with an X-ray luminosity of $\sim 10^{34}$ erg s^{-1}, results in a total of 24 SMC Be-XRBs within our *Chandra* fields. In this comparison we do not consider LMC sources since the LMC has not been surveyed as extensively and in the same depth as the Milky Way or the SMC.

We then estimate the number of OB stars using their locus on the CMD defined in §3.6. Based on the MCPS catalog (Zaritsky et al. 2002) we find $\sim$ 13720 OB stars within our *Chandra* fields ($\sim$2220, $\sim$4060, $\sim$2730, $\sim$3040, and $\sim$1670 OB stars for *Chandra* field 3, 4, 5, 6, and 7, respectively). The photometric data of these sources have been reddening corrected as described in §3.6. In the case of the Milky Way, Reed (2001) estimated that there are $\sim$ 25800 OB stars within 10 kpc of the Sun. Based on the above numbers we find that the Be-XRBs with $L_X \geq 10^{34}$ erg s^{-1} are ~ 2 times more common in the SMC when compared to the Milky Way, with respect to its populations of young stars. Therefore, we confirm the notion that the SMC has a large number of Be-XRBs (e.g. Liu et al. 2005; Coe et al. 2005b).

For completeness, we extend this comparison to the LMC, considering only sources with $L_X \geq 10^{36}$ erg s^{-1}, which is the average completeness level of the ROSAT observations of LMC fields. In this case we find 6 Be-XRBs in the LMC (Liu et al. 2005), 10 in the SMC, and 29 in the Milky Way (in the case of the LMC we find $\sim$ 42200 OB stars, in the area covered by the ROSAT fields where the 6 Be-XRBs were detected, based on the MCPS catalog of Zaritsky et al. (2004) and assuming $A_V \sim 0.55$ mag as in §3.8.1). Hence, the Be-XRBs are ~ 7 times more common in the SMC, with respect to the LMC, while when compared to the Milky Way we find almost equal ratios of Be-XRBs to OB stars. However, one caveat in the case of the LMC, is that its small number of Be-XRBs may be due to the fact that it has not been monitored as extensively and in the same depth as the SMC or the Milky Way.

[10]http://xray.sai.msu.ru/$\sim$raguzova/BeXcat/ as of 08/25/2006 for the Milky Way.

The comparable ratios of Be-XRBs to OB stars in the SMC and the Galaxy indicate that the higher number of Be-XRBs in the SMC is simply the result of enhanced star forming activity in the SMC $\sim$ 30 Myr ago (e.g. Majid et al. 2004). In particular, the formation and lifetimes of wind-fed HMXBs are driven by the stellar evolution of the donor. Be stars, which is the most common type of donor in wind-fed XRBs, develop their decretion disks at ages of $25 - 80$ Myr (McSwain & Gies 2005), with a peak at $\sim$ 35 Myr. Indeed, using the isochrones presented in §3.6, we determine that bright counterparts of the X-ray sources in our fields (of OB spectral types) have ages ranging from $\sim$ 15.5 to $\sim$ 85 Myr. Based on the SF history of the SMC (Harris & Zaritsky 2004), we find that for Z=0.008, the most recent major burst occurred $\sim$ 42 Myr ago. The only exceptions are *Chandra* field 6, where a similarly strong burst occured somewhat earlier ($\sim$ 27 Myr ago), and *Chandra* field 4 which shows an additional burst only $\sim$ 7 Myr ago. The duration of the major bursts is $\sim$ 40 Myr. In addition, there were older SF episodes ($\sim$ 0.4 Gyr ago) with lower intensity but longer duration. However, neither the relatively old ($\sim$ 0.4 Gyr) widespread star forming activity, nor the most recent episode ($\sim$ 7 Myr) are expected to produce a population of Be-XRBs. Therefore, the large number of Be-XRBs in the SMC is most likely due to its enchanced star-forming activity $\sim$ 42 Myr ago. OB stars formed during this episode are expected to reach now the maximum rate of decretion disk formation. Even in smaller spatial scales the excess of Be-XRBs in fields 4 and 5 is consistent with their higher SF rate $\sim$ 42 Myr ago, in comparison to the other fields, and with the fact that the age of their stellar populations is in the range of maximum Be-star formation.

However, the comparison of the ratios of Be-XRBs over OB stars in the SMC, and the Milky Way indicates that there is still a residual excess of a factor of $\sim$ 2 that cannot be accounted for by star-formation and age differences. This residual excess can be attributed to the different metallicity of the two galaxies. Population synthesis models predict a factor of $\sim$ 3 higher numbers of HMXBs in galaxies with metallicities similar to that of the SMC, when compared to the Milky Way (Dray 2006). This is in good agreement with the residual excess of HMXBs by a factor of $\sim$ 2 we find above from the comparison between the observed HMXBs populations in the two galaxies. In addition there is observational evidence for a trend for higher proportion of Be stars in lower metallicity environments (at least in the case of younger systems; Wisniewski & Bjorkman 2006). In particular they find a ratio of $\sim$ 2 for the numbers of Be stars in SMC and Galactic metallicities, which could also explain the residual excess of binaries in the SMC.

3.8.5 Local variations of the Be-XRB populations

When we compare the number of Be-XRBs in the different *Chandra* fields we find a slight excess of these objects in fields 4 and 5. In particular, these two fields have 10 and 13 Be-XRBs respectively versus an average of 3 Be-XRBs in each of the other 3 fields. Field 5 also has the largest number of identified pulsars (7; fields 3, 4, 6, and 7 have 3, 4, 4, and 1 pulsars respectively). Although given the small numbers of sources this excess is only marginally statistically significant, it is intriguing that fields 4 and 5 had the highest star-formation rate at the age of maximum Be star production ($\sim$ 42 Myr ago). In Figure 3.4 (lower panel), we present the height of the SF rate at the age of $\sim$ 42 Myr versus the number of Be-XBRs in each *Chandra* field. In the upper panel of Figure 3.4 we present the SFR versus the ratio of the number of Be-XBRs to the number of stars of OB spectral type in each field. In this plot we include all Be-XRBs detected in our *Chandra* fields (based on our survey and the census of Liu et al. 2005, 33 in total), and the OB stars in each field (selected as in §3.8.4) from the MCPS catalog. For completeness we also give these numbers for the 42 (in total) HMXBs that lie in our *Chandra* fields (6 for *Chandra* field 3, 13 for field 4, 16 for field 5, 5 for field 6, and 2 for field 7; shown in gray in these two panels). Predominantly, field 5 which has the most intense SF peak at the peak age of Be-star formation (almost two times more intense when compared to that of the other fields) appears to have at least double ratio of Be-XRBs to OB stars.

The direct comparison between the XRB populations and the SF history of different regions, may be complicated by kicks imparted on the compact object during the supernova explosion (e.g. van den Heuvel et al. 2000). The result of these kicks is that the XRBs may be spread over a larger volume with respect to their parent stellar population, and thus complicating the study of their connections. In the case of the SMC, and given a typical projected runaway velocity of 15 ± 6 km s^{-1} (van den Heuvel et al. 2000), we estimate that a Be-XRB would have traveled a maximum distance of $\sim$ 640 pc from the time it was formed (i.e. $\sim$ 42 Myr ago, given the SF history of the SMC). This distance is an upper limit, since the age of 42 Myr is only based on the formation time-scale of Be binaries, and it does not include the formation time-scale of the pulsar, which is a few Myr. For a distance of 60 kpc this translates to a projected angular distance of $\sim 36.7'$, roughly twice the dimension of the *Chandra* fields. However, the scales of the star forming regions at the age ranges of interest ($<$ 20Myr, $20 - 60$Myr, $>$ 60Myr) are

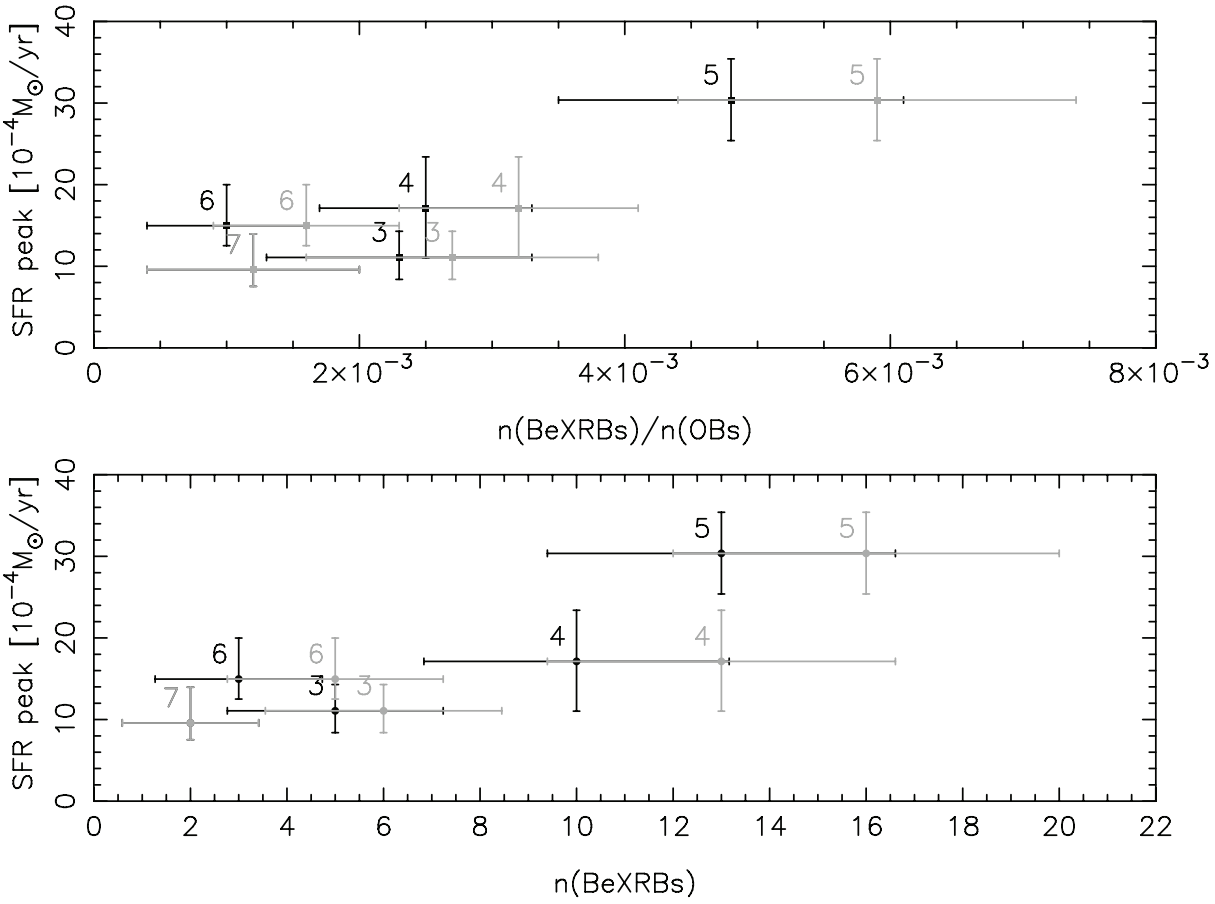

Figure 3.4 **(a)** *Lower panel*: The star-formation rate at the age of ~ 42 Myr versus the number of Be-XBRs in each *Chandra* field. **(b)** *Upper panel*: The star-formation rate at the age of ~ 42 Myr versus the ratio of the number of Be-XBRs to the number of OB spectral type stars in each field (Be-XRB systems are shown in black, while the overall population of HMXBs is shown in gray). The error bars in the x-axis were derived assuming Poisson statistics. In the y-axis error bars indicate lower and upper limits of the mean SF rate in each *Chandra* field.

much larger than the size of the *Chandra* fields. Therefore, our fields across the "bar" of the SMC provide a representative picture of the Be-XRB population in the main body of the SMC. Moreover, the excess of Be-XRBs at fields 4 and 5 which have the highest SF rates in ages of ~ 42 Myr (which corresponds to the age of maximum production of Be stars) gives further confidence that the kick velocities are small enough not to smear the correlation between X-ray sources and their parent stellar populations.

3.9 Conclusions

In this paper we report the results for the optical counterparts of the 153 X-ray sources detected in the *Chandra* survey of the central region of the SMC. For 120 sources we found optical matches in the OGLE-II and/or MCPS catalogs. Using the photometric data of these counterparts and the spectral and timing properties of the X-ray sources we propose the most likely optical counterpart for 113 *Chandra* sources, while for 7 sources the candidate counterparts are equally likely. In particular:

1. We find that 52 X-ray sources have a single counterpart, 68 have two or more matches, while 33 sources do not have counterpart in either OGLE-II or MCPS catalog within the 1σ search radius (7 out of these 33 sources have bright optical matches ($M_{V_o} \leq -0.25$) between the 1σ and 2σ search radii, but none of them is associated with an OB star).

2. Early type counterparts (of OB spectral type) have been identified for 32 X-ray sources (chance coincidence probability $\leq 19\%$). Based on spectroscopic observations of stars in the SMC we define the photometric locus of early type (OB) stars in the M_{V_o} vs. $(B-V)_o$ CMD. Based on the position on the CMD and their X-ray spectral properties, we propose: (a) 9 new candidate Be-XRBs, and (b) 2 new candidate HMXBs. In addition, we find 3 sources with hard X-ray spectra and an OB star counterpart within their 2σ search radius.

3. Based on the isochrones of Lejeune & Schaerer (2001), we estimate the age of the 11 new candidate Be-XRBs and HMXBs to be $\sim 15 - 85$ Myr, in agreement with the age of Be stars.

4. Eighteen X-ray sources with bright counterparts ($M_{V_o} \leq -0.25$) could not be classified, because we do not have X-ray spectral information for them and/or they have other than OB spectral type counterparts.

5. We find that the mixing of Be-XRBs with other than their natal stellar population is not an issue in our comparisons of Be-XRBs and stellar populations in the SMC, because the SF activity across the SMC "bar" is generally uniform in scales larger than the size of the *Chandra* fields. Instead we find indication for variation in the XRB populations across the "bar" and in scales of ~ 1 kpc: fields with higher SF rate at ages which are more prone to produce Be stars show increased number of Be-XRBs.

6. Using the catalogs of Liu et al. (2005, 2006) we find that for luminosities down to $L_X \sim 10^{34}$ erg s^{-1} (chosen as a moderate minimum cut-off between different SMC and Galactic X-ray surveys) the *Chandra* SMC fields contain ~ 2 times more Be-XRBs in comparison to the Milky Way (including 7 new candidate Be-XRBs from this study), even after taking into account the different OB star formation rates in the two galaxies. This residual excess can be explained when we account for the different metallicity of the SMC and the Milky Way. This is in good agreement with the factor of ~ 3 derived from population synthesis studies (Dray 2006), and the study of Wisniewski & Bjorkman (2006).

We would like to thank Dr. A. Udalski for providing unpublished light curves of the OGLE-II stars used in this paper. This research has made use of the SIMBAD database, operated at CDS, Strasbourg, France. This work was supported by NASA LTSA grant NAG5-13056, and NASA grant G02-3117X.

Bibliography

[1] Alcock, C., et al. 1997, Astrophys. J., 486, 697

[2] Azzopardi, M., & Vigneau, J. 1982, Astr. Astrophys. Suppl., 50, 291

[3] Bica, E. L. D., & Schmitt, H. R. 1995, Astrophys. J. Suppl., 101, 41

[4] Binney, J., & Merrifield, M. 1998, Galactic astronomy / James Binney and Michael Merrifield. Princeton, NJ : Princeton University Press, 1998. (Princeton series in astrophysics)

[5] Buckley, D. A. H., Coe, M. J., Stevens, J. B., van der Heyden, K., Angelini, L., White, N., & Giommi, P. 2001, Mon. Not. R. Astr. Soc., 320, 281

[6] Cardelli, J. A., Clayton, G. C., & Mathis, J. S. 1989, Astrophys. J., 345, 245

[7] Cioni, M.-R., et al. 2000, Astr. Astrophys. Suppl., 144, 235

[8] Clark, G., Doxsey, R., Li, F., Jernigan, J. G., & van Paradijs, J. 1978, Astrophys. J. Lett., 221, L37

[9] Coe, M. J., Edge, W. R. T., Galache, J. L., & McBride, V. A. 2005a, Mon. Not. R. Astr. Soc., 356, 502

[10] Coe, M. J., Negueruela, I., & McBride, V. A. 2005b, Mon. Not. R. Astr. Soc., 362, 952

[11] Coe, M. J., & Orosz, J. A. 2000, Mon. Not. R. Astr. Soc., 311, 169

[12] Corbet, R., Marshall, F. E., Lochner, J. C., Ozaki, M., & Ueda, Y. 1998, IAU Circ., 6803, 1

[13] Corbet, R., Markwardt, C. B., Marshall, F. E., Laycock, S., & Coe, M. 2002, IAU Circ., 7932, 2

[14] Cowley, A. P., Schmidtke, P. C., McGrath, T. K., Ponder, A. L., Fertig, M. R., Hutchings, J. B., & Crampton, D. 1997, Pub. Astr. Soc. Pacific., 109, 21

[15] Crowl, H. H., Sarajedini, A., Piatti, A. E., Geisler, D., Bica, E., Clariá, J. J., & Santos, J. F. C., Jr. 2001, Astron. Journ., 122, 220

[16] Dickey, J. M., & Lockman, F. J. 1990, Ann. Rev. Astron. Astrophys., 28, 215

[17] Dobrzycki, A., Macri, L. M., Stanek, K. Z., & Groot, P. J. 2003a, Astron. Journ., 125, 1330

[18] Dobrzycki, A., Stanek, K. Z., Macri, L. M., & Groot, P. J. 2003b, Astron. Journ., 126, 734

[19] Dray, L. M. 2006, Mon. Not. R. Astr. Soc., 370, 2079

[20] Edge, W. R. T., & Coe, M. J. 2003, Mon. Not. R. Astr. Soc., 338, 428

[21] Edge, W. R. T., Coe, M. J., Galache, J. L., McBride, V. A., Corbet, R. H. D., Markwardt, C. B., & Laycock, S. 2004, Mon. Not. R. Astr. Soc., 353, 1286

[22] Evans, C. J., Howarth, I. D., Irwin, M. J., Burnley, A. W., & Harries, T. J. 2004, Mon. Not. R. Astr. Soc., 353, 601

[23] Fabrycky, D. 2005, Mon. Not. R. Astr. Soc., 359, 117

[24] Garmany, C. D., Conti, P. S., & Massey, P. 1987, Astron. Journ., 93, 1070

[25] Garmire, G. P., Bautz, M. W., Ford, P. G., Nousek, J. A., & Ricker, G. R. 2003, Proc. SPIE, 4851, 28

[26] Gehrels, N. 1986, Astrophys. J., 303, 336

[27] Gordon, K. D., Clayton, G. C., Misselt, K. A., Landolt, A. U., & Wolff, M. J. 2003, Astrophys. J., 594, 279

[28] Haberl, F., Filipović, M. D., Pietsch, W., & Kahabka, P. 2000, Astr. Astrophys. Suppl., 142, 41

[29] Haberl, F., & Pietsch, W. 2004, Astr. Astrophys., 414, 667

[30] Haberl, F., Pietsch, W., Schartel, N., Rodriguez, P., & Corbet, R. H. D. 2004, Astr. Astrophys., 420, L19

[31] Haberl, F., & Sasaki, M. 2000, Astr. Astrophys., 359, 573

[32] Harries, T. J., Hilditch, R. W., & Howarth, I. D. 2003, Mon. Not. R. Astr. Soc., 339, 157

[33] Harris, J., & Zaritsky, D. 2004, Astron. Journ., 127, 1531

[34] Hilditch, R. W., Howarth, I. D., & Harries, T. J. 2005, Mon. Not. R. Astr. Soc., 357, 304

[35] Illarionov, A. F., & Sunyaev, R. A. 1975, Astr. Astrophys., 39, 185

[36] Israel, G. L., Stella, L., Angelini, L., White, N. E., & Giommi, P. 1995, IAU Circ., 6277, 1

[37] Ita, Y., et al. 2004, Mon. Not. R. Astr. Soc., 353, 705

[38] Kahabka, P., & Pietsch, W. 1996, Astr. Astrophys., 312, 919

[39] Kim, D.-W., et al. 2004, Astrophys. J. Suppl., 150, 19

[40] Larsen, S. S., Clausen, J. V., & Storm, J. 2000, Astr. Astrophys., 364, 455

[41] Laycock, S., Corbet, R. H. D., Coe, M. J., Marshall, F. E., Markwardt, C., & Lochner, J. 2005, Astrophys. J. Suppl., 161, 96

[42] Lejeune, T., & Schaerer, D. 2001, Astr. Astrophys., 366, 538

[43] Liu, Q. Z., van Paradijs, J., & van den Heuvel, E. P. J. 2001, Astr. Astrophys., 368, 1021

[44] Liu, Q. Z., van Paradijs, J., & van den Heuvel, E. P. J. 2005, Astr. Astrophys., 442, 1135

[45] Liu, Q. Z., van Paradijs, J., & van den Heuvel, E. P. J. 2006, Astr. Astrophys., 455, 1165

[46] Luck, R. E., Moffett, T. J., Barnes, T. G., III, & Gieren, W. P. 1998, Astron. Journ., 115, 605

[47] Macomb, D. J., Fox, D. W., Lamb, R. C., & Prince, T. A. 2003, Astrophys. J. Lett., 584, L79

[48] Majid, W. A., Lamb, R. C., & Macomb, D. J. 2004, Astrophys. J., 609, 133

[49] Marshall, F. E., et al. 1998, IAU Circ., 6818, 1

[50] Massey, P. 2002, Astrophys. J. Suppl., 141, 81

[51] Massey, P., & Duffy, A. S. 2001, Astrophys. J., 550, 713

[52] Massey, P., Lang, C. C., Degioia-Eastwood, K., & Garmany, C. D. 1995, Astrophys. J., 438, 188

[53] Matt, G., Fabian, A. C., Guainazzi, M., Iwasawa, K., Bassani, L., & Malaguti, G. 2000, Mon. Not. R. Astr. Soc., 318, 173

[54] McSwain, M. V., & Gies, D. R. 2005, Astrophys. J. Suppl., 161, 118

[55] Mennickent, R. E., Pietrzyński, G., Gieren, W., & Szewczyk, O. 2002, Astr. Astrophys., 393, 887

[56] Meyssonnier, N., & Azzopardi, M. 1993, Astr. Astrophys. Suppl., 102, 451

[57] Monet, D. G., et al. 2003, Astron. Journ., 125, 984

[58] Murphy, M. T., & Bessell, M. S. 2000, Mon. Not. R. Astr. Soc., 311, 741

[59] Oey, M. S., King, N. L., & Parker, J. W. 2004, Astron. Journ., 127, 1632

[60] Paczynski, B. 2001, Acta Astronomica, 51, 81

[61] Park, T., Kashyap, V. L., Siemiginowska, A., van Dyk, D. A., Zezas, A., Heinke, C., & Wargelin, B. J. 2006, Astrophys. J., 652, 610

[62] Raguzova, N. V., & Popov, S. B. 2005, Astronomical and Astrophysical Transactions, 24, 151

[63] Ratnatunga, K. U., & Bahcall, J. N. 1985, Astrophys. J. Suppl., 59, 63

[64] Reed, B. C. 2001, Pub. Astr. Soc. Pacific., 113, 537

[65] Russell, S. C., & Dopita, M. A. 1992, Astrophys. J., 384, 508

[66] Sasaki, M., Haberl, F., & Pietsch, W. 2000, Astr. Astrophys. Suppl., 147, 75

[67] Sasaki, M., Pietsch, W., & Haberl, F. 2003, Astr. Astrophys., 403, 901

[68] Schlegel, D. J., Finkbeiner, D. P., & Davis, M. 1998, Astrophys. J., 500, 525

[69] Schmidtke, P. C., & Cowley, A. P. 2005, Astron. Journ., 130, 2220

[70] Schmidtke, P. C., & Cowley, A. P. 2006, Astron. Journ., 132, 919

[71] Shtykovskiy, P., & Gilfanov, M. 2005, Mon. Not. R. Astr. Soc., 362, 879

[72] Silverman, J. D., et al. 2005, Astrophys. J., 618, 123

[73] Skrutskie, M. F., et al. 2006, Astron. Journ., 131, 1163

[74] Soszynski, I., et al. 2002, Acta Astronomica, 52, 143

[75] Stevens, J. B., Coe, M. J., & Buckley, D. A. H. 1999, Mon. Not. R. Astr. Soc., 309, 421

[76] Tucholke, H.-J., de Boer, K. S., & Seitter, W. C. 1996, Astr. Astrophys. Suppl., 119, 91

[77] Udalski, A., Soszynski, I., Szymanski, M., Kubiak, M., Pietrzynski, G., Wozniak, P., & Zebrun, K. 1999, Acta Astronomica, 49, 437

[78] Udalski, A., Soszynski, I., Szymanski, M., Kubiak, M., Pietrzynski, G., Wozniak, P., & Zebrun, K. 1998b, Acta Astronomica, 48, 563

[79] Udalski, A., Szymanski, M., Kubiak, M., Pietrzynski, G., Wozniak, P., & Zebrun, K. 1998a, Acta Astronomica, 48, 147

[80] van den Bergh, S. 2000, The galaxies of the Local Group, by Sidney Van den Bergh. Published by Cambridge, UK: Cambridge University Press, 2000 Cambridge Astrophysics Series Series, vol no: 35

[81] van den Heuvel, E. P. J., Portegies Zwart, S. F., Bhattacharya, D., & Kaper, L. 2000, Astr. Astrophys., 364, 563

[82] van Paradijs, J., & McClintock, J. E. 1995, X-ray Binaries, eds. W.H.G. Lewin, J. van Paradijs, and E.P.J. van den Heuvel (Cambridge: Cambridge Univ. Press), p. 58, 58

[83] Webster, B. L., Martin, W. L., Feast, M. W., & Andrews, P. J. 1972, Nature, 240, 183

[84] White, N. E., Nagase, F., & Parmar, A. N. 1995, X-ray Binaries, eds. W.H.G. Lewin, J. van Paradijs, and E.P.J. van den Heuvel (Cambridge: Cambridge Univ. Press), p. 1, 1

[85] Wisniewski, J. P., & Bjorkman, K. S. 2006, Astrophys. J., 652, 458

[86] Wyrzykowski, L., et al. 2004, Acta Astronomica, 54, 1

[87] Yokogawa, J., Imanishi, K., Tsujimoto, M., Koyama, K., & Nishiuchi, M. 2003, Pub. Astr. Soc. Japan., 55, 161

[88] Zacharias, N., Urban, S. E., Zacharias, M. I., Wycoff, G. L., Hall, D. M., Monet, D. G., & Rafferty, T. J. 2004, Astron. Journ., 127, 3043

[89] Zaritsky, D., Harris, J., Thompson, I. B., & Grebel, E. K. 2004, Astron. Journ., 128, 1606

[90] Zaritsky, D., Harris, J., Thompson, I. B., Grebel, E. K., & Massey, P. 2002, Astron. Journ., 123, 855

[91] Zebrun, K., et al. 2001, Acta Astronomica, 51, 317

[92] Zezas, A., Fabbiano, G., Rots, A. H., & Murray, S. S. 2002, Astrophys. J., 577, 710

[93] Zezas, A., McDowell, J. C., Hadzidimitriou, D., Kalogera, V., Fabbiano, G., & Taylor, P. 2003, The Local Group as an Astrophysical Laboratory, 111

Chapter 4

An *XMM-Newton* survey of the Small Magellanic Cloud

4.1 Observations and data analysis

Our *XMM-Newton* survey of the SMC is an extension of the *Chandra* survey to regions of different stellar content (Figure 4.1). It consists of 5 fields selected to sample stellar populations in a range of ages ($\sim 10 - 500$ Myr; Fig 4.2) based on the SF history of Harris & Zaritsky (2004). The observations were performed with the 3 EPIC (MOS1, MOS2 and PN; Turner et al. 2001, Strüder et al. 2001) detectors in the full frame mode which gives the maximum field-of-view ($\sim 30'$) and timing resolution of 73ms for PN and 2.6s for MOS detectors. In oder to minimize contamination by optical light while maximizing the sensitivity we used the Medium optical blocking Filter, except for field XMM_6, which was observed with the Thin Filter. One of the observations (XMM_5) was affected by high background flares and it is not included in the current study. Moreover, in field XMM_1 there are single reflections due to bright source outside the field-of-view. The log of the observations is presented in Table 4.1.

The data were analyzed with the SAS package v7.0.0, and the latest "Current Calibration Files" (CCFs) release as of August 2007. After processing the raw data with the *epchain* and *emchain* tasks to create the event lists, we filtered any bad columns/pixels and high background flares

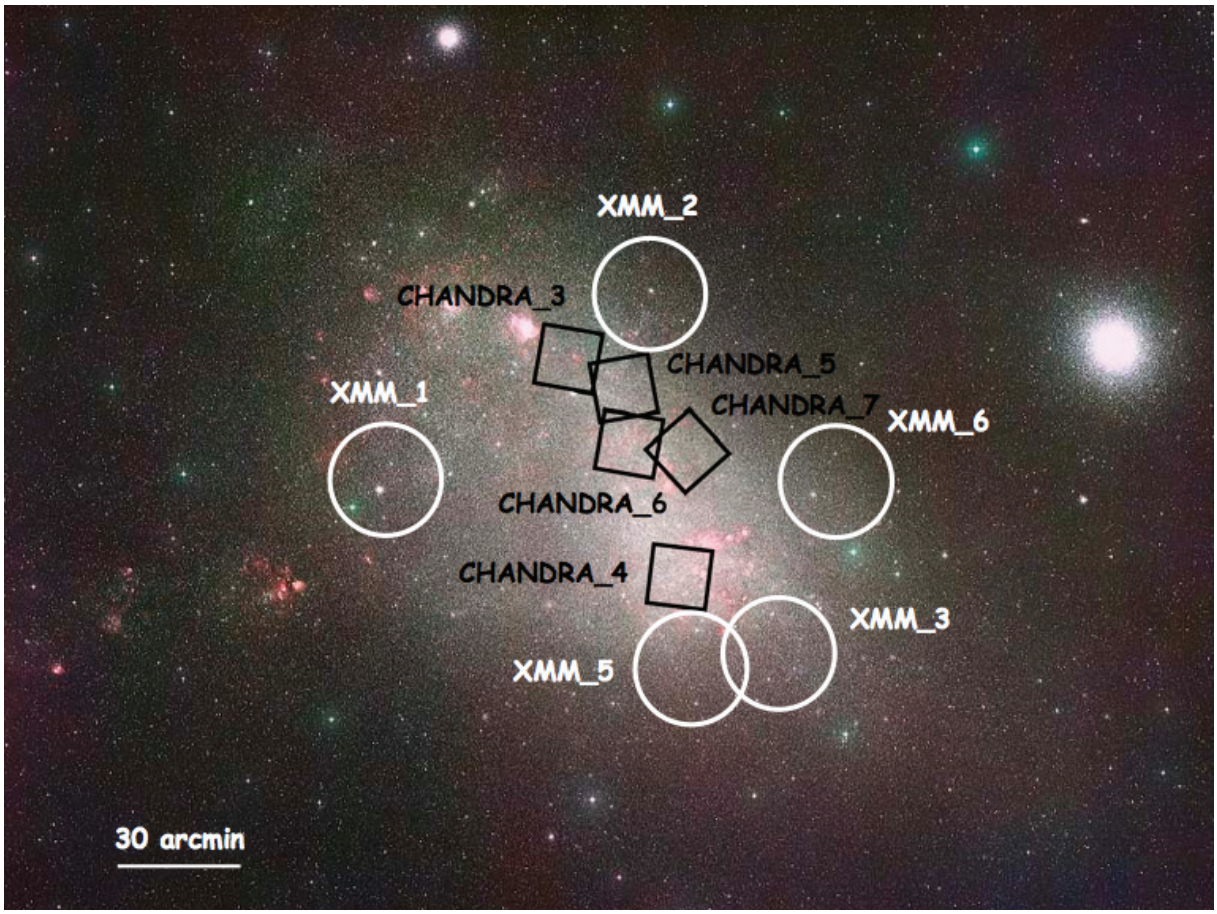

Figure 4.1 The observed fields of the *Chandra* and *XMM-Newton* surveys, which sample different stellar populations, are overlaid on an optical image (© Photo by D. Malin, Anglo-Australian Observatory/Royal Observatory, Edinburgh). The squares are $16' \times 16'$, while the circles have a diameter of $\sim 30'$.

(excluding times when the total count rate deviated more than 3σ from the mean). In addition, we only kept events corresponding to patterns 0-4 for the PN and 0-12 for the MOS detectors. Source detection was performed simultaneously on 5 energy bands (0.2-0.5 keV, 0.5-1.0 keV, 1.0-2.0 keV, 2.0-4.5 keV, and 4.5-12.0 keV), and the 3 EPIC detectors with the maximum likelihood method available in the *edetect_chain* task. *edetect_chain* provides net source counts corrected for aperture effects taking into account the Point Spread Function (PSF) at the position of the source. The background is estimated from a 7×7 pixels box around each source and it is corrected for any contamination by the source emission. The likelihood threshold was set to 10, and the final source-list was visually inspected for spurious sources especially near the edges of the CCDs, and in field XMM_1 due to the reflections mentioned above. We detected 186 sources

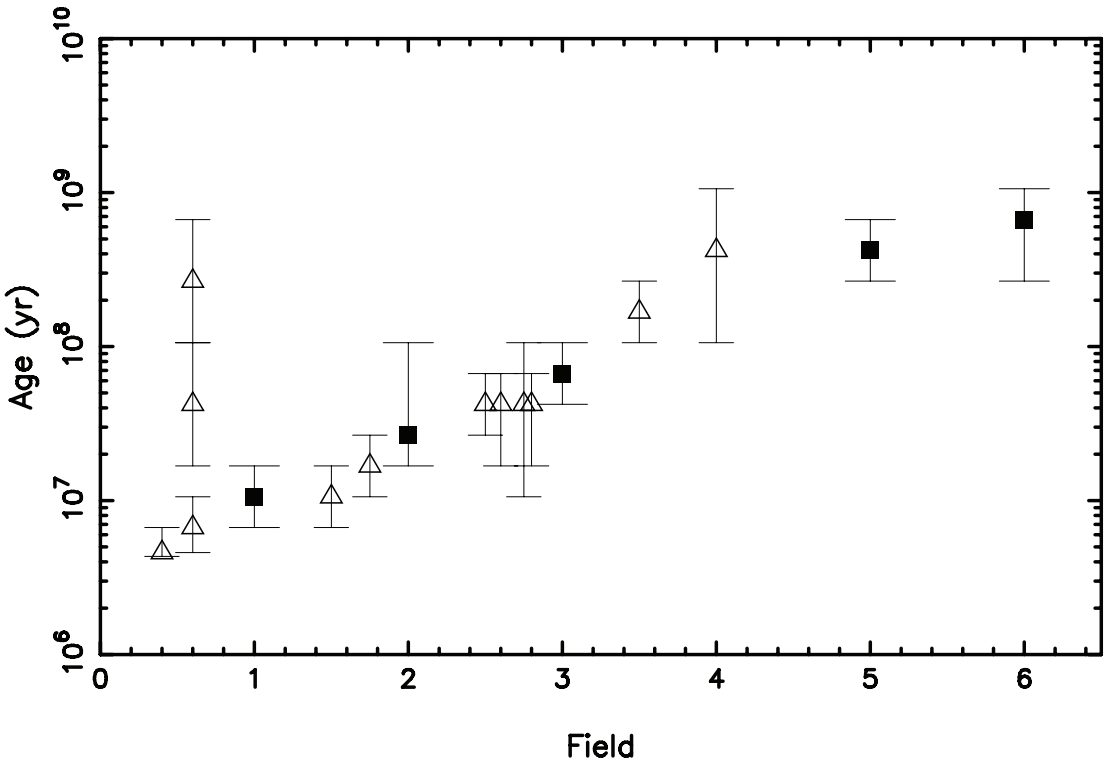

Figure 4.2 The age of various SMC fields observed with *Chandra* and *XMM-Newton*. Open triangles indicate archival observations, while filled squares show the fields used in the *XMM-Newton* study, which sample stellar populations in a wide range of ages.

down to a limiting luminosity of $\sim 3.5 \times 10^{33}$ erg s^{-1} in the 0.2-12 keV band.[1] In Figure 4.3 we present a full band (0.2-12.0keV) exposure-corrected mosaic image of the 3 EPIC instruments (PN, MOS1, MOS2) for *XMM-Newton* field 2.

An initial measurement of the spectral properties of the sources was based on hardness ratios between the soft (0.5-1.0 keV), medium (1.0-2.0 keV), and hard (2.0-4.5 keV) bands. Because of its higher sensitivity we use photometric analysis from the PN detector. Based on the net counts in each energy band for each source we derived hardness ratios for each X-ray source, while for their classification we used the HR2=(M-S)/(M+S) versus HR3=(H-M)/(H+M) plot, where S, M, and H correspond to the soft (0.5-1.0 keV), medium (1.0-2.0 keV), and hard (2.0-4.5 keV) band, respectively. On the same plot (Figure 4.4) we present a grid for a power-law model of different absorbing H_I column densities (diagonal lines with N_H given in units of 10^{22}cm^{-2}) and photon indices (Γ; horizontal lines). The grid is calculated based on the effective area on the

[1]Assuming a power-law spectrum of $\Gamma = 1.7$, and N_H from Column (9) of Table 4.1.

Table 4.1. Log of *XMM-Newton* observations

Field ID	Obs. ID	R.A.	Decl.	Date	Duration	Net Exp. Time[†]	Revolution	N_H[§]
		(J2000.0)		(UT)	(s)	(s)		(10^{20} cm^{-2})
[1]	[2]	[3]	[4]	[5]	[6]	[7]	[8]	[9]
XMM_1	0301170101	01 07 52.00	-72 53 41.6	2006-03-22	23410	19585	1151	4.81
XMM_2	0301170201	00 51 56.63	-72 02 53.2	2006-03-22	23809	21937	1151	6.63
XMM_3	0301170301	00 42 25.45	-73 36 29.4	2006-04-06	21856	19936	1158	4.51
XMM_5	0301170501	12.053886	-73.669342	2006-03-19	21313	... [‡]	1149	4.40
XMM_6	0301170601	00 40 05.19	-72 47 57.4	2006-03-27	25149	23167	1153	5.99

Note. — Units of right ascension are hours, minutes, and seconds, and units of declination are degrees, arcminutes, and arcseconds.

[†]Total exposure with all 3 EPIC instruments (MOS1, MOS2, PN).

[‡]This field was affected by high background flares and it is not included in the current study.

[§]Based on the H_I maps of Stanimirovic et al. (1999).

aimpoint of each field. Points outside the grid have large errors and/or complex multi-component spectra. In particular, in the left of the grid could have an additional thermal component. From this figure we see several sources with hard spectra ($\Gamma < 1.6$), indicative of pulsar binaries (e.g. Yokogawa et al. 2003).

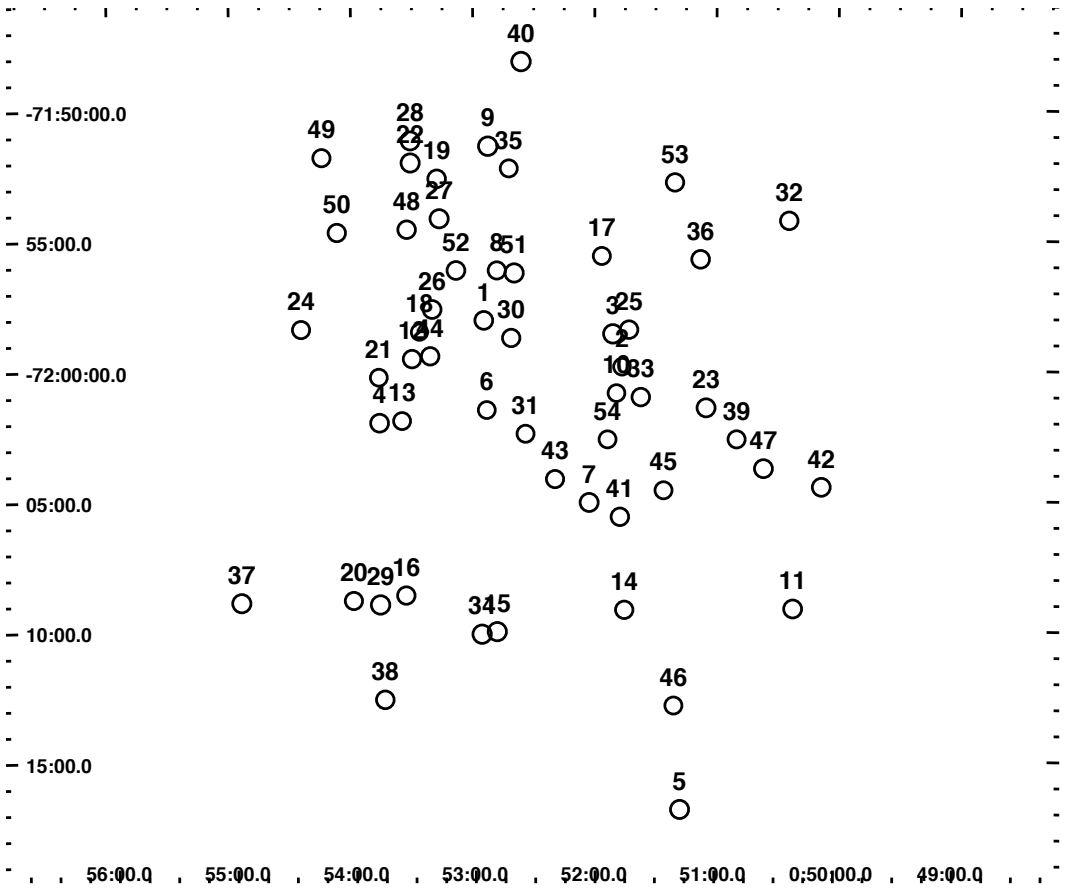

Figure 4.3 A full band (0.2-12.0keV) exposure-corrected mosaic image of the 3 EPIC cameras (PN, MOS1, MOS2) for *XMM-Newton* field 2. The detected sources are shown with circles of 5″ radius.

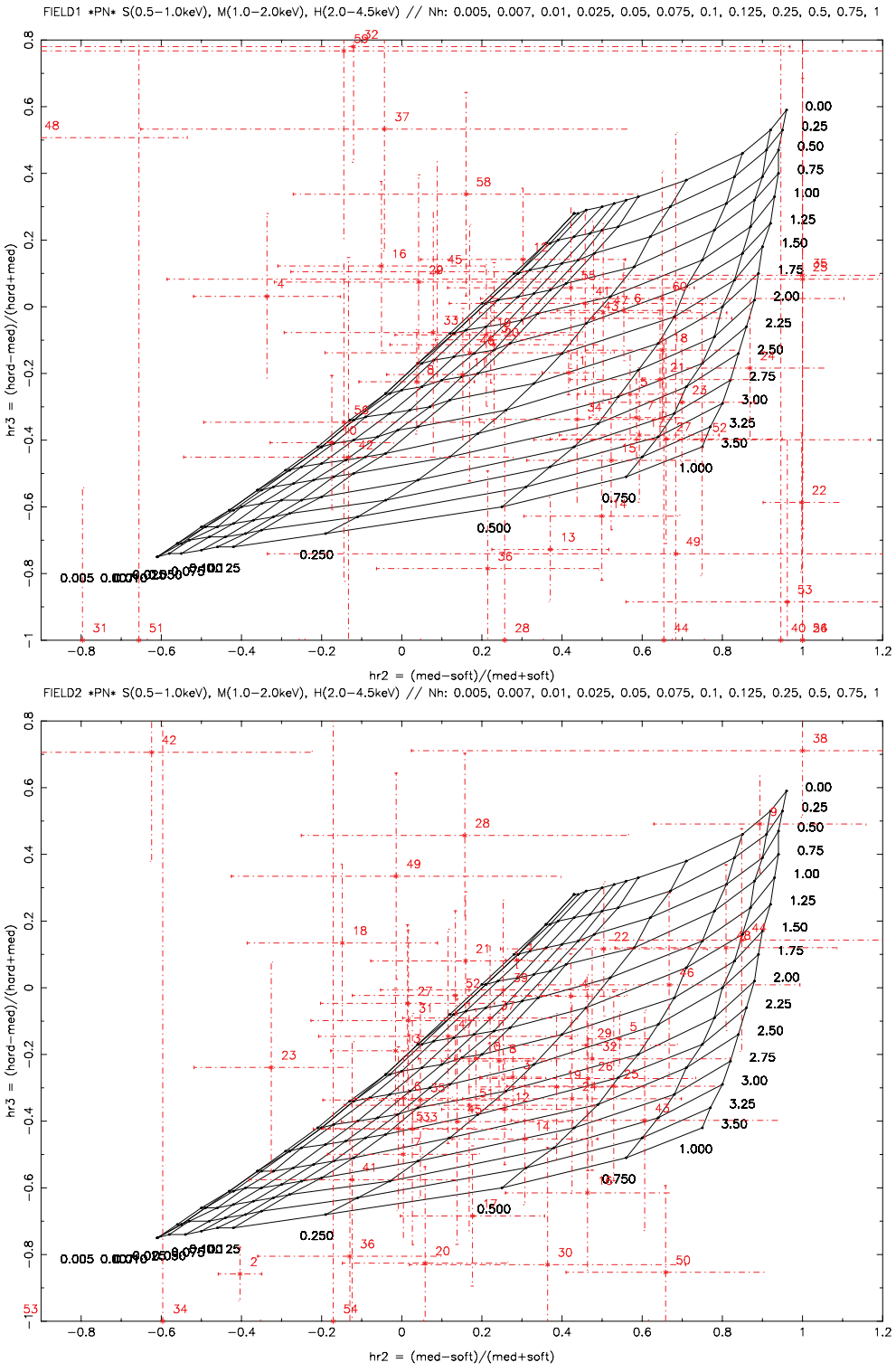

Figure 4.4 Hardness ratios plots used in this study. In order of appearance (from top to bottom) for *XMM-Newton* fields 1, 2, 3, and 6, respectively). Overlaid is a grid for different values of Γ (horizontal lines) and N_H (diagonal lines with N_H given in units of $10^{22}cm^{-2}$) derived by estimating the expected number of counts in each band for an absorbed power-law model, and assuming the effective area on the detector's aimpoint.

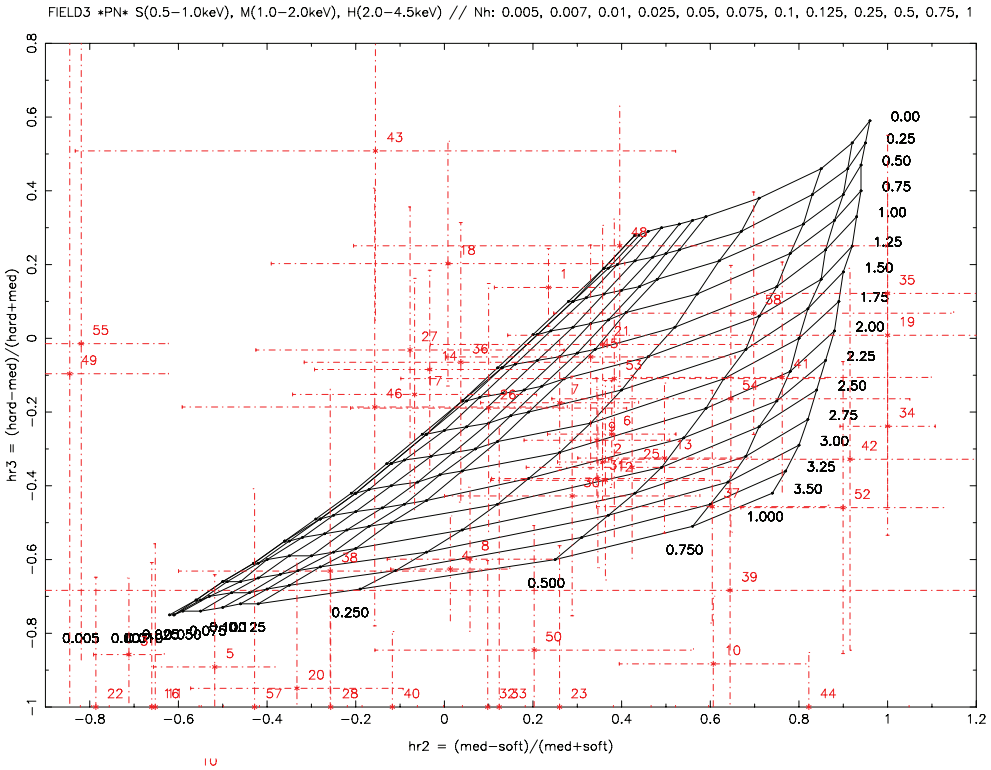
FIELD3 *PN* S(0.5−1.0keV), M(1.0−2.0keV), H(2.0−4.5keV) // Nh: 0.005, 0.007, 0.01, 0.025, 0.05, 0.075, 0.1, 0.125, 0.25, 0.5, 0.75, 1
hr3 = (hard−med)/(hard+med)
hr2 = (med−soft)/(med+soft)
0.00
0.25
0.50
0.75
1.00
1.25
1.50
1.75
2.00
2.25
2.50
2.75
3.00
3.25
3.50
1.000
0.750
0.500
0.250
0.005

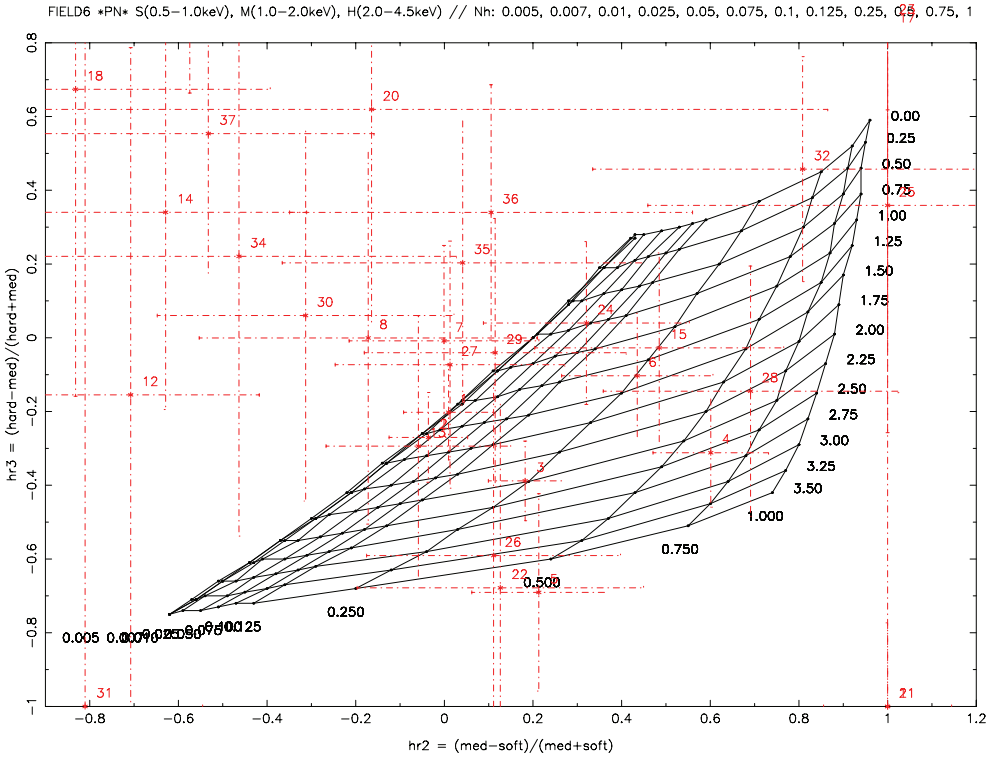
FIELD6 *PN* S(0.5−1.0keV), M(1.0−2.0keV), H(2.0−4.5keV) // Nh: 0.005, 0.007, 0.01, 0.025, 0.05, 0.075, 0.1, 0.125, 0.25, 0.5, 0.75, 1
hr3 = (hard−med)/(hard+med)
hr2 = (med−soft)/(med+soft)
0.00
0.25
0.50
0.75
1.00
1.25
1.50
1.75
2.00
2.25
2.50
2.75
3.00
3.25
3.50
1.000
0.750
0.500
0.250
0.005

4.2 Candidate Be-XRBs from the *XMM-Newton* survey

In order to identify HMXBs (or candidate Be-XRBs) we need to find their optical counterparts. Following the analysis of Antoniou et al. (2008a) and the criteria used for the classification of *Chandra* sources (see §3.8.1), we searched for optical counterparts in a $5''$ search radius around the *XMM-Newton* sources. This search radius reflects the absolute and relative astrometric uncertainty of *XMM-Newton* (Cappelluti et al. 2007). For the cross-correlation we use the MCPS catalog because the overlap of our fields with the OGLE-II catalog (Udalski et al. 1998; which has better astrometric and photometric accuracy) is less than 40%. Because of the uniform stellar density of bright stars (of O or B spectral type) in the *XMM-Newton* fields (in contrast to the *Chandra* fields that lie along the SMC "bar") there is no need to perform Monte-Carlo simulations in order to estimate the chance coincidence probability. Based on the MCPS catalog (Zaritsky et al. 2002) for OB stars (selected as in Antoniou et al. 2008a), we expect only ~ 0.3 spurious matches within a search radius of $5''$. This low chance coincidence probability indicates that the most likely counterpart is the brightest source within the search radius.

The identification of a hard X-ray source with an early-type star strongly suggests that it is a HMXB. This helps to exclude any chance associations with early-type stars from the cross-correlation with the MCPS catalog. From the hardness ratios analysis we find that 8 *XMM-Newton* sources satisfy the criterion of a hard X-ray spectrum. The X-ray properties of these sources are presented in Table 4.2 (the data given here refer to the photometric analysis of the EPIC PN data). In Column (1) we give the *XMM-Newton* source ID as F_NN, where F is the field number, and NN is the source ID in this field (from Antoniou et al. 2008b). In Column (2) we present the *XMM-Newton* source name, and in Columns (3) and (4) the right ascension and declination (J2000.0), respectively. The net counts of each X-ray source in the 0.2-12.0 keV energy band, the significance of the detection and the off-axis angle are listed in Columns (5) to (7), respectively. In Column (8) we give the X-ray luminosity in the 0.2-12.0 keV band, corrected for absorption assuming a power law of $\Gamma = 1.7$, N_H from Column (9) of Table 4.1, and a distance to the SMC equal to 60 kpc (e.g. Hilditch, Howarth & Harries 2005). In Columns (9) and (10) we list the hardness ratios HR_2 and HR_3 (output of task *edetect_chain*) defined as $HR_2 = (M - S)/(M + S)$ and $HR_3 = (H - M)/(H + M)$, where S, M and H correspond to the soft(0.5-1.0 keV), medium (1.0-2.0 keV), and hard (2.0-4.5 keV) band, respectively.

Table 4.2. X-ray properties of *XMM-Newton* sources with hard X-ray spectra

Src ID	Source Name XMMU J...	R.A. (J2000.0)	Decl. (J2000.0)	Net Counts	Sign. σ	Off-axis Angle	Lx^{un}	HR2	HR3
[1]	[2]	[3]	[4]	[5]	[6]	[7]	[8]	[9]	[10]
1_18	010835.5-724308	01 08 35.54	-72 43 08.4	63.87 ± 11.11	6.0	8.9	7.30	0.65 ± 0.19	-0.13 ± 0.19
1_19	010519.9-724943	01 05 19.90	-72 49 43.1	61.12 ± 10.49	5.8	11.7	6.99	0.21 ± 0.23	-0.08 ± 0.21
1_30	010620.0-724049	01 06 20.01	-72 40 49.1	$33.98 \pm 8.28^{\dagger}$	4.6	14.0	12.12	$0.29 \pm 0.37^{\dagger}$	$0.10 \pm 0.32^{\dagger}$
2_1	005255.1-715809	00 52 55.10	-71 58 08.7	4091.64 ± 77.47	82.0	4.8	1203.24	0.29 ± 0.03	0.08 ± 0.02
2_10	005149.3-720057	00 51 49.28	-72 00 56.5	124.82 ± 16.09	8.3	1.1	36.71	0.18 ± 0.14	-0.21 ± 0.15
3_1	004208.0-734502	00 42 08.01	-73 45 01.9	214.72 ± 18.26	17.5	10.7	87.23	0.24 ± 0.12	0.14 ± 0.11
3_17	004357.6-732840	00 43 57.57	-73 28 39.7	39.05 ± 8.92	4.2	8.1	5.11	-0.07 ± 0.28	-0.15 ± 0.31
3_58	004514.7-733601	00 45 14.73	-73 36 00.7	23.25 ± 7.91	2.6	11.0	3.04	0.70 ± 0.45	0.07 ± 0.33

Note. — Units of right ascension are hours, minutes, and seconds, and units of declination are degrees, arcminutes, and arcseconds. The properties of these sources are from the analysis of the EPIC PN data, and the energy band is the 0.2-12.0 keV. The off-axis angle is in units of arcminutes, and L_X is the absorption corrected luminosity in units of 10^{33}erg/s. HR_2 and HR_3 are defined as $HR_2 = (M - S)/(M + S)$ and $HR_3 = (H - M)/(H + M)$, where S, M and H correspond to the soft (0.5-1.0 keV), medium (1.0-2.0 keV), and hard (2.0-4.5 keV) band, respectively.

†These data are from the EPIC MOS2 camera, since this source is located outside the EPIC PN field-of-view, while it is marginally located within the EPIC MOS1 field-of-view.

The brightest (and therefore more likely) counterpart for each source is presented in Table 4.3. In Column (1) we give the *XMM-Newton* source ID (same as in Column (1) of Table 4.2). In Column (2) we give the proposed counterparts with a similar notation: MCPS sources are named as Z_NNNNNNN where NNNNNNN is the line number of the source in Table 1 of Zaritsky et al. (2002). In Columns (3) and (4) we present the right ascension and declination (J2000.0) of the counterparts. The distance (in arcseconds) of the counterpart to the *XMM-Newton* source is given in Column (5). The photometric data of the sources are presented in Columns (6) to (11) (these data are taken directly from the original catalogs without applying any reddening or zero-point correction): apparent magnitude in the V band (Column (6)), the $B - V$ and $U - B$ colors (Columns (8) and (10)), and their errors (Columns (7), (9) and (11), respectively). In Column (12) we indicate with an "n" if this is a new candidate counterpart for the X-ray source,

Table 4.3. Optical properties of candidate Be-XRBs detected with *XMM-Newton*

X-ray		Optical counterpart									Notes
Src	Src ID	R.A. (J2000.0)	Decl.	Offset ($''$)	V	δV	B-V	δ(B − V)	U-B	δ(U − B)	
[1]	[2]	[3]	[4]	[5]	[6]	[7]	[8]	[9]	[10]	[11]	[12]
1_18	Z_4467654	01 08 35.68	-72 43 12.1	3.73	17.86	0.03	-0.04	0.04	-0.46	0.05	n
1_19	Z_4119599	01 05 20.72	-72 49 41.5	4.01	16.98	0.03	-0.09	0.04	-0.92	0.30	n
1_30	Z_4232476	01 06 21.02	-72 40 48.8	4.53	16.38	0.03	0.02	0.03	-0.55	0.04	n
2_1	Z_2430066	00 52 55.27	-71 58 06.0	2.82	15.53	0.02	-0.05	0.04	-1.11	0.06	[MA93]623
2_10	Z_2274521	00 51 49.44	-72 00 53.1	3.46	18.38	0.03	-0.01	0.05	-0.34	0.06	n
3_1	Z_1132154	00 42 07.93	-73 45 02.2	0.40	16.78	0.04	-0.10	0.08	-0.49	0.08	n
3_17	Z_1324298	00 43 57.46	-73 28 39.7	0.54	18.18	0.04	0.12	0.05	-0.36	0.07	n
3_58	Z_1466431	00 45 14.58	-73 35 57.8	2.62	15.19	0.10	-0.23	0.11	-0.85	0.05	n

Note. — Units of right ascension are hours, minutes, and seconds, and units of declination are degrees, arcminutes, and arcseconds.

and if this is a Meyssonier & Azzopardi (1993; hereafter [MA93]) source along with its ID from the original catalog.

In Figure 4.5 we present the extinction corrected M_{V_o} vs. $(B-V)_o$ CMD diagram (absolute V magnitude vs. $B-V$ color) for all matches of our *XMM-Newton* sources (186 in total). Sources from the same *XMM-Newton* field are plotted with the same color. On the same diagram we overlay with small dots the stars from the MCPS catalog in the area covered by the *XMM-Newton* field 2. The source magnitudes and colors are corrected for reddening assuming $E(B-V)=0.09$ and A_V=0.29 (similar to the study of *Chandra* sources presented in Antoniou et al. 2008a), while we adopted a distance modulus of $(m-M)_V = 18.89 \pm 0.11$ mag (Harries, Hilditch & Howarth 2003). For the classification of the *XMM-Newton* sources we used the combined locus (blue curve) of early type stars (O, B) identified in the 2dF spectroscopic survey of Evans et al. (2004) and of the candidate Be stars of Mennickent et al. (2002). In Figure 4.6 we show that region in greater detail. From this figure, we see that all our 8 xmm sources have early-type (OB) counterparts, thus making them candidate Be-XRBs.

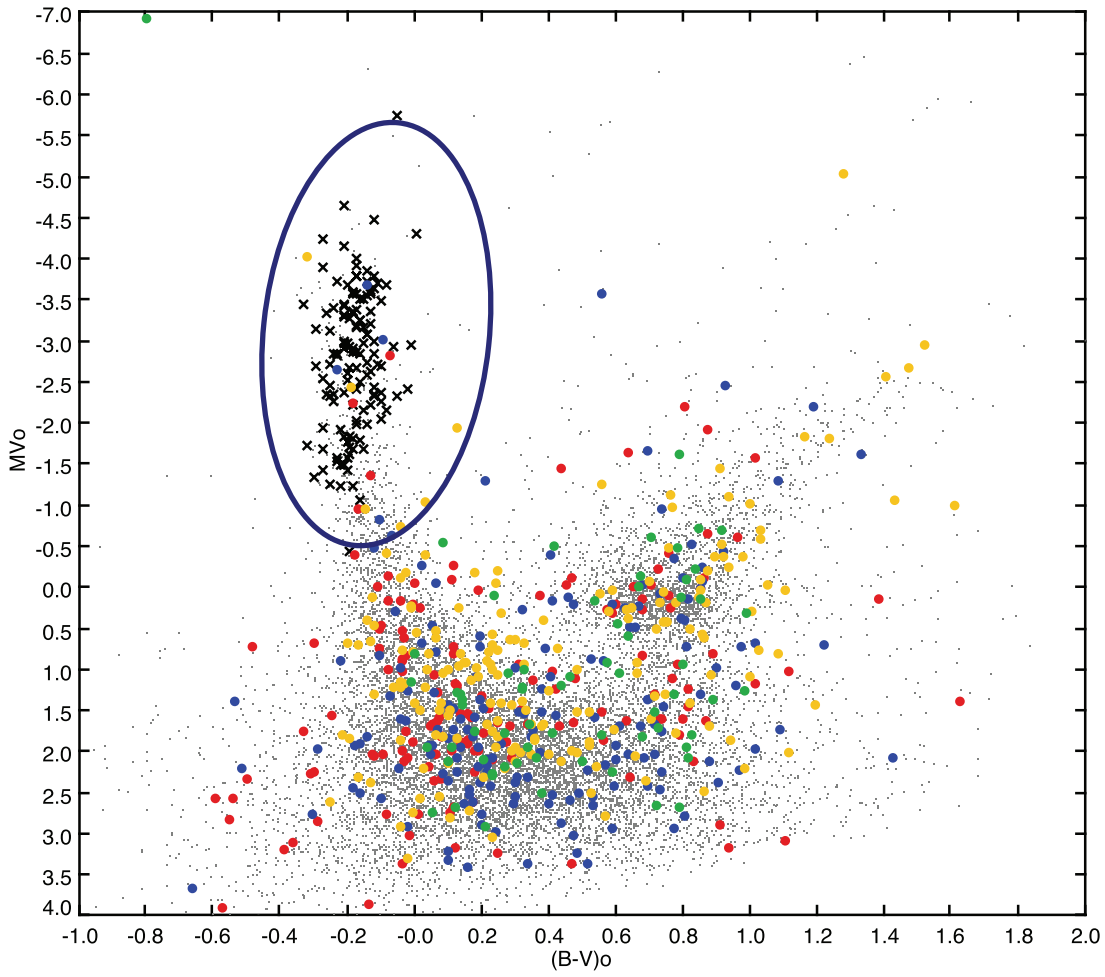

Figure 4.5 CMD of all multiple matches of our *XMM-Newton* sources.

We present the M_{V_o} vs. $(B-V)_o$ CMD of all multiple matches (filled circle) of our *XMM-Newton* sources from the MCPS catalog of (Zaritsky et al. 2002). The optical sources are color coded as, *XMM-Newton* field 1: red; 2: blue; 3: yellow; 4: green. For reference MCPS stars that lie in our *XMM-Newton* field 2 are plotted in grey small dots (for clarity not all stars are shown here). The MS, the red-giant branch and the red-clump loci are clearly seen. Overlaid in cyan are the Be stars in the NGC330 star-cluster (Martayan et al. 2007). The blue curve indicates the combined locus of early-type stars (O, B) identified in the 2dF spectroscopic survey of Evans et al. (2004) and the candidate Be stars of Mennickent et al. (2002).

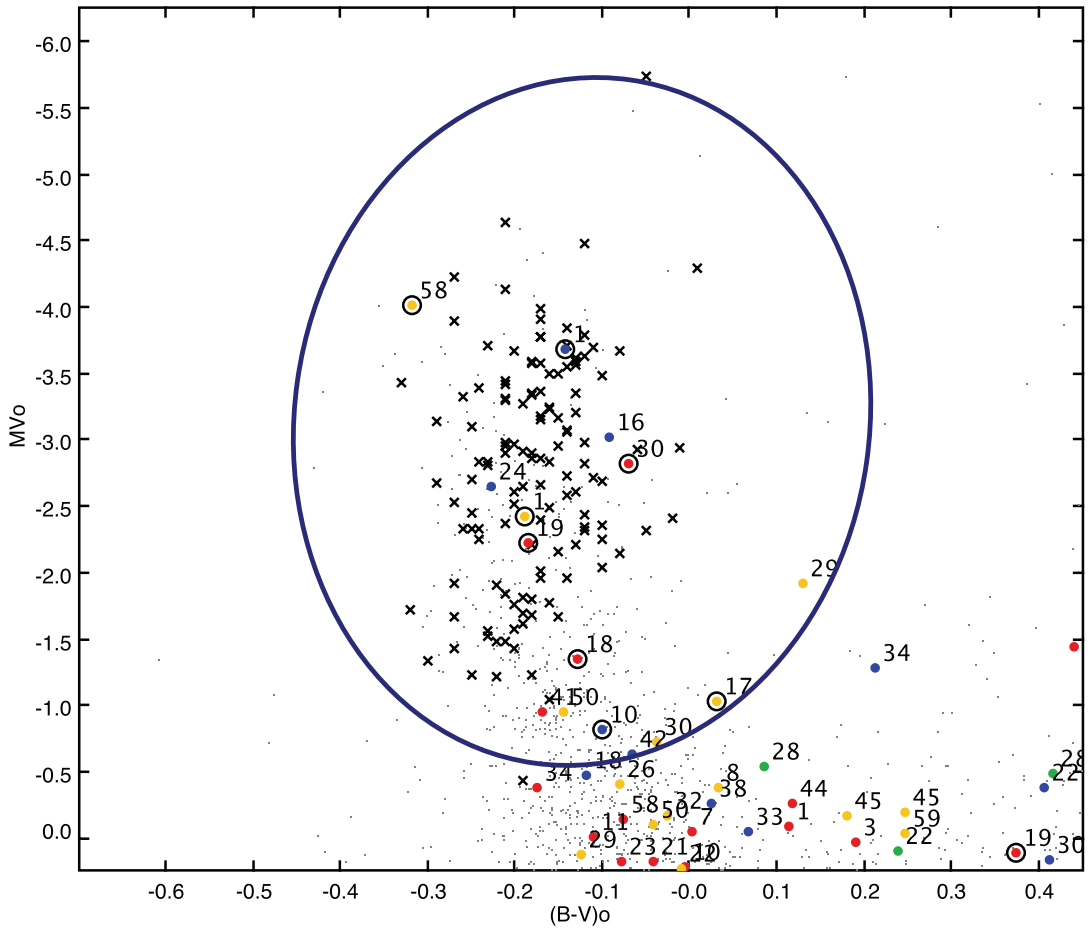

Figure 4.6 Part of the previous CMD (Figure 4.5) showing all optical matches of our *XMM-Newton* sources in greater detail.

The Be-XRBs detected in our *XMM-Newton* survey presented in Table 4.3 are indicated with a black circle.

4.3 Be-XRBs in the *Chandra* and *XMM-Newton* surveys of the SMC

From the above analysis we find 8 Be-XRBs in our *XMM-Newton* fields. From those, 7 are new candidates, while only one has been previously identified as a Be-XRB (src ID 2_1 in the previous tables). In *XMM-Newton* field2 we did not detect the X-ray source RX J0051.3-7216 (listed in the census of Liu et al. 2005). RX J0051.3-7216 is a transient pulsar with a pulse period of 91.1s (Corbet et al. 1997), while it has been identified as a Be/XRB with 15.06 V band magnitude and strong Hα emission (from optical spectroscopy; Stevens, Coe & Buckley 1999, Coe et al. 2005). In total, there are 9 candidate and confirmed Be-XRBs in the *XMM-Newton* fields, 8 detected in this survey and one more from previous detection.

On the other hand, in the *Chandra* fields there are 29 Be-XRBs in total. Of those, 9 are new candidate Be-XRBs from the study of Antoniou et al. (2008a), while 2 sources (XTE J0052-723 and RX J0054.5-7228) have not been detected in our survey. XTE J0052-723 is a transient pulsar with a pulse period of 4.78s (Corbet, Marshall & Markwardt 2001). Laycock et al. (2003) confirmed the pulsations and found the emission-line object [MA93] 537 as the optical counterpart of this transient Be-XRB pulsar. From optical photometry they find a V band magnitude of 15.8. RX J0054.5-7228 has been detected with an X-ray flux of 0.16μJy in the 0.5-10keV energy band (Haberl & Sasaki 2000), while it is listed as a candidate Be-XRB in the census of Haberl & Pietsch (2004; with suggested optical counterpart the emission-line object [MA93] 772). No X-ray pulsations have been reported for this source.

In addition, there are 19 and 3 X-ray pulsars[2] in the 5 *Chandra* and 4 *XMM-Newton* fields, respectively. These total numbers of Be-XRBs and X-ray pulsars are used in the next chapter in order to examine any correlation of the XRB formation and star-formation history.

Overall we find a small number of HMXBs in the *XMM-Newton* fields when compared to the *Chandra* fields (see Chapters 2 and 3). The implications of this result will be discussed in the next chapter.

[2]From the online census of Malcolm Coe: http://www.astro.soton.ac.uk/~mjc/ as of 06/05/2007

Bibliography

[1] Cappelluti, N., et al. 2007, Astrophys. J. Suppl., 172, 341

[2] Coe, M. J., Edge, W. R. T., Galache, J. L., & McBride, V. A. 2005a, Mon. Not. R. Astr. Soc., 356, 502

[3] Corbet, R., Marshall, F. E., Lochner, J. C., Ozaki, M., Ueda, Y., Whitlock, L. A., & Brandt, N. 1997, IAU Circ., 6788, 2

[4] Corbet, R., Marshall, F. E., & Markwardt, C. B. 2001, IAU Circ., 7562, 1

[5] Crowl, H. H., Sarajedini, A., Piatti, A. E., Geisler, D., Bica, E., Clariá, J. J., & Santos, J. F. C., Jr. 2001, Astron. Journ., 122, 220

[6] Dickey, J. M., & Lockman, F. J. 1990, Ann. Rev. Astron. Astrophys., 28, 215

[7] Evans, C. J., Howarth, I. D., Irwin, M. J., Burnley, A. W., & Harries, T. J. 2004, Mon. Not. R. Astr. Soc., 353, 601

[8] Frank, J., King, A., & Raine, D. J. 2002, Accretion Power in Astrophysics, by Juhan Frank and Andrew King and Derek Raine, pp. 398. ISBN 0521620538. Cambridge, UK: Cambridge University Press, February 2002.

[9] Giacconi, R., Gursky, H., Paolini, F. R., & Rossi, B. B. 1962, Physical Review Letters, 9, 439

[10] Haberl, F., & Pietsch, W. 2004, Astr. Astrophys., 414, 667

[11] Haberl, F., & Sasaki, M. 2000, Astr. Astrophys., 359, 573

[12] Habets, G. M. H. J. 1987, Astr. Astrophys., 184, 209

[13] Harries, T. J., Hilditch, R. W., & Howarth, I. D. 2003, Mon. Not. R. Astr. Soc., 339, 157

[14] Harris, J., & Zaritsky, D. 2004, Astron. Journ., 127, 1531

[15] Hilditch, R. W., Howarth, I. D., & Harries, T. J. 2005, Mon. Not. R. Astr. Soc., 357, 304

[16] Laycock, S., Corbet, R. H. D., Coe, M. J., Marshall, F. E., Markwardt, C., & Edge, W. 2003, Mon. Not. R. Astr. Soc., 339, 435

[17] Liu, Q. Z., van Paradijs, J., & van den Heuvel, E. P. J. 2005, Astr. Astrophys., 442, 1135

[18] Liu, Q. Z., van Paradijs, J., & van den Heuvel, E. P. J. 2006, Astr. Astrophys., 455, 1165

[19] Liu, Q. Z., van Paradijs, J., & van den Heuvel, E. P. J. 2007, Astr. Astrophys., 469, 807

[20] Lorimer, D. R., & Kramer, M. 2004, Handbook of pulsar astronomy, by D.R. Lorimer and M. Kramer. Cambridge observing handbooks for research astronomers, Vol. 4. Cambridge, UK: Cambridge University Press, 2004

[21] Mennickent, R. E., Pietrzyński, G., Gieren, W., & Szewczyk, O. 2002, Astr. Astrophys., 393, 887

[22] Meyssonnier, N., & Azzopardi, M. 1993, Astr. Astrophys. Suppl., 102, 451

[23] Negueruela, I., & Coe, M. J. 2002, Astr. Astrophys., 385, 517

[24] Stanimirovic, S., Staveley-Smith, L., Dickey, J. M., Sault, R. J., & Snowden, S. L. 1999, Mon. Not. R. Astr. Soc., 302, 417

[25] Strüder, L., et al. 2001, Astr. Astrophys., 365, L18

[26] Stevens, J. B., Coe, M. J., & Buckley, D. A. H. 1999, Mon. Not. R. Astr. Soc., 309, 421

[27] Tauris, T. M., & van den Heuvel, E. P. J. 2006, Compact stellar X-ray sources, 623

[28] Turner, M. J. L., et al. 2001, Astr. Astrophys., 365, L27

[29] van den Bergh, S. 2000, The galaxies of the Local Group, by Sidney Van den Bergh. Published by Cambridge, UK: Cambridge University Press, 2000 Cambridge Astrophysics Series Series, vol no: 35

[30] van den Heuvel, E. P. J., & van Paradijs, J. 1997, Astrophys. J., 483, 399

[31] Yokogawa, J., Imanishi, K., Tsujimoto, M., Koyama, K., & Nishiuchi, M. 2003, Pub. Astr. Soc. Japan., 55, 161

[32] Zaritsky, D., Harris, J., Thompson, I. B., Grebel, E. K., & Massey, P. 2002, Astron. Journ., 123, 855

Chapter 5

Small Magellanic Cloud: Star-formation history and X-ray binary populations

Using *Chandra*, *XMM-Newton* and optical photometric catalogs we study the young X-ray binary (XRB) populations of the Small Magellanic Cloud (SMC). We find that the Be/X-ray binaries (Be-XRBs) are observed in regions with star-formation (SF) rate bursts $\sim 30 - 70$ Myr ago, which coincides with the age of maximum Be-star formation. We also find strong evidence for a correlation of the number of Be-XRBs with the strength of the SF at the age of maximum Be-star formation, i.e. ~ 40 Myr ago, while regions with strong but more recent SF (e.g. the Wing) are deficient in Be-XRBs. Regions that host HMXBs, which however have not been proved yet to be Be-XRBs, show a similar SF episode (at ~ 40 Myr ago). We conclude that the majority of the optically unidentified SMC HMXBs have a Be nature. Small kicks imparted on the compact object during the supernova explosion are also implied. This is the first study which demonstrates the importance of the Be-XRBs as a dominant component of young XRB populations.

Subject headings: Magellanic Clouds—stars: early-type—stars: emission-line, Be—stars: formation—pulsars: general—X-rays: binaries

5.1 Introduction

Nearby star-forming galaxies offer a unique environment to study the population of young (< 100 Myr) XRBs. The SMC at ~ 60 kpc (e.g. van den Bergh 2000, Hilditch, Howarth & Harries 2005) is our second nearest star-forming galaxy, allowing us to identify the optical counterparts of the XRB population and therefore directly study their link with SF. Moreover, the SMC has been extensively studied in all wavelengths over the years allowing us to obtain a very good picture of its properties. Its proximity, well mapped extinction (Zaritsky et al. 2002), moderate Galactic foreground absorption ($N_H \simeq 6 \times 10^{20} cm^{-2}$; Dickey & Lockman 1990), small line-of-sight depth of its young, central stellar populations (<10 kpc; e.g. Crowl et al. 2001; Harries, Hilditch & Howarth 2003), and its well-determined recent SF history (Harris & Zaritsky 2004) make the SMC the ideal environment for XRB population studies.

More than one hundred XRBs with early-type donors (High-Mass XRBs; HMXBs) in the SMC have been identified, or proposed, in the last few years (see for example the latest census of Liu et al. 2005; and Antoniou et al. 2008a). Almost all of these sources have as optical counterparts an Oe or Be star of luminosity class III-IV (defining the Be-XRB subclass). There is only one confirmed supergiant system (SG-XRB) located in the Wing of the SMC, while no XRB with late-type donor (Low-Mass XRBs; LMXBs) or black-hole XRBs (BH-XRBs) have been identified so far.

Several studies have compared the number of Be-XRBs in the Magellanic Clouds and the Milky Way (e.g. Haberl & Sasaki 2000, Majid, Lamb & Macomb 2004, Coe et al. 2005a, Haberl & Pietsch 2004), concluding that the SMC hosts an unusually large number of Be-XRBs. This overabudance can be partly explained by the enhanced SF history of the SMC ~ 40 Myr ago (e.g. Majid et al. 2004, Shtykovskiy & Gilfanov 2007, Antoniou et al. 2008a). In addition, Antoniou et al. (2008a) show that even after accounting for the difference in the SF rate of the SMC and the Milky Way there is a residual excess by a factor of ~ 2 and concluded that it could be explained by the different metallicity environment of these galaxies, in agreement with population synthesis models (Dray 2006). Our study also indicated possible spatial variations of the Be-XRB populations within the SMC.

In the present paper we investigate the connection between spatially resolved SF history and

the number and spatial distribution of the XRBs in the SMC, on the basis of the results of our *Chandra* survey of the central, most actively star forming, region of the SMC (Zezas et al. 2008, Antoniou et al. 2008a), and of our *XMM-Newton* survey of the outer parts of the SMC with young and intermediate age populations ($\sim 10 - 500$ Myr; Antoniou et al. 2008b).

5.2 Observations and data analysis

5.2.1 X-ray observations

Using the ACIS-I detector on board *Chandra* we observed 5 fields in the central part of the SMC (the so called SMC "bar"), with typical exposure times of 8-12 ks. These observations yielded a total of 158 sources, down to a limiting luminosity of $\sim 4 \times 10^{33}$ erg s^{-1}(in the 0.7-10 keV band), reaching the luminosity range of quiescent HMXBs (typically $L_X \sim 10^{32} - 10^{34}$ erg s^{-1} ; van Paradijs & McClintock 1995). The analysis of the data, the source-list and their X-ray luminosity functions are presented in Zezas et al. (2008), while their optical counterparts and resulting classification are presented in Antoniou et al. (2008a).

Our *XMM-Newton* survey consists of 5 observations in the outer parts of the SMC, performed with the 3 EPIC (MOS1, MOS2 and PN) detectors in the full frame mode. The observed fields were selected to sample stellar populations in a range of ages ($\sim 10 - 500$ Myr; based on the SF history of Harris & Zaritsky (2004)). One of these fields was affected by high background flares and it is not included in the current study. The data were analyzed with the SAS package v7.0.0. After processing the raw data with the *epchain* and *emchain* tasks, we filtered any bad columns/pixels and high background flares (excluding times when the total count rate deviated more than 3σ from the mean); in addition, we only kept events corresponding to patterns 0-4 for the PN and 0-12 for the MOS detectors. Source detection was performed simultaneously on 5 energy bands (0.2-0.5 keV, 0.5-1.0 keV, 1.0-2.0 keV, 2.0-4.5 keV, and 4.5-12.0 keV), and the 3 EPIC detectors with the maximum likelihood method available in the *edetect_chain* task. The likelihood threshold was set to 10, and the final source-list was visually inspected for spurious sources especially near the edges of the CCDs. We detected 186 sources down to a limiting luminosity of $\sim 3.5 \times 10^{33}$ erg s^{-1} in the 0.2-12 keV band[1]. An initial measurement of the

spectral properties of the sources was based on hardness ratios between the soft (0.5-1.0 keV), medium (1.0-2.0 keV), and hard (2.0-4.5 keV) bands. These results along with more details on the analysis and the final source-list (including the X-ray luminosity functions) will be presented in Antoniou et al. (2008b).

5.2.2 Identification of candidate optical counterparts

In order to identify optical counterparts for the sources detected in the *XMM-Newton* observations, we cross-correlated their coordinates with the MCPS (Zaritsky et al. 2002) catalog, which fully overlaps with the observed fields. We searched for optical counterparts in a radius of $5''$ around each X-ray source (Cappelluti et al. 2007). This search radius results in $< 5\%$ spurious optical matches (based on the low and relatively uniform stellar density of these fields).

Following the analysis of Antoniou et al. (2008a) we propose new HMXBs, for several of which we can identify Be donors (Be-XRBs) based on the position of the counterparts on the $(V, B-V)$ color-magnitude diagram (CMD). In addition, from hardness ratio analysis we identify sources with hard spectra (equivalent to $\Gamma < 1.7$), strongly suggesting that they are XRB pulsars (e.g. White, Nagase & Parmar 1995). We find that 15 *XMM-Newton* sources have early-type (O, B) counterparts, while only 8 of those have hard hardness-ratios (Antoniou et al. 2008b).

5.3 Star-formation history and XRB populations

It is known that the SMC "bar" hosts stellar populations with ages < 100 Myr (e.g. Maragoudaki et al. 2001, Harris & Zaritsky 2004), and it also hosts the vast majority of the SMC X-ray pulsars (Galache et al. 2008). By reconstructing the SF history of the SMC, Shtykovskiy & Gilfanov (2007) found that the age distribution of the HMXBs peaks at $\sim 20-50$Myr after the SF event, while McSwain and Gies (2005) observed a strong evolution in the fraction of Galactic Be stars with age up to 100 Myr, with a maximum at $7.4 < \log(\text{age}) < 7.8$. These results motivated us to investigate the connection of the SF history of our *Chandra* and *XMM-Newton* fields with

[1]Assuming a power-law spectrum of $\Gamma = 1.7$, and N_H equal to 4.81, 6.63, 4.51 and 5.99 in units of 10^{20} cm^{-2} for fields 1, 2, 3, and 6, respectively.

their population of Be-XRBs.

5.3.1 SF history of observed fields

Using data from Harris & Zaritsky (2004) we derive the recent SF history in our *Chandra* and *XMM-Newton* fields, by calculating the average SF history of the MCPS regions ($\sim 12' \times 12'$) encompassed by them. We find that:
*(*i) For 3 out of the 5 *Chandra* fields, the most recent major burst peaked $\sim$ 42 Myr ago, while for the other 2 fields this occurred $\sim$ 67 and $\sim$ 27 Myr ago. These bursts have a duration (defined here as the time elapsed from the beginning to the end of the burst) of $\sim$ 90 Myr. In addition, there were older SF episodes ($\sim$ 0.4 Gyr ago) with lower intensity but longer duration, as well as a more recent episode ($\sim$ 7 Myr) observed only in one of the *Chandra* fields.
*(*ii) For one of the *XMM-Newton* fields, the most recent prominent burst occurred *at* $\sim$ 11 Myr ago with a duration of $\sim$ 20 Myr. For two of the remaining fields this burst peaked $\sim$ 67 Myr ago, and it had a duration of $\sim$ 65 Myr. The forth *XMM-Newton* field does not have any major burst, while all of these fields show additional older SF episodes ($\sim$ 0.4 Gyr ago).

5.3.2 Observed fields with known Be-XRBs and pulsars

In order to investigate the link between SF and the XRB populations, we calculate the average SF history only for the MCPS regions that host one or more Be-XRBs (candidate and confirmed) detected in our *Chandra* survey (27 in total; Antoniou et al. 2008a), and our *XMM-Newton* survey (8 in total; Antoniou et al. 2008b). The SF history at each region is weighted by the encompassed number of Be-XRBs, and the error bars were derived based on the 1σ errors given in Harris & Zaritsky (2004). We repeat this exercise for the MCPS regions that do not have any known Be-XRB in our surveys. The two SF histories are presented in Fig.5.1 (upper panel). The SF history of the Be-XRBs (shown in black) is strongly peaked at $\sim$ 42 Myr with a rate of $\sim 54.5^{+4.2}_{-4.0}[10^{-6}\mathrm{M}_{\odot}/\mathrm{yr}/\mathrm{arcmin}^2]$, and it has a duration of $\sim$ 40 Myr. On the other hand, fields without any Be-XRB (shown in gray) have minimal SF rate at $\sim$ 42 Myr, thus underscoring the difference in between the fields which host Be-XRBs and the rest of the SMC. In these fields there is a weaker peak at $\sim$ 11 Myr ago with a rate of $\sim 6.2^{+2.4}_{-1.5}[10^{-6}\mathrm{M}_{\odot}/\mathrm{yr}/\mathrm{arcmin}^2]$, and

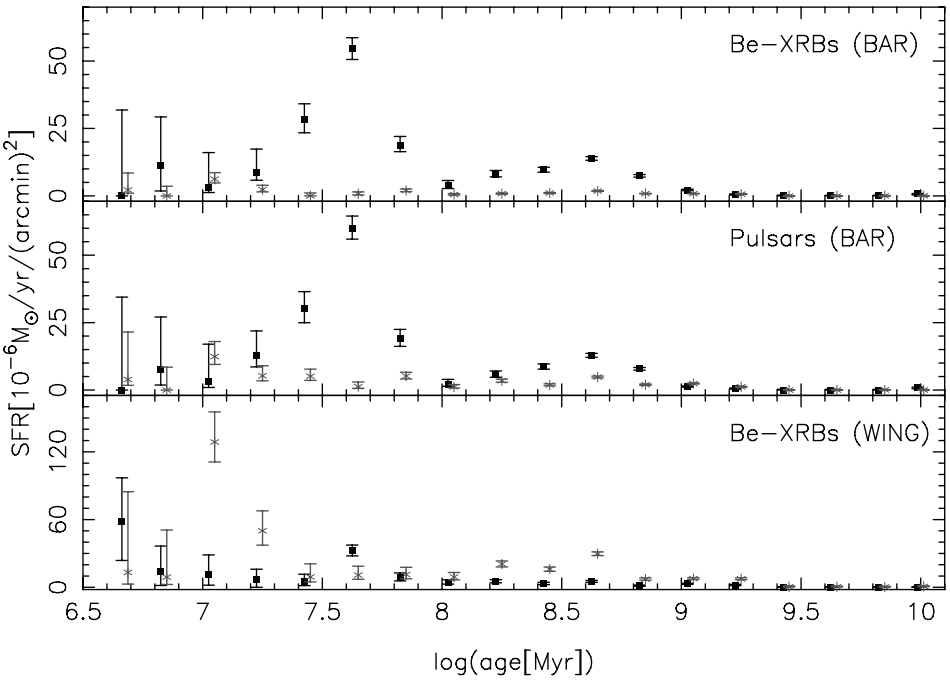

Figure 5.1 (*upper panel*) The black points show the average SF history for the MCPS regions (using data from Harris & Zaritsky 2004) which overlap with our *Chandra* and *XMM-Newton* fields and host one or more detected (candidate and confirmed) Be-XRBs. The SF history of MCPS regions which overlap with the same fields but they do not host any Be-XRBs is shown with gray points. (*middle panel*) The same plot as above but for MCPS regions with and without X-ray pulsars, and (*bottom panel*) with and without Be-XRBs from the *Chandra* Wing survey (P.I. Coe, AO6). For clarity a small offset of log(age[Myr]) ~ 0.025 has been applied in the distributions of areas without Be-XRBs and/or pulsars. Notice the difference in the y-axis of the bottom panel plot with respect to the other panels.

duration of only ~ 10 Myr.

Following the above comparison, we construct (middle panel of Fig.5.1) the SF history for the MCPS regions (overlapping with any of our fields) that host one or more known X-ray pulsars[2](shown in black), and for those that do not host such sources (shown in gray). We point out that a large fraction of these pulsars also appears in the Be-XRBs sample, since most of the companions of the SMC pulsars are Be stars. However, for completeness we present both (upper and middle panel, respectively), since the pulsars sample is X-ray selected while the Be-XRBs used earlier were selected based on the optical properties of the companion stars. In

[2]Using the on-line census of Malcolm Coe (http://www.astro.soton.ac.uk/∼mjc/ as of 06/05/2007).

total, in our *Chandra* fields lie 19 X-ray pulsars, while in the *XMM-Newton* fields only 3. As expected, the pattern in their SF history is very similar to that of Be-XRBs. For regions rich in X-ray pulsars we derive a rate of $\sim 60.1^{+4.4}_{-4.2}[10^{-6}\mathrm{M}_{\odot}/\mathrm{yr}/\mathrm{arcmin}^2]$ at ~ 42 Myr, while for regions without pulsars there is no peak at this age. In this case, the most intense peak is at ~ 11 Myr with a SF rate of $\sim 12.4^{+5.6}_{-2.9}[10^{-6}\mathrm{M}_{\odot}/\mathrm{yr}/\mathrm{arcmin}^2]$.

In Fig.5.1 (bottom panel) we also present the average SF history for the MCPS regions with any (shown in black) and without (shown in gray) Be-XRBs detected in the *Chandra* Wing survey (P.I. M. Coe, AO6). This survey covered 20 fields, however 3 of those were not used here because they do not overlap with any MCPS region, while all 4 Be-XRBs are also X-ray pulsars (Schurch et al. 2007). For fields with one or more Be-XRBs we derive a rate of $\sim 32.7^{+4.7}_{-4.9}[10^{-6}\mathrm{M}_{\odot}/\mathrm{yr}/\mathrm{arcmin}^2]$ at ~ 42 Myr. For regions without Wing Be-XRBs there is no SF burst at the age of Be-star formation, however an intense peak (and at the same time the most recent) appears at ~ 11 Myr with a rate of $\sim 128.7^{+26.7}_{-17.7}[10^{-6}\mathrm{M}_{\odot}/\mathrm{yr}/\mathrm{arcmin}^2]$.

All panels show a less intense peak at ~ 422 Myr ago. This is also observed in the global SF history of the SMC, and it temporally coincides with past perigalactic passages of the SMC with the Milky Way (Harris & Zaritsky 2004).

In Fig.5.2 we plot the number of Be-XRBs (normalized over the observed area) detected in our *Chandra* and *XMM-Newton* surveys versus the SF rate at ~ 42 Myr for the different fields. We chose to use Be-XRBs detected only in these surveys since we need a homogenous sample (refer to the above discussion). This also allows us to include the 4 Be-XRBs detected in the *Chandra* SMC Wing survey. Fig.5.2 shows a strong correlation of the Be-XRBs number and the strength of the SF at ~ 42 Myr. The best fit bisector line was calculated using the "Linear Regression Software" (Akritas, Bershady & Bird 1996), which takes into account heteroscedastic errors. We find a slope of 1.63 ± 0.66. We point out that this is the first such study for the investigation of the link between the population of only one class of X-ray sources (here Be-XRBs) and the SF rate at ages related to the observed populations. For this type of correlation we used a homogeneous sample within one galaxy, thus minimizing age, metallicity and distance effects that appear in studies which involve comparisons of different populations of X-ray sources in numerous galaxies.

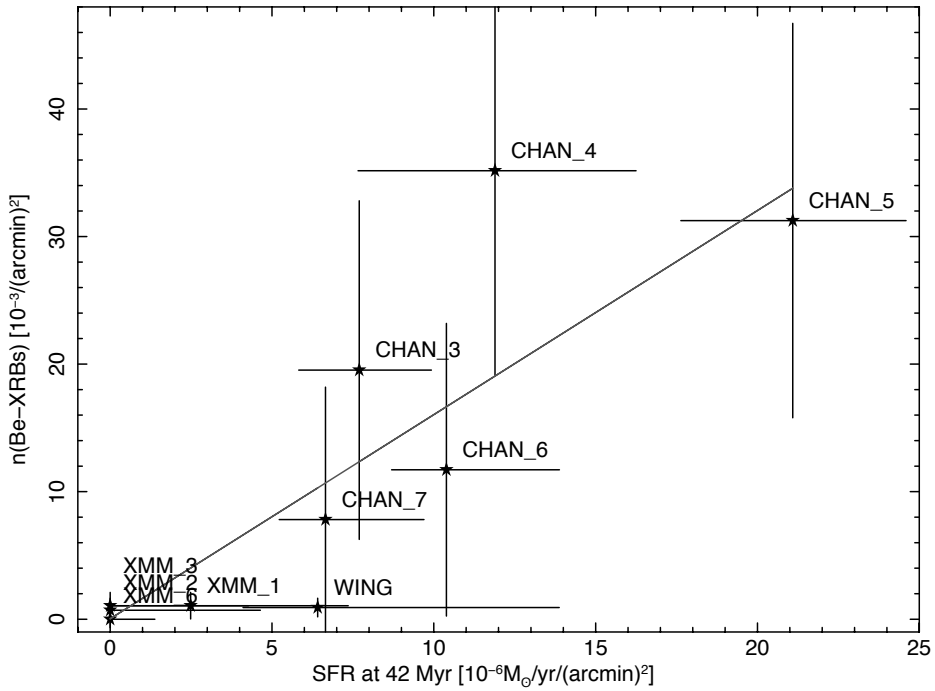

Figure 5.2 The number of observed Be-XRBs in the different studied fields versus the SF rate at the age of ~ 42 Myr. For the point labeled as Wing refer to the text (§5.3.2).

5.4 Discussion

From the above analysis we find that the number of Be-XRBs peaks for stellar populations of ages $\sim 30 - 70$ Myr. We also find that the other two peaks (~ 11 and ~ 422 Myr) observed in the SF history of regions with Be-XRBs do not give any Be-XRBs (Belczynski et al. 2008). The first one (at ~ 11 Myr) is too early to give any pulsar Be-XRBs, but could result in a population of black-holes with O or early B-type donors that due to their massive companion they evolve fast (e.g. Belczynski et al. 2008). Zhang, Li & Wang (2004) show that in low eccentricity systems the decretion disk around the Be star is effectively truncated, causing most of the Be/compact object binaries to appear as sources with very low L_X, thus making their detection very difficult. They suggest that this in turn could be a possible explanation for any "absence" of Be/BH-XRBs. In the Milky Way there are > 40 candidate BH-XRBs, in the LMC only 2, while in the SMC there is none (Liu et al. 2005). On the other hand, the second SF rate peak (at ~ 422 Myr) cannot result in Be-XRB formation, since by that time all OB stars have become supernovae.

The large number of Be-XRBs observed at ages $\sim 30 - 70$ Myr is consistent with the study of

McSwain & Gies (2005), who find that Be stars develop their decretion disks at ages of $\sim 25-80$ Myr, with a peak at ~ 35 Myr. OB stars formed during this episode are expected to reach the maximum rate of decretion disk formation at the current epoch.

A similar study by Shtykovskiy & Gilfanov (2007) for SMC HMXBs, reached the same conclusions, which they interpret as the result of (i) the evolution of the spin period of the pulsars; (ii) the evolution of the binary system, and (iii) the luminosity cutoff ($L_X \sim 10^{34}$ erg s^{-1}) due to the sensitivity of the observations. However, the fact that we observe relatively fast pulsars both in the SMC "bar" and the Wing indicates that spin evolution does not play a major role. The luminosity cutoff and evolution of the binary system may well result in variations of the XRB formation efficiency for different ages. However, based on the similarity between the ages of the stellar populations hosting X-ray pulsars in the SMC and the age of the maximum occurence of Be stars indicates that the development of a decretion disk plays a major role in the overall statistics of the X-ray source populations, by (a) increasing the number of active objects and (b) by increasing their observed luminosities due to the higher density and lower velocity of the outflow (Waters et al. 1988).

Furthermore, the lack of a large number of Be-XRBs in the SMC Wing is consistent with the present study. As it is shown in Fig.5.1 (bottom panel), the Wing has a weaker than the "bar" SF burst at the age of enhanced formation of Be stars (i.e. at ~ 42 Myr), while its most recent intense SF burst occurred only ~ 11 Myr ago. Thus we do not expect a significant number of SMC Wing Be-XRBs, at least comparable to that in the SMC "bar". Since in the present study we used the number of Be-XRBs from a single observation of each field and for fields covering both the SMC "bar" and the Wing, we were able to minimize the effects of the transient Be-XRB nature.

The above results also reinforce the argument for low kicks imparted on the compact object during the supernova explosion. For example, van den Heuvel et al. (2000) find kick velocities of the order of $\sim$ 15km/s for Galactic HMXBs, while Coe (2005) finds $\sim$ 30km/s for SMC HMXBs. If there were large kicks then the Be-XRBs and the pulsars would be distributed over larger scales and dilute the correlation with their parent stellar populations. In such a case the difference in the SF rate between MCPS regions with and without Be-XRBs would not be as large. In contrast, we find the Be-XRBs concentrated on the SMC "bar", thus the kicks must

have low velocities.

Another important result of this study is that even HMXBs that have not been proved yet to be Be-XRBs (mainly due to lack of spectroscopic data and of the transient Be nature) show a similar SF episode at $\sim$ 42Myr. In particular, following the procedure described in Section 5.3.2, and examining this time MCPS regions with non-Be HMXBs (from Liu et al. 2005), we derive a rate of $\sim 37.9^{+2.9}_{-2.5}[10^{-6}\mathrm{M}_{\odot}/\mathrm{yr}/\mathrm{arcmin}^2]$. This result is indicative of the true nature of these objects, and lead us to the conclusion that the majority of the optically unidentified SMC HMXBs have a Be nature.

In this letter we study a homogenous sample of Be-XRBs in the SMC based on a combination of *Chandra*, *XMM-Newton*, and optical photometric data. In particular, this is the first such study which demonstrates the importance of the Be-XRBs as a dominant component of young XRB populations. We find that regions with a significant number of Be-XRBs and/or pulsars have a burst in their SF histories at $\sim 30 - 70$ Myr ago. We also find strong evidence for a correlation between the observed number of Be-XRBs and the SF rate at the ages of Be-star formation ($\sim$ 42 Myr ago).

We thank Ewan O'Sullivan for advice with *XMM-Newton* data analysis. This work was supported by NASA LTSA grant NAG5-13056, and NASA grant G02-3117X.

Bibliography

[1] Antoniou, V., Zezas, A., Hatzidimitriou, D., McDowell, J. 2008a, Astrophys. J., submitted

[2] Cappelluti, N., et al. 2007, Astrophys. J. Suppl., 172, 341

[3] Belczynski, K., Kalogera, V., Rasio, F. A., Taam, R. E., Zezas, A., Bulik, T., Maccarone, T. J., & Ivanova, N. 2008, Astrophys. J. Suppl., 174, 223

[4] Coe, M. J. 2005, Mon. Not. R. Astr. Soc., 358, 1379

[5] Coe, M. J., Edge, W. R. T., Galache, J. L., & McBride, V. A. 2005a, Mon. Not. R. Astr. Soc., 356, 502

[6] Coe, M. J., Negueruela, I., & McBride, V. A. 2005b, Mon. Not. R. Astr. Soc., 362, 952

[7] Crowl, H. H., Sarajedini, A., Piatti, A. E., Geisler, D., Bica, E., Clariá, J. J., & Santos, J. F. C., Jr. 2001, AJ, 122, 220

[8] Dickey, J. M., & Lockman, F. J. 1990, ARA&A, 28, 215

[9] Dray, L. M. 2006, Mon. Not. R. Astr. Soc., 370, 2079

[10] Evans, C. J., Howarth, I. D., Irwin, M. J., Burnley, A. W., & Harries, T. J. 2004, Mon. Not. R. Astr. Soc., 353, 601

[11] Galache, J. L., Corbet, R. H. D., Coe, M. J., Laycock, S., Schurch, M. P. E., Markwardt, C., Marshall, F. E., & Lochner, J. 2008, ArXiv e-prints, 802, arXiv:0802.2118, Astrophys. J. Suppl., in press

[12] Haberl, F., & Pietsch, W. 2004, A&A, 414, 667

[13] Haberl, F., & Sasaki, M. 2000, A&A, 359, 573

[14] Harries, T. J., Hilditch, R. W., & Howarth, I. D. 2003, Mon. Not. R. Astr. Soc., 339, 157

[15] Harris, J., & Zaritsky, D. 2004, Astron. Journ., 127, 1531

[16] Hilditch, R. W., Howarth, I. D., & Harries, T. J. 2005, Mon. Not. R. Astr. Soc., 357, 304

[17] Liu, Q. Z., van Paradijs, J., & van den Heuvel, E. P. J. 2005, A&A, 442, 1135

[18] Majid, W. A., Lamb, R. C., & Macomb, D. J. 2004, Astrophys. J., 609, 133

[19] Maragoudaki, F., Kontizas, M., Morgan, D. H., Kontizas, E., Dapergolas, A., & Livanou, E. 2001, Astr. Astrophys., 379, 864

[20] McSwain, M. V., & Gies, D. R. 2005, Astrophys. J. Suppl., 161, 118

[21] Schurch, M. P. E., et al. 2007, Mon. Not. R. Astr. Soc., 381, 1561

[22] Shtykovskiy, P. E., & Gilfanov, M. R. 2007, Astronomy Letters, 33, 437

[23] Udalski, A., Szymanski, M., Kubiak, M., Pietrzynski, G., Wozniak, P., & Zebrun, K. 1998, Acta Astronomica, 48, 147

[24] van den Bergh, S. 2000, The galaxies of the Local Group, by Sidney Van den Bergh. Published by Cambridge, UK: Cambridge University Press, 2000 Cambridge Astrophysics Series Series, vol no: 35

[25] van den Heuvel, E. P. J., Portegies Zwart, S. F., Bhattacharya, D., & Kaper, L. 2000, Astr. Astrophys., 364, 563

[26] van Paradijs, J., & McClintock, J. E. 1995, X-ray Binaries, eds. W.H.G. Lewin, J. van Paradijs, and E.P.J. van den Heuvel (Cambridge: Cambridge Univ. Press), p. 58, 58

[27] Waters, L. B. F. M., van den Heuvel, E. P. J., Taylor, A. R., Habets, G. M. H. J., & Persi, P. 1988, Astr. Astrophys., 198, 200

[28] White, N. E., Nagase, F., & Parmar, A. N. 1995, X-ray Binaries, eds. W.H.G. Lewin, J. van Paradijs, and E.P.J. van den Heuvel (Cambridge: Cambridge Univ. Press), p. 1, 1

[29] Zaritsky, D., Harris, J., Thompson, I. B., Grebel, E. K., & Massey, P. 2002, Astron. Journ., 123, 855

[30] Zhang, F., Li, X.-D., & Wang, Z.-R. 2004, Astrophys. J., 603, 663

Chapter 6

Optical spectroscopy of High-Mass X-ray Binaries in the Small Magellanic Cloud

6.1 Introduction

We present a detailed optical spectroscopic study of 20 High Mass X-ray Binaries (HMXBs) in the Small Magellanic Cloud using the 2dF (Two-degree Field) spectrograph on the 3.9m Anglo-Australian Telescope (AAT). In this study we have used the 2dF spectrograph to confirm the classification of candidate Be-XRBs as emission line stars and identify the spectral type and luminosity class when possible. Our sample is selected from the *Chandra* survey (Zezas et al. 2008, Antoniou et al. 2008a) and it also includes candidate and known Be-XRBs from the census of Haberl & Pietsch 2004 (an *XMM-Newton* survey). Out of the 20 objects the spectra of which are presented here, only 2 have good quality published optical spectra in the full wavelength range ($\sim 3800 - 7000\mathring{A}$), while one source has been observed only in the red portion of the optical spectrum ($\sim 6000 - 7000\mathring{A}$) around H$\alpha$. With the present observations we will confirm or otherwise the Be-XRB nature of these 20 objects and we will study their spectral characteristics, in conjunction with their optical and near infrared properties. Although this is only a pilot study, it is the first public spectroscopic survey of a relatively large number of

Be-XRBs and candidates, over a large wavelength range.

The structure of this chapter is the following. In Section 6.2 we present the observations and data reduction, the sample of X-ray sources that we followed-up spectroscopically, and the criteria used for their classification. In Section 6.4 we present the optical and infrared properties of the studied stars, and the comparison of the classification of sources from this study with previous studies (whenever available). In the appendix we show their OGLE-II and MACHO light curves (§**??**), along with their optical spectra (§C.1).

6.2 Observations and data reduction

In this pilot study, the optical spectra were obtained during service time in November 2004, with the 2dF multiple-object dual spectroscopic facility at the prime focus of the 4-m Anglo-Australian Telescope (Lewis et al. 2002). The observations were taken at airmass between 1.35 and 1.48, while the seeing was 1.6″. We used a 300lines/mm grating (300B), which gave a 4400Å wavelength coverage (from 3640Å to 8040Å) region at an instrumental resolution of 8.9Å (4.3Å/pixel). Four 2250s exposures were obtained, providing a total exposure time of 9000s. The on-target exposures were preceded and followed by arc calibration exposures (CuAr and CuHe) and a fibre-flat-field exposures. Approximately 30 "sky" fibers (15 for each spectrograph) were assigned, to ensure good definition of the sky background.

The data preparation and spectral extraction were performed using the *2dfdr* software (Lewis et al. 2002). The main steps include bias subtraction, extraction of the spectra from the CCD image, division by a normalized flat-field, wavelength calibration, calibration of the fibre throughputs, and subtraction of the scaled median sky spectrum (derived from the sky fibre spectra). Spectral line fitting and equivalent width line measurements were performed with the *DIPSO* package Version 3.6-3 and FIGARO v4.11 of STARLINK.

Fibers that were assigned to fainter objects, yielded low signal-to-noise ratio (S/N) spectra, because of the relatively short exposure times (due to the maximum allowed duration of a service time observing run) and possible positional offsets. We defined the S/N ratio of each spectrum using the counts in the $5600 - 6200$Å range (measured using the *istat* package of

FIGARO v4.11) which can be considered representative of the continuum. Spectra with < 400 average counts in this wavelength range (which correspond to S/N ratio of $\sim 15 - 20$) were excluded from the present study, as it was difficult to perform accurate spectral classification for them, thus leaving 58 spectra for further consideration. The spectra are not flux calibrated[1].

The inner regions of the SMC show strong and variable diffuse emission from HII regions and SNRs. Due to the nature of multifiber spectroscopy it is not possible to remove accurately this variable local sky background. This would require the allocation of a sky fiber close to each target fiber. Due to hardware limitations this was very difficult to achieve in most cases. Therefore some of our object spectra may be contaminated by interstellar emission lines. Typical emission lines of HII regions are [NII] λ6548, Hα λ6563 (strongest line), [NII] λ6584, [SII] λ6716, and [SII] λ6731 (e.g. Smith et al. 1993).It is vital for our analysis to account properly for the contribution to Hα emission particularly from the HII regions, since the presence of Hα emission is one of the main classification criteria for Be-XRBs. Correction of the variable local sky in this type of observations is not trivial. We followed two different approaches in order to select objects with significant stellar Hα emission:

1. *Broad Hα emission.* Be stars exhibit broad Hα emission (e.g. Coe et al. 2005). We chose a limit for the Hα FWHM of $\geq$ 10Å, based on the the average FWHM of the Hα line of high signal-to-noise already confirmed Be-XRBs and Be-XRB pulsars. However, we note here, that the above Hα width limit does not rule out the possibility that some of the remaining sources may well prove to be Be-XRBs. This is mainly possible due to the transient nature of the Hα emission in Be stars (e.g. McSwain et al. 2008). However, we checked than none of the discarded sources with good S/N satisfy criterion *(ii)* discussed below, and this gives us confidence that at least we do not miss a significant population of Be-XRBs among the remaining sources. In total we find 20 sources with Hα line width $\geq$ 10Å. For the measurement of the above quantities we used the *DIPSO* package Version 3.6-3 of STARLINK.

2. Hα/[S$_{\rm II}$] *ratio.* If contamination from the diffuse interstellar emission is significant, an emission line of [S$_{\rm II}$] 6716Å should be seen in our spectra. The ratio of [S$_{\rm II}$] to Hα is

[1]With a multi-fiber instrument, such as the 2dF, flux calibration would require observation of a flux standard through each fiber.

higher for SNRs and lower for HII regions. We selected sources which have a ratio of relative strengths of Hα to [S$_{\rm II}$] 6716Å $> 2\sigma$ from the mean value of the corresponding ratio derived from sky fibers. From each spectrum we subtracted the local background (defined in the wavelength range between these 2 lines, i.e from $\sim$ 6600Åto $\sim$ 6680Å, using the *istat* package of FIGARO v4.11). We find a mean sky value of [S$_{\rm II}$] to Hα ratio of 0.15 ± 0.03. Then, assuming that both the [S$_{\rm II}$] and Hα emission in our stellar spectra are due to nebular emission, we can estimate the Hα nebular emission from the [S$_{\rm II}$] intensity and the above ratio. Then we compared the observed intensity of Hα emission against that expected from nebular emission. If the expected nebular emission is at least 3σ lower than the observed Hα emission, we considered that the spectrum had a significant stellar component.

Actually, both criteria yielded the same list of 20 objects. Therefore, we are confident that these stars have indeed significant Hα emission, and they are selected for further analysis. These 20 sources are presented in Table 6.1. In Column [1] we list the X-ray source ID as given in Antoniou et al. (2008a; (Field ID)_(Src ID within the field)). The XMM ID refers to sources from Haberl & Pietsch (2004), while other names for the *XMM-Newton* sources and their references (Column [2]) are taken from the latter work. In the remaining of this study, we will discuss results derived only for the 20 X-ray sources listed in Table 6.1.

In Table 6.2 we present for each selected X-ray source (Column [1]) the measurements of the center (Column [2]), the FWHM (Column [4]), and the EW (Column [6]) of the Hα emission, along with their errors (Column [3], Column [5], and Column [6], respectively) from the interactive fits. The derived errors represent 68% confidence intervals. We measured the center of each Hα line and its FWHM using a Gaussian fit (*elf* subroutine), while for the EW we used the *ew* subroutine of the *DIPSO* package. In the literature we found available Hα EW measurements for 8 of our sources. We present these values in Column [7] along with their reference (given in parenthesis). They are in quite good agreement, despite the fact that some variability is expected.

Table 6.1. The Be-XRB sample observed with 2dF

X-ray Src ID†	Other names for X-ray src
[1]	[2]
3_3 (XMM_33)	CXOU J005736.0-721934 (1) = CXOU J005736.2-721934 (23,24)
4_1 (XMM_12)	CXOU J005044.6-731605 (1) = XMMU J005045.2-731602 (42) = (RX J0050.8-7316 = AX J0051-733) (8,3)
4_5 (XMM_9)	CXOU J004929.7-731059 (1) = XMMU J004929.9-731058 (42) = (RX J0049.5-7310) (6)
4_8	CXOU J004814.2-731004 (1) = XMMU J004814.1-731003 (41)
5_16	CXOU J005355.3-722646 (1) **???** 1WGA 0053.8-7226,XTE J0053-724
5_2	CXOU J005323.9-722716 (1)
5_4	CXOU J005446.2-722523 (1)
5_7 (XMM_30)	CXOU J005456.3-722648 (1) = (XTE J0055-724 = 1SAX J0054.9-7226 = 1WGA J0054.9-7226) (21,22,23)
6_1	CXOU J005209.0-723804 (1)
6_2	CXOU J005455.8-724511 (1)
6_4	CXOU J005252.2-724830 (1)
XMM_14	XMMU J005057.6-731007 (42) = (RX J0050.9-7310, AX J0050.8-7310) (3)
XMM_15	AX J0051-722 (9)
XMM_17	XMMU J005152.2-731033 (42) = (RX J0051.9-7311 = AX J0051.6-7311) (8,3)
XMM_3	XMMU J004723.7-731226 (42) = (RX J0047.3-7312 AX J0047.3-7312) (3)
XMM_39	XMMU J010030.2-722035 (23)
XMM_47	RX J0104.5-7221 (43)
XMM_5	XMMU J004834.5-730230 (42) = (RX J0048.5-7302) (43)
XMM_7	XMMU J004913.8-731136 (42) = (RX J0049.2-7311) (6)
5_12	CXOU J005245.0-722844 (1)

†The X-ray source ID corresponds to *Chandra* sources as given in Antoniou et al. (2008a; (Field ID)_(Src ID within the field)). The XMM ID refers to sources presented in Haberl & Pietsch (2004), while the matches between the X-ray sources are taken from the same work, with only exception that of *Chandra* source 5_16

References. — (1) Zezas et al. (2008), (3) Yokogawa et al. (2003), (6) Filipovic et al. (2000b), (8) Schmidtke et al. (1999), (9) Corbet et al. (1998), (21) Marshall & Lochner (1998), (22) Santangelo et al. (1998), (23) Sasaki et al. (2003), (24) Macomb et al. (2003), (41) Haberl et al. (2008), (42) Haberl & Pietsch (2004), (43) Haberl & Sasaki (2000)

Table 6.2. Measurements of the Hα emission in the Be-XRBs sample

X-ray Src ID[†]	Center (Å)	δ(Center)[‡] (Å)	FWHM (Å)	δ(FWHM)[‡] (Å)	EW (Å)	δ(EW)[‡] (Å)	EW (Refer.) (Å)
[1]	[2]	[3]	[4]	[5]	[6]	[7]	[8]
3_3 (XMM_33)	6565.78	0.09	11.98	0.22	-32.08	0.45	-28 ± 2 (6)
4_1	6566.27	0.08	14.11	0.21	-28.30	0.82	-24.5 ± 0.7
4_5 (XMM_9)	6566.09	0.08	15.51	0.21	-38.47	0.70	···
4_8	6565.61	0.12	11.08	0.26	-15.68	0.33	···
5_16	6566.00	0.05	11.76	0.12	-19.48	0.46	-21.9 ± 0.7 (6)
5_2	6565.92	0.09	13.26	0.24	-24.02	0.63	···
5_4	6566.84	0.09	12.83	0.24	-36.19	1.06	···
5_7 (XMM_30)	6565.67	0.04	10.90	0.10	-19.97	0.66	-25 ± 2 (10)
6_1	6566.94	0.04	10.56	0.09	-23.87	0.38	···
6_2	6566.14	0.03	12.40	0.08	-56.00	0.95	···
6_4	6565.83	0.16	13.05	0.38	-6.59	0.18	···
XMM_14	6564.99	0.05	10.53	0.11	-20.37	0.35	···
XMM_15	6566.12	0.04	14.83	0.10	-32.04	1.07	-22 (10)
XMM_17	6566.71	0.10	11.97	0.25	-16.16	0.26	-13.1 ± 0.5 (6)
XMM_3	6564.57	0.06	11.32	0.14	-24.40	0.48	-31.6 ± 0.9
XMM_39	6565.74	0.03	10.33	0.07	-65.02	1.44	···
XMM_47	6565.82	0.06	11.94	0.16	-38.64	0.60	···
XMM_5	6566.06	0.03	12.55	0.08	-36.03	0.24	···
XMM_7	6565.49	0.03	12.13	0.08	-32.41	0.40	-29.6 ± 1.5 (6)
5_12	6565.67	0.26	10.44	0.62	-5.38	0.11	···

[†]The X-ray source ID corresponds to *Chandra* sources as given in Antoniou et al. (2008a; (Field ID)_(Src ID within the field)). The XMM ID refers to sources from Haberl & Pietsch (2004). This also explains why there is different accuracy in the coordinates of the X-ray sources.

[‡]All errors are 68% confidence intervals.

References. — (4) Edge & Coe (2003), (6) Coe et al. (2005a), (7) Schmidtke, Cowley & Levenson (2003), (10) Stevens, Coe & Buckley (1999)

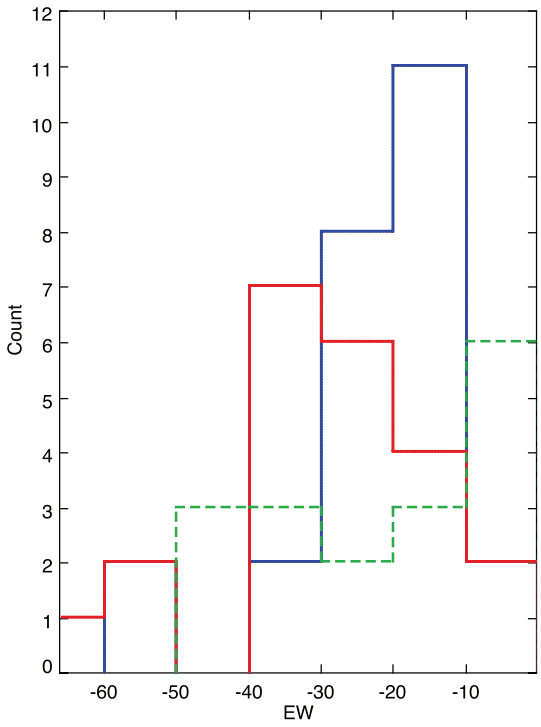

Figure 6.1 Distribution of Hα equivalent widths. Our 2dF Be-XRB sample is indicated with a red solid line, Be-XRBs from the sample of Coe et al. 2005 are shown with a blue solid line, while EWs for isolated Be stars (data are taken from Ashok et al. 1984) are presented with a dotted green line.

In Figure 6.1 we show the distribution of the Hα EWs of our 2dF Be-XRB sample (red solid line). Our objects mainly have EWs in the range ~ -40 to ~ -10, in agreement with values from the Be-XRB sample of Coe et al. (2005; blue solid line). We also show for comparison the distribution of isolated Be stars (green dotted line) using data from (Ashok et al. 1984).

The Hα emission line profiles normalized by the local continuum for the spectra of Table 6.2 are presented in Figure 6.2.

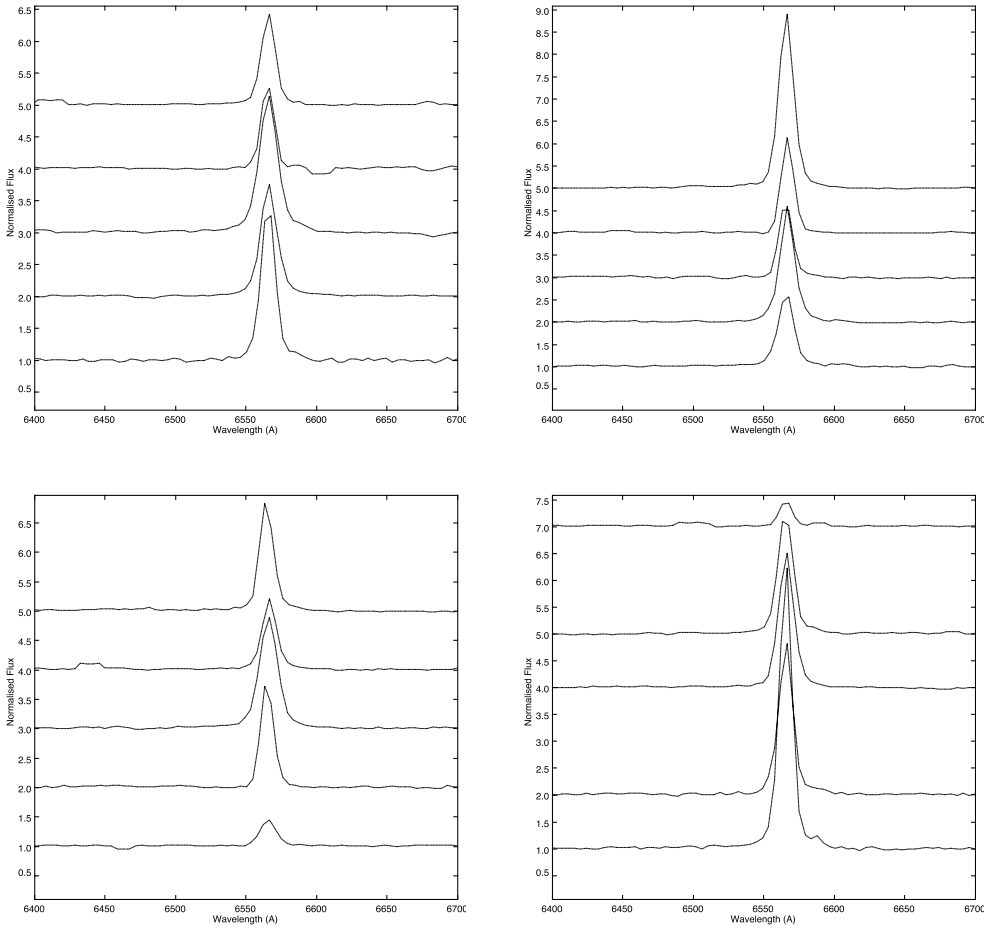

Figure 6.2 Hα emission line profiles normalized by the local continuum. From bottom to top in each panel we show the following sources: *(Left-Top)* 3_3 (XMM_33), 4_1, 4_5 (XMM_9), 4_8, 5_16, *(Right-Top)* 5_2, 5_4, 5_7 (XMM_30), 6_1, 6_2, *(Left-Bottom)* 6_4, XMM_14, XMM_15, XMM_17, XMM_3, *(Right-Bottom)* XMM_39, XMM_47, XMM_5, XMM_7, 5_12. For clarity we applied a y-axis offset to the different spectra of each panel.

6.3 Determination of spectral types

The primary spectral classification criteria for OB stars are usually based on metal line strengths except for the earliest subtypes (e.g. Lennon 1997). Due to the low metallicity and the relatively low luminosity of the 2dF targets, the metal lines are very weak (see also Evans et al. 2004). Overall, we have adopted the same classification scheme as in Evans et al. (2004), although, due to the lower resolution of our spectra, it was not always possible to use the same indicators.

The presence of HeII absorption lines (HeII λ4686, HeII λ4541, HeII λ4200) lines indicate spectral type B0 or earlier. Strong HeI lines are also indicative of early spectral type. In B0.5 stars, HeII λ4541 and HeII λ4200 are absent, while HeII λ4686 is weak. In B1 stars, HeII λ4686 disappears, while SiIV $\lambda\lambda 4088, 4116$ appear. For spectral types later than B1.5 the OII+CIII $\lambda 4640-4650$ blend decreases rapidly, and disappears for stars later than B3. For spectral types B2 or later MgII λ4481 and SiIII λ4553 become stronger. Comparison between the strengths of these two lines are used to distinguish between B2, B2.5, and B3.

The resulting spectral types for the 2dF targets are shown in Table 6.3, while sample normalized spectra in the 3800Å-5000Å wavelength range are shown in Figure 6.3, with characteristic spectral features marked. The full wavelength spectra (3800Å-8000Å) are given in the appendix (§C.1). In Table 6.3 we give the X-ray source ID (Column [1]), the derived spectral classification from this study (Column [2]), and any previous classification of the same sources (Column [3]) along with their reference (given in parenthesis). A "Be?" (i.e. tentative Be) input in Column [3] indicates sources for which the classification as a Be star is based on the positional coincidence of a hard X-ray source with an emission-line object from the catalog of Meyssonnier & Azzopardi (1993; hereafter [MA93]) and/or with an early-type (OB) star (e.g. Antoniou et al. 2008a). A "Be" input in Column [3] indicates sources that have been previously classified as Be-XRBs and have a hard X-ray spectrum, an emission-line object from [MA93] as counterpart, and detection of X-ray pulses. In total, 15 out of the 20 sources studied here have been assigned a general B-class. Our study examines this classification, since only spectroscopy can unambiguously identify the nature of the companion object with that of a Be star. Due to the absence of flux calibration and relatively low resolution it was usually not possible to assign with certainty a spectral luminosity class to our objects, with the only exception source 6_4 (see discussion below). For the same reason the luminosity class given by Evans et al. (2004), who have used

the same spectrograph, is uncertain. As these authors note their luminosity class assignment is the result of a photometric/spectroscopic approach due to their low signal-to-noise ratio spectra. Evans et al. (2004) sources appear in Column [3] in Table 6.3 as [2dF]ID, where ID comes from the original catalog. Despite the fact that a spectroscopic luminosity class was not attempted to be assigned in most cases, good quality photometric observations are available for all our stars (see §6.4.2), which allowed us to assign a tentative photometric class to our objects.

Except for one object (XMM_33) which is of type B3-B5, all the other stars are earlier than B2. Source 4_1, which is classified here as B0.5, was classified as B0III-Ve by Coe et al. (2002). Source XMM_47 was classified as B0.5(IV)e by Evans et al. (2004), however, following the above criteria, we classify it as B1.5e. The spectral classification of B-type stars 6_1, XMM_39, and XMM_5 derived from this work is in agreement with the broad subclass of 0-5 given by Evans et al. (2004). However, two sources (6_4 and XMM_15) appear to have different spectra. Source 6_4 is assigned an O3If* spectral class, while source XMM_15 has a peculiar B0-2 spectrum. These two sources are discussed in detail in the discussion (§6.4.5 and 6.4.4). To summarise, for all but two sources the previous classifications are in good agreement with the present work. We estimate that our spectral types are accurate to better than ± 1 subclass in most cases.

Table 6.3. Spectral classification

X-ray Src ID†	Classification	
	This study	Previous
[1]	[2]	[3]
3_3 (XMM_33)	B3-5e	Be (6,9)
4_1	B0.5e	B0III-Ve (11)
4_5 (XMM_9)	B1e	Be (12)
4_8	B1.5e	Be? (13)
5_16	B0.5e	Be (14,6)
5_2	B0.5e	Be (15)
5_4	B1-1.5e	Be? (13)
5_7 (XMM_30)	B1.5e	Be (10,6)
6_1	B1.5e	B1-5(II)e = [2dF]5054 (17), Be(6)
6_2	B1-1.5e	Be (16)
6_4	O3If*	Be (1)
XMM_14	B0.5e	Be? (3)
XMM_15	B0-2e, peculiar?	Be (10,6)
XMM_17	B0e	Be ((6), peculiar (8))
XMM_3	B2e	Be (6)
XMM_39	B1e	B0-5(II) = [2dF]1475 (17), Be? (3)
XMM_47	B1.5e	B0.5(IV)e = [2dF]1905 (17), Be? (1)
XMM_5	B1.5e	B0-5(II) = [2dF]690 (17), Be? (1)
XMM_7	B1.5e	Be (6)
5_12	B0e	Be? (13)

†The X-ray source ID corresponds to *Chandra* sources as given in Antoniou et al. (2008a; (Field ID)_(Src ID within the field)). The XMM ID refers to sources from Haberl & Pietsch (2004). This also explains why there is different accuracy in the coordinates of the X-ray sources.

References. — (1) Haberl & Sasaki (2000),(2) Stevens et al. (1999), (3) Haberl & Pietsch (2004), (4) Edge & Coe (2003), (5) Coe & Orosz (2000), (6) Coe et al. (2005a), (7) Schmidtke, Cowley & Levenson (2003), (8) Schmidtke et al. (1999), (9) Macomb et al. (2003), (10) Stevens, Coe & Buckley (1999), (11) Coe et al. (2002), (12) Schmidtke et al. (2004), (13) Antoniou et al. 2008a, (14) Buckley et al. (2001), (15) Edge et al. (2004), (16) Haberl et al. (2004), (17) Evans et al. (2004)

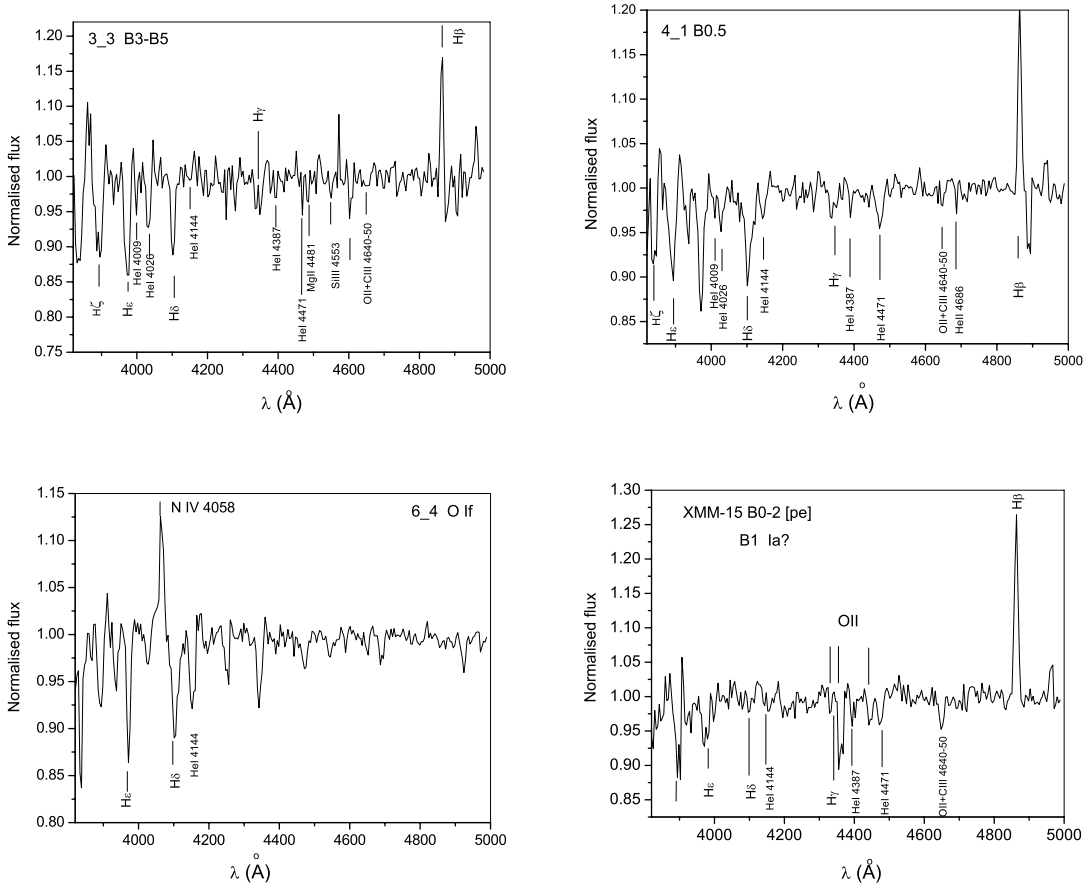

Figure 6.3 Sample normalized spectra in the 3800Å-5000Å wavelength range are shown, with characteristic spectral features marked.

6.4 Discussion

6.4.1 Distribution of spectral types

The distribution of spectral types of the 18 confirmed Be-XRBs (excluding sources 6_4 and XMM_15, described in §6.4.4 and 6.4.5, respectively) show a peak at B1.5. In Figure 6.4 (top panel) we show the Be-XRBs with available spectral types in the SMC (filled bars) and the LMC (solid line) from the catalog of Liu et al. (2005). In this SMC sample we added the classification of the 18 sources studied here. Data for the Milky Way are taken from the catalog of Liu et al. (2006). Whenever only a broad spectral class was available, we adopted the average subtype. Negative spectral subtypes are used to describe O-type stars. We also show (bottom panel) the spectral distribution of isolated Be stars from the Bright Star Catalog (BSC; using data from Porter et al. 1996).

From the above comparison we see that in the SMC spectral types later than B5 are "missing", when compared to the Galactic spectral type distribution of Be-XRBs. Moreover, there is only one SMC source with a spectral classification of B3-B5, derived in the present study. Coe et al. (2005) observed a similar distribution, though they chose to allocate in fractions the broad subtype classifications based on their (B-V) color. They suggested that the fact that the distributions of the SMC and the Milky Way are indeed different may reflect a different evolutionary path due to the much lower metallicity of the SMC and more recent star-formation.

On the other hand, the Be stars in X-ray binaries have a different spectral distribution when compared to that of isolated Be stars. The BSC contains stars brighter than $V \leq 6.5$, and it is therefore biased towards earlier spectral types. However, in a volume, rather than in a magnitude limited sample the peak of the spectral distribution would be towards later spectral types (Negueruela 1998), thus the difference would be even more prominent. As suggested by Negueruela (1998) this difference must reflect a real difference in the populations from which the field and in binary Be stars are drawn.

We note that the earliest spectral type for Be-XRBs, shown in Figure 6.4, is an O5Ve star (counterpart of the SMC X-ray source RX J0103.6-7201).

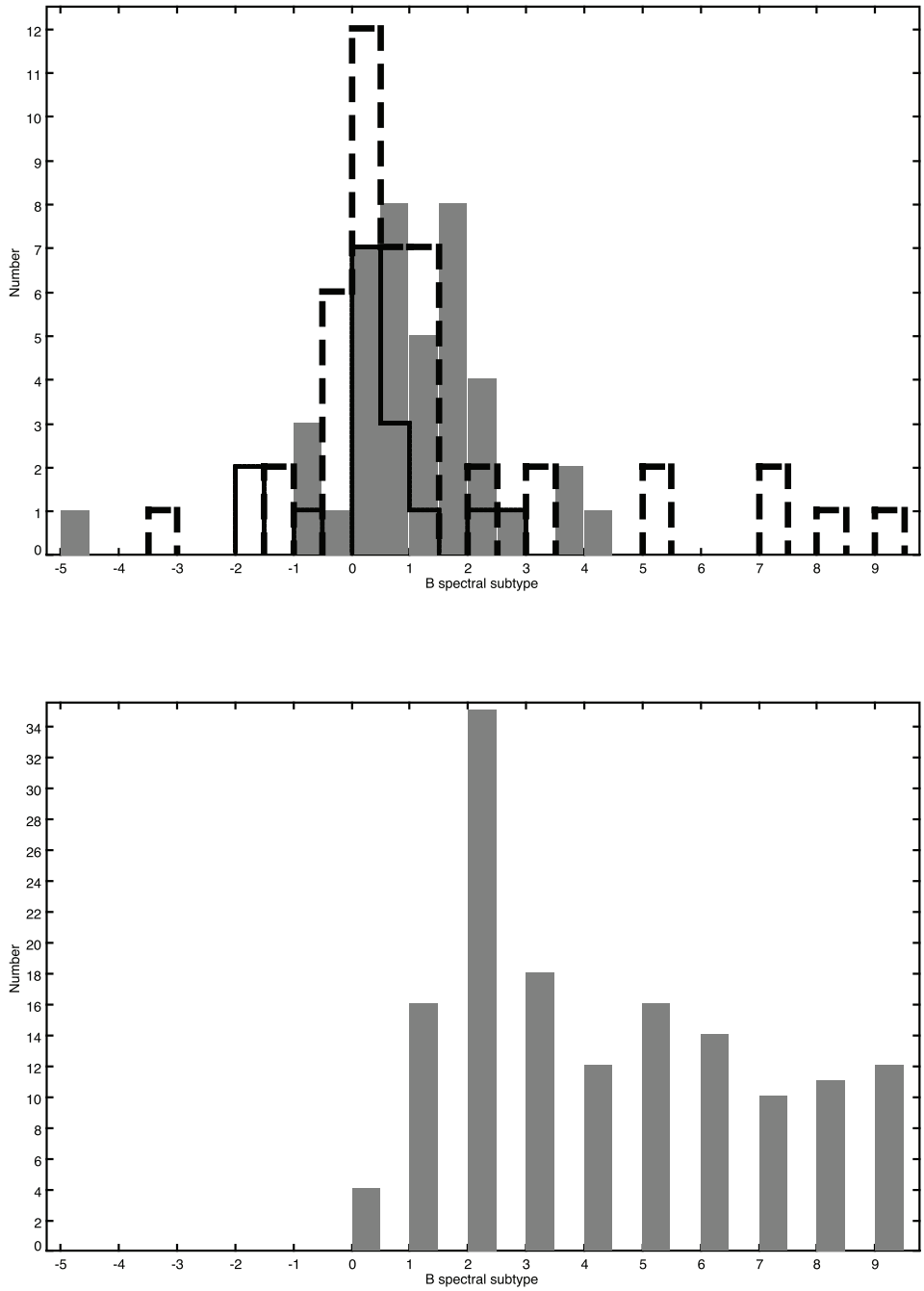

Figure 6.4 Comparison of the B spectral subtype distributions of Be-XRBs to isolated Be stars. Negative spectral subtypes correspond to O-type stars. *(Top panel)* The spectral distribution of Be-XRBs in the SMC (solid bars), the LMC (solid line), and the Milky Way (dashed line) is shown. The SMC and LMC data are taken from Liu et al. (2005), while in the SMC sample we have added our classification using the 2dF spectrograph. Data for the Milky Way are taken from Liu et al. (2006). *(Bottom panel)* The spectral distribution of isolated Be stars from the Bright Star Catalog (using data from Porter et al. 1996).

6.4.2 Optical and near-infrared photometry of the Be-XRB 2dF sample

In Table 6.4 we present the optical counterparts of the X-ray sources. In Column [1] we give the X-ray source ID, and in Columns [2] and [3] the X-ray source coordinates (R.A. and Decl., respectively). In Column [4] we present the optical counterpart of the X-ray source. For *Chandra* sources (named as (Field ID)_(Src ID within the field)) this ID (along with the photometric data) is taken from Antoniou et al. (2008a). For *XMM-Newton* sources (named as XMM_(Src ID in Haberl & Pietsch 2004)) we searched for optical counterparts within $5''$ from the X-ray source position. In both cases (*Chandra* and *XMM-Newton* sources) we list the optical source ID in Column [4]. OGLE-II sources are named as O_F_NNNNNN, where F and NNNNNN are the field and optical source number, respectively (from Udalski et al. 1998a), and MCPS sources are named as Z_NNNNNN where NNNNNN is the line number of the source in Table 1 of Zaritsky et al. (2002). The distance (in arcseconds) of the counterpart to the X-ray source is given in Column [5]. The optical (V,B-V) data of the sources are presented in Columns [6] and [7] along with their errors given in parenthesis (these data are taken directly from the original catalogs without applying any reddening or zero-point correction): apparent magnitude in the V band (Column [6]), and B - V color (Column [7]). In Column [8] we list the emission line object from the catalog of Meyssonnier & Azzopardi (1993).

In Figure 6.5 we present the M_{V_o} vs. $(B-V)_o$ CMD of the counterparts (red circles) of the X-ray sources with 2dF spectra. The magnitudes, colors and their errors are from the OGLE-II catalog (Udalski et al. 1998), except for sources with matches only in the MCPS catalog (Zaritsky et al. 2002). With blue crosses are also shown the NGC330 Be stars from Martayan et al. (2007), while with gray small dots we present the OGLE-II stars that lie in our *Chandra* field 4 and have < 0.2 magnitude errors in the V and B band (Antoniou et al. 2008a). The MS, the red giant branch and the red clump loci are clearly shown. All X-ray sources with 2dF spectra fall well within the above locus, while their position in the CMD agrees well within their errors with the Be stars from the study of Martaryan et al. (2007). The Be stars are generally redder than B type stars (e.g. McSwain & Gies 2005), and this is in agreement with the position off the main sequence of our Be-XRBs with 2dF spectra.

Table 6.4. Optical counterparts of selected X-ray sources with 2dF spectra from this study

Src ID‡	X-ray R.A.(J2000.0) (h m s)	Decl.(J2000.0) (° ′ ″)	Optical Src ID	Off.† X-O (″)	V (mag)	$(B-V)$ (mag)	[MA93]
[1]	[2]	[3]	[4]	[5]	[6]	[7]	[8]
3_3	00 57 36.00	-72 19 33.9	O-8_49531	0.14	16.01(02)	-0.02(04)	1020
(XMM_33)			Z_3103982	0.53	15.99(03)	0.01(17)	
4_1	00 50 44.61	-73 16 5.3	O-5_180026	0.55	15.44(04)	-0.04(05)	387
			Z_2131651	0.60	15.48(04)	-0.11(05)	
4_5	00 49 29.74	-73 10 58.5	O-5_111500	0.61	16.30(01)	0.09(02)	300
(XMM_9)			Z_1971979	0.65	16.15(03)	0.20(05)	
4_8	00 48 14.15	-73 10 4.1	O-4_171264	0.63	15.74(04)	0.00(05)	···
			Z_1816472	0.30	15.30(05)	0.26(06)	
5_16	00 53 55.25	-72 26 45.8	Z-2573354	0.83	14.72(03)	-0.07(03)	···
5_2	00 53 23.86	-72 27 15.5	Z-2498173	0.24	16.19(12)	-0.09(12)	667
5_4	00 54 46.22	-72 25 23.0	O-7_70843	0.79	15.58(02)	0.14(06)	798
			Z_2707354	0.83	15.36(05)	0.14(06)	
5_7	00 54 56.34	-72 26 48.4	O-7_70829	1.19	15.30(01)	-0.04(02)	810
(XMM_30)			Z_2730786	1.21	15.27(03)	-0.05(04)	
6_1	00 52 8.95	-72 38 3.5	O-6_77228	0.58	15.03(02)	0.14(03)	···
			Z_2319498	0.64	15.23(03)	-0.08(03)	
6_2	00 54 55.78	-72 45 10.7	O-7_47103	0.40	15.01(01)	-0.02(01)	809
			Z_2729974	0.61	15.00(03)	-0.03(04)	
6_4	00 52 52.22	-72 48 29.8	O-6_147662	0.27	14.42(05)	-0.10(05)	618
			Z_2423181	0.56	14.36(03)	-0.05(04)	
XMM_14	00 50 57.6	-73 10 08	O-5_271074	2.10	14.54(01)	-0.06(01)	414
			Z-2159045	1.93	14.35(05)	0.08(06)	
XMM_15	00 50 56.9	-72 13 31	Z-2158744	3.22	15.06(06)	-0.08(06)	413::
XMM_17	00 51 52.3	-73 10 33	O-6_22749	1.36	14.48(02)	-0.08(02)	504
			Z-2280409	1.32	14.45(05)	-0.07(06)	
XMM_3	00 47 23.7	-73 12 27	O-4_116979	1.52	16.14(01)	-0.04(01)	172
			Z-1713720	1.25	16.03(03)	0.08(04)	
XMM_39	01 00 30.2	-72 20 35	O-9_35989	2.04	14.65(02)	-0.06(03)	1208
			Z-3499823	2.13	14.64(03)	-0.06(14)	
XMM_47	01 04 35.7	-72 21 43	O-10_61612	5.28	15.19(02)	-0.01(03)	1470
			Z-4031467	4.91	15.13(03)	0.05(03)	
XMM_5	00 48 34.5	-73 02 30	O-4_178950	1.85	14.95(04)	-0.09(06)	238
			=O-5_43566	1.89	15.11(12)	-0.23(13)	
			Z-1857369	1.64	14.78(03)	0.00(04)	
XMM_7	00 49 13.8	-73 11 37	O-5_111490	0.84	16.52(02)	0.10(04)	···

Table 6.4—Continued

Src ID‡	X-ray R.A.(J2000.0) (h m s)	Decl.(J2000.0) (° ′ ″)	Optical Src ID	Off.† X-O (″)	V (mag)	$(B-V)$ (mag)	[MA93]
[1]	[2]	[3]	[4]	[5]	[6]	[7]	[8]
			Z-1938257	0.75	16.44(04)	0.19(05)	
5_12	00 52 45.04	-72 28 43.6	Z-2406014	0.35	14.92(08)	0.00(09)	···

†The distance (in arcseconds) of the counterpart to the X-ray source.

‡The X-ray source ID corresponds to *Chandra* sources as given in Antoniou et al. (2008a; (Field ID)_(Src ID within the field)). The XMM ID refers to sources from Haberl & Pietsch (2004). This also explains why there is different accuracy in the coordinates of the X-ray sources.

⁝The Halpha emission-line nature of the object is very doubtful, mainly due to its severe faintness or because it is a late-type star (Meyssonnier & Azzopardi 1993).

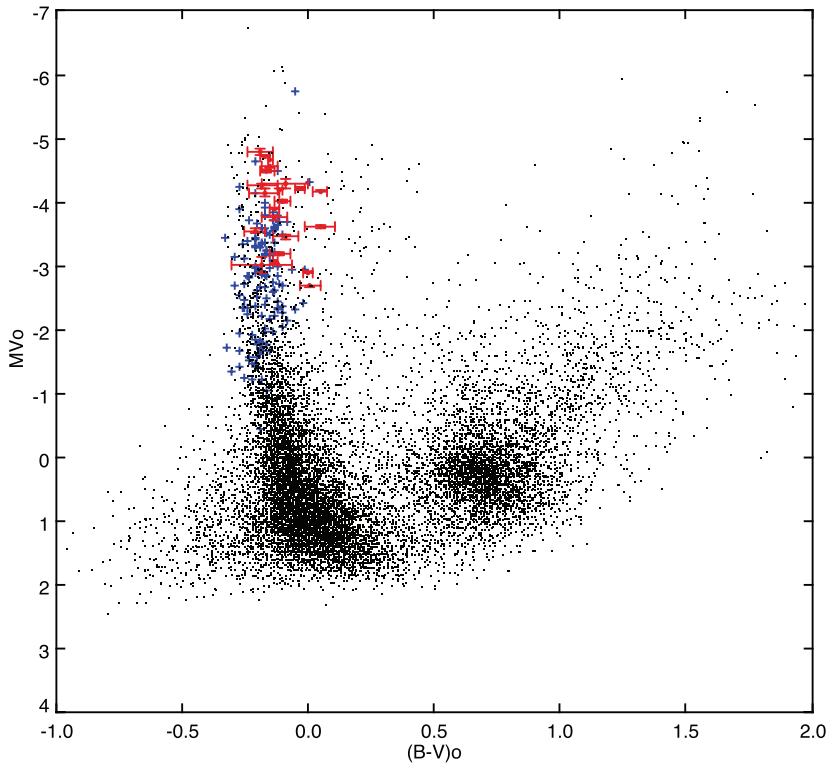

Figure 6.5 CMD of optical counterparts of X-ray sources with 2dF spectra

We present the M_{V_o} vs. $(B-V)_o$ CMD of the optical counterparts (red circles) of the X-ray sources with 2dF spectra. With blue crosses are also shown the NGC330 Be stars from Martayan et al. (2007), while with gray small dots we present the OGLE-II stars that lie in our *Chandra* field 4 and have < 0.2 magnitude errors in the V and B band (Antoniou et al. 2008a). The MS, the red giant branch and the red clump loci are clearly shown.

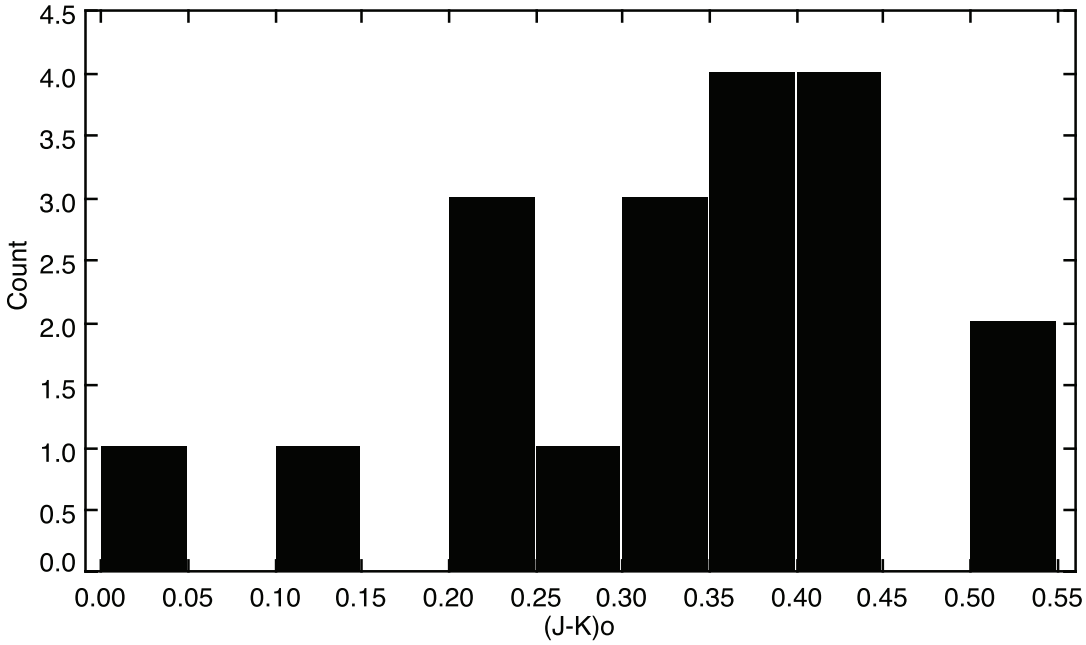

Figure 6.6 Histogram of (J-K)o values of the Be-XRBs from this sample.

Most Be stars exhibit infrared excess (Gehrz, Hackwell & Jones 1974) due to the disk contribution to the continuum emission. Several authors have observed a similar excess (e.g. Negueruela & Coe 2002). In Table 6.5 we give the infrared counterparts of the Be-XRBs studied here based on the 2MASS catalog (Skrutskie et al. . 2006). Column [1] presents the X-ray source ID, Column [2] the closest 2MASS counterpart ID within $5''$ from the X-ray source position, and Columns [3], [5], and [7] the J, K magnitudes, and (J-K) color, respectively. In Columns [4], [6], and [8] we give the errors of the aforementioned quantities. Column [9] lists the (J-K)o color derived from extinction corrected (J-K) color, assuming E(J-K)=0.56E(B-V) (Bessell & Brett 1988), and E(B-V)=0.09 (as in all the study). In Figure 6.6 we present the distribution of the (J-K)o color of Be-XRBs from this sample (shown in black). In comparison, OB main sequence stars (Binney & Merrifield 1998) have $-0.3 \leq (J-K)_o \leq -0.05$. Three sources (5_2, XMM_3, and XMM_7) are not included in the above figure because of their uncertain derived magnitudes given in the 2MASS catalog. Therefore, it is obvious that all Be-XRBs from this study with 2MASS measurements show infrared excess with respect to normal OB stars.

There is a known correlation of Hα EW and the (J-K) color as both are indicators of the size

Table 6.5. Infrared counterparts of our 2dF Be-XRB sample

X-ray Src ID†	2MASS ID‡	J	errJ	K	errK (mag)	JK	errJK	(J-K)o
[1]	[2]	[3]	[4]	[5]	[6]	[7]	[8]	[9]
3_3 (XMM_33)	J00573602-7219341	15.74	0.07	15.33	0.20	0.40	0.21	0.35
4_1	J00504470-7316054	15.30	0.05	14.81	0.11	0.49	0.12	0.44
4_5 (XMM_9)	J00492984-7310583	15.59	0.11	15.01	0.16	0.57	0.20	0.52
4_8	J00481410-7310045	15.017	0.06	14.69	0.12	0.33	0.14	0.28
5_16	J00535518-7226448	14.41	0.04	14.00	0.07	0.41	0.08	0.36
5_2	J00532381-7227152	16.27	0.11	16.51	···	-0.23	···	-0.28
5_4	J00544633-7225228	15.29	0.06	14.84	0.12	0.45	0.14	0.40
5_7 (XMM_30)	J00545618-7226478	15.18	0.05	15.01	0.13	0.17	0.14	0.12
6_1	J00520896-7238032	14.63	0.03	14.21	0.06	0.42	0.07	0.37
6_2	J00545586-7245108	14.77	0.04	14.403	0.07	0.37	0.08	0.32
6_4	J00525230-7248301	14.24	0.05	13.98	0.08	0.26	0.09	0.21
XMM_14	J00505713-7310080	14.44	0.04	14.04	0.06	0.41	0.07	0.36
XMM_15	J00505698-7213343	14.84	0.04	14.37	0.07	0.47	0.08	0.42
XMM_17	J00515203-7310340	14.43	0.03	14.17	0.07	0.26	0.08	0.21
XMM_3	J00472330-7312275	15.88	0.10	14.84	···	1.04	···	0.99
XMM_39	J01003000-7220335	14.50	0.04	14.13	0.07	0.37	0.07	0.32
XMM_47	J01043544-7221485	14.99	0.03	14.53	0.10	0.47	0.10	0.42
XMM_5	J00483409-7302312	14.70	0.05	14.44	0.08	0.27	0.09	0.22
XMM_7	J00491360-7311378	16.11	0.09	15.88	···	0.23	···	0.18
5_12	J00524508-7228437	14.97	0.05	14.90	0.12	0.07	0.13	0.02

†The X-ray source ID corresponds to *Chandra* sources as given in Antoniou et al. (2008a; (Field ID)_(Src ID within the field)). The XMM ID refers to sources from Haberl & Pietsch (2004). This also explains why there is different accuracy in the coordinates of the X-ray sources.

‡Closest counterpart within 5″ from the X-ray source position, with only exception the 2MASS counterpart of source XMM_47 that was found within 6″ from the X-ray source position.

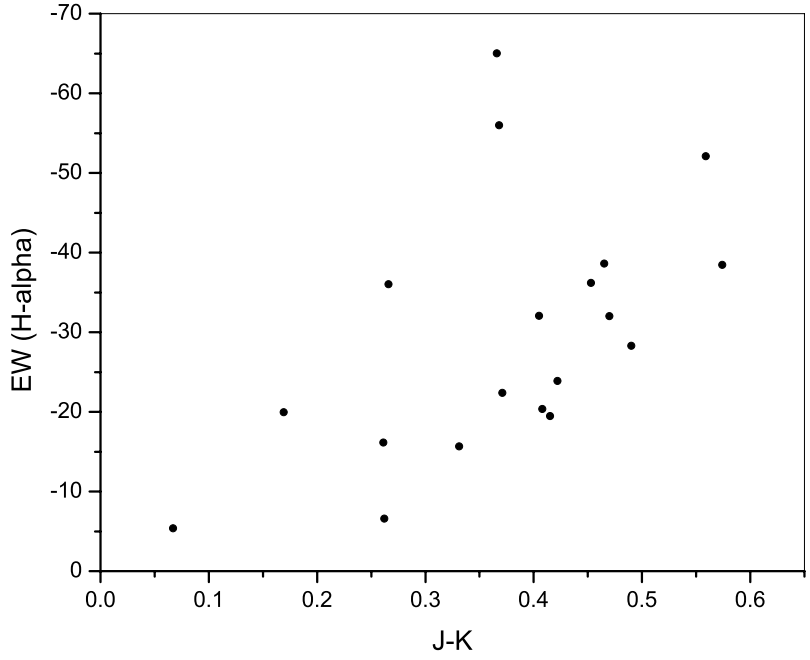

Figure 6.7 A (J-K) color versus EW(Hα) plot for the 2dF Be-XRB sample.

of the circumstellar disc (e.g. Coe et al. 2005). Using the Hα EW measurements presented in Table 6.2 and the (J-K) from Table 6.5, we construct the (J-K) color versus EW(Hα) plot (shown in Figure 6.7). We see that these quantities, that are both used as constraints for the size of the circumstellar disc, are correlated. However, we note that these objects are not observed simultaneously in the optical and the infrared. As noted in a similar study by Coe et al. (2005), usually high values in Hα will not match the IR colors taken at some other epoch. This can account, at least qualitatively, for the relatively large scatter in the plot.

6.4.3 Optical variability

The long-term (multiyear) optical light curves of Be stars show high variability (e.g. Mennickent et al. 2002). Multiyear optical light curves for SMC, LMC, and Milky Way sources can be found in the OGLE-II[2] (Udalski, Kubiak & Szymański 1997; Zebruń et al. 2001) and MACHO[3]

[2]http://ogle.astrouw.edu.pl/

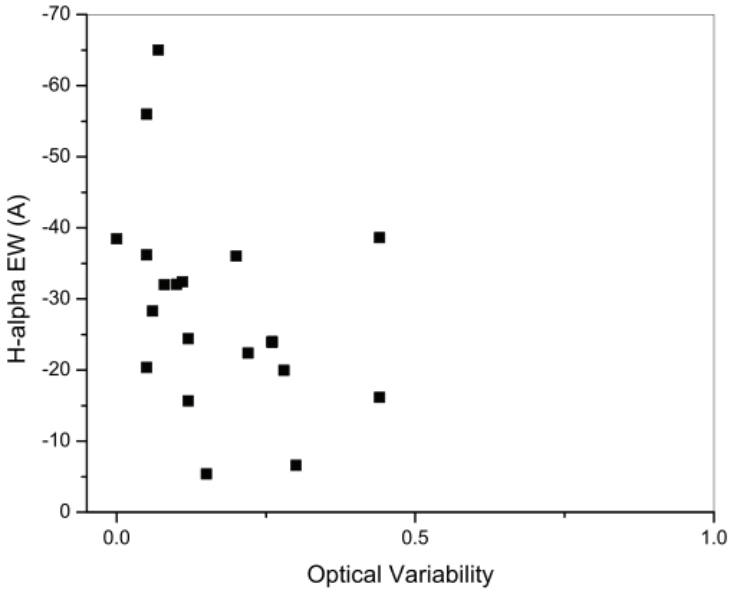

Figure 6.8 Estimated variability from the OGLE-II and MACHO light curves for our 2dF sample against the Hα equivalent width.

database (Alcock et al. 1999). Some show clear periodic outbursts, others exhibit a slow change in mean brightness, and some show extreme variability with swoops and dips that may last months or years: in such studies, the challenge is to find any underlying periodic behavior that persists even through the long-term changes (Schmidtke et al. 2004).

We also investigated the optical photometric variability of our 2dF Be-XRB sample. In the appendix (Figure D.1) we present the I band light curves from the OGLE-II database. For 4 out of the 20 Be-XRBs we present the light curves from the MACHO database (Figure D.2) because these X-ray sources do not have counterparts in the OGLE-II catalog. We find that most of our objects are indeed variable to some degree (typical ~ 0.2 mag). There is a suggested correlation between long-term photometric variability and Hα EW (e.g. Coe et al. 2005). We visually estimated the variability from the OGLE-II and MACHO light curves of our objects. We plot in Figure 6.8 this estimate of the variability against the Hα EW. Despite the large scatter, the behavior is very similar to that found by Coe et al. (2005). Therefore, the optical variability of our objects is broadly consistent with Be-XRBs.

[3]http://wwwmacho.mcmaster.ca/Data/MachoData.html

6.4.4 The second supergiant X-ray binary discovered in the SMC

Chandra source CXOU J005252.2-724830 (Zezas et al. 2008; 6_4 in the text) is within the 40″ error circle (90% confidence) of Einstein IPC source 2E 0051.1-7304 (No.31 in the catalogue of Wang & Wu 1992). It was not detected in the ROSAT HRI & PSPC observations, while it has a maximum observed L_x of about 1.6×10^{35}ergs^1 and coincides with the emission-line object [MA93]618 (Haberl & Sasaki 2000). Zezas et al. (2008) detected CXOU J005252.2-724830 with an unabsorbed L_x of 1.35×10^{34}ergs^{-1} in the (0.5-7.0) keV energy band. Antoniou et al. (2008a) indicated a possibly hard X-ray spectrum (not certain due to low number of counts, thus large errors), and found an early-type counterpart (OGLE-II source 6_147662, same as MCPS source Z_2423181; Udalski et al. 1998 and Zaritsky et al. 2002, respectively). OGLE-II source 6_147662 has a 0.27″offset from the X-ray source and it has a V band magnitude of 14.42 ± 0.05 and a B-V color of -0.10 ± 0.05 mag, which is marginally consistent with a supergiant. Moreover, its optical I band light curve (from OGLE-II) is highly variable (Figure D.1 in the appendix): it increased its luminosity by 0.33 ± 0.01 mag in about 2 years.

OGLE-II source 6_147662 has an optical spectrum very similar to HD93129A that has been classified as O3If* by Walborn (1977). The notation "f*" means NIV λ4058 emission stronger than NIII $\lambda 4634 - 4640 - 4642$, while all known Of* objects have weak SiIV emission in their spectra (Walborn 1977). The strong NIV λ4058 emission is the most prominent feature of source 6_4 in the blue portion of its optical spectrum ($3800 - 5000\mathring{A}$; Figure 6.3). In its normalized spectrum we have also marked the Hϵ λ3970, Hδ λ4101, and HeI λ4144 lines, while the Hγ λ4340, and Hβ λ4861 are also seen in absorption. Because of the presence of the emission line NIV λ4058, we classify source 6_4 as an O3If*. In any case, based only on the absorption lines, the star is classified as an O star.

This is only the second supergiant X-ray binary (SG/XRB) that has been discovered in the SMC. The other known source of this class is SMC X-1 (Webster et al. 1972), located in the eastern wing of the SMC. Nagase (1989) discovered SMC X-1 as an X-ray pulsar with 0.72s pulse period, 3.89d orbital period, while it has been identified as a B0Ib supergiant (optical companion source Sk 160; Sanduleak 1968). Bradt & McClintock (1983) found an L_x of $\sim 6 \times 10^{38}$ergs^1 in the 2-11keV band (derived from the maximum observed flux density). Sk 160 has V$\sim$ 13.3mag, (B-V)~ -0.14, and (U-B)~ -0.98.

6.4.5 The peculiar optical spectrum of X-ray source AX J0051-722

Corbet et al. (1998) reported the detection of source AX J0051-722, a new transient X-ray pulsar detected with ASCA. Source AX J0051-722 (=XMM_15 in the text) is located at R.A.=0h51m04s, Decl.=-72°13′44″ (equinox 2000.0; ±1.2′, 90% confidence) with a 2-10keV flux of 1.05×10^{-11} ergs^{-1}cm−2, while it exhibits 91.12s (±0.05s) pulsations. A ROSAT HRI observation on 1997 Dec. 11 detected AX J0051-722 at R.A. = 0h50m55s.8, Decl. =-72°13′38″ (±10″; Corbet et al. 1998). AX J0051-722 was not detected by the ROSAT PSPC (Haberl et al. 2000), while it is found as source 37 in the ROSAT HRI catalog (Sasaki, Haberl & Pietsch 2000). Haberl & Sasaki (2000) found only the emission-line object [MA93]413 within the ASCA error circle. Thus, source AX J0051-722 was listed as an optically identified Be-XRB. On the other hand, the brightest source in the reduced error circle of ROSAT was observed at the red portion of the optical spectrum (6295-7042Å) by Stevens, Coe & Buckley (1999). They identified this source as a Be star based on strong Hα emission (EW= $-22\mathring{A}$), and a V band magnitude of ~ 15 that was derived from Digitised Sky Survey images (because of lack of photometric data).

We propose here for the first time MCPS source Z-2158744 (Zaritsky et al. 2002) as the optical counterpart of AX J0051-722 (see Table 6.4). It is located 3.22″ from the center of AX J0051-722 as given in the census of Haberl & Pietsch 2004 (R.A. = 0h50m56s.9, Decl. =-72°13′31″, with ±7.1″). Z-2158744 has a V band magnitude of 15.06 ± 0.06 and a B-V color of -0.08 ± 0.06 mag. In Figure 6.3 we present the blue portion ($3800 - 5000\mathring{A}$) of its optical spectrum. We see Hϵ λ3970, and Hδ λ4101 in absorption, while Hγ λ4340 is weak (probably filled in by emission), and Hβ λ4861 is in emission. Hβ is the most prominent feature of this blue part of the spectrum. Souce Z-2158744 has also HeI $\lambda 4144, 4387, 4471$ and the blend OII + CIII $\lambda 4640 - 4650$, as well as OII λ4367 lines in absorption. Based on the relative ratio of OII λ4367 and Hγ λ4340, we estimate that the star is probably a B1-1.5Ia+, according to Walborn & Fitzpatrick (1990). However a ~ 15 V band magnitude prevents us from making a firm identification with a supergiant, and thus we classify the optical counterpart of X-ray source AX J0051-722 as a B0-2 star with peculiar spectrum. Further observations of this source are needed (i.e. with higher spectral resolution) in order to assign a more definite classification.

6.5 Conclusions

We presented a comprehensive optical spectroscopic study of 20 High-Mass X-ray Binaries (HMXBs) in the Small Magellanic Cloud using the 2dF (Two-degree Field) spectrograph on the 3.9m Anglo-Australian Telescope (AAT). In this study we have used the 2dF spectrograph to confirm the classification of candidate Be-XRBs as emission line stars and identify the spectral type and luminosity class when possible. Our sample was selected from the *Chandra* survey (Zezas et al. 2008, Antoniou et al. 2008a) and it also included candidate and known Be-XRBs from the census of Haberl & Pietsch 2004 (an *XMM-Newton* survey).

Eighteen of the 20 stars were confirmed to be Be-XRBs with spectral classes from B0 to B2, plus one B3-5. One more object shows a peculiar B0-2 spectrum, probably suggesting a supergiant, although the absolute visual magnitude of the star is not consistent with a supergiant. A further object (OGLE-II source 6_147662) is an O star, with clear Hα emission, as well as broad NIV λ4058 emission, suggestive of O3If* spectral type. Photometric data are marginally consistent with a supergiant. Therefore, we have proposed source CXOU J005252.2-724830 (6_4 in the text; optical counterpart OGLE-II source 6_147662) to be the second recorded supergiant X-ray binary in the SMC, the first one being SMC X-1 (Webster et al. 1972).

The distribution of spectral types of the 18 confirmed Be-XRBs show a peak at B1.5. It is similar to the spectral distribution of LMC Be-XRBs, while when compared to the Milky Way, later than B4-B5 spectral types are "missing". Coe et al. (2005) has suggested that this could be attributed to the different metallicities of the two galaxies, and maybe to the tidal interaction of the Magellanic Clouds. For the observed difference in the spectral distributions of field Be stars and Be stars in X-ray binaries, Negueruela (1998) concluded that it must reflect a real difference in the populations from which these samples are drawn.

All objects show infrared excess as expected from Be-XRBs due to the presence of the circumstellar disk. Moreover, there is a clear correlation between the Hα EW and the $(J-K)_o$ color. Finally, we investigated the optical variability of the objects, using the OGLE-II and MACHO databases, and we found variability broadly consistent with that seen in Be-XRBs (Schmidtke et al. 2004).

We would like to thank Dr. A. Udalski for providing unpublished light curves of the OGLE-II stars used in this study, and Rob Sharp for performing the 2dF observing run during service time. VA acknowledges support from Marie Curie grant no. 39965 to the Foundation for Research and Technology - Hellas, and NASA LTSA grant NAG5-13056. This paper utilizes public domain data originally obtained by the MACHO Project, whose work was performed under the joint auspices of the U.S. Department of Energy, National Nuclear Security Administration by the University of California, Lawrence Livermore National Laboratory under contract No. W-7405-Eng-48, the National Science Foundation through the Center for Particle Astrophysics of the University of California under cooperative agreement AST-8809616, and the Mount Stromlo and Siding Spring Observatory, part of the Australian National University. This study also makes use of data products from the Two Micron All Sky Survey, which is a joint project of the University of Massachusetts and the Infrared Processing and Analysis Center/California Institute of Technology, funded by the National Aeronautics and Space Administration and the National Science Foundation."

Bibliography

[1] Antoniou, V., Zezas, A., Hatzidimitriou, D., McDowell, J. 2008a, Astrophys. J., submitted

[2] Ashok, N. M., Bhatt, H. C., Kulkarni, P. V., & Joshi, S. C. 1984, Mon. Not. R. Astr. Soc., 211, 471

[3] Bessell, M. S., & Brett, J. M. 1988, Pub. Astr. Soc. Pacific., 100, 1134

[4] Binney, J., & Merrifield, M. 1998, Galactic astronomy / James Binney and Michael Merrifield. Princeton, NJ : Princeton University Press, 1998. (Princeton series in astrophysics) QB857 .B522 1998

[5] Bradt, H. V. D., & McClintock, J. E. 1983, Ann. Rev. Astron. Astrophys., 21, 13

[6] Buckley, D. A. H., Coe, M. J., Stevens, J. B., van der Heyden, K., Angelini, L., White, N., & Giommi, P. 2001, Mon. Not. R. Astr. Soc., 320, 281

[7] Coe, M. J., Haigh, N. J., Laycock, S. G. T., Negueruela, I., & Kaiser, C. R. 2002, Mon. Not. R. Astr. Soc., 332, 473

[8] Coe, M. J., Edge, W. R. T., Galache, J. L., & McBride, V. A. 2005, Mon. Not. R. Astr. Soc., 356, 502

[9] Coe, M. J., & Orosz, J. A. 2000, Mon. Not. R. Astr. Soc., 311, 169

[10] Corbet, R., Marshall, F. E., Lochner, J. C., Ozaki, M., & Ueda, Y. 1998, IAU Circ., 6803, 1

[11] Crowl, H. H., Sarajedini, A., Piatti, A. E., Geisler, D., Bica, E., Clariá, J. J., & Santos, J. F. C., Jr. 2001, Astron. Journ., 122, 220

[12] Dickey, J. M., & Lockman, F. J. 1990, Ann. Rev. Astron. Astrophys., 28, 215

[13] Edge, W. R. T., & Coe, M. J. 2003, Mon. Not. R. Astr. Soc., 338, 428

[14] Edge, W. R. T., Coe, M. J., Galache, J. L., McBride, V. A., Corbet, R. H. D., Markwardt, C. B., & Laycock, S. 2004, Mon. Not. R. Astr. Soc., 353, 1286

[15] Evans, C. J., Howarth, I. D., Irwin, M. J., Burnley, A. W., & Harries, T. J. 2004, Mon. Not. R. Astr. Soc., 353, 601

[16] Gehrz, R. D., Hackwell, J. A., & Jones, T. W. 1974, Astrophys. J., 191, 675

[17] Haberl, F., Filipović, M. D., Pietsch, W., & Kahabka, P. 2000, Astr. Astrophys. Suppl., 142, 41

[18] Haberl, F., & Sasaki, M. 2000, Astr. Astrophys., 359, 573

[19] Haberl, F., & Pietsch, W. 2004, Astr. Astrophys., 414, 667

[20] Haberl, F., Pietsch, W., Schartel, N., Rodriguez, P., & Corbet, R. H. D. 2004, Astr. Astrophys., 420, L19

[21] Harries, T. J., Hilditch, R. W., & Howarth, I. D. 2003, Mon. Not. R. Astr. Soc., 339, 157

[22] Harris, J., & Zaritsky, D. 2004, Astron. Journ., 127, 1531

[23] Hilditch, R. W., Howarth, I. D., & Harries, T. J. 2005, Mon. Not. R. Astr. Soc., 357, 304

[24] Lennon, D. J. 1997, Astr. Astrophys., 317, 871

[25] Lewis, I. J., et al. 2002, Mon. Not. R. Astr. Soc., 333, 279

[26] Liu, Q. Z., van Paradijs, J., & van den Heuvel, E. P. J. 2005, Astr. Astrophys., 442, 1135

[27] Macomb, D. J., Fox, D. W., Lamb, R. C., & Prince, T. A. 2003, Astrophys. J. Lett., 584, L79

[28] McSwain, M. V., & Gies, D. R. 2005, Astrophys. J. Suppl., 161, 118

[29] McSwain, M. V., Huang, W., Gies, D. R., Grundstrom, E. D., & Townsend, R. H. D. 2008, Astrophys. J., 672, 590

[30] Mennickent, R. E., Pietrzyński, G., Gieren, W., & Szewczyk, O. 2002, Astr. Astrophys., 393, 887

[31] Meyssonnier, N., & Azzopardi, M. 1993, Astr. Astrophys. Suppl., 102, 451

[32] Nagase, F. 1989, Pub. Astr. Soc. Japan., 41, 1

[33] Negueruela, I., & Coe, M. J. 2002, Astr. Astrophys., 385, 517

[34] Sanduleak, N. 1968, Astron. Journ., 73, 246

[35] Sasaki, M., Haberl, F., & Pietsch, W. 2000, Astr. Astrophys. Suppl., 147, 75

[36] Sasaki, M., Pietsch, W., & Haberl, F. 2003, Astr. Astrophys., 403, 901

[37] Schmidtke, P. C., Cowley, A. P., Crane, J. D., Taylor, V. A., McGrath, T. K., Hutchings, J. B., & Crampton, D. 1999, Astron. Journ., 117, 927

[38] Schmidtke, P. C., Cowley, A. P., & Levenson, L. 2003, Astron. Journ., 126, 1017

[39] Schmidtke, P. C., Cowley, A. P., Levenson, L., & Sweet, K. 2004, Astron. Journ., 127, 3388

[40] Schurch, M. P. E., et al. 2007, Mon. Not. R. Astr. Soc., 381, 1561

[41] Skrutskie, M. F., et al. 2006, Astron. Journ., 131, 1163

[42] Smith, R. C., Kirshner, R. P., Blair, W. P., Long, K. S., & Winkler, P. F. 1993, Astrophys. J., 407, 564

[43] Stevens, J. B., Coe, M. J., & Buckley, D. A. H. 1999, Mon. Not. R. Astr. Soc., 309, 421

[44] Udalski, A., Szymanski, M., Kubiak, M., Pietrzynski, G., Wozniak, P., & Zebrun, K. 1998, Acta Astronomica, 48, 147

[45] van den Bergh, S. 2000, The galaxies of the Local Group, by Sidney Van den Bergh. Published by Cambridge, UK: Cambridge University Press, 2000 Cambridge Astrophysics Series Series, vol no: 35

[46] Walborn, N. R. 1977, Astrophys. J., 215, 53

[47] Wang, Q., & Wu, X. 1992, Astrophys. J. Suppl., 78, 391

[48] Webster, B. L., Martin, W. L., Feast, M. W., & Andrews, P. J. 1972, Nature, 240, 183

[49] Zaritsky, D., Harris, J., Thompson, I. B., Grebel, E. K., & Massey, P. 2002, Astron. Journ., 123, 855

Chapter 7

Conclusions and future work

7.1 An overview of the presented work

We presented the analysis of shallow ($\sim$ 10 ksec) *Chandra* observations of the central part of the SMC (Chapter 2). We detect a total of 158 discrete X-ray sources down to a detection limit of 4×10^{33} erg s^{-1}. Of those only 27 sources are found to be associated with early-type stars in the SMC (Antoniou et al. 2008a). From the spectral characteristics and luminosity function of the X-ray sources associated with early-type stars we found that:

- They have hard X-ray spectra typical of pulsar X-ray binaries.
- There is a trend for lower-luminosity sources to have softer spectra, which is consistent with a weaker accretion component and a stronger relative contribution of thermal emission from the surface of the neutron star.
- Their X-ray luminosity function can be represented by a flat power-law with a cumulative slope of $(0.35^{+0.12}_{-0.11})$. There is also an indication for a break at $\sim 10^{35}$ erg s^{-1}, with low and high luminosity cumulative slopes of ~ 0.6 and ~ 0.18, respectively.
- The high end of the XLF is consistent with the XLFs observed in other star-forming galaxies.

- The flattening of the XLF can be explained in terms of the standard Be-XRB model, where the pulsar undergoes intermittent accretion episodes during its passage through the decretion disk of the donor. The transition between the accretion and quiescent phase can be quite sharp resulting in a "desert range" on their XLF.

- There is indication for a steepening of the XLF in low luminosities ($< 10^{34}$ erg s^{-1}) which, in combination with the softer spectra of the low-luminisity sources, indicates that we are observing the brightest quiescent X-ray binaries.

Moreover, we presented the results for the optical counterparts of the 153 X-ray sources detected in the *Chandra* survey of the central region of the SMC (Chapter3). For 120 sources we found optical matches in the OGLE-II and/or MCPS catalogs. Using the photometric data of these counterparts and the spectral and timing properties of the X-ray sources we propose the most likely optical counterpart for 113 *Chandra* sources, while for 7 sources the candidate counterparts are equally likely. In particular:

- We find that 52 X-ray sources have a single counterpart, 68 have two or more matches, while 33 sources do not have counterpart in either OGLE-II or MCPS catalog within the 1σ search radius (7 out of these 33 sources have bright optical matches ($M_{V_o} \leq -0.25$) between the 1σ and 2σ search radii, but none of them is associated with an OB star).

- Early type counterparts (of OB spectral type) have been identified for 32 X-ray sources (chance coincidence probability $\leq 19\%$). Based on spectroscopic observations of stars in the SMC we define the photometric locus of early type (OB) stars in the M_{V_o} vs. $(B-V)_o$ CMD. Based on the position on the CMD and their X-ray spectral properties, we propose: (a) 9 new candidate Be-XRBs, and (b) 2 new candidate HMXBs. In addition, we find 3 sources with hard X-ray spectra and an OB star counterpart within their 2σ search radius.

- Based on the isochrones of Lejeune & Schaerer (2001), we estimate the age of the 11 new candidate Be-XRBs and HMXBs to be $\sim 15 - 85$ Myr, in agreement with the age of Be stars.

- Eighteen X-ray sources with bright counterparts ($M_{V_o} \leq -0.25$) could not be classified, because we do not have X-ray spectral information for them and/or they have other than OB spectral type counterparts.

- We find that the mixing of Be-XRBs with other than their natal stellar population is not an issue in our comparisons of Be-XRBs and stellar populations in the SMC, because the SF activity across the SMC "bar" is generally uniform in scales larger than the size of the *Chandra* fields. Instead we find indication for variation in the XRB populations across the "bar" and in scales of ~ 1 kpc: fields with higher SF rate at ages which are more prone to produce Be stars show increased number of Be-XRBs.

- Using the catalogs of Liu et al. (2005, 2006) we find that for luminosities down to $L_X \sim 10^{34}$ erg s^{-1} (chosen as a moderate minimum cut-off between different SMC and Galactic X-ray surveys) the *Chandra* SMC fields contain ~ 2 times more Be-XRBs in comparison to the Milky Way (including 7 new candidate Be-XRBs from this study), even after taking into account the different OB star formation rates in the two galaxies. This residual excess can be explained when we account for the different metallicity of the SMC and the Milky Way. This is in good agreement with the factor of ~ 3 derived from population synthesis studies (Dray 2006), and the study of Wisniewski & Bjorkman (2006).

In addition, we present the analysis of *XMM-Newton* observations (Chapter 4) of the outer part of the SMC selected to sample stellar populations in a range of ages ($\sim 10 - 500$ Myr; Fig 4.2) based on the SF history of Harris & Zaritsky (2004). We detected 186 sources down to a limiting luminosity of $\sim 3.5 \times 10^{33}$ erg s^{-1} in the 0.2-12 keV energy band. From the cross-correlation of the *XMM-Newton* sources and MCPS stars (Zaritsky et al. 2002), and hardness ratios analysis, we propose 7 new candidate Be-XRBs in our *XMM-Newton* fields (following the analysis of Antoniou et al. 2008a; Chapter 3). We have also detected one more Be-XRB, previously identified. Thus, the total number of Be-XRBs (confirmed and candidate) in the *XMM-Newton* fields is 8.

Using *Chandra*, *XMM-Newton* and optical photometric catalogs we study the young X-ray binary (XRB) populations of the SMC (Chapter 5). We find that the Be/X-ray binaries (Be-XRBs) are observed in regions with star-formation (SF) rate bursts $\sim 30 - 70$ Myr ago, which coincides with the age of maximum Be-star formation. We also find strong evidence for a correlation of the number of Be-XRBs with the strength of the SF at the age of maximum Be-star formation, i.e. ~ 40 Myr ago, while regions with strong but more recent SF (e.g. the Wing) are deficient in Be-XRBs. Regions that host HMXBs, which however have not been proved yet to be Be-XRBs,

show a similar SF episode (at $\sim$ 40 Myr ago). We conclude that the majority of the optically unidentified SMC HMXBs have a Be nature. Small kicks imparted on the compact object during the supernova explosion are also implied. This is the first study which demonstrates the importance of the Be-XRBs as a dominant component of young XRB populations.

We presented a comprehensive optical spectroscopic study of 20 High-Mass X-ray Binaries (HMXBs) in the SMC (Chapter 6) using the 2dF (Two-degree Field) spectrograph on the 3.9m Anglo-Australian Telescope (AAT). In this study we have used the 2dF spectrograph to confirm the classification of candidate Be-XRBs as emission line stars and identify the spectral type and luminosity class when possible. Our sample was selected from the *Chandra* survey (Zezas et al. 2008, Antoniou et al. 2008a) and it also included candidate and known Be-XRBs from the census of Haberl & Pietsch 2004 (an *XMM-Newton* survey).

Eighteen of the 20 stars were confirmed to be Be-XRBs with spectral classes from B0 to B2, plus one B3-5. One more object shows a peculiar B0-2 spectrum, probably suggesting a supergiant, although the absolute visual magnitude of the star is not consistent with a supergiant. A further object (OGLE-II source 6_147662) is an O star, with clear Hα emission, as well as broad NIV λ4058 emission, suggestive of O3If* spectral type. Photometric data are marginally consistent with a supergiant. Therefore, we have proposed source CXOU J005252.2-724830 (6_4 in the text; optical counterpart OGLE-II source 6_147662) to be the second recorded supergiant X-ray binary in the SMC, the first one being SMC X-1 (Webster et al. 1972).

The distribution of spectral types of the 18 confirmed Be-XRBs show a peak at B1.5. It is similar to the spectral distribution of LMC Be-XRBs, while when compared to the Milky Way, later than B4-B5 spectral types are "missing". Coe et al. (2005) has suggested that this could be attributed to the different metallicities of the two galaxies, and maybe to the more recent star-formation of the SMC. For the observed difference in the spectral distributions of field Be stars and Be stars in X-ray binaries, Negueruela (1998) concluded that it must reflect a real difference in the populations from which these samples are drawn.

All objects show infrared excess as expected from Be-XRBs due to the presence of the circumstellar disk. Moreover, there is a clear correlation between the Hα EW and the $(J-K)_o$ color. Finally, we investigated the optical variability of the objects, using the OGLE-II and MACHO

databases, and we found variability broadly consistent with that seen in Be-XRBs (Schmidtke et al. 2004).

7.2 Relevant Future work

7.2.1 Analysis of high quality optical photometric data

In order to derive a more accurate star-formation history for the central most active parts of the SMC, we need optical data of high astrometric and photometric accuracy. We have obtained $BVRI$ imaging data with the IMACS camera at the 6.5m Baade Magellan Telescope (at Las Campanas, Chile) for 5 fields, covering the area of the *Chandra* survey of Zezas et al. (2008; described in Chapter 2). For these data, we have obtained an astrometric solution with a rms error of $\sim 0.2''$, when compared to the 2MASS astrometry. Using these accurate positions, I plan to:

- Obtain unique counterpart for X-ray sources, which are currently associated with more than one optical sources (due to the large positional uncertainties of the catalogs used in this study).
- Identify counterparts for X-ray sources currently unidentified. This way I will study the nature of the complete X-ray source populations and possibly identify active stars and/or the elusive LMXBs in the SMC.

  Based on the high quality 4-band photometric data for these fields I will:

- Derive an accurate star-formation history for the intermediate age populations ($<$ 100Myr ago).
- Study in more detail the correlation between the star-formation history and the number of Be-XRBs in the *Chandra* fields.

These star-formation histories will provide a more detailed picture of the connection at the age range $\sim 20 - 70$Myr, where strong evolution of the X-ray binary populations has been observed (Antoniou et al. 2005).

7.2.2 Investigate the Be nature of currently candidate SMC Be-XRBs

I plan to follow-up spectroscopically the remaining candidate Be-XRBs from *Chandra* and *XMM-Newton* surveys performed so far. This way, we will obtain a more complete and more accurate picture of the companion star in the XRB population of the SMC. For example, as it was shown in Chapter 6, although Be counterparts have been suggested for 20 X-ray binaries, selected to be observed with the 2dF spectrograph at the AAT, 2 were proved to have different spectra. One was proposed here as the second supergiant XRB in the SMC. With these observations I will search for more missed supergiant-XRBs and I will study the spectral types and luminosity classes of the complete set of known Be-XRBs in the SMC, in the context of similar systems in the Galaxy and the LMC (which have different metallicity and star-formation history).

7.2.3 Optical identification of X-ray sources in the *Chandra* deep fields

Two years ago, we have obtained deep ($\sim$ 100ks) *Chandra* follow-up observations of two of our shallow *Chandra* fields. These data will give a unique opportunity to study the very faint end of the X-ray source populations (including quiescent X-ray binaries and even normal stars). I plan to perform cross-correlation analysis with the high quality IMACS photometric and astrometric data. Identifying the optical counterpart with such a positional accuracy, will allow us to follow-up these targets spectroscopically, and thus, determining the nature of the X-ray sources.

I also plan to extend the above work in the Large Magellanic Cloud, thus examining the effects of different metallicity and/or different star-formation episodes in the X-ray binary populations.

Appendices

Appendix A

Properties of *Chandra* X-ray sources

We present the properties of the *Chandra* X-ray sources from Chapter 1.

Table A.1 FIELD 3: Master Source List

Src_ID	Source Name	R.A.	Dec.	Obs.	Eff.Area	Bkg.	Area	Net	Significance	Off axis	Lx^{un}
	CXOUJ...	(J2000)	(J2000)	Counts	Ratio	Counts	Ratio	Counts	(σ)		
(1)	(2)	(3)	(4)	(5)	(6)	(7)	(8)	(9)	(10)	(11)	(12)
1	005719.83-722534.0	00 57 19.83	-72 25 34.0	335	0.96	115	1.34	$349.98^{+18.39}_{-19.67}$	17.26	6.69	15.32
2	005527.69-721058.7	00 55 27.69	-72 10 58.7	270	0.93	191	1.65	$285.06^{+18.28}_{-16.70}$	15.29	4.98	12.26
3	005736.00-721933.9	00 57 36.00	-72 19 33.9	117	0.88	169	0.11	$132.75^{+12.16}_{-12.28}$	9.86	5.72	5.37
4	005732.70-721302.4	00 57 32.70	-72 13 2.4	95	0.90	201	0.37	$105.21^{+9.72}_{-11.69}$	8.74	7.92	4.33
5	005816.75-721805.5	00 58 16.75	-72 18 5.5	93	0.94	342	0.57	$96.68^{+10.25}_{-10.12}$	8.52	8.17	4.18
6	005641.62-722026.4	00 56 41.62	-72 20 26.4	30	0.97	205	0.04	$30.15^{+6.17}_{-4.99}$	4.57	4.67	1.38
7	005723.77-722357.0	00 57 23.77	-72 23 57.0	33	0.85	125	0.49	$37.52^{+6.77}_{-6.52}$	4.76	6.17	1.49
8	005640.86-721704.3	00 56 40.86	-72 17 4.3	26	0.95	201	0.06	$26.48^{+5.94}_{-4.64}$	4.19	10.18	1.19
9	005652.52-721203.3	00 56 52.52	-72 12 3.3	27	0.97	141	0.40	$27.34^{+5.06}_{-5.54}$	4.22	6.76	1.22
10	005541.64-721809.2	00 55 41.64	-72 18 9.2	16	0.85	199	0.16	$18.16^{+4.69}_{-4.57}$	3.08	3.00	0.72
11	005534.02-721840.1	00 55 34.02	-72 18 40.1	15	0.87	120	0.32	$16.18^{+4.94}_{-3.87}$	2.94	4.02	0.67
12	005713.29-722358.5	00 57 13.29	-72 23 58.5	16	0.94	162	0.28	$16.30^{+4.11}_{-4.23}$	3.05	6.41	0.71
13	005721.03-722406.1	00 57 21.03	-72 24 6.1	12	0.73	135	0.32	$15.49^{+4.59}_{-4.67}$	2.53	3.34	0.53
14	005759.81-721620.1	00 57 59.81	-72 16 20.1	11	0.91	192	0.30	$10.86^{+3.89}_{-3.23}$	2.35	6.23	0.48
15	005744.41-722215.5	00 57 44.41	-72 22 15.5	11	0.92	155	0.33	$11.17^{+3.57}_{-3.53}$	2.37	4.71	0.48
16	005848.09-722446.5	00 58 48.09	-72 24 46.5	17	0.90	134	2.84	$13.68^{+5.25}_{-3.83}$	2.53	4.60	0.61
17	005722.95-721757.8	00 57 22.95	-72 17 57.8	8	0.84	169	0.10	$9.45^{+3.00}_{-3.60}$	1.98	9.74	0.36
18	005605.42-722159.3	00 56 5.42	-72 21 59.3	7	0.43	161	0.13	$14.75^{+6.49}_{-5.41}$	1.79	6.34	0.31
19	005713.14-721045.3	00 57 13.14	-72 10 45.3	12	0.88	152	0.63	$12.39^{+3.83}_{-3.93}$	2.41	4.51	0.51
20	005726.21-721648.6	00 57 26.21	-72 16 48.6	7	0.89	192	0.06	$7.33^{+3.15}_{-2.64}$	1.82	6.41	0.32
21	005611.79-721938.5	00 56 11.79	-72 19 38.5	7	1.00	156	0.13	$6.38^{+2.86}_{-2.31}$	1.80	5.65	0.31
22	005607.77-721133.2	00 56 7.77	-72 11 33.2	8	0.90	193	0.28	$8.08^{+2.95}_{-3.17}$	1.89	1.83	0.34
23	005656.83-721523.2	00 56 56.83	-72 15 23.2	5	0.98	168	0.05	$4.51^{+2.49}_{-1.89}$	1.45	4.08	0.23
24	005647.33-722250.9	00 56 47.33	-72 22 50.9	5	0.86	138	0.16	$4.70^{+3.13}_{-1.89}$	1.41	6.35	0.22
25	005619.17-721507.9	00 56 19.17	-72 15 7.9	5	0.84	225	0.04	$5.29^{+2.93}_{-2.22}$	1.44	7.85	0.23
26	005556.08-721731.9	00 55 56.08	-72 17 31.9	5	0.97	206	0.16	$4.37^{+2.47}_{-2.00}$	1.37	6.33	0.21

Table A.1 FIELD 3: Master Source List *continued*

Src_ID	Source Name	R.A.	Dec.	Obs.	Eff.Area	Bkg.	Area	Net	Significance	Off axis	Lx^{un}
	CXOUJ...	(J2000)	(J2000)	Counts	Ratio	Counts	Ratio	Counts	(σ)		
(1)	(2)	(3)	(4)	(5)	(6)	(7)	(8)	(9)	(10)	(11)	(12)
27	005606.60-722046.0	00 56 6.60	-72 20 46.0	4	0.75	155	0.08	$4.49^{+2.98}_{-2.12}$	1.22	7.86	0.18
28	005723.37-722142.9	00 57 23.37	-72 21 42.9	4	0.80	141	0.09	$4.22^{+2.84}_{-1.98}$	1.22	7.60	0.18

Notes: RA is in units of hours, minutes, and seconds, and Dec. is in units of degrees, arcminutes, and arcseconds. The area ratio is in units of 10^{-2}, the off-axis angle is in units of arcminutes, while the luminosity is corrected for absorption and in units of 10^{34}erg/s.

Table A.2 FIELD 4: Master Source List

Src_ID	Source Name	R.A.	Dec.	Obs.	Eff.Area	Bkg.	Area	Net	Significance	Off axis	Lx^{un}
	CXOUJ...	(J2000)	(J2000)	Counts	Ratio	Counts	Ratio	Counts	(σ)		
(1)	(2)	(3)	(4)	(5)	(6)	(7)	(8)	(9)	(10)	(11)	(12)
1	005044.61-731605.3	00 50 44.61	-73 16 5.3	386	0.88	104	0.71	$437.46^{+21.09}_{-23.19}$	18.64	6.69	14.18
2	004913.57-731137.8	00 49 13.57	-73 11 37.8	209	0.89	124	0.73	$232.01^{+16.94}_{-15.25}$	13.44	4.98	7.66
3	005057.16-731007.9	00 50 57.16	-73 10 7.9	249	0.74	80	4.06	$332.29^{+22.75}_{-19.83}$	14.62	5.72	9.04
4	004818.79-732059.9	00 48 18.79	-73 20 59.9	128	0.90	124	0.84	$140.62^{+12.84}_{-12.15}$	10.28	7.92	4.67
5	004929.74-731058.5	00 49 29.74	-73 10 58.5	103	0.42	67	1.01	$243.51^{+23.48}_{-24.31}$	9.15	8.17	3.76
6	004948.19-732211.4	00 49 48.19	-73 22 11.4	78	0.93	161	0.60	$81.72^{+10.48}_{-8.41}$	7.80	4.67	2.83
7	004853.37-732458.1	00 48 53.37	-73 24 58.1	106	0.85	118	3.57	$118.66^{+11.88}_{-12.02}$	8.98	6.17	3.75
8	004814.15-731004.1	00 48 14.15	-73 10 4.1	86	0.81	90	3.78	$101.25^{+11.93}_{-10.81}$	8.00	10.18	3.04
9	004815.27-732524.2	00 48 15.27	-73 25 24.2	45	0.81	110	3.39	$50.81^{+7.83}_{-8.57}$	5.31	6.76	1.52
10	004832.90-732353.7	00 48 32.90	-73 23 53.7	38	0.86	133	1.04	$42.20^{+7.14}_{-7.07}$	5.07	3.00	1.35
11	004803.49-731700.4	00 48 3.49	-73 17 0.4	16	0.90	107	0.44	$17.11^{+4.32}_{-4.44}$	3.05	4.02	0.57
12	004821.12-731328.3	00 48 21.12	-73 13 28.3	14	0.79	80	0.38	$16.49^{+5.26}_{-4.06}$	2.83	6.41	0.50
13	004950.98-732459.3	00 49 50.98	-73 24 59.3	27	0.74	150	0.95	$34.34^{+6.92}_{-6.98}$	4.08	3.34	0.94
14	004941.98-732312.3	00 49 41.98	-73 23 12.3	18	0.43	134	0.62	$38.99^{+10.52}_{-9.10}$	3.22	6.23	0.63
15	004910.69-731717.4	00 49 10.69	-73 17 17.4	13	0.99	136	0.12	$12.49^{+3.83}_{-3.31}$	2.73	4.71	0.47
16	004905.22-731410.8	00 49 5.22	-73 14 10.8	17	0.95	373	0.18	$17.32^{+3.99}_{-4.57}$	3.13	4.60	0.60
17	005048.11-731818.4	00 50 48.11	-73 18 18.4	14	0.90	101	0.67	$13.64^{+5.01}_{-3.13}$	2.75	9.74	0.49
18	004949.67-732306.1	00 49 49.67	-73 23 6.1	13	0.90	131	0.84	$12.53^{+4.33}_{-3.52}$	2.53	6.34	0.44
19	005055.20-731803.7	00 50 55.20	-73 18 3.7	12	0.89	101	0.51	$12.78^{+3.70}_{-3.94}$	2.51	4.51	0.42
20	005059.09-732055.8	00 50 59.09	-73 20 55.8	22	0.86	1706	0.36	$17.95^{+5.39}_{-5.45}$	2.74	6.41	0.58
21	005102.25-732134.8	00 51 2.25	-73 21 34.8	66	0.80	1757	0.44	$72.36^{+10.22}_{-9.88}$	6.35	5.65	2.14
22	004956.64-732518.0	00 49 56.64	-73 25 18.0	14	0.70	121	1.88	$15.55^{+6.06}_{-4.45}$	2.42	1.83	0.43
23	004957.18-731655.2	00 49 57.18	-73 16 55.2	9	0.89	87	0.11	$9.25^{+3.85}_{-2.76}$	2.16	4.08	0.33
24	005009.95-731931.4	00 50 9.95	-73 19 31.4	9	0.91	132	0.33	$8.85^{+3.58}_{-2.89}$	2.08	6.35	0.32
25	005042.45-732139.7	00 50 42.45	-73 21 39.7	10	0.81	314	0.53	$9.86^{+3.94}_{-3.73}$	1.95	7.85	0.31
26	005005.35-731146.3	00 50 5.35	-73 11 46.3	9	0.81	54	1.02	$9.46^{+4.27}_{-2.94}$	2.05	6.33	0.31

Table A.2 FIELD 4: Master Source List *continued*

Src_ID	Source Name	R.A.	Dec.	Obs.	Eff.Area	Bkg.	Area	Net	Significance	Off axis	Lx^{un}
	CXOUJ...	(J2000)	(J2000)	Counts	Ratio	Counts	Ratio	Counts	(σ)		
(1)	(2)	(3)	(4)	(5)	(6)	(7)	(8)	(9)	(10)	(11)	(12)
27	005023.58-731820.1	00 50 23.58	-73 18 20.1	8	0.95	113	0.26	$8.02^{+2.86}_{-2.98}$	1.95	7.86	0.28
28	004847.17-731719.1	00 48 47.17	-73 17 19.1	7	0.97	112	0.14	$6.54^{+2.92}_{-2.38}$	1.81	7.60	0.25
29	005110.28-731334.2	00 51 10.28	-73 13 34.2	14	0.83	105	1.09	$14.52^{+5.04}_{-3.77}$	2.66	3.56	0.47
30	004854.42-731715.4	00 48 54.42	-73 17 15.4	6	0.98	134	0.07	$5.72^{+2.48}_{-2.35}$	1.64	7.43	0.22
31	004844.82-731027.6	00 48 44.82	-73 10 27.6	10	0.85	78	0.87	$10.10^{+4.35}_{-2.96}$	2.18	5.91	0.34
32	004927.00-731211.8	00 49 27.00	-73 12 11.8	7	0.86	113	0.26	$7.38^{+3.10}_{-2.87}$	1.77	6.98	0.25
33	004955.80-732036.9	00 49 55.80	-73 20 36.9	6	0.95	145	0.16	$5.50^{+2.83}_{-2.16}$	1.60	3.89	0.21
34	005013.98-731351.7	00 50 13.98	-73 13 51.7	5	0.92	65	0.50	$4.61^{+2.63}_{-2.05}$	1.37	5.93	0.17
35	004942.86-731721.5	00 49 42.86	-73 17 21.5	5	0.43	103	0.07	$10.33^{+5.76}_{-4.23}$	1.45	1.06	0.18
36	005045.25-731541.5	00 50 45.25	-73 15 41.5	7	0.79	121	0.35	$7.86^{+3.58}_{-2.98}$	1.74	8.04	0.24
37	004808.57-731547.4	00 48 8.57	-73 15 47.4	6	0.86	76	0.58	$5.70^{+3.33}_{-2.23}$	1.55	5.92	0.20
38	004743.77-73939.9	00 47 43.77	-73 9 39.9	34	0.67	119	6.40	$37.87^{+10.20}_{-7.29}$	3.80	10.58	0.97

Notes: RA is in units of hours, minutes, and seconds, and Dec. is in units of degrees, arcminutes, and arcseconds. The area ratio is in units of 10^{-2}, the off-axis angle is in units of arcminutes, while the luminosity is corrected for absorption and in units of 10^{34}erg/s.

Table A.3 FIELD 5: Master Source List

Src_ID	Source Name	R.A.	Dec.	Obs.	Eff.Area	Bkg.	Area	Net	Significance	Off axis	Lx^{un}
	CXOUJ...	(J2000)	(J2000)	Counts	Ratio	Counts	Ratio	Counts	(σ)		
(1)	(2)	(3)	(4)	(5)	(6)	(7)	(8)	(9)	(10)	(11)	(12)
1	005205.61-722604.4	00 52 5.61	-72 26 4.4	1968	0.90	219	0.52	$2188.34^{+44.74}_{-53.14}$	43.35	6.69	109.39
2	005323.86-722715.5	00 53 23.86	-72 27 15.5	147	0.72	122	0.09	$202.43^{+16.32}_{-16.90}$	11.17	4.98	8.17
3	005153.16-723148.8	00 51 53.16	-72 31 48.8	104	0.82	188	0.74	$125.44^{+12.21}_{-12.54}$	9.13	5.72	5.71
4	005446.22-722523.0	00 54 46.22	-72 25 23.0	74	0.76	146	0.69	$95.68^{+11.05}_{-11.36}$	7.57	7.92	4.06
5	005331.68-722240.8	00 53 31.68	-72 22 40.8	45	0.85	95	0.25	$52.56^{+7.77}_{-7.82}$	5.77	8.17	2.49
6	005504.40-722230.4	00 55 4.40	-72 22 30.4	72	0.80	148	2.17	$85.08^{+10.58}_{-10.32}$	7.22	4.67	3.83
7	005456.34-722648.4	00 54 56.34	-72 26 48.4	43	0.88	96	1.43	$47.31^{+6.78}_{-7.91}$	5.47	6.17	2.32
8	005437.08-722638.2	00 54 37.08	-72 26 38.2	34	0.95	75	0.92	$35.05^{+6.00}_{-6.17}$	4.83	10.18	1.85
9	005337.77-722409.2	00 53 37.77	-72 24 9.2	16	0.68	113	0.10	$22.63^{+6.19}_{-5.35}$	3.12	6.76	0.88
10	005444.91-722358.6	00 54 44.91	-72 23 58.6	24	0.84	144	0.64	$27.17^{+5.71}_{-5.79}$	3.86	3.00	1.28
11	005157.86-721731.9	00 51 57.86	-72 17 31.9	21	0.86	123	2.20	$20.77^{+5.44}_{-5.04}$	3.23	4.02	1.02
12	005245.04-722843.6	00 52 45.04	-72 28 43.6	13	0.93	172	0.05	$13.60^{+3.92}_{-3.72}$	2.74	6.41	0.72
13	005351.08-721818.8	00 53 51.08	-72 18 18.8	14	0.94	103	1.85	$11.86^{+4.63}_{-3.20}$	2.50	3.34	0.67
14	005450.78-722631.8	00 54 50.78	-72 26 31.8	14	0.90	122	0.78	$13.43^{+4.90}_{-3.26}$	2.69	6.23	0.73
15	005448.86-722544.7	00 54 48.86	-72 25 44.7	11	0.41	132	0.74	$23.44^{+8.75}_{-7.21}$	2.26	4.71	0.56
16	005355.25-722645.8	00 53 55.25	-72 26 45.8	8	0.97	123	0.05	$7.79^{+3.07}_{-2.65}$	2.01	4.60	0.44
17	005233.59-722437.6	00 52 33.59	-72 24 37.6	8	0.96	143	0.05	$7.87^{+3.08}_{-2.69}$	2.00	9.74	0.44
18	005118.70-723002.8	00 51 18.70	-72 30 2.8	11	0.97	99	1.22	$9.79^{+3.39}_{-3.35}$	2.21	6.34	0.54
19	005235.09-722517.0	00 52 35.09	-72 25 17.0	8	0.93	160	0.14	$8.40^{+2.74}_{-3.19}$	1.97	4.51	0.43
20	005408.64-722356.8	00 54 8.64	-72 23 56.8	8	0.90	153	0.15	$8.68^{+2.84}_{-3.30}$	1.96	6.41	0.43
21	005352.43-723159.5	00 53 52.43	-72 31 59.5	8	0.84	100	0.42	$9.04^{+3.01}_{-3.57}$	1.91	5.65	0.42
22	005159.15-723058.0	00 51 59.15	-72 30 58.0	8	0.83	159	0.32	$8.80^{+3.26}_{-3.41}$	1.89	1.83	0.42
23	005155.96-722038.2	00 51 55.96	-72 20 38.2	11	0.76	136	0.63	$12.47^{+4.82}_{-3.75}$	2.29	4.08	0.56
24	005403.78-722633.2	00 54 3.78	-72 26 33.2	7	0.86	42	0.35	$7.17^{+3.59}_{-2.41}$	1.81	6.35	0.38
25	005438.22-722210.3	00 54 38.22	-72 22 10.3	9	0.78	160	0.71	$9.86^{+3.53}_{-3.99}$	1.91	7.85	0.44
26	005145.44-722150.9	00 51 45.44	-72 21 50.9	9	0.87	118	0.84	$8.73^{+3.66}_{-3.08}$	1.94	6.33	0.45

Table A.3 FIELD 5: Master Source List *continued*

Src_ID	Source Name	R.A.	Dec.	Obs.	Eff.Area	Bkg.	Area	Net	Significance	Off axis	Lx^{un}
	CXOUJ...	(J2000)	(J2000)	Counts	Ratio	Counts	Ratio	Counts	(σ)		
(1)	(2)	(3)	(4)	(5)	(6)	(7)	(8)	(9)	(10)	(11)	(12)
27	005348.54-722803.3	00 53 48.54	-72 28 3.3	6	0.84	132	0.11	$6.47^{+3.15}_{-2.53}$	1.63	7.86	0.33
28	005225.88-722311.5	00 52 25.88	-72 23 11.5	6	0.80	136	0.21	$6.09^{+3.79}_{-2.16}$	1.59	7.60	0.32
29	005358.51-722615.1	00 53 58.51	-72 26 15.1	6	0.86	58	0.26	$6.10^{+3.21}_{-2.29}$	1.63	3.56	0.33
30	005429.12-723106.1	00 54 29.12	-72 31 6.1	8	0.83	168	0.48	$8.65^{+3.04}_{-3.59}$	1.82	7.43	0.40
31	005350.95-722124.1	00 53 50.95	-72 21 24.1	6	0.90	161	0.28	$5.42^{+3.08}_{-2.21}$	1.54	5.91	0.31
32	005207.83-722126.9	00 52 7.83	-72 21 26.9	5	0.81	131	0.41	$4.91^{+2.99}_{-2.35}$	1.31	6.98	0.25
33	005357.20-722442.8	00 53 57.20	-72 24 42.8	4	0.91	121	0.11	$3.71^{+2.50}_{-1.74}$	1.22	3.89	0.22
34	005404.61-723052.9	00 54 4.61	-72 30 52.9	4	0.84	109	0.29	$3.67^{+2.77}_{-1.80}$	1.16	5.93	0.20
35	005258.37-722606.8	00 52 58.37	-72 26 6.8	3	0.96	46	0.09	$2.73^{+1.95}_{-1.49}$	1.01	1.06	0.16
36	005329.26-721834.1	00 53 29.26	-72 18 34.1	7	0.44	84	1.03	$12.79^{+6.29}_{-5.39}$	1.62	8.04	0.34
37	005359.17-723112.9	00 53 59.17	-72 31 12.9	4	0.92	108	0.32	$3.35^{+2.45}_{-1.71}$	1.15	5.92	0.20

Notes: RA is in units of hours, minutes, and seconds, and Dec. is in units of degrees, arcminutes, and arcseconds. The area ratio is in units of 10^{-2}, the off-axis angle is in units of arcminutes, while the luminosity is corrected for absorption and in units of 10^{34}erg/s.

Table A.4 FIELD 6: Master Source List

Src_ID	Source Name	R.A.	Dec.	Obs.	Eff.Area	Bkg.	Area	Net	Significance	Off axis	Lx^{un}
	CXOUJ...	(J2000)	(J2000)	Counts	Ratio	Counts	Ratio	Counts	(σ)		
(1)	(2)	(3)	(4)	(5)	(6)	(7)	(8)	(9)	(10)	(11)	(12)
1	005208.95-723803.5	00 52 8.95	-72 38 3.5	5123	0.86	449	0.97	$5977.17^{+77.33}_{-88.65}$	70.52	6.69	234.20
2	005455.78-724510.7	00 54 55.78	-72 45 10.7	491	0.85	179	1.53	$575.09^{+24.93}_{-26.86}$	21.07	4.98	22.34
3	005242.26-724719.6	00 52 42.26	-72 47 19.6	47	0.91	156	0.26	$51.19^{+6.96}_{-7.91}$	5.89	5.72	2.13
4	005252.22-724829.8	00 52 52.22	-72 48 29.8	30	0.85	164	0.29	$34.53^{+6.43}_{-6.37}$	4.51	7.92	1.35
5	005203.31-723831.0	00 52 3.31	-72 38 31.0	27	0.70	416	0.39	$34.66^{+8.57}_{-6.08}$	4.05	8.17	1.16
6	005245.69-724917.9	00 52 45.69	-72 49 17.9	19	0.87	168	0.35	$19.74^{+6.13}_{-3.73}$	3.38	4.67	0.84
7	005239.19-724117.7	00 52 39.19	-72 41 17.7	16	0.90	202	0.08	$17.16^{+4.51}_{-4.24}$	3.11	6.17	0.72
8	005422.01-724532.6	00 54 22.01	-72 45 32.6	16	0.79	117	0.42	$19.41^{+4.90}_{-5.04}$	3.05	10.18	0.71
9	005332.20-724316.5	00 53 32.20	-72 43 16.5	14	1.00	190	0.14	$13.00^{+4.22}_{-3.12}$	2.84	6.76	0.63
10	005259.02-724511.3	00 52 59.02	-72 45 11.3	13	0.97	168	0.09	$12.81^{+3.93}_{-3.39}$	2.73	3.00	0.59
11	005427.20-723719.2	00 54 27.20	-72 37 19.2	15	0.84	105	1.01	$16.10^{+4.91}_{-4.21}$	2.81	4.02	0.64
12	005338.95-724717.4	00 53 38.95	-72 47 17.4	11	0.93	100	0.29	$10.71^{+4.22}_{-2.80}$	2.42	6.41	0.49
13	005231.41-724916.1	00 52 31.41	-72 49 16.1	11	0.86	154	0.44	$11.54^{+4.04}_{-3.52}$	2.33	3.34	0.47
14	005244.85-723637.8	00 52 44.85	-72 36 37.8	11	0.73	229	0.30	$13.61^{+4.76}_{-4.15}$	2.33	6.23	0.47
15	005211.00-724357.7	00 52 11.00	-72 43 57.7	10	0.82	161	0.13	$11.24^{+4.20}_{-3.33}$	2.29	4.71	0.45
16	005315.98-724850.0	00 53 15.98	-72 48 50.0	10	0.89	158	0.35	$10.01^{+3.79}_{-3.15}$	2.21	4.60	0.43
17	005333.45-723721.4	00 53 33.45	-72 37 21.4	10	0.87	113	0.40	$10.60^{+3.66}_{-3.45}$	2.23	9.74	0.44
18	005210.14-724357.5	00 52 10.14	-72 43 57.5	9	0.92	175	0.09	$9.04^{+3.66}_{-2.76}$	2.14	6.34	0.40
19	005411.18-723512.4	00 54 11.18	-72 35 12.4	14	0.83	121	1.87	$13.09^{+5.10}_{-3.75}$	2.42	4.51	0.54
20	005409.57-724143.5	00 54 9.57	-72 41 43.5	8	0.83	186	0.23	$9.03^{+3.13}_{-3.51}$	1.91	6.41	0.35
21	005324.91-723941.3	00 53 24.91	-72 39 41.3	7	0.97	126	0.06	$6.55^{+3.05}_{-2.25}$	1.83	5.65	0.32
22	005450.21-724502.4	00 54 50.21	-72 45 2.4	10	0.86	165	0.68	$9.62^{+3.97}_{-3.25}$	2.07	1.83	0.41
23	005239.93-724244.9	00 52 39.93	-72 42 44.9	6	0.98	153	0.06	$5.76^{+2.57}_{-2.30}$	1.64	4.08	0.27
24	005413.67-724528.1	00 54 13.67	-72 45 28.1	6	0.90	104	0.35	$5.41^{+3.26}_{-2.01}$	1.57	6.35	0.26
25	005308.60-723451.5	00 53 8.60	-72 34 51.5	7	0.85	117	1.04	$6.16^{+3.31}_{-2.77}$	1.53	7.85	0.26
26	005350.48-724307.4	00 53 50.48	-72 43 7.4	5	0.92	190	0.05	$4.82^{+2.67}_{-2.03}$	1.44	6.33	0.22

Table A.4 FIELD 6: Master Source List *continued*

Src_ID	Source Name	R.A.	Dec.	Obs.	Eff.Area	Bkg.	Area	Net	Significance	Off axis	Lx^{un}
	CXOUJ...	(J2000)	(J2000)	Counts	Ratio	Counts	Ratio	Counts	(σ)		
(1)	(2)	(3)	(4)	(5)	(6)	(7)	(8)	(9)	(10)	(11)	(12)
27	005334.07-724815.5	00 53 34.07	-72 48 15.5	4	0.84	95	0.42	$3.68^{+2.61}_{-1.97}$	1.13	7.86	0.16
28	005138.99-724631.5	00 51 38.99	-72 46 31.5	9	0.84	201	0.46	$9.10^{+3.80}_{-3.22}$	1.96	7.60	0.37

Notes: RA is in units of hours, minutes, and seconds, and Dec. is in units of degrees, arcminutes, and arcseconds. The area ratio is in units of 10^{-2}, the off-axis angle is in units of arcminutes, while the luminosity is corrected for absorption and in units of 10^{34}erg/s.

Table A.5 FIELD 7: Master Source List

Src_ID	Source Name	R.A.	Dec.	Obs.	Eff.Area	Bkg.	Area	Net	Significance	Off axis	Lx^{un}
	CXOUJ...	(J2000)	(J2000)	Counts	Ratio	Counts	Ratio	Counts	(σ)		
(1)	(2)	(3)	(4)	(5)	(6)	(7)	(8)	(9)	(10)	(11)	(12)
1	004903.37-725052.5	00 49 3.37	-72 50 52.5	165	0.94	130	0.69	$173.20^{+15.80}_{-11.45}$	11.83	6.69	7.92
2	004932.10-723925.5	00 49 32.10	-72 39 25.5	44	0.88	96	0.31	$49.13^{+8.32}_{-6.68}$	5.68	4.98	2.11
3	005000.21-724928.9	00 50 0.21	-72 49 28.9	33	0.76	123	0.24	$42.51^{+7.88}_{-7.12}$	4.80	5.72	1.58
4	004944.37-725210.4	00 49 44.37	-72 52 10.4	36	0.83	117	0.64	$41.56^{+7.96}_{-6.39}$	4.99	7.92	1.70
5	004736.15-724538.6	00 47 36.15	-72 45 38.6	32	0.93	161	0.73	$32.90^{+5.98}_{-6.03}$	4.58	8.17	1.49
6	004916.75-723944.9	00 49 16.75	-72 39 44.9	25	0.91	117	0.27	$26.70^{+5.67}_{-5.20}$	4.06	4.67	1.19
7	004829.81-724900.4	00 48 29.81	-72 49 0.4	25	0.84	124	0.35	$28.90^{+5.84}_{-5.89}$	4.04	6.17	1.19
8	004709.13-724304.2	00 47 9.13	-72 43 4.2	33	0.79	73	2.55	$38.49^{+7.61}_{-6.75}$	4.57	10.18	1.50
9	005049.65-724153.1	00 50 49.65	-72 41 53.1	25	0.87	190	0.41	$27.98^{+5.34}_{-6.03}$	3.99	6.76	1.17
10	004955.27-724223.3	00 49 55.27	-72 42 23.3	20	0.74	184	0.06	$26.32^{+6.67}_{-5.32}$	3.58	3.00	0.96
11	005019.14-724403.4	00 50 19.14	-72 44 3.4	18	0.88	154	0.10	$19.84^{+5.10}_{-4.43}$	3.35	4.02	0.86
12	004820.12-724010.9	00 48 20.12	-72 40 10.9	15	0.90	75	0.48	$15.23^{+5.02}_{-3.42}$	2.95	6.41	0.71
13	004934.38-724106.8	00 49 34.38	-72 41 6.8	14	0.88	85	0.10	$15.25^{+4.47}_{-3.84}$	2.87	3.34	0.67
14	005003.36-723850.7	00 50 3.36	-72 38 50.7	13	0.93	99	0.42	$13.01^{+4.08}_{-3.50}$	2.67	6.23	0.61
15	004833.71-724137.5	00 48 33.71	-72 41 37.5	12	0.91	135	0.15	$12.55^{+4.00}_{-3.50}$	2.58	4.71	0.57
16	004832.81-724651.9	00 48 32.81	-72 46 51.9	11	0.80	134	0.19	$12.43^{+4.90}_{-3.25}$	2.43	4.60	0.52
17	004944.00-725401.1	00 49 44.00	-72 54 1.1	13	0.91	89	1.56	$12.35^{+4.10}_{-3.70}$	2.47	9.74	0.56
18	005015.48-723916.4	00 50 15.48	-72 39 16.4	9	0.79	113	0.48	$10.43^{+3.70}_{-3.73}$	2.05	6.34	0.41
19	004941.43-724843.8	00 49 41.43	-72 48 43.8	8	0.90	114	0.28	$8.41^{+2.87}_{-3.24}$	1.94	4.51	0.37
20	005035.01-724038.2	00 50 35.01	-72 40 38.2	8	0.93	145	0.39	$7.86^{+2.82}_{-3.10}$	1.88	6.41	0.36
21	004927.63-725001.4	00 49 27.63	-72 50 1.4	7	0.79	119	0.27	$8.05^{+3.35}_{-3.18}$	1.77	5.65	0.32
22	004923.46-724612.6	00 49 23.46	-72 46 12.6	6	0.98	112	0.05	$5.33^{+2.98}_{-1.85}$	1.65	1.83	0.29
23	004842.35-724657.1	00 48 42.35	-72 46 57.1	6	0.78	106	0.08	$7.17^{+3.24}_{-2.82}$	1.64	4.08	0.29
24	004808.02-724710.1	00 48 8.02	-72 47 10.1	6	0.82	191	0.24	$5.96^{+3.39}_{-2.42}$	1.54	6.35	0.27
25	004913.33-725211.0	00 49 13.33	-72 52 11.0	5	0.84	113	0.63	$4.78^{+2.67}_{-2.52}$	1.26	7.85	0.21
26	004850.14-725009.8	00 48 50.14	-72 50 9.8	5	0.84	143	0.30	$4.84^{+2.95}_{-2.21}$	1.34	6.33	0.22

Table A.5 FIELD 7: Master Source List *continued*

Src_ID	Source Name	R.A.	Dec.	Obs.	Eff.Area	Bkg.	Area	Net	Significance	Off axis	Lx^{un}
	CXOUJ...	(J2000)	(J2000)	Counts	Ratio	Counts	Ratio	Counts	(σ)		
(1)	(2)	(3)	(4)	(5)	(6)	(7)	(8)	(9)	(10)	(11)	(12)
27	005018.82-725110.4	00 50 18.82	-72 51 10.4	9	0.85	104	0.68	$9.22^{+3.74}_{-3.16}$	2.01	7.86	0.40

Notes: RA is in units of hours, minutes, and seconds, and Dec. is in units of degrees, arcminutes, and arcseconds. The area ratio is in units of 10^{-2}, the off-axis angle is in units of arcminutes, while the luminosity is corrected for absorption and in units of 10^{34}erg/s.

Table A.6 FIELD 3: Source Photometry and X-ray Colors

Src_ID	SOFT BAND (0.5 - 1.0 keV)				MEDIUM BAND (1.0 - 2.5 keV)				HARD BAND (2.5 - 7.0 keV)				Col1	Col2	Col3
	Counts			Eff.Area	Counts			Eff.Area	Counts			Eff.Area			
	Obs.	Bkg.	Net	Ratio	Obs.	Bkg.	Net	Ratio	Obs.	Bkg.	Net	Ratio			
(1)	(2)	(3)	(4)	(5)	(6)	(7)	(8)	(9)	(10)	(11)	(12)	(13)	(14)	(15)	(16)
1	24	24	$25.52^{+5.57}_{-5.04}$	0.91	216	44	$224.71^{+14.77}_{-15.65}$	0.96	95	47	$98.89^{+9.78}_{-10.48}$	0.96	$-0.92^{+0.08}_{-0.10}$	$0.35^{+0.06}_{-0.05}$	$-0.57^{+0.10}_{-0.10}$
2	58	35	$64.57^{+8.13}_{-8.77}$	0.89	145	61	$152.50^{+13.42}_{-12.03}$	0.94	67	95	$70.39^{+8.34}_{-9.13}$	0.93	$-0.38^{+0.07}_{-0.07}$	$0.34^{+0.06}_{-0.07}$	$-0.04^{+0.07}_{-0.08}$
3	7	42	$7.21^{+3.42}_{-2.44}$	0.88	61	49	$67.90^{+8.58}_{-8.72}$	0.89	49	78	$55.37^{+8.56}_{-7.39}$	0.87	$-0.91^{+0.16}_{-0.18}$	$0.08^{+0.09}_{-0.08}$	$-0.83^{+0.17}_{-0.18}$
4	19	58	$19.90^{+5.46}_{-4.05}$	0.90	63	51	$67.64^{+9.52}_{-7.70}$	0.91	13	92	$13.89^{+3.99}_{-3.91}$	0.90	$-0.52^{+0.12}_{-0.11}$	$0.67^{+0.15}_{-0.12}$	$0.15^{+0.17}_{-0.14}$
5	11	69	$11.19^{+4.28}_{-3.06}$	0.89	54	140	$55.98^{+7.82}_{-7.62}$	0.94	28	133	$28.08^{+6.35}_{-4.81}$	0.94	$-0.65^{+0.13}_{-0.17}$	$0.29^{+0.10}_{-0.10}$	$-0.36^{+0.14}_{-0.17}$
6	1	44	$0.53^{+1.28}_{-0.53}$	0.95	18	71	$17.91^{+4.80}_{-3.80}$	0.97	11	90	$10.90^{+3.60}_{-3.12}$	0.97	$-1.10^{+0.36}_{-0.45}$	$0.20^{+0.17}_{-0.16}$	$-0.91^{+0.40}_{-0.43}$
7	8	34	$9.70^{+3.64}_{-3.39}$	0.78	13	38	$13.95^{+4.61}_{-3.51}$	0.87	12	53	$13.47^{+4.15}_{-3.85}$	0.85	$-0.16^{+0.20}_{-0.20}$	$0.02^{+0.18}_{-0.17}$	$-0.13^{+0.19}_{-0.21}$
8	2	40	$1.48^{+1.89}_{-0.93}$	0.93	17	60	$16.67^{+5.11}_{-3.38}$	0.96	7	101	$6.99^{+2.82}_{-2.61}$	0.95	$-0.84^{+0.29}_{-0.33}$	$0.39^{+0.18}_{-0.21}$	$-0.48^{+0.33}_{-0.34}$
9	2	42	$1.19^{+1.90}_{-0.87}$	0.95	16	40	$15.79^{+4.23}_{-3.85}$	0.97	9	59	$8.57^{+3.39}_{-2.67}$	0.97	$-0.86^{+0.34}_{-0.34}$	$0.26^{+0.17}_{-0.19}$	$-0.61^{+0.35}_{-0.36}$
10	2	49	$1.76^{+2.31}_{-1.18}$	0.75	8	62	$8.74^{+3.40}_{-3.00}$	0.86	6	88	$6.49^{+2.97}_{-2.64}$	0.85	$-0.50^{+0.34}_{-0.34}$	$0.12^{+0.23}_{-0.24}$	$-0.38^{+0.34}_{-0.36}$
11	1	24	$0.00^{+2.00}_{-0.00}$	0.81	7	41	$7.26^{+3.39}_{-2.52}$	0.87	7	55	$7.21^{+3.41}_{-2.55}$	0.87	$-0.65^{+0.38}_{-0.56}$	$-0.01^{+0.25}_{-0.22}$	$-0.65^{+0.38}_{-0.56}$
12	1	36	$0.00^{+1.69}_{-0.00}$	0.93	11	56	$10.77^{+3.91}_{-2.96}$	0.95	4	70	$3.39^{+2.47}_{-1.60}$	0.94	$-0.90^{+0.40}_{-0.54}$	$0.43^{+0.26}_{-0.25}$	$-0.47^{+0.46}_{-0.56}$
13	1	35	$0.00^{+2.81}_{-0.00}$	0.55	8	47	$9.79^{+4.17}_{-3.18}$	0.75	3	53	$3.32^{+2.53}_{-1.95}$	0.74	$-0.72^{+0.50}_{-0.47}$	$0.40^{+0.31}_{-0.29}$	$-0.27^{+0.52}_{-0.57}$
14	1	43	$0.00^{+1.81}_{-0.00}$	0.85	8	60	$7.80^{+3.54}_{-2.45}$	0.92	2	89	$1.38^{+1.41}_{-1.38}$	0.91	$-0.78^{+0.46}_{-0.52}$	$0.61^{+0.38}_{-0.40}$	$-0.17^{+0.59}_{-0.68}$
15	0	38	$0.00^{+0.58}_{-0.00}$	0.86	6	36	$5.87^{+2.82}_{-2.31}$	0.93	5	81	$4.65^{+2.66}_{-2.05}$	0.92	$-1.06^{+0.57}_{-0.99}$	$0.08^{+0.27}_{-0.27}$	$-0.99^{+0.60}_{-0.98}$
16	1	16	$0.00^{+1.45}_{-0.00}$	0.82	13	49	$12.19^{+4.15}_{-3.66}$	0.91	3	69	$0.00^{+2.06}_{-0.00}$	0.90	$-0.95^{+0.48}_{-0.75}$	$0.77^{+0.77}_{-0.42}$	$-0.14^{+0.94}_{-0.98}$
17	0	40	$0.00^{+0.65}_{-0.00}$	0.76	6	47	$6.23^{+3.46}_{-2.17}$	0.84	2	82	$1.70^{+1.98}_{-1.16}$	0.84	$-1.08^{+0.60}_{-0.96}$	$0.46^{+0.34}_{-0.37}$	$-0.54^{+0.59}_{-1.10}$
18	0	20	$0.00^{+1.22}_{-0.00}$	0.41	6	59	$12.33^{+6.21}_{-4.64}$	0.44	1	82	$0.00^{+3.62}_{-0.00}$	0.43	$-1.06^{+0.57}_{-1.00}$	$0.66^{+0.56}_{-0.43}$	$-0.37^{+0.78}_{-1.14}$
19	1	28	$0.00^{+1.72}_{-0.00}$	0.85	6	61	$5.48^{+3.31}_{-2.03}$	0.89	5	63	$4.83^{+2.69}_{-2.27}$	0.87	$-0.64^{+0.48}_{-0.59}$	$0.07^{+0.29}_{-0.27}$	$-0.56^{+0.47}_{-0.63}$
20	0	38	$0.00^{+0.60}_{-0.00}$	0.82	7	63	$7.01^{+3.38}_{-2.35}$	0.90	0	91	$0.00^{+0.56}_{-0.00}$	0.89	$-1.27^{+0.73}_{-0.83}$	$1.20^{+0.94}_{-0.62}$	$0.01^{+1.21}_{-1.15}$
21	0	37	$0.00^{+0.48}_{-0.00}$	1.02	2	46	$1.32^{+1.78}_{-0.85}$	1.00	5	73	$4.54^{+2.40}_{-1.94}$	0.99	$-0.59^{+0.58}_{-1.10}$	$-0.34^{+0.33}_{-0.39}$	$-1.07^{+0.61}_{-0.96}$
22	1	42	$0.00^{+1.90}_{-0.00}$	0.82	5	55	$4.87^{+2.66}_{-2.08}$	0.91	2	96	$1.27^{+1.55}_{-1.27}$	0.90	$-0.49^{+0.40}_{-0.61}$	$0.35^{+0.46}_{-0.36}$	$-0.15^{+0.57}_{-0.68}$
23	0	22	$0.00^{+0.51}_{-0.00}$	0.97	0	58	$0.00^{+0.50}_{-0.00}$	0.99	5	88	$4.30^{+2.76}_{-1.62}$	0.99	$0.01^{+1.18}_{-1.18}$	$-1.04^{+0.60}_{-0.98}$	$-0.96^{+0.53}_{-1.05}$
24	1	30	$0.47^{+1.62}_{-0.47}$	0.79	1	41	$0.00^{+1.87}_{-0.00}$	0.87	3	67	$2.75^{+2.30}_{-1.53}$	0.86	$0.02^{+0.67}_{-0.60}$	$-0.31^{+0.40}_{-0.62}$	$-0.36^{+0.48}_{-0.51}$
25	0	43	$0.00^{+0.64}_{-0.00}$	0.78	3	67	$3.04^{+2.24}_{-1.62}$	0.85	2	115	$1.67^{+2.04}_{-1.10}$	0.84	$-0.80^{+0.64}_{-0.98}$	$0.15^{+0.39}_{-0.39}$	$-0.67^{+0.70}_{-0.98}$
26	1	53	$0.00^{+1.71}_{-0.00}$	0.94	3	61	$2.66^{+1.84}_{-1.56}$	0.97	1	92	$0.00^{+1.56}_{-0.00}$	0.97	$-0.38^{+0.49}_{-0.55}$	$0.38^{+0.63}_{-0.48}$	$-0.02^{+0.76}_{-0.66}$

Table A.6 FIELD 3: Source Photometry and X-ray Colors

Src_ID	SOFT BAND (0.5 - 1.0 keV)				MEDIUM BAND (1.0 - 2.5 keV)				HARD BAND (2.5 - 7.0 keV)				Col1	Col2	Col3
	Counts			Eff.Area	Counts			Eff.Area	Counts			Eff.Area			
	Obs.	Bkg.	Net	Ratio	Obs.	Bkg.	Net	Ratio	Obs.	Bkg.	Net	Ratio			
(1)	(2)	(3)	(4)	(5)	(6)	(7)	(8)	(9)	(10)	(11)	(12)	(13)	(14)	(15)	(16)
27	0	29	$0.00^{+0.78}_{-0.00}$	0.63	2	42	$1.80^{+2.25}_{-1.16}$	0.77	2	84	$1.89^{+2.21}_{-1.29}$	0.75	$-0.63^{+0.71}_{-0.96}$	$-0.01^{+0.44}_{-0.42}$	$-0.51^{+0.58}_{-1.10}$
28	0	30	$0.00^{+0.72}_{-0.00}$	0.69	1	46	$0.54^{+1.54}_{-0.54}$	0.81	3	65	$3.20^{+2.35}_{-1.77}$	0.80	$-0.39^{+0.79}_{-1.05}$	$-0.39^{+0.46}_{-0.53}$	$-0.79^{+0.66}_{-0.97}$

Notes: The area ratio is in units of 10^{-2}. The colors are defined as Col1=$\log_{10}(S/M)$, Col2=$\log_{10}(M/H)$, and Col3=$\log_{10}(S/H)$.

Table A.7 FIELD 4: Source Photometry and X-ray Colors

Src_ID	SOFT BAND (0.5 - 1.0 keV)				MEDIUM BAND (1.0 - 2.5 keV)				HARD BAND (2.5 - 7.0 keV)				Col1	Col2	Col3
	Counts			Eff.Area	Counts			Eff.Area	Counts			Eff.Area			
	Obs.	Bkg.	Net	Ratio	Obs.	Bkg.	Net	Ratio	Obs.	Bkg.	Net	Ratio			
(1)	(2)	(3)	(4)	(5)	(6)	(7)	(8)	(9)	(10)	(11)	(12)	(13)	(14)	(15)	(16)
1	29	22	$33.16^{+6.79}_{-5.71}$	0.85	166	33	$183.53^{+15.97}_{-12.69}$	0.89	191	49	$217.72^{+15.03}_{-16.28}$	0.88	$-0.73^{+0.08}_{-0.09}$	$-0.07^{+0.05}_{-0.05}$	$-0.80^{+0.08}_{-0.09}$
2	3	17	$3.16^{+2.10}_{-1.88}$	0.83	81	33	$88.28^{+11.04}_{-8.78}$	0.90	125	74	$139.20^{+12.79}_{-12.15}$	0.89	$-1.38^{+0.26}_{-0.25}$	$-0.19^{+0.06}_{-0.07}$	$-1.57^{+0.26}_{-0.24}$
3	12	22	$17.70^{+5.33}_{-5.68}$	0.62	118	22	$154.48^{+15.20}_{-13.44}$	0.75	119	36	$159.35^{+14.74}_{-14.78}$	0.74	$-0.90^{+0.11}_{-0.17}$	$-0.01^{+0.06}_{-0.06}$	$-0.93^{+0.13}_{-0.15}$
4	1	25	$0.00^{+1.74}_{-0.00}$	0.82	10	37	$10.14^{+3.75}_{-3.06}$	0.91	117	62	$130.13^{+11.38}_{-12.55}$	0.90	$-0.85^{+0.45}_{-0.61}$	$-1.05^{+0.13}_{-0.16}$	$-1.92^{+0.42}_{-0.59}$
5	5	7	$11.24^{+6.26}_{-4.72}$	0.39	33	21	$75.15^{+14.40}_{-12.14}$	0.43	65	39	$154.68^{+17.85}_{-20.29}$	0.42	$-0.73^{+0.18}_{-0.23}$	$-0.30^{+0.09}_{-0.09}$	$-1.06^{+0.19}_{-0.21}$
6	2	30	$1.30^{+2.04}_{-0.96}$	0.88	48	55	$51.10^{+7.06}_{-7.61}$	0.94	28	76	$29.52^{+5.71}_{-5.61}$	0.93	$-1.30^{+0.31}_{-0.35}$	$0.23^{+0.10}_{-0.11}$	$-1.05^{+0.30}_{-0.37}$
7	0	18	$0.00^{+0.67}_{-0.00}$	0.74	7	39	$5.88^{+3.23}_{-2.75}$	0.87	99	61	$113.20^{+11.39}_{-11.77}$	0.85	$-0.99^{+0.61}_{-0.99}$	$-1.21^{+0.19}_{-0.23}$	$-2.37^{+0.69}_{-0.81}$
8	1	17	$0.00^{+1.62}_{-0.00}$	0.66	23	27	$26.61^{+5.68}_{-5.86}$	0.82	62	46	$73.98^{+9.76}_{-9.53}$	0.81	$-1.21^{+0.47}_{-0.81}$	$-0.43^{+0.10}_{-0.12}$	$-1.69^{+0.50}_{-0.76}$
9	1	18	$0.00^{+1.66}_{-0.00}$	0.65	28	27	$32.35^{+6.48}_{-6.15}$	0.83	16	65	$16.21^{+5.32}_{-4.44}$	0.81	$-1.26^{+0.44}_{-0.83}$	$0.30^{+0.14}_{-0.17}$	$-0.99^{+0.46}_{-0.83}$
10	3	19	$3.45^{+2.22}_{-2.18}$	0.75	27	55	$30.04^{+5.92}_{-5.84}$	0.87	8	59	$8.40^{+3.18}_{-3.27}$	0.86	$-0.86^{+0.27}_{-0.28}$	$0.52^{+0.20}_{-0.17}$	$-0.34^{+0.32}_{-0.31}$
11	0	17	$0.00^{+0.61}_{-0.00}$	0.81	7	31	$6.87^{+3.29}_{-2.38}$	0.91	9	59	$9.81^{+2.97}_{-3.54}$	0.90	$-1.25^{+0.72}_{-0.83}$	$-0.10^{+0.22}_{-0.22}$	$-1.36^{+0.72}_{-0.83}$
12	0	18	$0.00^{+0.69}_{-0.00}$	0.71	3	21	$3.28^{+2.26}_{-1.87}$	0.80	11	41	$13.50^{+4.19}_{-4.05}$	0.79	$-0.79^{+0.64}_{-0.98}$	$-0.53^{+0.27}_{-0.29}$	$-1.31^{+0.58}_{-0.96}$
13	5	25	$6.62^{+3.76}_{-2.91}$	0.65	13	52	$16.37^{+4.70}_{-4.70}$	0.75	9	73	$10.37^{+4.57}_{-3.41}$	0.74	$-0.33^{+0.22}_{-0.25}$	$0.16^{+0.20}_{-0.20}$	$-0.16^{+0.25}_{-0.26}$
14	2	22	$3.32^{+4.17}_{-2.48}$	0.40	6	44	$11.44^{+6.83}_{-4.16}$	0.43	10	68	$20.91^{+8.41}_{-6.17}$	0.43	$-0.39^{+0.36}_{-0.38}$	$-0.20^{+0.21}_{-0.25}$	$-0.58^{+0.30}_{-0.40}$
15	0	40	$0.00^{+0.50}_{-0.00}$	0.98	1	46	$0.00^{+1.67}_{-0.00}$	0.99	12	50	$11.90^{+3.37}_{-3.50}$	0.99	$-0.47^{+0.81}_{-1.05}$	$-0.95^{+0.41}_{-0.47}$	$-1.54^{+0.73}_{-0.81}$
16	1	162	$0.00^{+1.46}_{-0.00}$	0.92	6	159	$5.42^{+2.86}_{-2.12}$	0.95	10	52	$9.76^{+3.80}_{-2.74}$	0.95	$-0.72^{+0.53}_{-0.63}$	$-0.23^{+0.23}_{-0.23}$	$-0.88^{+0.43}_{-0.69}$
17	3	16	$3.10^{+2.08}_{-1.83}$	0.84	7	32	$7.57^{+2.52}_{-3.13}$	0.91	4	53	$3.46^{+2.52}_{-1.74}$	0.90	$-0.29^{+0.28}_{-0.33}$	$0.22^{+0.33}_{-0.26}$	$-0.04^{+0.32}_{-0.38}$
18	1	20	$0.00^{+1.77}_{-0.00}$	0.84	5	43	$4.62^{+2.59}_{-2.13}$	0.92	7	68	$6.43^{+3.36}_{-2.36}$	0.90	$-0.51^{+0.44}_{-0.65}$	$-0.13^{+0.27}_{-0.28}$	$-0.66^{+0.43}_{-0.62}$
19	3	19	$3.18^{+2.21}_{-1.81}$	0.82	5	30	$4.70^{+2.87}_{-1.94}$	0.90	4	52	$3.66^{+2.48}_{-1.83}$	0.89	$-0.15^{+0.30}_{-0.34}$	$0.09^{+0.32}_{-0.29}$	$-0.06^{+0.33}_{-0.35}$
20	5	1036	$0.00^{+2.87}_{-0.00}$	0.77	8	522	$6.17^{+3.65}_{-2.74}$	0.87	9	148	$9.49^{+3.58}_{-3.28}$	0.86	$-0.36^{+0.45}_{-0.84}$	$-0.14^{+0.26}_{-0.26}$	$-0.56^{+0.47}_{-0.75}$
21	43	1057	$54.44^{+9.20}_{-9.32}$	0.70	22	529	$23.57^{+6.02}_{-5.37}$	0.81	1	171	$0.00^{+1.27}_{-0.00}$	0.80	$0.35^{+0.13}_{-0.12}$	$1.50^{+0.61}_{-0.72}$	$1.69^{+0.77}_{-0.54}$
22	2	24	$0.00^{+3.79}_{-0.00}$	0.60	7	38	$8.03^{+4.08}_{-3.12}$	0.72	5	59	$4.55^{+3.61}_{-2.67}$	0.70	$-0.47^{+0.44}_{-0.48}$	$0.20^{+0.31}_{-0.33}$	$-0.25^{+0.47}_{-0.56}$
23	0	11	$0.00^{+0.55}_{-0.00}$	0.91	3	40	$2.92^{+2.08}_{-1.60}$	0.89	6	36	$6.11^{+3.15}_{-2.22}$	0.88	$-0.88^{+0.67}_{-0.95}$	$-0.25^{+0.27}_{-0.33}$	$-1.15^{+0.61}_{-0.95}$
24	2	24	$1.56^{+1.92}_{-1.06}$	0.88	4	33	$3.85^{+2.35}_{-1.86}$	0.91	3	75	$2.70^{+1.92}_{-1.72}$	0.91	$-0.24^{+0.36}_{-0.40}$	$0.12^{+0.37}_{-0.33}$	$-0.11^{+0.41}_{-0.43}$
25	2	159	$0.00^{+2.50}_{-0.00}$	0.74	5	98	$4.57^{+3.27}_{-2.00}$	0.82	3	57	$2.74^{+2.36}_{-1.72}$	0.81	$-0.38^{+0.48}_{-0.68}$	$0.20^{+0.35}_{-0.36}$	$-0.19^{+0.52}_{-0.72}$
26	1	9	$0.00^{+2.05}_{-0.00}$	0.77	3	22	$3.08^{+2.03}_{-1.96}$	0.83	5	23	$5.28^{+3.00}_{-2.34}$	0.81	$-0.36^{+0.53}_{-0.55}$	$-0.25^{+0.37}_{-0.31}$	$-0.55^{+0.44}_{-0.55}$

Table A.7 FIELD 4: Source Photometry and X-ray Colors

Src_ID	SOFT BAND (0.5 - 1.0 keV)				MEDIUM BAND (1.0 - 2.5 keV)				HARD BAND (2.5 - 7.0 keV)				Col1	Col2	Col3
	Counts			Eff.Area	Counts			Eff.Area	Counts			Eff.Area			
	Obs.	Bkg.	Net	Ratio	Obs.	Bkg.	Net	Ratio	Obs.	Bkg.	Net	Ratio			
(1)	(2)	(3)	(4)	(5)	(6)	(7)	(8)	(9)	(10)	(11)	(12)	(13)	(14)	(15)	(16)
27	0	17	$0.00^{+0.54}_{-0.00}$	0.91	2	34	$1.45^{+1.78}_{-0.99}$	0.95	6	62	$5.72^{+2.79}_{-2.23}$	0.95	$-0.58^{+0.60}_{-1.09}$	$-0.39^{+0.31}_{-0.41}$	$-1.07^{+0.57}_{-0.99}$
28	1	22	$0.50^{+1.29}_{-0.50}$	0.95	3	31	$2.67^{+1.90}_{-1.46}$	0.98	3	59	$2.49^{+2.04}_{-1.33}$	0.98	$-0.36^{+0.45}_{-0.52}$	$-0.02^{+0.38}_{-0.33}$	$-0.34^{+0.44}_{-0.53}$
29	1	18	$0.00^{+1.93}_{-0.00}$	0.75	9	45	$9.76^{+3.36}_{-3.54}$	0.85	4	42	$3.25^{+3.02}_{-1.61}$	0.83	$-0.72^{+0.39}_{-0.66}$	$0.35^{+0.29}_{-0.29}$	$-0.43^{+0.51}_{-0.66}$
30	2	36	$1.43^{+1.85}_{-0.87}$	0.96	2	42	$1.41^{+1.78}_{-0.89}$	0.99	2	56	$1.47^{+1.69}_{-0.98}$	0.98	$0.02^{+0.41}_{-0.43}$	$-0.02^{+0.44}_{-0.41}$	$0.02^{+0.41}_{-0.44}$
31	0	12	$0.00^{+0.67}_{-0.00}$	0.74	3	28	$3.01^{+1.86}_{-1.99}$	0.86	7	38	$8.08^{+2.63}_{-3.45}$	0.85	$-0.86^{+0.75}_{-0.90}$	$-0.33^{+0.29}_{-0.35}$	$-1.18^{+0.67}_{-0.89}$
32	0	21	$0.00^{+0.61}_{-0.00}$	0.82	4	33	$3.96^{+2.55}_{-1.85}$	0.87	3	59	$2.85^{+2.14}_{-1.68}$	0.86	$-0.96^{+0.67}_{-0.92}$	$0.11^{+0.35}_{-0.33}$	$-0.96^{+0.80}_{-0.83}$
33	0	30	$0.00^{+0.54}_{-0.00}$	0.92	3	43	$2.74^{+1.89}_{-1.54}$	0.96	3	72	$2.58^{+2.00}_{-1.46}$	0.95	$-0.84^{+0.66}_{-0.96}$	$-0.01^{+0.38}_{-0.33}$	$-0.83^{+0.65}_{-0.99}$
34	1	13	$0.00^{+1.79}_{-0.00}$	0.91	1	23	$0.00^{+1.66}_{-0.00}$	0.94	3	29	$2.66^{+2.02}_{-1.56}$	0.92	$-0.03^{+0.76}_{-0.60}$	$-0.41^{+0.52}_{-0.57}$	$-0.38^{+0.48}_{-0.54}$
35	0	21	$0.00^{+1.12}_{-0.00}$	0.44	4	29	$8.11^{+5.05}_{-3.76}$	0.44	1	53	$1.25^{+2.69}_{-1.25}$	0.43	$-0.95^{+0.62}_{-0.97}$	$0.47^{+0.52}_{-0.42}$	$-0.47^{+0.75}_{-1.07}$
36	1	26	$0.00^{+2.10}_{-0.00}$	0.76	4	39	$4.21^{+2.84}_{-1.97}$	0.80	2	56	$1.56^{+2.13}_{-1.22}$	0.78	$-0.49^{+0.48}_{-0.53}$	$0.25^{+0.44}_{-0.37}$	$-0.20^{+0.54}_{-0.64}$
37	0	11	$0.00^{+0.64}_{-0.00}$	0.78	1	21	$0.00^{+1.79}_{-0.00}$	0.86	5	44	$4.96^{+2.85}_{-2.18}$	0.86	$-0.41^{+0.85}_{-1.08}$	$-0.58^{+0.46}_{-0.56}$	$-0.94^{+0.57}_{-1.02}$
38	15	40	$24.78^{+7.36}_{-8.08}$	0.50	18	60	$20.70^{+5.96}_{-6.56}$	0.68	1	19	$0.00^{+1.29}_{-0.00}$	0.67	$0.09^{+0.18}_{-0.20}$	$1.11^{+0.98}_{-0.44}$	$1.21^{+0.96}_{-0.46}$

Notes: The area ratio is in units of 10^{-2}. The colors are defined as Col1=$\log_{10}(S/M)$, Col2=$\log_{10}(M/H)$, and Col3=$\log_{10}(S/H)$.

Table A.8 FIELD 5: Source Photometry and X-ray Colors

Src_ID	SOFT BAND (0.5 - 1.0 keV)				MEDIUM BAND (1.0 - 2.5 keV)				HARD BAND (2.5 - 7.0 keV)				Col1	Col2	Col3
	Counts			Eff.Area	Counts			Eff.Area	Counts			Eff.Area			
	Obs.	Bkg.	Net	Ratio	Obs.	Bkg.	Net	Ratio	Obs.	Bkg.	Net	Ratio			
(1)	(2)	(3)	(4)	(5)	(6)	(7)	(8)	(9)	(10)	(11)	(12)	(13)	(14)	(15)	(16)
1	98	25	$115.53^{+11.51}_{-11.74}$	0.85	807	56	$886.16^{+31.29}_{-30.80}$	0.91	1063	138	$844.42^{+25.26}_{-26.40}$	1.26	$-0.88^{+0.04}_{-0.05}$	$0.02^{+0.02}_{-0.02}$	$-0.86^{+0.04}_{-0.05}$
2	14	15	$23.48^{+7.18}_{-5.68}$	0.57	48	37	$64.32^{+9.21}_{-9.27}$	0.74	85	70	$82.35^{+9.08}_{-8.75}$	1.03	$-0.40^{+0.11}_{-0.15}$	$-0.11^{+0.08}_{-0.07}$	$-0.52^{+0.12}_{-0.12}$
3	5	27	$6.00^{+3.47}_{-2.57}$	0.71	45	57	$52.60^{+8.32}_{-7.59}$	0.84	54	104	$45.20^{+7.10}_{-5.54}$	1.15	$-0.89^{+0.22}_{-0.20}$	$0.07^{+0.08}_{-0.09}$	$-0.79^{+0.19}_{-0.23}$
4	4	27	$5.08^{+3.22}_{-2.53}$	0.67	33	30	$41.27^{+8.11}_{-6.52}$	0.78	37	89	$33.97^{+5.30}_{-5.93}$	1.07	$-0.83^{+0.22}_{-0.24}$	$0.10^{+0.11}_{-0.10}$	$-0.73^{+0.22}_{-0.24}$
5	3	24	$3.34^{+2.33}_{-1.90}$	0.78	28	33	$31.45^{+6.68}_{-5.39}$	0.87	14	38	$10.98^{+3.59}_{-2.55}$	1.20	$-0.88^{+0.25}_{-0.27}$	$0.44^{+0.13}_{-0.15}$	$-0.45^{+0.27}_{-0.27}$
6	9	34	$10.13^{+3.93}_{-3.54}$	0.79	44	52	$52.34^{+7.90}_{-8.17}$	0.82	19	62	$15.44^{+3.80}_{-3.82}$	1.13	$-0.68^{+0.17}_{-0.17}$	$0.53^{+0.12}_{-0.13}$	$-0.18^{+0.20}_{-0.17}$
7	3	14	$2.93^{+1.87}_{-1.86}$	0.88	23	26	$24.82^{+5.53}_{-5.06}$	0.90	17	56	$12.50^{+3.67}_{-2.91}$	1.24	$-0.85^{+0.26}_{-0.30}$	$0.28^{+0.15}_{-0.14}$	$-0.55^{+0.26}_{-0.31}$
8	4	16	$3.52^{+2.30}_{-1.72}$	0.95	23	22	$23.20^{+5.42}_{-4.45}$	0.96	7	37	$5.06^{+1.72}_{-2.17}$	1.33	$-0.72^{+0.21}_{-0.26}$	$0.66^{+0.20}_{-0.19}$	$-0.10^{+0.29}_{-0.26}$
9	2	23	$2.51^{+3.20}_{-1.58}$	0.55	10	34	$13.71^{+4.82}_{-4.12}$	0.69	4	56	$3.58^{+2.33}_{-1.67}$	0.96	$-0.53^{+0.29}_{-0.35}$	$0.54^{+0.24}_{-0.27}$	$-0.00^{+0.34}_{-0.39}$
10	5	34	$6.02^{+3.42}_{-2.65}$	0.71	14	35	$15.26^{+4.99}_{-3.65}$	0.85	5	75	$3.43^{+2.09}_{-1.60}$	1.18	$-0.34^{+0.21}_{-0.25}$	$0.58^{+0.26}_{-0.22}$	$0.22^{+0.31}_{-0.28}$
11	2	23	$0.00^{+2.93}_{-0.00}$	0.76	11	36	$11.27^{+3.81}_{-3.65}$	0.87	8	64	$4.92^{+2.57}_{-2.03}$	1.21	$-0.68^{+0.41}_{-0.49}$	$0.32^{+0.24}_{-0.23}$	$-0.36^{+0.45}_{-0.51}$
12	1	40	$0.54^{+1.36}_{-0.54}$	0.90	4	46	$3.77^{+2.38}_{-1.74}$	0.93	8	86	$5.94^{+2.22}_{-2.08}$	1.29	$-0.49^{+0.44}_{-0.47}$	$-0.12^{+0.23}_{-0.29}$	$-0.61^{+0.40}_{-0.45}$
13	1	16	$0.00^{+1.41}_{-0.00}$	0.94	7	29	$6.49^{+2.88}_{-2.59}$	0.94	6	58	$3.28^{+2.11}_{-1.57}$	1.30	$-0.71^{+0.46}_{-0.71}$	$0.23^{+0.31}_{-0.26}$	$-0.49^{+0.54}_{-0.69}$
14	3	22	$2.94^{+1.90}_{-1.81}$	0.89	7	32	$6.99^{+3.08}_{-2.61}$	0.90	4	68	$2.26^{+1.86}_{-1.23}$	1.25	$-0.32^{+0.28}_{-0.34}$	$0.41^{+0.30}_{-0.30}$	$0.06^{+0.38}_{-0.36}$
15	1	25	$0.00^{+3.61}_{-0.00}$	0.40	8	34	$18.51^{+6.80}_{-6.67}$	0.41	2	73	$0.00^{+3.83}_{-0.00}$	0.57	$-0.85^{+0.52}_{-0.53}$	$0.78^{+0.49}_{-0.44}$	$0.01^{+0.70}_{-0.79}$
16	3	20	$2.77^{+2.00}_{-1.49}$	0.94	3	33	$2.67^{+1.96}_{-1.42}$	0.97	2	70	$1.11^{+1.24}_{-0.72}$	1.34	$0.01^{+0.34}_{-0.35}$	$0.30^{+0.39}_{-0.38}$	$0.31^{+0.39}_{-0.38}$
17	0	42	$0.00^{+0.53}_{-0.00}$	0.93	3	27	$2.78^{+1.90}_{-1.51}$	0.96	5	74	$3.16^{+2.06}_{-1.18}$	1.33	$-0.84^{+0.64}_{-0.98}$	$-0.05^{+0.30}_{-0.32}$	$-0.92^{+0.63}_{-0.95}$
18	3	12	$2.75^{+1.80}_{-1.68}$	0.95	6	24	$5.04^{+3.09}_{-1.81}$	0.97	2	63	$0.00^{+1.43}_{-0.00}$	1.34	$-0.24^{+0.29}_{-0.35}$	$0.68^{+0.62}_{-0.46}$	$0.41^{+0.65}_{-0.52}$
19	0	46	$0.00^{+0.56}_{-0.00}$	0.89	6	30	$5.53^{+3.19}_{-1.88}$	0.94	2	84	$1.10^{+1.23}_{-0.80}$	1.30	$-1.10^{+0.60}_{-0.96}$	$0.54^{+0.42}_{-0.30}$	$-0.42^{+0.59}_{-1.11}$
20	0	31	$0.00^{+0.59}_{-0.00}$	0.84	4	51	$3.70^{+2.55}_{-1.67}$	0.91	4	71	$2.64^{+1.88}_{-1.17}$	1.26	$-0.99^{+0.71}_{-0.88}$	$0.12^{+0.34}_{-0.28}$	$-0.77^{+0.63}_{-0.96}$
21	0	17	$0.00^{+0.61}_{-0.00}$	0.81	3	27	$3.09^{+2.07}_{-1.83}$	0.84	5	56	$3.63^{+2.11}_{-1.59}$	1.17	$-0.82^{+0.65}_{-0.98}$	$-0.05^{+0.31}_{-0.34}$	$-0.86^{+0.60}_{-0.98}$
22	2	28	$1.85^{+2.28}_{-1.27}$	0.74	4	43	$3.95^{+2.71}_{-1.83}$	0.85	2	88	$0.95^{+1.21}_{-0.95}$	1.17	$-0.18^{+0.35}_{-0.42}$	$0.45^{+0.43}_{-0.43}$	$0.27^{+0.46}_{-0.53}$
23	1	25	$0.00^{+2.31}_{-0.00}$	0.65	6	46	$6.80^{+3.42}_{-2.73}$	0.77	4	65	$2.95^{+1.98}_{-1.62}$	1.07	$-0.53^{+0.42}_{-0.63}$	$0.34^{+0.29}_{-0.32}$	$-0.26^{+0.50}_{-0.62}$
24	2	11	$1.89^{+2.22}_{-1.24}$	0.76	4	11	$4.03^{+2.51}_{-1.89}$	0.87	1	20	$0.00^{+1.35}_{-0.00}$	1.21	$-0.22^{+0.38}_{-0.36}$	$0.61^{+0.56}_{-0.42}$	$0.45^{+0.56}_{-0.53}$
25	1	43	$0.00^{+2.02}_{-0.00}$	0.65	5	48	$5.25^{+3.04}_{-2.37}$	0.80	3	69	$1.68^{+1.82}_{-1.18}$	1.10	$-0.57^{+0.55}_{-0.65}$	$0.37^{+0.39}_{-0.36}$	$-0.18^{+0.64}_{-0.71}$
26	0	26	$0.00^{+0.63}_{-0.00}$	0.78	6	30	$5.59^{+3.37}_{-2.00}$	0.89	3	62	$1.52^{+1.58}_{-1.13}$	1.23	$-1.06^{+0.61}_{-0.96}$	$0.48^{+0.37}_{-0.36}$	$-0.69^{+0.80}_{-0.93}$

Table A.8 FIELD 5: Source Photometry and X-ray Colors

Src_ID	SOFT BAND (0.5 - 1.0 keV)				MEDIUM BAND (1.0 - 2.5 keV)				HARD BAND (2.5 - 7.0 keV)				Col1	Col2	Col3
	Counts			Eff.Area	Counts			Eff.Area	Counts			Eff.Area			
	Obs.	Bkg.	Net	Ratio	Obs.	Bkg.	Net	Ratio	Obs.	Bkg.	Net	Ratio			
(1)	(2)	(3)	(4)	(5)	(6)	(7)	(8)	(9)	(10)	(11)	(12)	(13)	(14)	(15)	(16)
27	0	18	$0.00^{+0.65}_{-0.00}$	0.76	2	34	$1.56^{+2.11}_{-0.98}$	0.85	4	80	$2.82^{+2.01}_{-1.25}$	1.18	$-0.66^{+0.71}_{-0.97}$	$-0.11^{+0.34}_{-0.40}$	$-0.86^{+0.74}_{-0.86}$
28	1	38	$0.00^{+2.24}_{-0.00}$	0.72	2	34	$1.69^{+2.13}_{-1.10}$	0.81	3	64	$2.31^{+1.54}_{-1.39}$	1.13	$-0.19^{+0.53}_{-0.58}$	$0.02^{+0.38}_{-0.43}$	$-0.20^{+0.49}_{-0.54}$
29	1	9	$0.66^{+1.54}_{-0.66}$	0.77	3	16	$2.96^{+2.13}_{-1.61}$	0.88	2	33	$1.23^{+1.29}_{-0.87}$	1.22	$-0.33^{+0.47}_{-0.48}$	$0.30^{+0.41}_{-0.39}$	$-0.02^{+0.50}_{-0.54}$
30	7	34	$8.34^{+4.12}_{-2.86}$	0.74	1	52	$0.00^{+1.62}_{-0.00}$	0.85	0	82	$0.00^{+0.42}_{-0.00}$	1.17	$0.79^{+0.66}_{-0.45}$	$0.59^{+1.07}_{-0.97}$	$1.41^{+0.91}_{-0.64}$
31	2	31	$1.67^{+2.02}_{-1.14}$	0.83	3	40	$2.73^{+2.01}_{-1.58}$	0.91	1	90	$0.00^{+1.09}_{-0.00}$	1.26	$-0.10^{+0.38}_{-0.43}$	$0.52^{+0.72}_{-0.49}$	$0.42^{+0.72}_{-0.56}$
32	0	26	$0.00^{+0.68}_{-0.00}$	0.73	4	41	$4.10^{+2.68}_{-1.98}$	0.82	1	64	$0.00^{+1.20}_{-0.00}$	1.14	$-0.91^{+0.64}_{-0.96}$	$0.65^{+0.68}_{-0.50}$	$-0.20^{+0.92}_{-1.13}$
33	0	25	$0.00^{+0.58}_{-0.00}$	0.85	2	35	$1.50^{+1.91}_{-0.96}$	0.92	2	61	$1.10^{+1.32}_{-0.75}$	1.27	$-0.68^{+0.71}_{-0.97}$	$0.12^{+0.45}_{-0.41}$	$-0.41^{+0.59}_{-1.10}$
34	0	22	$0.00^{+0.64}_{-0.00}$	0.77	4	34	$3.79^{+2.89}_{-1.63}$	0.85	0	53	$0.00^{+0.42}_{-0.00}$	1.18	$-0.91^{+0.64}_{-0.96}$	$1.10^{+0.94}_{-0.65}$	$0.18^{+1.19}_{-1.17}$
35	1	6	$0.54^{+1.38}_{-0.49}$	0.93	1	15	$0.52^{+1.27}_{-0.52}$	0.96	1	25	$0.48^{+0.81}_{-0.48}$	1.33	$0.01^{+0.58}_{-0.57}$	$0.15^{+0.56}_{-0.60}$	$0.17^{+0.56}_{-0.59}$
36	0	14	$0.00^{+1.12}_{-0.00}$	0.44	5	25	$9.53^{+5.57}_{-4.19}$	0.44	2	45	$0.00^{+3.71}_{-0.00}$	0.61	$-0.98^{+0.57}_{-1.02}$	$0.55^{+0.52}_{-0.42}$	$-0.39^{+0.74}_{-1.14}$
37	1	21	$0.00^{+1.90}_{-0.00}$	0.86	1	30	$0.00^{+1.70}_{-0.00}$	0.93	2	57	$0.96^{+1.28}_{-0.76}$	1.29	$-0.01^{+0.72}_{-0.62}$	$-0.09^{+0.56}_{-0.62}$	$-0.03^{+0.54}_{-0.61}$

Notes: The area ratio is in units of 10^{-2}. The colors are defined as Col1=$\log_{10}(S/M)$, Col2=$\log_{10}(M/H)$, and Col3=$\log_{10}(S/H)$.

Table A.9 FIELD 6: Source Photometry and X-ray Colors

Src_ID	SOFT BAND (0.5 - 1.0 keV)				MEDIUM BAND (1.0 - 2.5 keV)				HARD BAND (2.5 - 7.0 keV)				Col1	Col2	Col3
	Counts			Eff.Area	Counts			Eff.Area	Counts			Eff.Area			
	Obs.	Bkg.	Net	Ratio	Obs.	Bkg.	Net	Ratio	Obs.	Bkg.	Net	Ratio			
(1)	(2)	(3)	(4)	(5)	(6)	(7)	(8)	(9)	(10)	(11)	(12)	(13)	(14)	(15)	(16)
1	202	63	$247.35^{+16.68}_{-17.95}$	0.82	2772	172	$3182.30^{+53.13}_{-66.77}$	0.87	2149	214	$1774.27^{+42.27}_{-34.33}$	1.21	$-1.11^{+0.03}_{-0.03}$	$0.25^{+0.01}_{-0.01}$	$-0.85^{+0.03}_{-0.04}$
2	18	32	$23.20^{+6.14}_{-5.33}$	0.73	203	44	$234.05^{+15.81}_{-16.88}$	0.87	270	103	$223.90^{+13.83}_{-13.49}$	1.20	$-0.97^{+0.10}_{-0.11}$	$0.02^{+0.04}_{-0.04}$	$-0.94^{+0.09}_{-0.13}$
3	3	24	$3.08^{+2.11}_{-1.76}$	0.85	33	48	$35.66^{+6.20}_{-6.16}$	0.92	11	84	$8.06^{+2.82}_{-2.30}$	1.27	$-0.97^{+0.25}_{-0.26}$	$0.61^{+0.16}_{-0.15}$	$-0.33^{+0.25}_{-0.30}$
4	1	31	$0.00^{+2.09}_{-0.00}$	0.76	14	58	$15.24^{+5.04}_{-3.57}$	0.85	15	75	$11.95^{+3.64}_{-2.82}$	1.18	$-1.01^{+0.44}_{-0.47}$	$0.11^{+0.17}_{-0.15}$	$-0.84^{+0.39}_{-0.52}$
5	5	51	$6.09^{+4.11}_{-2.40}$	0.66	11	162	$13.94^{+4.89}_{-4.25}$	0.71	11	203	$9.73^{+3.68}_{-2.93}$	0.99	$-0.28^{+0.23}_{-0.25}$	$0.17^{+0.17}_{-0.22}$	$-0.14^{+0.24}_{-0.24}$
6	1	41	$0.00^{+1.98}_{-0.00}$	0.76	12	56	$12.70^{+4.36}_{-3.37}$	0.88	6	71	$4.49^{+2.04}_{-1.87}$	1.22	$-0.83^{+0.37}_{-0.61}$	$0.46^{+0.21}_{-0.24}$	$-0.41^{+0.39}_{-0.64}$
7	0	48	$0.00^{+0.54}_{-0.00}$	0.91	10	56	$10.23^{+3.94}_{-2.89}$	0.91	6	98	$4.37^{+2.07}_{-1.72}$	1.26	$-1.28^{+0.55}_{-0.99}$	$0.35^{+0.23}_{-0.21}$	$-0.97^{+0.59}_{-0.97}$
8	1	26	$0.00^{+2.15}_{-0.00}$	0.73	11	33	$12.70^{+4.62}_{-3.49}$	0.80	4	58	$2.88^{+2.10}_{-1.36}$	1.11	$-0.89^{+0.41}_{-0.53}$	$0.56^{+0.28}_{-0.25}$	$-0.31^{+0.48}_{-0.55}$
9	0	40	$0.00^{+0.50}_{-0.00}$	0.99	9	55	$8.27^{+3.37}_{-2.50}$	1.00	5	95	$3.09^{+1.87}_{-1.25}$	1.38	$-1.23^{+0.55}_{-1.00}$	$0.37^{+0.26}_{-0.23}$	$-0.83^{+0.53}_{-1.05}$
10	0	38	$0.00^{+0.53}_{-0.00}$	0.94	6	56	$5.57^{+2.87}_{-2.03}$	0.97	7	74	$4.55^{+2.42}_{-1.43}$	1.34	$-1.11^{+0.60}_{-0.96}$	$0.07^{+0.25}_{-0.23}$	$-1.15^{+0.73}_{-0.83}$
11	1	17	$0.00^{+1.99}_{-0.00}$	0.74	7	34	$7.46^{+3.13}_{-2.93}$	0.85	7	54	$4.94^{+2.57}_{-1.82}$	1.18	$-0.70^{+0.49}_{-0.55}$	$0.13^{+0.27}_{-0.22}$	$-0.54^{+0.48}_{-0.57}$
12	1	20	$0.00^{+1.92}_{-0.00}$	0.86	5	31	$4.60^{+2.80}_{-1.83}$	0.93	5	49	$3.49^{+1.83}_{-1.52}$	1.29	$-0.55^{+0.44}_{-0.51}$	$0.13^{+0.29}_{-0.26}$	$-0.36^{+0.39}_{-0.55}$
13	1	35	$0.00^{+2.01}_{-0.00}$	0.75	7	48	$7.08^{+3.50}_{-2.42}$	0.87	3	71	$2.04^{+1.38}_{-1.37}$	1.20	$-0.64^{+0.43}_{-0.60}$	$0.48^{+0.37}_{-0.29}$	$-0.20^{+0.57}_{-0.60}$
14	0	85	$0.00^{+0.71}_{-0.00}$	0.70	2	62	$1.56^{+2.39}_{-1.15}$	0.74	9	82	$8.14^{+3.09}_{-2.63}$	1.02	$-0.69^{+0.77}_{-0.96}$	$-0.47^{+0.34}_{-0.38}$	$-1.18^{+0.66}_{-0.89}$
15	0	28	$0.00^{+0.63}_{-0.00}$	0.78	3	48	$3.11^{+2.22}_{-1.74}$	0.83	7	85	$5.31^{+2.79}_{-1.70}$	1.15	$-0.83^{+0.66}_{-0.96}$	$-0.18^{+0.28}_{-0.32}$	$-1.14^{+0.73}_{-0.83}$
16	2	39	$1.63^{+2.07}_{-1.21}$	0.80	5	53	$4.77^{+2.77}_{-2.02}$	0.90	3	66	$1.98^{+1.43}_{-1.22}$	1.25	$-0.31^{+0.38}_{-0.38}$	$0.35^{+0.35}_{-0.32}$	$0.05^{+0.41}_{-0.45}$
17	2	15	$1.61^{+2.11}_{-1.08}$	0.82	5	37	$4.98^{+2.82}_{-2.09}$	0.88	3	61	$2.01^{+1.47}_{-1.24}$	1.22	$-0.32^{+0.35}_{-0.38}$	$0.34^{+0.35}_{-0.31}$	$0.02^{+0.42}_{-0.40}$
18	1	32	$0.62^{+1.33}_{-0.62}$	0.87	7	52	$7.09^{+3.07}_{-2.51}$	0.92	1	91	$0.00^{+1.25}_{-0.00}$	1.28	$-0.69^{+0.40}_{-0.48}$	$0.81^{+0.58}_{-0.37}$	$0.21^{+0.62}_{-0.65}$
19	1	20	$0.00^{+1.75}_{-0.00}$	0.72	6	37	$5.63^{+3.13}_{-2.50}$	0.85	7	64	$4.31^{+2.58}_{-1.82}$	1.18	$-0.64^{+0.54}_{-0.70}$	$0.10^{+0.29}_{-0.29}$	$-0.55^{+0.57}_{-0.67}$
20	0	34	$0.00^{+0.61}_{-0.00}$	0.81	5	68	$5.24^{+2.89}_{-2.23}$	0.84	3	84	$2.10^{+1.56}_{-1.27}$	1.17	$-0.97^{+0.55}_{-1.03}$	$0.34^{+0.34}_{-0.32}$	$-0.83^{+0.81}_{-0.83}$
21	0	32	$0.00^{+0.52}_{-0.00}$	0.95	6	41	$5.50^{+2.90}_{-1.99}$	0.97	1	53	$0.35^{+0.91}_{-0.35}$	1.35	$-1.12^{+0.61}_{-0.95}$	$0.77^{+0.51}_{-0.38}$	$-0.30^{+0.75}_{-1.07}$
22	0	32	$0.00^{+0.66}_{-0.00}$	0.75	4	39	$3.54^{+2.69}_{-1.69}$	0.88	6	94	$4.02^{+2.16}_{-1.77}$	1.21	$-0.82^{+0.58}_{-1.03}$	$-0.06^{+0.36}_{-0.25}$	$-0.87^{+0.63}_{-0.96}$
23	3	25	$2.70^{+1.96}_{-1.44}$	0.97	3	39	$2.50^{+2.10}_{-1.27}$	0.98	0	89	$0.00^{+0.37}_{-0.00}$	1.35	$0.01^{+0.35}_{-0.34}$	$1.07^{+0.89}_{-0.73}$	$1.07^{+0.89}_{-0.73}$
24	1	21	$0.00^{+1.93}_{-0.00}$	0.84	5	36	$4.84^{+2.67}_{-2.06}$	0.91	0	47	$0.00^{+0.39}_{-0.00}$	1.26	$-0.49^{+0.38}_{-0.58}$	$1.23^{+0.90}_{-0.67}$	$0.71^{+0.99}_{-0.90}$
25	1	34	$0.00^{+1.68}_{-0.00}$	0.76	5	44	$4.57^{+2.95}_{-2.06}$	0.87	1	39	$0.00^{+1.02}_{-0.00}$	1.20	$-0.58^{+0.55}_{-0.69}$	$0.76^{+0.77}_{-0.51}$	$0.31^{+0.84}_{-1.02}$
26	0	39	$0.00^{+0.55}_{-0.00}$	0.90	4	61	$3.78^{+2.42}_{-1.74}$	0.92	1	90	$0.32^{+0.99}_{-0.32}$	1.28	$-0.94^{+0.63}_{-0.96}$	$0.62^{+0.53}_{-0.42}$	$-0.30^{+0.79}_{-1.05}$

Table A.9 FIELD 4: Source Photometry and X-ray Colors

Src_ID	SOFT BAND (0.5 - 1.0 keV)				MEDIUM BAND (1.0 - 2.5 keV)				HARD BAND (2.5 - 7.0 keV)				Col1	Col2	Col3
	Counts			Eff.Area	Counts			Eff.Area	Counts			Eff.Area			
	Obs.	Bkg.	Net	Ratio	Obs.	Bkg.	Net	Ratio	Obs.	Bkg.	Net	Ratio			
(1)	(2)	(3)	(4)	(5)	(6)	(7)	(8)	(9)	(10)	(11)	(12)	(13)	(14)	(15)	(16)
27	2	15	$1.82^{+2.24}_{-1.20}$	0.76	2	31	$1.63^{+1.89}_{-1.21}$	0.85	0	49	$0.00^{+0.42}_{-0.00}$	1.17	$0.07^{+0.45}_{-0.45}$	$0.86^{+0.97}_{-0.74}$	$0.82^{+1.05}_{-0.63}$
28	1	50	$0.00^{+1.95}_{-0.00}$	0.72	2	55	$1.36^{+1.67}_{-1.36}$	0.85	6	96	$4.36^{+2.23}_{-1.82}$	1.17	$-0.14^{+0.61}_{-0.75}$	$-0.27^{+0.35}_{-0.45}$	$-0.48^{+0.51}_{-0.61}$

Notes: The area ratio is in units of 10^{-2}. The colors are defined as Col1=$\log_{10}(S/M)$, Col2=$\log_{10}(M/H)$, and Col3=$\log_{10}(S/H)$.

Table A.10 FIELD 7: Source Photometry and X-ray Colors

Src_ID	SOFT BAND (0.5 - 1.0 keV)				MEDIUM BAND (1.0 - 2.5 keV)				HARD BAND (2.5 - 7.0 keV)				Col1	Col2	Col3
	Counts			Eff.Area	Counts			Eff.Area	Counts			Eff.Area			
	Obs.	Bkg.	Net	Ratio	Obs.	Bkg.	Net	Ratio	Obs.	Bkg.	Net	Ratio			
(1)	(2)	(3)	(4)	(5)	(6)	(7)	(8)	(9)	(10)	(11)	(12)	(13)	(14)	(15)	(16)
1	3	25	$2.91^{+1.86}_{-1.81}$	0.90	81	45	$85.72^{+9.22}_{-9.73}$	0.94	81	60	$86.12^{+9.32}_{-9.79}$	0.94	$-1.40^{+0.26}_{-0.26}$	$-0.01^{+0.07}_{-0.06}$	$-1.40^{+0.27}_{-0.25}$
2	8	26	$9.58^{+3.48}_{-3.40}$	0.80	27	21	$29.50^{+6.52}_{-5.06}$	0.89	9	49	$10.77^{+2.53}_{-4.20}$	0.87	$-0.45^{+0.15}_{-0.20}$	$0.46^{+0.17}_{-0.17}$	$-0.01^{+0.21}_{-0.21}$
3	0	20	$0.00^{+0.71}_{-0.00}$	0.70	15	41	$18.89^{+5.38}_{-4.58}$	0.76	18	62	$22.78^{+5.92}_{-5.13}$	0.76	$-1.56^{+0.69}_{-0.84}$	$-0.08^{+0.15}_{-0.15}$	$-1.65^{+0.70}_{-0.83}$
4	2	16	$1.87^{+2.29}_{-1.28}$	0.74	23	46	$26.68^{+5.80}_{-5.50}$	0.84	11	55	$12.46^{+4.10}_{-3.78}$	0.83	$-0.96^{+0.32}_{-0.32}$	$0.31^{+0.17}_{-0.15}$	$-0.66^{+0.36}_{-0.31}$
5	3	36	$2.50^{+2.16}_{-1.55}$	0.89	19	46	$19.05^{+5.20}_{-3.94}$	0.94	10	79	$9.63^{+3.58}_{-3.10}$	0.93	$-0.76^{+0.28}_{-0.29}$	$0.28^{+0.18}_{-0.17}$	$-0.49^{+0.32}_{-0.29}$
6	0	23	$0.00^{+0.59}_{-0.00}$	0.83	4	36	$3.77^{+2.38}_{-1.81}$	0.92	21	58	$21.97^{+5.73}_{-4.24}$	0.91	$-0.91^{+0.64}_{-0.96}$	$-0.69^{+0.23}_{-0.24}$	$-1.71^{+0.69}_{-0.84}$
7	2	22	$1.92^{+2.36}_{-1.31}$	0.72	16	38	$18.11^{+4.83}_{-4.41}$	0.85	7	64	$7.52^{+3.37}_{-2.75}$	0.84	$-0.75^{+0.29}_{-0.35}$	$0.35^{+0.20}_{-0.20}$	$-0.41^{+0.33}_{-0.37}$
8	4	18	$4.58^{+2.97}_{-2.59}$	0.69	11	24	$12.28^{+4.40}_{-3.64}$	0.81	18	31	$21.05^{+5.68}_{-4.93}$	0.79	$-0.35^{+0.26}_{-0.31}$	$-0.21^{+0.15}_{-0.20}$	$-0.56^{+0.23}_{-0.30}$
9	2	34	$1.66^{+2.10}_{-1.23}$	0.79	14	53	$14.79^{+4.86}_{-3.49}$	0.88	9	103	$9.05^{+4.01}_{-2.76}$	0.87	$-0.76^{+0.34}_{-0.34}$	$0.17^{+0.22}_{-0.16}$	$-0.54^{+0.32}_{-0.39}$
10	2	34	$2.31^{+2.95}_{-1.45}$	0.60	13	59	$17.12^{+4.37}_{-5.02}$	0.76	5	91	$6.40^{+3.07}_{-2.82}$	0.74	$-0.67^{+0.33}_{-0.30}$	$0.37^{+0.25}_{-0.20}$	$-0.25^{+0.33}_{-0.38}$
11	2	31	$1.59^{+2.03}_{-0.99}$	0.87	11	48	$11.60^{+4.29}_{-3.10}$	0.88	5	75	$5.37^{+2.52}_{-2.42}$	0.88	$-0.69^{+0.33}_{-0.31}$	$0.33^{+0.23}_{-0.23}$	$-0.33^{+0.32}_{-0.39}$
12	1	11	$0.00^{+1.89}_{-0.00}$	0.87	10	23	$9.91^{+4.25}_{-2.58}$	0.91	4	41	$3.81^{+2.33}_{-1.93}$	0.90	$-0.81^{+0.36}_{-0.53}$	$0.37^{+0.28}_{-0.24}$	$-0.44^{+0.42}_{-0.55}$
13	0	20	$0.00^{+0.59}_{-0.00}$	0.84	9	23	$9.19^{+3.84}_{-2.69}$	0.90	5	42	$4.81^{+3.09}_{-1.81}$	0.88	$-1.20^{+0.55}_{-1.00}$	$0.23^{+0.24}_{-0.23}$	$-1.05^{+0.63}_{-0.94}$
14	2	23	$1.51^{+1.85}_{-1.03}$	0.91	6	25	$5.80^{+2.80}_{-2.27}$	0.94	5	51	$4.68^{+2.59}_{-2.05}$	0.93	$-0.38^{+0.31}_{-0.41}$	$0.07^{+0.28}_{-0.26}$	$-0.33^{+0.36}_{-0.39}$
15	2	29	$1.63^{+2.07}_{-1.05}$	0.84	9	36	$9.71^{+3.06}_{-3.34}$	0.92	1	70	$0.00^{+1.73}_{-0.00}$	0.91	$-0.58^{+0.34}_{-0.32}$	$0.90^{+0.46}_{-0.50}$	$0.29^{+0.59}_{-0.54}$
16	0	36	$0.00^{+0.63}_{-0.00}$	0.78	7	32	$7.87^{+3.70}_{-2.68}$	0.81	4	66	$4.38^{+2.74}_{-2.09}$	0.79	$-1.13^{+0.56}_{-1.00}$	$0.22^{+0.28}_{-0.27}$	$-1.12^{+0.80}_{-0.79}$
17	0	13	$0.00^{+0.56}_{-0.00}$	0.89	10	30	$9.96^{+3.50}_{-3.21}$	0.92	3	46	$1.71^{+1.76}_{-1.71}$	0.90	$-1.38^{+0.67}_{-0.87}$	$0.51^{+0.45}_{-0.31}$	$-0.80^{+0.80}_{-0.99}$
18	2	26	$2.14^{+2.71}_{-1.53}$	0.62	5	30	$5.51^{+3.06}_{-2.33}$	0.80	2	57	$1.45^{+1.75}_{-1.45}$	0.79	$-0.23^{+0.36}_{-0.39}$	$0.36^{+0.45}_{-0.38}$	$0.19^{+0.45}_{-0.55}$
19	0	27	$0.00^{+0.59}_{-0.00}$	0.84	4	31	$3.67^{+2.53}_{-1.66}$	0.92	4	56	$3.52^{+2.62}_{-1.64}$	0.90	$-0.92^{+0.63}_{-0.96}$	$0.01^{+0.30}_{-0.32}$	$-1.10^{+0.82}_{-0.78}$
20	0	25	$0.00^{+0.56}_{-0.00}$	0.88	5	42	$4.62^{+2.64}_{-1.97}$	0.94	3	78	$2.55^{+1.87}_{-1.67}$	0.93	$-0.95^{+0.53}_{-1.05}$	$0.20^{+0.38}_{-0.31}$	$-0.75^{+0.64}_{-1.03}$
21	0	22	$0.00^{+0.67}_{-0.00}$	0.73	1	40	$0.00^{+1.96}_{-0.00}$	0.80	6	57	$6.86^{+3.35}_{-2.68}$	0.79	$-0.42^{+0.85}_{-1.07}$	$-0.67^{+0.44}_{-0.54}$	$-1.06^{+0.57}_{-1.00}$
22	1	13	$0.51^{+1.31}_{-0.47}$	0.97	3	43	$2.64^{+1.92}_{-1.41}$	0.99	2	56	$1.57^{+1.62}_{-1.05}$	0.98	$-0.39^{+0.46}_{-0.47}$	$0.16^{+0.38}_{-0.39}$	$-0.21^{+0.47}_{-0.52}$
23	6	25	$6.95^{+3.58}_{-2.54}$	0.78	0	25	$0.00^{+0.62}_{-0.00}$	0.80	0	56	$0.00^{+0.64}_{-0.00}$	0.78	$1.15^{+0.94}_{-0.62}$	$-0.01^{+1.19}_{-1.16}$	$1.07^{+1.01}_{-0.55}$
24	1	43	$0.00^{+2.07}_{-0.00}$	0.76	4	52	$4.11^{+2.66}_{-1.95}$	0.83	1	96	$0.00^{+1.72}_{-0.00}$	0.82	$-0.47^{+0.48}_{-0.54}$	$0.51^{+0.66}_{-0.49}$	$0.09^{+0.75}_{-0.76}$
25	2	17	$2.03^{+2.26}_{-1.44}$	0.71	1	42	$0.00^{+1.60}_{-0.00}$	0.85	2	54	$1.13^{+1.78}_{-1.13}$	0.84	$0.38^{+0.69}_{-0.62}$	$-0.25^{+0.68}_{-0.76}$	$0.10^{+0.55}_{-0.48}$
26	1	25	$0.00^{+2.14}_{-0.00}$	0.76	2	39	$1.62^{+1.92}_{-1.18}$	0.85	2	79	$1.46^{+1.62}_{-1.46}$	0.84	$-0.16^{+0.53}_{-0.60}$	$0.02^{+0.49}_{-0.49}$	$-0.17^{+0.59}_{-0.60}$

Table A.10 FIELD 7: Source Photometry and X-ray Colors

Src_ID	SOFT BAND (0.5 - 1.0 keV)				MEDIUM BAND (1.0 - 2.5 keV)				HARD BAND (2.5 - 7.0 keV)				Col1	Col2	Col3
	Counts			Eff.Area	Counts			Eff.Area	Counts			Eff.Area			
	Obs.	Bkg.	Net	Ratio	Obs.	Bkg.	Net	Ratio	Obs.	Bkg.	Net	Ratio			
(1)	(2)	(3)	(4)	(5)	(6)	(7)	(8)	(9)	(10)	(11)	(12)	(13)	(14)	(15)	(16)
27	0	11	$0.00^{+0.68}_{-0.00}$	0.73	5	39	$4.95^{+2.80}_{-2.20}$	0.86	4	54	$3.66^{+2.60}_{-1.91}$	0.85	$-0.91^{+0.57}_{-1.02}$	$0.11^{+0.31}_{-0.32}$	$-0.87^{+0.66}_{-0.96}$

Notes: The area ratio is in units of 10^{-2}. The colors are defined as Col1=$\log_{10}(S/M)$, Col2=$\log_{10}(M/H)$, and Col3=$\log_{10}(S/H)$.

Appendix B

Notes on individual *Chandra* sources

B.1 Sources with uncertain nature

Chandra **source 3_4:** A single optical match was identified in both OGLE-II and MCPS catalogs. However, its $V = 18.19$ magnitude and $B - V = 0.37$ color are not indicative of the nature of the companion star. Its soft spectrum (Taylor et al. 2008, in preparation) make us believe this is possibly an AGN.

Chandra **sources 4_10, 5_6, 5_24, 5_32 & 6_3:** The soft spectrum of these sources (HR method, more details in Table 3.6 and its description in §3.8.3) and their early type counterparts make us believe that these sources could be candidate black-hole binaries (BHBs). However, only spectral fits from the X-ray data and optical spectroscopy of the companion star could possibly help us identify their nature.

Chandra **source 7_17:** This is the sixth source (additional to the 5 sources described above) with a possibly soft spectrum. The large search radius for this source ($5.29''$, maximum search radius used in this study; due to the large off-axis angle) resulted in the identification of multiple matches. However, only 2 sources are bright ($V \sim 18.4$ mag, small chance coincidence). One of the two sources lies on the red giant branch, while the other one falls just outside the locus of OB spectral type stars. Without further information, we cannot propose the most likely counterpart and classify source 7_17.

Chandra **source 5_23:** We identify MCPS source Z_2288276 (no OGLE overlap) as the optical counterpart of X-ray source 5_23 (lies in the locus of OB stars; criterion (i)). However, the small number of counts of this source (< 10 counts; Zezas et al. 2008, in preparation) does not allow us to derive spectral information, and thus we classify this source only as a possible new candidate HMXB.

Chandra **source 6_20:** See §B.4 for more details about the nature of this source.

B.2 Sources with Be candidate counterparts from Mennickent et al. 2002

All sources that are presented below have been classified as type-4 stars (light curves similar to Galactic Be stars) in the compilation of Be candidate stars by Mennickent et al. 2002 (hereafter [MPG02]).

Chandra **source 3_3:** The identified counterpart O_8_49531 (single match) of X-ray source 3_3 is a Be candidate star ([MPG02]No.494), in agreement with the identification of Sasaki et al. 2003.

Chandra **source 4_2:** We find two matches for X-ray source 4_2. Although none of them is located within the locus of OB stars (criterion (i)), we identify source O_5_111490 as the counterpart for 4_2, because it is a Be star ([MPG02]No.206) and it was also found to be variable (Ita et al. 2004). This is in agreement with the identification of Coe et al. (2005a).

Chandra **source 4_8:** We present source O_4_171264 as the newly identified optical counterpart of X-ray source 4_8. This OGLE source is also reported as a Be candidate star ([MPG02]No.157).

Chandra **source 4_17:** Source O_5_180008 is presented here as the new optical counterpart of X-ray source 4_17, while it is also identified as a Be candidate star ([MPG02]No.265).

Chandra **source 5_3:** The identified optical counterpart O_6_85614 (in agreement with Schmidtke & Cowley 2006) is a Be candidate star [MPG02]No.321, while it is of B0-5 spectral type (source [2dF]No.0828; see below §B.4). It has also been found to be the emission line object [MA93]No.506 (Haberl & Sasaki 2000).

Chandra **source 5_7:** The identified optical counterpart of X-ray source 5_7 is source O_7_70829. It is identified as a Be candidate star ([MPG02]No.426), while Sasaki et al. (2003) present the same counterpart, identified also as emission line object [MA93]No.810.

Chandra **source 5_15:** We identify source O_7_71429 as the optical counterpart of X-ray source 5_15. This is also reported as a Be candidate star ([MPG02]No.423). However, Dobrzycki et al. (2003a) identified this object as a quasar ($z = 1.79$) located behind the SMC, based on a spectroscopic study.

Chandra **source 6_1:** The identified counterpart O_6_77228 is source [MPG02]No.341 (for more details see §B.4).

Chandra **source 6_4:** Source O_6_147662 is identified as the optical counterpart for X-ray source 6_4. This optical source is also reported as a candidate Be star ([MPG02]No.364), while it is located $\sim 0.57''$ away from the emission line object [MA93]618, that has been proposed as the counterpart of this Be-XRB (Haberl & Sasaki 2000; source [MA93] is located $\sim 0.82''$ away from the X-ray source).

Chandra **source 7_1:** We identify source O_5_65517 as the optical counterpart of X-ray source 7_1. This is star 1 of Stevens et al. (1999), and it is also in agreement with Coe & Orosz (2000). This OGLE source is identified as a Be candidate star ([MPG02]No.199).

B.3 Sources identified with OGLE variable stars

Chandra **source 3_1:** We identify source O_7_267163 as the optical counterpart of *Chandra* source 3_1. From visual inspection of the finding chart, from comparison of the V magnitude for sources O_7_267163 and O_7_267132, and taking into account the $\sim 0.7''$ astrometric accuracy of OGLE, we believe these are a single source. Although none of the identified matches is an early type star, and the parameter ξ cannot distinguish in this case the right counterpart, source O_7_267163 is identified as a variable star (OGLE00571981-72253375) in the study of Zebrun et al. (2001). Sasaki et al. (2003) found the same object as in the latter study, while they also associate it with star USNOA2.0 0150-00625436. The soft spectrum of 3_1 and the

identification of the optical counterpart as a background quasar (Dobrzycki et al. 2003b), make us believe that this is possibly an AGN (suggested also by Sasaki et al. 2003).

Chandra source 4_2: Source O_5_111490 is also identified as a variable star in the analysis of Ita et al. (2004). For more details about this source see §B.2.

Chandra **source 4_5:** We present as counterpart of X-ray source 4_5 the variable star O_5_111500 (single optical match; $P_{pulse,opt} = 89.835$ days, Ita et al. (2004)).

B.4 Sources with available spectral classification for their counterparts

The sources presented here (with the exception of *Chandra* source 5_16) have been identified spectroscopically in the 2dF survey of the SMC by Evans et al. (2004; hereafter [2dF]) and/or are reported in the emission line object compilation of Meyssonnier & Azzopardi (1993; hereafter [MA93]). The luminosity classes shown in parenthesis indicate an hybrid photometric/spectroscopic approach and are not true, MK-process, morphological types (for more details see Evans et al. 2004).

Chandra **source 5_1:** The identified optical counterpart in this case is MCPS source Z_2311496, in agreement with Coe et al. 2005. This source is also defined as a B0-5 (II)e star in the 2dF spectroscopic catalog of Evans et al. (2004; source [2dF]No.0839).

Chandra **source 5_3:** The optical counterpart O_6_85614 is identified as a B0-5 (II) spectral type source ([2dF]No.0828).

Chandra **source 5_16:** A single match (source Z_2573354) is identified from the MCPS catalog as the optical counterpart of this source (no OGLE overlap), in agreement with Coe et al. (2005a). However, the nature of this source (transient pulsar; Buckley et al. 2001), and thus its positional uncertainty, makes it difficult to conclude if source [MACHO]207.16202.30 (unlikely the correct counterpart; Coe et al. 2005a) is the right match (the latter lies $> 14''$ away of X-ray source 5_16). Buckley et al. (2001) classify spectroscopically the suggested counterpart (star A or B

mentioned in this study) as a B1-B2 III-Ve star.

Chandra **source 6_1:** We identify source O_6_77228 as the optical counterpart of X-ray source 6_1 (in agreement with Coe et al. 2005a). This is source [2dF]No.5054 and is a B1-5 (II)e star. It also appears as a candidate Be star in the compilation of Mennickent et al. (2002; [MPG02]No.341).

Chandra **source 6_20:** Source O_6_311169 (single match) is proposed here as the optical counterpart of X-ray source 6_20. It is the brightest counterpart identified in this study, while it has been identified as emission line object [MA93]No.739 (peculiar Hα emission-line star with FeII and [FeII] emission; $\sim 0.17''$ from the OGLE-II source, and $\sim 0.57''$ from the X-ray source). In particular, the latter source has been identified as a B[e] star by Massey & Duffy (2001). Furthermore, the source is really faint in X-rays and no spectral information could be derived (< 10 counts, large HR errors; Zezas et al. 2008, in preparation). Thus, we only propose the above OGLE-II source as the candidate counterpart of *Chandra* source 6_20, and we note that further analysis of this peculiar system is required so as to confirm its nature.

B.5 *Chandra* sources with bright optical counterparts ($M_{V_o} \leq -0.25$) only between the 1σ and 2σ search radii

Out of the 33 X-ray sources without optical counterparts in the 1σ search radius, there are 7 *Chandra* sources with counterparts in the 2σ search radius. These sources are described in Table B.1 below. The description of this table can be found in §3.3.1 with the only difference that there is only one table for all the sources found in the different *Chandra* fields (separated by triple horizontal lines). We also present in Table B.2 below their optical and X-ray properties. The description for this table can be found in §3.8.3.

Table B.1. Bright optical counterparts ($M_{V_o} \leq -0.25$) of X-ray sources within the 2σ search radius (no match(es) found in the 1σ search radius)

X-ray			Optical counterpart								
Src	Rad.	Src ID	Position (J2000.0)		Offset	V	δV	B-V	δ(B − V)	U-B	δ(U − B)
			R.A.	Decl.							
	($''$)				($''$)						
[1]	[2]	[3]	[4]	[5]	[6]	[7]	[8]	[9]	[10]	[11]	[12]
3_10	3.00	Z_2838059†	00 55 41.83	-72 18 10.9	1.93	14.18	0.04	1.46	0.26	1.28	0.26
3_24	3.00	Z_2989515†	00 56 46.83	-72 22 50.9	2.23	18.55	0.09	0.62	0.10	0.09	0.08
3_25	3.00	Z_2924823†	00 56 18.97	-72 15 09.8	2.08	17.90	0.03	1.16	0.04	0.91	0.12
3_27	3.00	Z_2894870†	00 56 06.19	-72 20 47.0	2.13	16.57	0.03	1.70	0.05	1.83	0.12
5_35	3.00	Z_2438540	00 52 58.84	-72 26 05.3	2.58	18.84	0.05	0.00	0.06	-0.48	0.08
5_37‡	3.38	O_6_324148	00 53 58.77	-72 31 14.3	2.25	16.94	0.04	1.09	0.08	···	···
		00 53 58.82	-72 31 14.3	-72.52064	2.07	16.90	0.03	1.11	0.04	0.74	0.07
6_27‡	3.81	O_6_227467	00 53 33.75	-72 48 17.9	2.77	18.30	0.03	1.02	0.04	···	···
		Z_2521669	00 53 33.81	-72 48 17.9	2.63	18.23	0.05	1.10	0.09	1.29	0.23

†Single counterpart within the 2σ search radius.

‡For this source there is a finding chart.

B.6 *Chandra* sources with optical counterparts in the locus of OB stars and hard or possibly hard spectrum between the 1σ and 2σ search radii

***Chandra* source 3_2:** This source is a pulsar (Edge et al. 2004). However, both of its optical matches in the MCPS catalog presented in Table 3.2 (no overlap with OGLE-II) are faint stars. Due to the high chance coincidence probabiblity of faint sources, we do not propose any of them as counterpart of X-ray source 3_2. Instead, looking for counterparts between the 1σ and 2σ search radii, we find MCPS source Z_2806702, in agreement with Edge et al. (2004). This is a bright star ($V = 16.78$, $B - V = -0.12$), that is located $4.27''$ away from the X-ray position. The value of ξ parameter for this source is equal to 11.25, within the range of intermediate state XRBs (i.e. soon after outburst). Although no spectroscopic data for these 3 sources are available, the early type nature of MCPS source Z_2806702, make us believe this is the most

Table B.2. Summary of optical and X-ray properties of sources presented in Table B.1

X-ray	Optical properties			X-ray properties			ξ	Classification
src. ID	M_{V_o}	$(B-V)_o$	Offset ($''$)	spectrum	pulsations	observed flux†		
[1]	[2]	[3]	[4]	[5]	[6]	[7]	[8]	[9]
3_10	-5.01	1.37	1.93	possibly hard	···	0.39 ± 0.10	5.50	unclassified
3_24	-0.64	0.53	2.23	···	···	0.11 ± 0.05	8.51	unclassified
3_25	-1.29	1.07	2.08	···	···	0.11 ± 0.05	7.86	unclassified
3_27	-2.62	1.61	2.13	···	···	0.09 ± 0.05	6.49	unclassified
5_35	-0.35	-0.09	2.58	···	···	0.16 ± 0.10	9.24	unclassified
5_37‡	-2.25	1.00	2.25	···	···	0.05 ± 0.04	5.91	unclassified
	-2.29	1.02	2.07	···			5.87	
6_27‡	-0.89	0.93	2.77	···	···	0.09 ± 0.05	8.02	unclassified
	-0.96	1.01	2.63	···			7.95	

†Calculated from net counts, in units $\times 10^{-13}$ erg cm^{-2} s^{-1} for the full energy band ($0.7 - 10.0$ keV; Zezas et al. 2008, in preparation).

‡For these sources we present all the optical matches as we cannot propose the most likely counterpart.

likely counterpart.

Chandra **source 4_13:** In Table B.3, we have identified the optical source O_5_90858 as the counterpart of 4_13 (observed flux in the 0.7-10.0 keV energy band equal to $(0.37 \pm 0.09) \times 10^{-13}$ erg cm^{-2} s^{-1}). However, when we look for counterparts between the 1σ and 2σ search radii, we find 2 sources brighter than O_5_90858. These sources, O_5_90493 and O_5_90535, ($5.47''$ and $4.10''$ away from the X-ray source, respectively) are both OB spectral type stars ($V = 15.57$, $B - V = -0.07$ and $V = 16.34$, $B - V = 0.23$, respectively). The value of the ξ parameter for sources O_5_90493 and O_5_90535 is equal to 6.86 and 7.63, respectively, while the possibly hard spectrum of 4_13, makes us believe that this is a new candidate Be-XRB pulsar. However, only optical spectroscopy could determine the exact type of these bright stars and finally the most likely counterpart of *Chandra* source 4_13.

Chandra **source 4_19:** Between the 1σ and 2σ search radius for *Chandra* source 4_19, we find the optical source O_5_261182, $2.27''$ away from this X-ray source (which has an observed flux in the 0.7-10.0 keV energy band equal to $(0.20 \pm 0.06) \times 10^{-13}$ erg cm^{-2} s^{-1}). This optical source is an OB spectral type star ($V = 18.16$, $B - V = -0.08$) with a value of ξ parameter

equal to 8.87. *Chandra* source 4_19 has a possibly hard spectrum, suggesting that this source is a new candidate Be-XRB pulsar. Nevertheless, as in the case of *Chandra* source 4_13, only optical spectroscopy could determine the exact type of this bright star and finally the most likely counterpart of X-ray source 4_19.

Table B.3. Optical counterparts of X-ray sources in *Chandra* field 4

X-ray			Optical counterpart									Notes
Src	Rad.	Src ID	Position (J2000.0)		Offset	V	δV	B-V	δ(B − V)	U-B	δ(U − B)	
			R.A.	Decl.								
	($''$)				($''$)							
[1]	[2]	[3]	[4]	[5]	[6]	[7]	[8]	[9]	[10]	[11]	[12]	[13]
4_1	1.50	**O_5_180026**	00 50 44.71	-73 16 05.0	0.55	15.44	0.04	-0.04	0.05	···	···	c
		Z_2131651	00 50 44.75	-73 16 05.3	0.60	15.48	0.04	-0.11	0.05	-0.91	0.04	
4_2	1.50	**O_5_111490**	00 49 13.63	-73 11 37.4	0.47	16.52	0.02	0.10	0.04	···	···	c
		Z_1938257	00 49 13.68	-73 11 37.5	0.54	16.44	0.04	0.19	0.05	-0.92	0.04	
		O_5_115042	00 49 13.57	-73 11 39.1	1.31	21.53	0.48	99.99	99.99	···	···	
4_3	2.10	**O_5_271074**	00 50 57.12	-73 10 07.7	0.28	14.54	0.01	-0.06	0.01	···	···	c
		Z_2159045	00 50 57.16	-73 10 07.8	0.14	14.35	0.05	0.08	0.06	-0.88	0.04	
4_4	1.50	**O_4_159896**	00 48 18.67	-73 20 59.7	0.54	16.58	0.02	-0.10	0.03	···	···	n, c
		Z_1825706	00 48 18.71	-73 20 59.7	0.38	16.18	0.04	0.25	0.04	-0.77	0.04	
		O_4_159964	00 48 18.86	-73 20 59.5	0.53	19.70	0.38	0.42	0.67	···	···	
		O_4_160861	00 48 18.69	-73 21 00.6	0.80	99.99	99.99	99.99	99.99	···	···	
		O_4_161021	00 48 18.58	-73 20 59.3	1.08	20.11	0.40	99.99	99.99	···	···	
		O_4_161025	00 48 18.90	-73 20 58.8	1.22	19.50	0.27	1.38	0.41	···	···	
		O_4_162035	00 48 19.05	-73 20 59.9	1.13	20.35	0.39	-0.02	0.47	···	···	
4_5	1.50	**O_5_111500**	00 49 29.81	-73 10 58.0	0.61	16.30	0.01	0.09	0.02	···	···	c
		Z_1971979	00 49 29.87	-73 10 58.2	0.65	16.15	0.03	0.20	0.05	-0.88	0.05	
4_6	1.50	**O_5_96912**	00 49 48.26	-73 22 10.9	0.59	21.29	0.40	-0.89	0.41	···	···	u
		Z_2010981	00 49 48.28	-73 22 11.1	0.53	19.99	0.06	0.70	0.12	-0.11	0.31	
		O_5_98236	00 49 48.12	-73 22 11.7	0.41	21.18	0.44	99.99	99.99	···	···	
4_7	1.82	O_5_11870	00 48 53.48	-73 24 56.9	1.26	99.99	99.99	99.99	99.99	···	···	c
		O_5_13241	00 48 53.44	-73 24 57.5	0.65	20.00	0.20	99.99	99.99	···	···	
		(Z_1896638)	00 48 53.51	-73 24 57.3	0.96	18.66	0.09	1.56	0.22	99.99	99.99	
		O_5_13232	00 48 53.27	-73 24 59.8	1.78	19.71	0.08	0.10	0.10	···	···	
		O_5_13242	00 48 53.68	-73 24 57.9	1.33	20.47	0.19	99.99	99.99	···	···	
		O_5_13244	00 48 53.33	-73 24 56.7	1.39	20.23	0.29	99.99	99.99	···	···	
		O_5_13245	00 48 53.25	-73 24 57.8	0.60	21.67	0.53	99.99	99.99	···	···	
		O_5_14615	00 48 53.54	-73 24 58.7	0.95	21.32	0.30	99.99	99.99	···	···	
		O_5_16026	00 48 53.68	-73 24 57.0	1.70	20.32	0.41	99.99	99.99	···	···	
4_8	3.99	**O_4_171264**	00 48 14.13	-73 10 03.5	0.63	15.74	0.04	0.00	0.05	···	···	n, c
		Z_1816472	00 48 14.18	-73 10 03.9	0.30	15.30	0.05	0.26	0.06	-0.50	0.05	
		O_4_171332	00 48 14.09	-73 10 04.6	0.55	17.78	0.05	1.64	0.28	···	···	
		O_4_171856	00 48 13.26	-73 10 04.8	3.93	19.42	0.06	0.62	0.13	···	···	
		Z_1814706	00 48 13.31	-73 10 04.8	3.70	19.60	0.15	0.13	0.17	99.99	99.99	
		O_4_171863	00 48 14.47	-73 10 03.2	0.67	18.54	0.16	-0.03	0.19	···	···	

Table B.3—Continued

X-ray			Optical counterpart									Notes
Src	Rad.	Src ID	Position (J2000.0)		Offset	V	δV	B-V	δ(B − V)	U-B	δ(U − B)	
			R.A.	Decl.								
	($''$)				($''$)							
[1]	[2]	[3]	[4]	[5]	[6]	[7]	[8]	[9]	[10]	[11]	[12]	[13]
		O_4_172639	00 48 13.57	-73 10 03.9	2.53	19.62	0.14	0.20	0.25	···	···	
		O_4_173769	00 48 13.57	-73 10 01.7	3.49	20.86	0.13	0.53	0.30	···	···	
		O_4_174934	00 48 14.77	-73 10 04.4	2.71	99.99	99.99	99.99	99.99	···	···	
		O_4_174937	00 48 14.70	-73 10 01.0	3.93	99.99	99.99	99.99	99.99	···	···	
4_10	3.30	O_4_156816†	00 48 32.97	-73 23 56.6	2.96	19.04	0.03	0.71	0.09	···	···	n
		O_5_11978†	00 48 32.96	-73 23 56.6	2.95	19.01	0.04	0.75	0.07	···	···	
		Z_1854839	00 48 32.97	-73 23 56.8	3.11	19.05	0.06	0.86	0.10	0.20	0.18	
		O_4_156830†	00 48 32.62	-73 23 54.2	1.32	17.80	0.02	-0.10	0.04	···	···	
		O_5_11982†	00 48 32.61	-73 23 54.2	1.36	17.81	0.02	-0.07	0.03	···	···	
		Z_1854152	00 48 32.64	-73 23 54.2	1.27	17.67	0.09	0.07	0.10	-0.57	0.07	
		O_4_158666	00 48 33.23	-73 23 50.7	3.28	20.52	0.09	0.81	0.26	···	···	
		O_5_15242	00 48 32.94	-73 23 54.1	0.47	21.02	0.32	-0.30	0.44	···	···	
		O_5_15268	00 48 32.91	-73 23 52.4	1.26	20.60	0.10	0.45	0.22	···	···	
		Z_1854803	00 48 32.95	-73 23 52.6	1.13	20.68	0.16	0.43	0.24	99.99	99.99	
4_11	1.87	**O_4_164855**	00 48 03.69	-73 16 59.8	1.05	18.88	0.04	-0.10	0.05	···	···	n
		Z_1795179	00 48 03.81	-73 17 00.1	1.40	18.20	0.07	0.36	0.09	-0.85	0.10	
4_13	3.39	**O_5_90858**	00 49 50.80	-73 25 01.1	1.96	18.41	0.05	0.10	0.09	···	···	n
		Z_2016443	00 49 50.90	-73 25 01.3	2.07	18.35	0.08	0.09	0.10	-0.47	0.09	
		O_5_91343	00 49 51.51	-73 24 58.3	2.48	19.26	0.04	0.00	0.05	···	···	
		Z_2017849	00 49 51.57	-73 24 58.8	2.59	18.98	0.09	0.33	0.11	-0.55	0.12	
		O_5_92158	00 49 51.00	-73 25 00.3	1.00	20.62	0.23	-0.19	0.28	···	···	
		O_5_92159	00 49 51.35	-73 25 00.2	1.82	20.21	0.11	0.06	0.14	···	···	
		O_5_93600	00 49 50.48	-73 25 01.2	2.87	21.64	0.47	99.99	99.99	···	···	
		O_5_93617	00 49 51.76	-73 24 59.7	3.36	20.57	0.16	0.08	0.20	···	···	
4_14	1.93	**O_5_90506**	00 49 42.02	-73 23 14.2	1.93	14.98	0.02	0.05	0.03	···	···	c
		O_5_94651	00 49 41.68	-73 23 13.0	1.49	21.16	0.64	0.16	0.92	···	···	
		O_5_94669	00 49 42.34	-73 23 11.2	1.87	21.74	0.38	99.99	99.99	···	···	
4_15	1.50	O_5_21583	00 49 10.74	-73 17 16.9	0.51	20.18	0.22	99.99	99.99	···	···	n, c
		O_5_22301	00 49 10.95	-73 17 16.9	1.20	19.28	0.18	0.58	0.18	···	···	
		Z_1932585	00 49 10.91	-73 17 17.1	1.00	18.81	0.07	1.00	0.09	0.06	0.17	
		O_5_23325	00 49 10.51	-73 17 16.9	0.92	20.33	0.40	99.99	99.99	···	···	
		(Z_1931568)	00 49 10.44	-73 17 16.4	1.47	19.94	0.09	0.73	0.11	99.99	99.99	
4_16	1.50	**O_5_27768**	00 49 05.48	-73 14 10.2	1.29	19.93	0.07	0.84	0.20	···	···	n
4_17	1.61	**O_5_180008**	00 50 47.99	-73 18 17.6	0.99	15.30	0.07	0.05	0.10	···	···	n, c

Table B.3—Continued

X-ray			Optical counterpart									Notes
Src	Rad.	Src ID	Position (J2000.0)		Offset	V	δV	B-V	δ(B − V)	U-B	δ(U − B)	
			R.A.	Decl.								
	($''$)				($''$)							
[1]	[2]	[3]	[4]	[5]	[6]	[7]	[8]	[9]	[10]	[11]	[12]	[13]
		Z_2138888	00 50 48.03	-73 18 17.9	0.67	15.07	0.03	0.12	0.05	-1.00	0.05	
		O_5_180929	00 50 48.27	-73 18 17.4	1.27	19.42	0.30	-0.42	0.38	···	···	
4_18	1.92	**O_5_92756**	00 49 49.51	-73 23 06.8	0.99	19.91	0.07	-0.02	0.10	···	···	n
		Z_2013579	00 49 49.52	-73 23 06.9	1.05	19.94	0.08	0.24	0.10	-0.29	0.19	
		O_5_94741	00 49 49.96	-73 23 04.9	1.72	21.09	0.23	0.38	0.34	···	···	
4_19	1.82	**O_5_262679**	00 50 55.26	-73 18 02.3	1.40	19.41	0.09	-0.26	0.10	···	···	n
		Z_2154899	00 50 55.29	-73 18 02.6	1.15	19.05	0.06	0.16	0.08	-0.24	0.11	
4_20	2.72	**O_5_259514**	00 50 59.04	-73 20 57.7	1.87	21.07	0.15	0.54	0.25	···	···	n
4_21	3.22	**O_5_256084**	00 51 01.70	-73 21 35.9	2.59	17.93	0.06	0.88	0.15	···	···	n, c
		(Z_2169351)	00 51 01.74	-73 21 36.3	2.63	17.18	0.11	2.03	0.13	-1.22	0.12	
		O_5_256315	00 51 01.93	-73 21 34.7	1.39	18.63	0.04	0.76	0.09	···	···	
		Z_2169776	00 51 01.93	-73 21 35.0	1.38	18.36	0.10	0.81	0.12	-0.81	0.12	
		O_5_256826	00 51 02.26	-73 21 36.6	1.75	18.33	0.04	-0.18	0.05	···	···	
		Z_2170562	00 51 02.28	-73 21 37.0	2.20	18.06	0.10	0.16	0.11	-0.62	0.06	
		O_5_259099	00 51 01.88	-73 21 37.5	3.09	20.13	0.10	0.12	0.15	···	···	
		O_5_259115	00 51 02.66	-73 21 36.1	2.16	21.16	0.31	0.76	0.58	···	···	
		O_5_259158	00 51 01.97	-73 21 32.7	2.47	20.88	0.17	-0.48	0.20	···	···	
		O_5_260535	00 51 01.61	-73 21 33.9	2.91	21.25	0.27	-0.13	0.36	···	···	
4_22	3.81	O_5_90840	00 49 55.97	-73 25 16.6	3.20	18.40	0.03	0.68	0.06	···	···	n
		Z_2027202	00 49 56.01	-73 25 17.0	2.87	18.21	0.04	0.96	0.24	99.99	99.99	
		O_5_91270	00 49 56.15	-73 25 19.0	2.32	18.26	0.03	-0.07	0.03	···	···	
		Z_2027575	00 49 56.20	-73 25 19.3	2.32	18.13	0.04	0.04	0.07	-0.41	0.08	
		O_5_92049	00 49 56.66	-73 25 21.3	3.29	19.49	0.05	-0.05	0.07	···	···	
		Z_2028724	00 49 56.74	-73 25 21.7	3.66	19.43	0.07	0.03	0.09	99.99	99.99	
		O_5_92063	00 49 56.97	-73 25 16.5	2.06	21.28	0.23	0.65	0.36	···	···	
		O_5_92077	00 49 56.77	-73 25 14.5	3.55	20.74	0.11	0.76	0.18	···	···	
		O_5_93443	00 49 55.90	-73 25 17.8	3.18	20.23	0.15	0.01	0.21	···	···	
4_23[d]	1.50	**O_5_101577**	00 49 57.52	-73 16 55.1	1.46	99.99	99.99	99.99	99.99	···	···	u
		Z_2029266	00 49 57.00	-73 16 54.1	1.39	19.30	0.12	1.43	0.17	99.99	99.99	
4_24	1.50	**O_5_179505**	00 50 10.08	-73 19 30.8	0.83	20.96	0.40	0.13	0.47	···	···	n, c
4_25	2.33	**O_5_176711**	00 50 42.94	-73 21 40.0	2.13	19.49	0.11	-0.18	0.11	···	···	n
		(Z_2127712)	00 50 42.95	-73 21 40.5	2.29	18.86	0.06	0.27	0.07	-0.12	0.09	
		O_5_178210	00 50 42.72	-73 21 40.2	1.27	20.26	0.33	0.31	0.37	···	···	
4_26	1.58	**O_5_193908**	00 50 05.32	-73 11 45.7	0.61	21.54	0.32	99.99	99.99	···	···	n

Table B.3—Continued

X-ray			Optical counterpart									Notes
Src	Rad.	Src ID	Position (J2000.0)		Offset	V	δV	B-V	δ(B − V)	U-B	δ(U − B)	
			R.A.	Decl.								
	($''$)				($''$)							
[1]	[2]	[3]	[4]	[5]	[6]	[7]	[8]	[9]	[10]	[11]	[12]	[13]
4_28	1.50	**O_5_25130**	00 48 47.13	-73 17 20.3	1.20	21.61	0.38	99.99	99.99	···	···	n
4_29	3.06	**O_5_266399**	00 51 09.80	-73 13 34.8	2.15	19.20	0.04	0.66	0.08	···	···	n
		O_5_268082	00 51 10.02	-73 13 34.2	1.11	20.28	0.26	1.01	0.39	···	···	
		(Z_2187387)	00 51 09.93	-73 13 34.3	1.51	18.99	0.12	1.18	0.24	0.25	0.38	
		O_5_267042	00 51 10.35	-73 13 35.4	1.27	20.37	0.30	0.14	0.41	···	···	
		O_5_268096	00 51 09.89	-73 13 32.1	2.66	20.84	0.26	0.51	0.43	···	···	
		O_5_269842	00 51 10.48	-73 13 34.3	0.89	20.11	0.22	0.19	0.26	···	···	
4_30	1.50	**O_5_25176**	00 48 54.33	-73 17 16.1	0.80	20.47	0.15	0.29	0.33	···	···	n
4_31	2.48	**O_5_33605**	00 48 44.36	-73 10 26.3	2.39	20.33	0.25	1.06	0.39	···	···	n
		O_5_34786	00 48 44.83	-73 10 27.4	0.24	21.22	0.29	1.20	0.59	···	···	
		O_5_37833	00 48 45.24	-73 10 29.0	2.29	21.35	0.25	0.12	0.39	···	···	
4_32	1.50	**O_5_111737**	00 49 27.21	-73 12 12.8	1.34	18.62	0.04	0.76	0.07	···	···	n, c
		O_5_114647	00 49 27.07	-73 12 11.7	0.34	20.98	0.47	0.33	0.59	···	···	
4_33	1.50	**O_5_99201**	00 49 56.12	-73 20 37.2	1.39	20.73	0.10	0.03	0.16	···	···	n
4_35	1.50	**O_5_101481**	00 49 42.72	-73 17 20.2	1.47	19.36	0.23	0.88	0.55	···	···	n
		O_5_101851	00 49 42.87	-73 17 21.2	0.35	20.98	0.49	99.99	99.99	···	···	
4_36[d]	1.51	**O_5_187956**	00 50 45.14	-73 15 40.3	1.33	20.53	0.40	99.99	99.99	···	···	n, c
		Z_2132222[o]	00 50 45.02	-73 15 40.7	1.29	18.27	0.04	0.91	0.06	-0.04	0.13	
4_37	1.73	O_4_166430	00 48 08.62	-73 15 48.6	1.26	21.05	0.18	-0.12	0.21	···	···	n
		Z_1805231	00 48 08.68	-73 15 49.0	1.68	19.71	0.12	-0.12	0.18	99.99	99.99	
		O_4_166445	00 48 08.41	-73 15 46.4	1.17	20.60	0.14	0.26	0.20	···	···	

[†]Sources detected in two neighboring OGLE-II fields.

[o]Just outside the error circle of the X-ray source there is another OGLE-II source (not listed in these tables), that it is most likely related with the detected MCPS source within the search radius.

[d]The detection algorithm gave probably more than one sources for the same star (suggested also by the visual inspection of the finding charts).

Table B.4. Optical counterparts of X-ray sources in *Chandra* field 5

X-ray			Optical counterpart									Notes
Src	Rad.	Src ID	Position (J2000.0)		Offset	V	δV	B-V	δ(B − V)	U-B	δ(U − B)	
			R.A.	Decl.								
	($''$)				($''$)							
[1]	[2]	[3]	[4]	[5]	[6]	[7]	[8]	[9]	[10]	[11]	[12]	[13]
5_1	1.50	**Z_2311496**[!]	00 52 05.69	-72 26 04.0	0.55	14.91	0.02	0.00	0.03	-0.97	0.04	c
5_2	1.50	**Z_2498173**	00 53 23.90	-72 27 15.4	0.24	16.19	0.12	-0.09	0.12	-1.05	0.04	c
5_3	1.62	**O_6_85614**	00 51 53.11	-72 31 48.3	0.54	14.90	0.12	-0.27	0.13	···	···	c
		Z_2282823	00 51 53.18	-72 31 48.4	0.43	14.38	0.02	0.41	0.03	-1.13	0.11	
		O_6_85986	00 51 53.30	-72 31 49.1	0.69	99.99	99.99	99.99	99.99	···	···	
5_4	2.50	**O_7_70843**	00 54 46.37	-72 25 22.6	0.79	15.58	0.02	99.99	99.99	···	···	n, c
		Z_2707354	00 54 46.39	-72 25 22.7	0.83	15.36	0.05	0.14	0.06	-1.11	0.13	
		O_7_71473	00 54 46.06	-72 25 24.0	1.23	19.57	0.13	99.99	99.99	···	···	
		O_7_71474	00 54 45.79	-72 25 23.3	1.97	19.30	0.05	99.99	99.99	···	···	
		O_7_71481	00 54 46.08	-72 25 21.4	1.73	18.83	0.09	99.99	99.99	···	···	
		O_7_73194	00 54 46.02	-72 25 21.9	1.43	19.68	0.24	99.99	99.99	···	···	
5_6	4.85	**Z_2748033**	00 55 03.63	-72 22 31.2	3.60	17.86	0.03	-0.03	0.05	-0.79	0.06	n
		Z_2749296	00 55 04.18	-72 22 25.9	4.61	20.82	0.11	0.79	0.21	99.99	99.99	
		Z_2749725	00 55 04.37	-72 22 30.3	0.16	20.03	0.05	2.01	0.20	99.99	99.99	
		Z_2750215	00 55 04.58	-72 22 34.5	4.22	20.34	0.12	-0.02	0.15	-0.52	0.15	
		Z_2751240	00 55 04.99	-72 22 27.6	3.83	19.94	0.06	0.58	0.11	99.99	99.99	
5_7	3.07	**O_7_70829**	00 54 56.17	-72 26 47.6	1.19	15.30	0.01	-0.04	0.02	···	···	c
		Z_2730786	00 54 56.26	-72 26 47.4	1.21	15.27	0.03	-0.05	0.04	-1.07	0.04	
		O_7_72789	00 54 56.10	-72 26 49.4	1.41	20.62	0.27	0.43	0.43	···	···	
		O_7_72806	00 54 56.67	-72 26 46.0	2.92	20.37	0.22	0.24	0.43	···	···	
		O_7_74196	00 54 55.76	-72 26 49.1	2.70	20.84	0.33	0.47	0.54	···	···	
5_8	1.97	**O_7_71334**	00 54 36.72	-72 26 38.1	1.61	19.16	0.05	0.78	0.06	···	···	n
		Z_2683599	00 54 36.80	-72 26 37.8	1.34	19.10	0.05	0.83	0.07	0.30	0.14	
5_9	1.50	Z_2530728	00 53 37.65	-72 24 10.4	1.28	19.68	0.11	0.40	0.14	0.10	0.18	n, c
		Z_2531366	00 53 37.93	-72 24 08.1	1.33	18.19	0.06	0.59	0.07	-0.13	0.09	
5_10	2.70	**Z_2702542**	00 54 44.44	-72 23 58.1	2.17	19.37	0.07	0.85	0.09	-0.47	0.16	n
		Z_2702553	00 54 44.45	-72 24 00.0	2.53	21.23	0.17	0.06	0.21	99.99	99.99	
		Z_2705059	00 54 45.46	-72 23 58.5	2.50	21.92	0.37	-0.22	0.41	99.99	99.99	
5_12	1.50	**Z_2406014**[!]	00 52 45.10	-72 28 43.4	0.35	14.92	0.08	0.00	0.09	-0.97	0.04	n, c
5_13	3.92	Z_2561198	00 53 50.54	-72 18 19.4	2.54	19.95	0.06	-0.53	0.14	1.16	0.19	n
		Z_2563156[!]	00 53 51.34	-72 18 17.4	1.84	19.65	0.14	-0.40	0.16	-0.06	0.14	
5_14	2.69	**O_7_72871**	00 54 51.25	-72 26 31.1	2.23	20.70	0.21	-0.58	0.23	···	···	n
		O_7_74351	00 54 50.61	-72 26 30.6	1.43	21.73	0.32	0.53	0.50	···	···	
5_15	2.61	**O_7_71429**	00 54 48.97	-72 25 44.6	0.50	19.00	0.10	0.18	0.12	···	···	c

Table B.4—Continued

X-ray			Optical counterpart									Notes
Src	Rad.	Src ID	Position (J2000.0)		Offset	V	δV	B-V	δ(B − V)	U-B	δ(U − B)	
			R.A.	Decl.								
	($''$)				($''$)							
[1]	[2]	[3]	[4]	[5]	[6]	[7]	[8]	[9]	[10]	[11]	[12]	[13]
		(Z_2713702)	00 54 49.04	-72 25 45.2	0.92	18.81	0.05	0.42	0.08	-0.98	0.09	
		O_7_72057	00 54 48.31	-72 25 45.1	2.53	19.22	0.04	-0.05	0.07	···	···	
		Z_2712098	00 54 48.36	-72 25 45.3	2.36	19.21	0.08	-0.01	0.13	-0.34	0.12	
		O_7_72059	00 54 48.74	-72 25 43.4	1.44	20.54	0.08	0.18	0.16	···	···	
		(Z_2713147)	00 54 48.81	-72 25 44.0	0.76	20.25	0.18	0.76	0.25	99.99	99.99	
		O_7_73093	00 54 48.79	-72 25 47.3	2.59	20.57	0.15	1.17	0.57	···	···	
		O_7_73100	00 54 48.88	-72 25 46.1	1.37	20.12	0.09	-0.13	0.12	···	···	
5_16	1.50	**Z_2573354**[!]	00 53 55.38	-72 26 45.3	0.83	14.72	0.03	-0.07	0.03	-1.02	0.04	c
5_18	4.51	Z_2205777	00 51 18.29	-72 30 01.4	2.34	21.38	0.18	0.51	0.26	99.99	99.99	n
		Z_2207680	00 51 19.15	-72 30 01.0	2.74	18.90	0.05	0.31	0.06	-0.22	0.08	
		Z_2208320	00 51 19.45	-72 30 05.8	4.50	21.61	0.18	-0.03	0.24	99.99	99.99	
5_21	1.88	O_6_324429	00 53 52.41	-72 32 01.2	1.67	19.26	0.22	0.69	0.32	···	···	n
		(Z_2565806)	00 53 52.40	-72 32 01.1	1.58	18.51	0.06	1.63	0.23	-2.24	0.23	
		O_6_324585	00 53 52.20	-72 32 01.1	1.87	19.08	0.12	0.02	0.15	···	···	
		O_6_327160	00 53 52.44	-72 31 59.0	0.53	21.46	0.42	99.99	99.99	···	···	
5_22	2.34	**O_6_87363**	00 51 58.97	-72 30 57.6	0.88	19.63	0.06	-0.03	0.08	···	···	n, c
		Z_2296070	00 51 59.01	-72 30 57.5	0.75	19.64	0.08	0.07	0.09	-0.41	0.08	
5_23	3.34	**Z_2288276**	00 51 55.61	-72 20 40.2	2.57	17.99	0.03	-0.06	0.04	-0.69	0.05	n
		Z_2289471	00 51 56.13	-72 20 35.8	2.51	19.35	0.05	0.48	0.10	0.30	0.20	
5_24	1.50	**Z_2595629**[!]	00 54 03.92	-72 26 32.8	0.78	14.95	0.03	0.01	0.04	-1.13	0.06	n, c
5_25	3.02	**Z_2686280**	00 54 37.90	-72 22 11.4	1.81	18.48	0.04	0.98	0.07	0.08	0.11	n
		Z_2687267	00 54 38.30	-72 22 08.9	1.38	20.83	0.09	0.22	0.14	99.99	99.99	
5_26	3.15	Z_2264995	00 51 45.19	-72 21 53.5	2.80	19.57	0.06	0.83	0.10	0.53	0.34	n, c
		Z_2266383	00 51 45.82	-72 21 50.2	1.88	19.22	0.09	-0.03	0.10	-0.39	0.08	
5_27	1.50	**Z_2556246**	00 53 48.53	-72 28 01.9	1.48	19.65	0.06	0.98	0.11	0.74	0.40	n
5_28	1.50	**Z_2359566**	00 52 25.73	-72 23 12.0	0.87	19.40	0.07	0.88	0.09	0.02	0.16	n, c
5_29	1.50	**Z_2581383**	00 53 58.50	-72 26 14.4	0.78	17.81	0.04	-0.14	0.05	-0.82	0.06	n, c
5_30	2.64	**O_6_324153**[†]	00 54 28.58	-72 31 06.5	2.45	19.39	0.04	1.71	0.19	···	···	n, c
		O_7_66235[†]	00 54 28.59	-72 31 06.5	2.40	19.38	0.04	1.69	0.13	···	···	
		O_6_327594	00 54 29.65	-72 31 06.2	2.41	99.99	99.99	99.99	99.99	···	···	
		Z_2663497[o]	00 54 28.90	-72 31 08.5	2.62	19.96	0.12	0.03	0.14	-0.34	0.14	
5_31	1.68	**Z_2562687**	00 53 51.14	-72 21 24.1	0.90	20.96	0.17	0.49	0.24	99.99	99.99	n, c
5_32	2.30	**Z_2315739**	00 52 07.48	-72 21 25.3	2.22	15.20	0.03	-0.07	0.03	-0.62	0.04	n
5_33	1.50	**Z_2578607**	00 53 57.43	-72 24 43.0	1.07	20.80	0.14	0.38	0.19	99.99	99.99	n

Table B.4—Continued

X-ray			Optical counterpart									Notes
Src	Rad.	Src ID	Position (J2000.0)		Offset	V	δV	B-V	δ(B − V)	U-B	δ(U − B)	
			R.A.	Decl.								
	($''$)				($''$)							
[1]	[2]	[3]	[4]	[5]	[6]	[7]	[8]	[9]	[10]	[11]	[12]	[13]
5_34	1.69	**O_6_327685**	00 54 04.67	-72 30 54.1	1.20	20.78	0.15	0.20	0.21	···	···	n
		Z_2598422^{o}	00 54 04.96	-72 30 53.5	1.69	19.51	0.07	0.42	0.10	-0.35	0.12	
5_36	3.19	Z_2510874	00 53 29.23	-72 18 31.6	2.48	21.31	0.19	-0.04	0.23	0.21	0.44	n
		Z_2511547	00 53 29.52	-72 18 35.6	1.89	19.70	0.10	0.15	0.11	-0.08	0.14	

†Sources detected in two neighboring OGLE-II fields.

$^{!}$The fit with stellar atmosphere models was unsuccesful (quality flag +20, see Zaritsky et al. (2002) for more details).

^{o}Just outside the error circle of the X-ray source there is another OGLE-II source (not listed in these tables), that it is most likely related with the detected MCPS source within the search radius.

Table B.5. Optical counterparts of X-ray sources in *Chandra* field 6

X-ray			Optical counterpart									Notes
Src	Rad.	Src ID	Position (J2000.0)		Offset	V	δV	B-V	δ(B − V)	U-B	δ(U − B)	
			R.A.	Decl.								
	($''$)				($''$)							
[1]	[2]	[3]	[4]	[5]	[6]	[7]	[8]	[9]	[10]	[11]	[12]	[13]
6_1	1.50	**O_6_77228**	00 52 08.95	-72 38 02.9	0.58	15.03	0.02	0.14	0.03	···	···	c
		Z_2319498	00 52 09.07	-72 38 03.1	0.64	15.23	0.03	-0.08	0.03	-0.81	0.04	
6_2	1.91	**O_7_47103**	00 54 55.87	-72 45 10.7	0.40	15.01	0.01	-0.02	0.01	···	···	c
		Z_2729974	00 54 55.91	-72 45 10.6	0.61	15.00	0.03	-0.03	0.04	-0.93	0.18	
6_3	1.50	**O_6_153267**	00 52 42.20	-72 47 21.0	1.38	18.15	0.07	-0.14	0.08	···	···	n
		Z_2399147	00 52 42.27	-72 47 20.9	1.30	17.81	0.06	0.04	0.08	-0.52	0.07	
		O_6_154606	00 52 42.24	-72 47 19.1	0.54	20.16	0.09	0.52	0.15	···	···	
		O_6_155950	00 52 42.40	-72 47 20.6	1.15	20.39	0.21	0.09	0.27	···	···	
6_4	1.86	**O_6_147662**	00 52 52.28	-72 48 29.8	0.27	14.42	0.05	-0.10	0.05	···	···	c
		Z_2423181	00 52 52.35	-72 48 29.8	0.56	14.36	0.03	-0.05	0.04	-0.97	0.04	
		O_6_152322	00 52 51.93	-72 48 28.5	1.84	99.99	99.99	99.99	99.99	···	···	
6_5	1.69	**O_6_79076**	00 52 03.31	-72 38 30.2	0.84	20.44	0.17	0.37	0.19	···	···	n
		Z_2305973	00 52 03.30	-72 38 30.4	0.64	19.88	0.06	0.39	0.12	99.99	99.99	
6_6	2.41	O_6_148861	00 52 45.77	-72 49 19.1	1.30	19.76	0.08	0.88	0.14	···	···	n, c
		Z_2407810	00 52 45.86	-72 49 19.0	1.41	19.76	0.07	1.19	0.16	99.99	99.99	
		O_6_149910	00 52 45.24	-72 49 18.2	2.00	19.55	0.05	-0.02	0.06	···	···	
		Z_2406433	00 52 45.28	-72 49 18.2	1.82	19.48	0.07	0.10	0.08	99.99	99.99	
6_8	2.06	**O_6_306524**	00 54 21.68	-72 45 34.0	2.02	17.60	0.01	1.12	0.06	···	···	n
		Z_2644493	00 54 21.71	-72 45 34.0	1.95	17.37	0.06	1.26	0.07	0.74	0.11	
		O_6_307574	00 54 22.34	-72 45 32.0	1.58	19.14	0.05	0.03	0.07	···	···	
		Z_2646086	00 54 22.33	-72 45 31.9	1.57	18.99	0.06	0.20	0.14	-0.38	0.14	
		O_6_308458	00 54 22.06	-72 45 34.5	1.89	19.88	0.14	0.14	0.15	···	···	
		O_6_310253	00 54 22.00	-72 45 32.5	0.13	21.24	0.32	0.51	0.39	···	···	
		O_6_310266	00 54 22.08	-72 45 31.1	1.55	20.46	0.14	0.10	0.21	···	···	
6_9	1.50	**O_6_238962**	00 53 32.39	-72 43 17.3	1.15	19.93	0.14	-0.14	0.16	···	···	n
		O_6_240354	00 53 32.43	-72 43 15.6	1.37	99.99	99.99	99.99	99.99	···	···	
6_10	1.50	**O_6_157291**	00 52 59.08	-72 45 10.2	1.12	20.65	0.15	0.27	0.20	···	···	n
6_11	3.09	O_6_322008†	00 54 27.55	-72 37 20.6	2.13	21.07	0.19	0.12	0.24	···	···	n
		O_7_60612†	00 54 27.55	-72 37 20.7	2.19	21.12	0.33	0.05	0.41	···	···	
		O_6_322014†	00 54 26.64	-72 37 19.5	2.53	21.10	0.44	-0.11	0.44	···	···	
		O_7_59068†	00 54 26.68	-72 37 19.3	2.33	20.41	0.13	0.24	0.27	···	···	
		Z_2657832	00 54 26.75	-72 37 19.3	2.01	20.07	0.20	0.29	0.22	0.36	0.26	
		O_6_322031†	00 54 27.53	-72 37 18.2	1.77	21.43	0.31	0.47	0.46	···	···	
		O_7_60644†	00 54 27.49	-72 37 18.2	1.63	21.50	0.20	0.29	0.35	···	···	

Table B.5—Continued

X-ray		Optical counterpart										Notes
Src	Rad.	Src ID	Position (J2000.0)		Offset	V	δV	B-V	δ(B − V)	U-B	δ(U − B)	
			R.A.	Decl.								
	($''$)				($''$)							
[1]	[2]	[3]	[4]	[5]	[6]	[7]	[8]	[9]	[10]	[11]	[12]	[13]
		O_6_323805†	00 54 27.80	-72 37 18.2	2.86	21.07	0.16	0.29	0.22	···	···	
		O_7_60649†	00 54 27.84	-72 37 18.1	3.07	21.15	0.16	0.22	0.22	···	···	
		Z_2657679○	00 54 26.69	-72 37 17.3	2.92	17.07	0.03	0.36	0.05	0.03	0.05	
6_12	1.55	**O_6_235232**	00 53 39.01	-72 47 17.4	0.27	99.99	99.99	99.99	99.99	···	···	n
6_13	2.60	O_6_151822	00 52 31.58	-72 49 15.4	1.03	21.24	0.21	0.48	0.35	···	···	n
		Z_2373703	00 52 31.66	-72 49 15.4	1.31	21.61	0.24	1.24	0.55	99.99	99.99	
		O_6_152785	00 52 31.33	-72 49 18.1	2.01	20.74	0.17	0.12	0.26	···	···	
6_14	1.66	O_6_168813	00 52 44.92	-72 36 36.3	1.48	21.17	0.26	99.99	99.99	···	···	n
		O_6_169942	00 52 44.90	-72 36 38.5	0.78	20.79	0.28	0.68	0.38	···	···	
		O_6_169953	00 52 44.50	-72 36 37.7	1.57	20.47	0.34	99.99	99.99	···	···	
		O_6_169962	00 52 45.04	-72 36 37.1	1.07	20.36	0.12	0.22	0.14	···	···	
6_15	1.50	**O_6_74072**	00 52 11.10	-72 43 57.2	0.63	21.05	0.14	0.43	0.32	···	···	n
		Z_2324388	00 52 11.15	-72 43 57.3	0.79	21.35	0.23	0.99	0.49	99.99	99.99	
6_16	2.05	**O_6_228490**	00 53 15.78	-72 48 49.1	1.30	19.68	0.07	0.67	0.12	···	···	n
		Z_2478947	00 53 15.86	-72 48 49.1	1.10	19.59	0.06	0.72	0.10	0.01	0.26	
		O_6_231394	00 53 16.33	-72 48 49.5	1.62	21.09	0.21	0.44	0.33	···	···	
6_17	1.50	**O_6_248830**	00 53 33.42	-72 37 22.9	1.49	21.03	0.12	0.11	0.19	···	···	n
6_18[fc]	1.50	**O_6_74071**	00 52 10.10	-72 43 57.2	0.39	20.27	0.08	0.38	0.13	···	···	n
		Z_2322033	00 52 10.15	-72 43 57.3	0.29	20.41	0.14	0.78	0.25	-0.93	0.34	
6_19	3.87	**O_6_321630**	00 54 11.42	-72 35 12.0	1.14	21.02	0.20	99.99	99.99	···	···	n
		O_6_323167	00 54 11.05	-72 35 11.6	0.96	21.41	0.24	0.26	0.32	···	···	
		Z_2615243	00 54 11.06	-72 35 12.0	0.65	21.37	0.17	0.46	0.31	-0.37	0.47	
6_20	1.50	**O_6_311169**	00 54 09.53	-72 41 42.9	0.62	13.71	0.14	0.39	0.19	···	···	n, c
		Z_2611188‡	00 54 09.57	-72 41 42.9	0.64	13.82	0.05	-0.05	0.13	-0.67	0.12	
6_21	1.50	**O_6_242351**	00 53 25.24	-72 39 41.5	1.47	19.14	0.05	0.75	0.06	···	···	n, c
		O_6_245027	00 53 24.89	-72 39 42.3	0.96	20.97	0.19	0.37	0.26	···	···	
6_22	3.46	**O_7_48946**	00 54 49.96	-72 45 02.3	1.11	20.08	0.08	-0.09	0.13	···	···	n
		O_7_50553	00 54 49.86	-72 45 03.4	1.84	20.28	0.07	0.09	0.16	···	···	
		(Z_2715848)	00 54 49.95	-72 45 02.6	1.16	19.50	0.06	0.05	0.07	-0.07	0.08	
		O_7_48950	00 54 50.25	-72 45 02.5	0.21	21.47	0.32	1.00	0.81	···	···	
		O_7_50544	00 54 50.55	-72 45 04.4	2.51	21.35	0.11	0.33	0.31	···	···	
		(Z_2717021)	00 54 50.44	-72 45 05.3	3.06	21.50	0.20	0.98	0.46	99.99	99.99	
		O_7_50568	00 54 49.59	-72 45 02.1	2.77	21.26	0.16	0.40	0.30	···	···	
		O_7_50583	00 54 49.72	-72 45 00.7	2.76	21.67	0.28	-0.36	0.35	···	···	

Table B.5—Continued

X-ray			Optical counterpart									Notes
Src	Rad.	Src ID	Position (J2000.0)		Offset	V	δV	B-V	δ(B − V)	U-B	δ(U − B)	
			R.A.	Decl.								
	($''$)				($''$)							
[1]	[2]	[3]	[4]	[5]	[6]	[7]	[8]	[9]	[10]	[11]	[12]	[13]
		(Z_2715501)	00 54 49.80	-72 45 00.9	2.36	20.77	0.14	0.28	0.26	99.99	99.99	
		O_7_50584	00 54 50.52	-72 45 00.9	2.04	21.55	0.29	0.01	0.35	···	···	
6_23	1.50	**O_6_158108**	00 52 40.00	-72 42 44.4	0.56	17.10	0.05	1.42	0.15	···	···	n, c
		Z_2393742	00 52 40.01	-72 42 44.5	0.49	16.92	0.05	1.21	0.07	1.92	0.16	
		O_6_159120	00 52 39.85	-72 42 46.1	1.29	18.95	0.05	-0.08	0.06	···	···	
6_25	2.66	O_6_247697	00 53 08.98	-72 34 51.5	1.73	20.06	0.09	0.72	0.14	···	···	n
		O_6_250104	00 53 08.63	-72 34 53.9	2.42	20.95	0.23	0.36	0.28	···	···	
		O_6_250120	00 53 08.91	-72 34 53.4	2.38	21.31	0.27	-0.01	0.30	···	···	
		O_6_250136	00 53 08.23	-72 34 51.1	1.68	19.93	0.08	-0.08	0.09	···	···	
		Z_2461085	00 53 08.32	-72 34 51.3	1.28	20.04	0.13	-0.13	0.14	0.06	0.29	
		O_6_250146	00 53 08.66	-72 34 50.0	1.52	99.99	99.99	99.99	99.99	···	···	

[†]Sources detected in two neighboring OGLE-II fields.

[‡]The I band photometry in the MCPS catalog was replaced with that from the OGLE-II (see Zaritsky et al. (2002) for more details).

[o]Just outside the error circle of the X-ray source there is another OGLE-II source (not listed in these tables), that it is most likely related with the detected MCPS source within the search radius.

[fc]The finding chart of *Chandra* source 6_18 includes also source 6_15 as they are too near to each other.

Table B.6. Optical counterparts of X-ray sources in *Chandra* field 7

X-ray			Optical counterpart									Notes
Src	Rad.	Src ID	Position (J2000.0)		Offset	V	δV	B-V	δ(B − V)	U-B	δ(U − B)	
			R.A.	Decl.								
	($''$)				($''$)							
[1]	[2]	[3]	[4]	[5]	[6]	[7]	[8]	[9]	[10]	[11]	[12]	[13]
7_1	1.50	**O_5_65517**	00 49 03.34	-72 50 52.1	0.45	16.94	0.06	0.09	0.10	···	···	c
		Z_1916984	00 49 03.41	-72 50 52.3	0.35	16.78	0.04	0.08	0.06	-0.84	0.05	
		O_5_65743	00 49 03.30	-72 50 53.7	1.20	18.86	0.23	0.15	0.38	···	···	
		(Z_1916967)	00 49 03.40	-72 50 53.9	1.35	18.08	0.06	0.07	0.12	-0.32	0.13	
		O_5_66768	00 49 03.24	-72 50 53.2	0.86	18.89	0.28	-0.08	0.37	···	···	
7_2	1.50	**Z_1976595**	00 49 32.05	-72 39 25.2	0.40	20.50	0.09	0.33	0.13	99.99	99.99	n
7_3	1.60	O_5_147467	00 50 00.38	-72 49 28.9	0.76	20.75	0.29	99.99	99.99	···	···	n, c
		O_5_149072	00 50 00.17	-72 49 28.8	0.19	20.78	0.42	99.99	99.99	···	···	
		O_5_149088	00 50 00.50	-72 49 28.0	1.56	22.12	0.53	99.99	99.99	···	···	
		O_5_146630	00 50 00.30	-72 49 28.1	0.88	20.60	0.35	99.99	99.99	···	···	
		(Z_2036310)	00 50 00.34	-72 49 28.4	0.78	19.53	0.07	1.30	0.11	0.01	0.35	
		O_5_147479	00 50 00.20	-72 49 27.6	1.28	21.77	0.42	99.99	99.99	···	···	
7_4	3.08	**O_5_140754**	00 49 44.22	-72 52 08.4	2.10	17.52	0.07	1.58	0.17	···	···	u, c
		Z_2002622	00 49 44.34	-72 52 08.6	1.83	17.28	0.07	1.52	0.08	99.99	99.99	
		O_5_141207	00 49 44.43	-72 52 09.7	0.76	17.85	0.05	0.23	0.16	···	···	
		Z_2003040	00 49 44.52	-72 52 10.0	0.79	17.60	0.08	0.01	0.09	-0.48	0.07	
		O_5_141868	00 49 44.41	-72 52 10.7	0.36	19.82	0.12	1.09	0.44	···	···	
		O_5_142924	00 49 44.25	-72 52 09.9	0.72	20.83	0.41	-0.64	0.53	···	···	
		O_5_144727	00 49 44.95	-72 52 11.8	2.93	21.32	0.26	0.50	0.40	···	···	
		O_5_144764	00 49 44.74	-72 52 08.3	2.67	21.20	0.44	1.23	0.65	···	···	
7_5	3.32	**O_4_144169**	00 47 36.44	-72 45 41.0	3.32	21.73	0.22	-0.54	0.32	···	···	n
		(Z_1739792)	00 47 36.51	-72 45 40.8	2.73	21.18	0.16	0.41	0.25	99.99	99.99	
		O_4_144189	00 47 36.13	-72 45 37.7	0.93	22.00	0.26	99.99	99.99	···	···	
		Z_1739697	00 47 36.46	-72 45 36.8	2.33	21.41	0.23	0.83	0.33	99.99	99.99	
7_6	1.50	Z_1944671	00 49 16.78	-72 39 43.4	1.48	21.64	0.21	0.01	0.32	99.99	99.99	n, c
		Z_1945182	00 49 17.04	-72 39 45.5	1.45	17.70	0.04	-0.18	0.04	-0.61	0.05	
7_7	1.81	**O_4_195564**†	00 48 30.01	-72 49 00.3	0.90	21.75	0.15	99.99	99.99	···	···	n
		O_5_68900†	00 48 29.99	-72 49 00.3	0.81	21.86	0.27	99.99	99.99	···	···	
7_9	2.16	O_5_235644	00 50 49.19	-72 41 52.5	2.12	99.99	99.99	99.99	99.99	···	···	c
		O_5_316703	00 50 49.60	-72 41 53.8	0.77	13.49	0.03	1.61	0.04	···	···	
		Z_2142356‡	00 50 49.61	-72 41 53.6	0.59	13.51	0.07	1.41	0.12	1.22	0.12	
		O_5_317836	00 50 49.99	-72 41 51.8	1.98	19.49	0.57	1.85	0.70	···	···	
		O_5_318825	00 50 50.09	-72 41 52.9	1.97	19.90	0.45	99.99	99.99	···	···	
7_10	1.50	**O_5_157856**	00 49 55.41	-72 42 22.9	0.73	20.79	0.17	0.50	0.26	···	···	n

Table B.6—Continued

X-ray			Optical counterpart									Notes
Src	Rad.	Src ID	Position (J2000.0)		Offset	V	δV	B-V	δ(B − V)	U-B	δ(U − B)	
			R.A.	Decl.								
	($''$)				($''$)							
[1]	[2]	[3]	[4]	[5]	[6]	[7]	[8]	[9]	[10]	[11]	[12]	[13]
		Z_2025973	00 49 55.45	-72 42 22.5	1.12	21.32	0.20	0.39	0.24	-1.00	0.37	
7_12	1.94	**O_4_199309**	00 48 20.06	-72 40 11.8	0.91	19.50	0.04	0.77	0.10	···	···	n
7_13	1.50	**O_5_158486**	00 49 34.46	-72 41 06.8	0.37	21.19	0.16	0.16	0.21	···	···	n
7_16	1.50	**O_4_195333**†	00 48 32.77	-72 46 52.8	0.90	21.40	0.21	99.99	99.99	···	···	u
		O_5_72601†	00 48 32.83	-72 46 52.9	0.98	21.37	0.34	0.47	0.38	···	···	
		O_4_195340†	00 48 33.02	-72 46 51.9	0.93	21.35	0.26	99.99	99.99	···	···	
		O_5_71331†	00 48 32.98	-72 46 51.7	0.78	21.48	0.24	99.99	99.99	···	···	
		Z_1853924o	00 48 32.53	-72 46 51.5	1.32	20.33	0.13	0.72	0.16	99.99	99.99	
7_17	5.29	**O_5_140807**	00 49 45.01	-72 54 00.9	4.47	18.36	0.06	0.94	0.11	···	···	u
		(Z_2004363)o	00 49 45.15	-72 54 00.7	5.08	17.19	0.06	1.75	0.17	0.41	0.19	
		O_5_141493	00 49 44.80	-72 54 00.3	3.63	19.91	0.08	0.68	0.17	···	···	
		O_5_140992	00 49 43.85	-72 54 02.2	1.28	18.38	0.03	0.04	0.03	···	···	
		Z_2001696	00 49 43.90	-72 54 02.3	1.31	18.36	0.04	0.13	0.05	-0.49	0.07	
		O_5_142293	00 49 44.43	-72 54 00.0	2.20	21.13	0.15	0.48	0.34	···	···	
		O_5_142299	00 49 44.54	-72 53 58.4	3.61	19.56	0.04	-0.01	0.07	···	···	
		Z_2003145	00 49 44.57	-72 53 58.6	3.54	19.48	0.23	0.08	0.23	-0.36	0.10	
		O_5_143631	00 49 44.31	-72 54 05.4	4.51	20.48	0.13	0.23	0.21	···	···	
		Z_2002614	00 49 44.33	-72 54 05.4	4.51	20.65	0.10	0.54	0.21	-0.76	0.28	
		O_5_143643	00 49 43.48	-72 54 04.9	4.43	21.39	0.22	0.53	0.48	···	···	
		O_5_143656	00 49 42.93	-72 54 03.0	5.07	20.86	0.15	0.13	0.21	···	···	
		Z_1999724	00 49 42.97	-72 54 03.0	4.89	21.22	0.22	1.03	0.47	-1.54	0.63	
		O_5_143702	00 49 44.22	-72 53 58.4	2.87	21.18	0.18	0.42	0.21	···	···	
		O_5_145404	00 49 44.94	-72 53 59.1	4.62	21.29	0.45	99.99	99.99	···	···	
7_18	1.90	**Z_2068590**	00 50 15.46	-72 39 17.8	1.35	21.76	0.25	0.15	0.36	99.99	99.99	n
7_19	1.50	**O_5_146766**	00 49 41.66	-72 48 42.9	1.36	17.16	0.55	0.27	0.60	···	···	n, c
		O_5_147711	00 49 41.74	-72 48 43.7	1.36	19.77	0.44	-0.85	0.59	···	···	
		O_5_149497	00 49 41.49	-72 48 44.2	0.46	20.92	0.39	0.17	0.58	···	···	
		O_5_149522	00 49 41.53	-72 48 42.6	1.29	20.52	0.32	-0.17	0.53	···	···	
		O_5_150426	00 49 41.36	-72 48 44.8	1.03	21.53	0.63	-0.64	0.68	···	···	
7_20	1.94	**O_5_237353**	00 50 34.65	-72 40 38.3	1.62	20.30	0.07	99.99	99.99	···	···	n
		Z_2109958	00 50 34.67	-72 40 38.4	1.53	20.29	0.16	0.21	0.18	99.99	99.99	
		O_5_239470	00 50 34.96	-72 40 38.5	0.35	21.80	0.31	99.99	99.99	···	···	
7_21	1.57	**O_5_148716**	00 49 27.53	-72 50 01.6	0.47	21.22	0.23	0.33	0.30	···	···	n
		Z_1967182	00 49 27.61	-72 50 01.6	0.22	21.54	0.17	-0.01	0.21	99.99	99.99	

Table B.6—Continued

X-ray Src	Rad.	Src ID	Optical counterpart Position (J2000.0) R.A.	Decl.	Offset	V	δV	B-V	δ(B − V)	U-B	δ(U − B)	Notes
	($''$)				($''$)							
[1]	[2]	[3]	[4]	[5]	[6]	[7]	[8]	[9]	[10]	[11]	[12]	[13]
7_23	1.50	**O_5_70749**	00 48 42.34	-72 46 56.9	0.21	19.43	0.04	-0.06	0.07	···	···	n
		Z_1874185	00 48 42.40	-72 46 57.0	0.21	19.46	0.04	0.07	0.07	-1.00	0.10	
7_24	1.91	O_4_194141	00 48 08.11	-72 47 10.7	0.73	20.56	0.14	0.53	0.28	···	···	n
		O_4_195236	00 48 08.29	-72 47 09.3	1.42	20.25	0.08	0.27	0.13	···	···	
7_25	3.01	O_5_64642	00 49 12.95	-72 52 10.5	1.75	20.91	0.19	0.60	0.26	···	···	n
		Z_1937045	00 49 13.08	-72 52 10.5	1.22	20.82	0.12	1.17	0.46	99.99	99.99	
		O_5_64650	00 49 13.30	-72 52 10.3	0.71	21.68	0.26	0.07	0.36	···	···	
		O_5_141206	00 49 13.72	-72 52 10.3	1.86	19.35	0.05	0.69	0.10	···	···	
		Z_1938468	00 49 13.79	-72 52 10.6	2.08	18.86	0.07	0.65	0.09	0.44	0.16	
		O_5_142914	00 49 13.68	-72 52 11.5	1.62	19.99	0.09	0.26	0.13	···	···	
7_27	3.02	**O_5_221350**	00 50 18.35	-72 51 10.4	2.10	20.17	0.07	0.72	0.19	···	···	n
		O_5_224747	00 50 18.71	-72 51 08.6	1.87	20.98	0.12	0.28	0.21	···	···	
		O_5_224753	00 50 18.95	-72 51 08.3	2.17	21.26	0.23	0.10	0.34	···	···	
		(Z_2076011)	00 50 18.92	-72 51 08.8	1.70	20.83	0.14	-0.28	0.17	99.99	99.99	

†Sources detected in two neighboring OGLE-II fields.

‡The I band photometry in the MCPS catalog was replaced with that from the OGLE-II (see Zaritsky et al. (2002) for more details).

°Just outside the error circle of the X-ray source there is another OGLE-II source (not listed in these tables), that it is most likely related with the detected MCPS source within the search radius.

Table B.7. Additional optical info

X-ray source ID	Type*	Ref.	C/part of associated X-ray source	Ref.	Other sources within 1.5″	Ref.
[1]	[2]	[3]	[4]	[5]	[6]	[7]
3_1	AGN	[DSM03]	OGLE00571981-7225337	[SPH03]	[USNO-A2.0]0150-00625436	[SPH03]
	variable	[ZSW01]				
3_2	Be-XBP	[ECG04]	Z_2806702	[ECG04],[CEG05]	...	...
3_3	Be-XBP	[MFL03]	[MA93]1020	[MFL03],[HP04]	[M02]40790	[M02]
	Be?	[SPH03]	[MA93]1020≡O_8_49531	[SPH03]		
	Be candidate	[MPG02]	O_8_49531≡	[CEG05]		
			≡[MACHO]207.16432.1575	[CEG05]		
3_4	...	...	...	...	[USNO-B1.0]0177-0042040	[MLC03]
					J005732.7-721302	[DENIS05]
					J005732.7-721301	[DENIS05]
					S01020206684	[GSC2.2]
					[2MASS]J00573272-7213022	[SCS06]
3_7	HMXB?	[SG05]	[2dF]1224≡Z_3075967	[SG05]	S0102022296901	[GSC2.2]
	blue star	[M02]			[M02]40184	[M02]
					[USNO-B1.0]0176-0040752	[MLC03]
					[UCACA2]01162515	[ZA04]
					[2MASS]J00572397-7223566	[SCS06]
					J005723.8-722356	[DENIS05]
3_18	HMXB?, P	[SPH03]	[MA93]904	[HP04]	[2MASS]J00560554-7221595	[SCS06]
	Be?	[HP04]	Z_2893439≡[MA93]904≡	[CEG05]		
	Be-XBP	[CEG05]	≡[MACHO]207.16374.21	[CEG05]		
			[MACHO]207.16374.21≡	[SC06]		
			≡[MA93]904	[SC06]		
4_1	HMXB, Be star	[SHP00]	star1	[CSM97]	[M02]17504	[M02]
	blue star	[M02]	O_5_180026≡	[CEG05]	[MACS#013]0050-732	[TBS96]
	HMXB,Be/X	[HFP00]	≡[MACHO]212.16019.30	[CEG05]		
	Be-XBP	[YIT03]	[MA93]387	[SC05]		
	B0.5V-B1V	[CNM05]				
	eclips.binary#550	[WUK04]				
4_2	Be-XBP	[CEG05]	O_5_111490≡	[CEG05]	[USNO-B1.0]0168-0025357	[MLC03]
	variable star	[ITM04]	≡[MACHO]212.15906.2446	[CEG05]	[M02]12955	[M02]
	Be candidate	[MPG02]			J004913.6-731137	[DENIS05]
					S0102311264259	[GSC2.2]
					[2MASS]J00491360-7311378	[SCS06]
4_3	Be?	[HP04]	[MA93]414	[HP04],[HS00]	[M02]18200	[M02]
	Be/X?	[HS00]			OB 114, O 53	[OKP04]
	blue star	[M02]			[MACS#023]0050-731	[TBS96]
					S0102311270531	[GSC2.2]
					[UCAC2]01000912	[ZA04]
					J005057.11-731008.0	[CI00]
					J005057.1-731007	[DENIS05]
4_4	...	...	...	...	S0102330258235	[GSC2.2]
					[USNO-B1.0]0166-0028183	[MLC03]
					[M02]10496	[M02]
					[2MASS]J00481877-7320598	[SCS06]
					J004818.7-732100	[DENIS05]
4_5	Be?	[HP04]	[MA93]300	[HP04],[HS00]	[M02]13712	[M02]
	Be/X?	[HS00]			S0102311265986	[GSC2.2]
	variable star	[ITM04]			[USNO-B1.0]0168-0025726	[MLC03]
					J004929.8-731058	[DENIS03]

Table B.7—Continued

X-ray source ID	Type*	Ref.	C/part of associated X-ray source	Ref.	Other sources within 1.5″	Ref.
[1]	[2]	[3]	[4]	[5]	[6]	[7]
					[2MASS]J00492984-7310583	[SCS06]
4_7	...	...	...	...	[2MASS]J00485340-7324573	[SCS06]
					[USNO-B1.0]0165-0028919	[MLC03]
					J004853.5-732457	[DENIS05]
4_8	Be candidate	[MPG02]	...	...	[M02]10291	[M02]
					J004814.1-731003	[DENIS05]
					S0102311267622	[GSC2.2]
					[UCAC2]01000224	[ZA04]
					[2MASS]J00481410-7310045	[SCS06]
					[USNO-B1.0]0168-0024147	[MLC03]
4_14	Be-XBP	[EC03]	O_5_90506 ?	[EC03]	...	...
			[MA93]315	[HS00]		
			O_5_90506≡	[CEG05]		
			≡[MACHO]212.15960.12	[CEG05]		
4_15	...	...	...	...	[2MASS]J00491077-7317171	[SCS06]
					J004910.7-731717	[DENIS05]
4_17	Be candidate	[MPG02]	...	...	OB 110	[OKP04]
					J005047.9-731817	[DENIS05]
					[2MASS]J00504799-7318180	[SCS06]
					S0102330234535	[GSC2.2]
					J005048.05-731818.1	[CI00]
4_21	...	...	...	...	[USNO-B1.0]0166-0031693	[MLC03]
4_24	...	...	...	...	[USNO-B1.0]0166-0030591	[MLC03]
					S0102330259641	[GSC2.2]
4_32	...	...	...	...	[USNO-B1.0]0167-0029373	[MLC03]
					[USNO-B1.0]0167-0029382	[MLC03]
					J004926.7-731211	[DENIS05]
					S0102311263515	[GSC2.2]
4_36	...	...	...	...	J005044.9-731540	[DENIS05]
5_1	SMC-X3	[CDL78]	[MA93]531	[HS00]	[2dF]0839≡Z_2311496	[EHI04]
	Be-XRB	[HS00],[HP04]	Z_2311496	[CEG05]	[USNO-B1.0]0175-0027384	[MLC03]
	P	[ECG04]			[M02]22302	[M02]
	B0-5 (II)e	[EHI04]			OB 143	[OKP04]
	blue star	[M02]			J005205.6-722604	[DENIS05]
					J005205.63-722604.0	[CI00]
					J005205.7-722603	[DENIS05]
					[MACS#001]0052-724	[TBS96]
					S0102022289632	[GSC2.2]
					[2MASS]00520563-7226042	[SCS06]
5_2	Be/X?	[HS00]	[MA93]667	[HS00]	[USNO-B1.0]0175-0030153	[MLC03]
	Be?	[HP04]	[MA93]667≡	[ECG04]	[M02]26743	[M02]
	Be-XBP or	[ECG04]	≡[MACHO]207.16202.50	[ECG04]	S0102022287762	[GSC2.2]
	source not located		Z_2498173	[CEG05]	[2MASS]00532381-7227152	[SCS06]
	in the SMC ?				J005323.95-722715.5	[CI00]
	($N_H < 0.01 \times 10^{22} cm^{-2}$)				[MACS#010]0053-724	[TBS96]
5_3	Be-XRB	[HS00],[HP04]	[MA93]506	[HS00]	[2dF]0828≡O_6_85614	[EHI04]
	P	[ISA95]	star 1≡[MA93]506	[SCB99]	[M02]21514	[M02]
	B0-5	[EHI04]	or star 2 ?		OB 135, O 64	[OKP04]
	Be candidate	[MPG02]	O_6_85614≡[MA93]506≡	[SC06]	[MACS#016]0051-725	[TBS96]
	B2	[AV82]	≡[MACHO]208.16087.9	[SC06]	[USNO-B1.0]0174-0029686	[MLC03]

Table B.7—Continued

X-ray source ID	Type*	Ref.	C/part of associated X-ray source	Ref.	Other sources within 1.5″	Ref.
[1]	[2]	[3]	[4]	[5]	[6]	[7]
					J005153.1-723148≡	[DENIS05]
					≡J005153.20-723148.5	[SCS06]
					S0102311350027	[GSC2.2]
					[2MASS]00515317-7231487	[SCS06]
					[UCAC2]01078761	[ZA04]
5_4	...	...	...	...	[MB00]134	[MB00]
					[MA93]798	[MA93]
					[M02]31155	[M02]
					OB 191, O 93	[OKP04]
					[USNO-B1.0]0175-0032932	[MLC03]
					J005446.3-722522	[DENIS05]
					J005446.3-722521	[DENIS05]
					J005446.31-722522.7	[CI00]
					S0102022292484	[GSC2.2]
					[2MASS]00544633-7225228	[SCS06]
					[UCAC2]01162180	[ZA04]
5_7	Be-XRB	[HS00]	O_7_70829≡[MA93]810	[SPH03]	[M02]31710	[M02]
	Be candidate	[MPG02]	[MACHO]207.16259.23≡	[SC05]	J005456.1-722647	[DENIS05]
	P	[MLS98]	≡O_7_70829≡[MA93]810	[SC05]	J005456.2-722647	[DENIS05]
	variable	[ZSW01]	[MA93]810	[HS00]	[USNO-B1.0]0175-0033267	[MLC03]
					J005456.18-722647.6	[CI00]
					S0102022341688	[GSC2.2]
					[2MASS]00545618-7226478	[SCS06]
					[UCAC2]01162201	[ZA04]
5_9	...	...	...	...	J005337.9-722408	[DENIS05]
					J005337.9-722408	[DENIS05]
					S0102022297258	[GSC2.2]
					[2MASS]00533785-7224088	[SCS06]
5_12	blue star	[M02]	...	...	[M02]24501	[M02]
					OB 155	[OKP04]
					J005245.1-722843	[DENIS05]
					J005245.1-722843	[DENIS05]
					[2MASS]00524508-7228437	[SCS06]
					[UCACA2]01161880	[ZA04]
5_15	Quasar	[DMS03]	O_7_71429	[DMS03]	[USNO-B1.0]0175-0033000	[MLC03]
	Be candidate	[MPG02]			S0102022342014	[GSC2.2]
5_16	Be-XRB, P	[BCS01]	star A	[BCS01]	OB 179, O 84	[OKP04]
	B1-B2 III-Ve	[BCS01]	star B	[BCS01]	[M02]28479	[M02]
	blue star	[M02]	[MACHO]207.16202.30 ?	[CEG05]	[USNO-B1.0]0175-0031247	[MLC03]
			Z_2573354	[CEG05]	J005355.2-722645	[DENIS05]
					J005355.3-722645	[DENIS05]
					J005355.26-722645.0	[CI00]
					S0102022289128	[GSC2.2]
					[2MASS]00535518-7226448	[SCS06]
					[UCACA2]01162023	[ZA04]
5_22	...	...	...	...	[USNO-B1.0]0174-0029946	[MLC03]
5_24	blue star	[M02]	...	...	[M02]28942	[M02]
					[USNO-B1.0]0175-0031564	[MLC03]
					OB 179, O 84	[OKP04]
					J005403.8-722632	[DENIS05]

Table B.7—Continued

X-ray source ID	Type*	Ref.	C/part of associated X-ray source	Ref.	Other sources within 1.5″	Ref.
[1]	[2]	[3]	[4]	[5]	[6]	[7]
					J005403.9-722632	[DENIS05]
					J005403.88-722632.8	[CI00]
					S0102022290686	[GSC2.2]
					[2MASS]00540389-7226329	[SCS06]
					[UCACA2]01162049	[ZA04]
5_26	...	...	...	...	[USNO-B1.0]0176-0028501	[MLC03]
					[USNO-B1.0]0176-0028511	[MLC03]
5_28	...	...	...	...	[USNO-B1.0]0176-0029993	[MLC03]
5_29	...	...	...	...	[M02]28644	[M02]
					[USNO-B1.0]0175-0031361	[MLC03]
					S0102022289800	[GSC2.2]
5_30	high proper motion star	[SZU02]	...	...	...	...
5_31	...	...	...	...	[USNO-B1.0]0176-0032854	[MLC03]
6_1	transient P	[CMM02],[ECG04]	[MACS#004]0052-726	[ECG04]	[2dF]5054≡O_6_77228	[EHI04]
	Be-XBP	[SC05]	[MACHO]208.16085.24≡	[CEG05]	S0102311339902	[GSC2.2]
	Be candidate	[MPG02],[SC05]	≡O_6_77228	[CEG05]	[M02]22496	[M02]
	B1-5 (II)e	[EHI04]			[USNO-B1.0]0173-0035041	[MLC03]
	blue star	[M02]			[UCACA2]01078809	[ZA04]
					J005208.9-723803	[DENIS05]
					J005209.0-723802	[DENIS05]
					J005209.05-723803.2	[CI00]
					[2MASS]00520896-7238032	[SCS06]
6_2	Be-XBP	[HPS04]	[MACHO]207.16254.16≡	[SC05]	OB 194	[OKP04]
	P	[ECG04]	≡[MA93]809	[SC05]	[USNO-B1.0]0172-0041290	[MLC03]
	O9V	[HPS04]	[M02]31699≡O_7_47103	[HPS04]	J005455.9-724510	[DENIS05]
	blue star	[M02]	[MA93]809	[HS00]	J005455.9-724511	[DENIS05]
			[MACHO]207.16254.16≡	[F05]	J005455.92-724510.7	[CI00]
			≡O_7_47103	[F05]	S0102311327234	[GSC2.2]
					[2MASS]00545586-7245108	[SCS06]
6_4	Be-XRB	[HS00]	[MA93]618≡AV138	[HS00]	[MACS#013]0053-728	[TBS96]
	blue star	[M02]			[M02]24914	[M02]
	Be candidate	[MPG02]			OB 162, O 72	[OKP04]
	B extr	[GCM87]			[USNO-B1.0]0171-0032820	[MLC03]
					J005252.2-724830	[DENIS05]
					J005252.2-724829	[DENIS05]
					J005252.09-724828.7	[CI00]
					S0102311317724	[GSC2.2]
					[2MASS]00525230-7248301	[SCS06]
6_6	...	...	...	...	[USNO-B1.0]0171-0032607	[MLC03]
6_20	B[e]	[MD01]	...	...	[MA93]739≡AV154	[MA93]
	candidate binary	[PAC01]			OB 182	[OKP04]
					[M02]29267	[M02]
					[USNO-B1.0]0173-0039498	[MLC03]
					J005409.5-724143	[DENIS05]
					J005409.4-724143	[DENIS05]
					J005409.61-724143.0	[CI00]
					S0102311333762	[GSC2.2]
					[2MASS]00540955-7241431	[SCS06]
					[UCAC2]01079173	[ZA04]
6_21	...	...	...	...	[USNO-B1.0]0173-0037830	[MLC03]

Table B.7—Continued

X-ray source ID	Type*	Ref.	C/part of associated X-ray source	Ref.	Other sources within 1.5″	Ref.
[1]	[2]	[3]	[4]	[5]	[6]	[7]
6_23	...	...	...	...	[USNO-B1.0]0172-0036877	[MLC03]
					J005239.9-724244	[DENIS05]
					J005239.9-724244	[DENIS05]
					J005239.70-724243.7	[CI00]
					S0102311364037	[GSC2.2]
					[2MASS]00523999-7242447	[SCS06]
7_1	P	[CML98]	star1(≡O_5_65517)	[SCB99](≡[CO00])	[M02]12482	[M02]
	Be-XRB	[SCB99]	star2(≡O_5_60831)	[SCB99](≡[CO00])	[USNO-B1.0]0171-0026413	[MLC03]
	Be candidate	[MPG02]			J004903.3-725052	[DENIS05]
					S0102311308679	[GSC2.2]
					[2MASS]00490331-7250527	[SCS06]
7_3	...	...	...	...	[USNO-B1.0]0171-0028042	[MLC03]
7_4	...	...	...	...	[USNO-B1.0]0171-0027633	[MLC03]
					J004944.35-725209.0	[CI00]
					S0102311307192	[GSC2.2]
7_6	...	...	...	...	[USNO-B1.0]0173-0028925	[MLC03]
					J004916.9-723945	[DENIS05]
7_9	foreground star	[SHP00]	SkKM62	[SHP00]	[M02]17794	[M02]
					[USNO-B1.0]0173-0032145	[MLC03]
					J005049.6-724153	[DENIS05]
					J005049.68-724154.0	[CI00]
					S0102311364618	[GSC2.2]
					[2MASS]00504958-7241541	[SCS06]
					[MACS#012]0050-726	[TBS96]
7_19	star cluster	[BS95]	...	...	SMC-N32	[BS95]
	emission PN	[MB00]	...	...	[MB00]61	[MB00]
					[USNO-B1.0]0171-0027566	[MLC03]

*Be? Hα emission line object as possible counterpart, no optical spectrum is available in the literature in this case, HMXB?: HMXB candidate, P: pulsar, Be/X?: very promising candidate for Be-XRBs, Be-XBP: Be-XRB pulsar

References. — Azzopardi & Vigneau (1982) [AV82], Bica et al. (1995) [BS95], Buckley et al. (2001) [BCS01], Cioni et al. (2000) [CI00], Clark et al. (1978) [CDL78], Coe et al. (2005a) [CEG05], Coe et al. (2005b) [CNM05], Coe & Orosz (2000) [CO00], Corbet et al. (1998) [CML98], Corbet et al. (2002) [CMM02], Cowley et al. (1997) [CSM97], DENIS Consortium (2003) [DENIS03], DENIS Consortium (2005) [DENIS05], Dobrzycki et al. (2003a) [DMS03], Dobrzycki et al. (2003b) [DSM03], Edge & Coe (2003) [EC03], Edge et al. (2004) [ECG04], Evans et al. (2004) [EHI04], Fabrycky, D. (2005) [F05], Garmany, Conti & Massey (1987) [GCM87], Haberl et al. (2000) [HFP00], Haberl & Pietsch (2004) [HP04], Haberl et al. (2004) [HPS04], Haberl & Sasaki (2000) [HS00], Israel et al. (1995) [ISA95], Ita et al. (2004) [ITM04], Macomb et al. (2003) [MFL03], Marshall et al. (1998) [MLS98], Massey 2002 [M02], Massey & Duffy (2001) [MD01], Mennickent et al. (2002) [MPG02], Meyssonnier & Azzopardi (1993) [MA93], Monet et al. (2003) [MLC03], Murphy & Bessell (2000) [MB00], Oey et al. (2004) [OKP04], Paczynski, B. (2001) [PAC01], Sasaki et al. (2000) [SHP00], Sasaki et al. (2003) [SPH03], Schmidtke & Cowley (2005) [SC05], Schmidtke & Cowley (2006) [SC06], Shtykovskiy & Gilfanov (2005) [SG05], Soszynski et al. (2002) [SZU02], Stevens, Coe & Buckley (1999) [SCB99], STScI 2001 [GSC2.2], Tucholke, de Boer & Seitter (1996) [TBS96], Wyrzykowski et al. (2004) [WUK04], Yokogawa et al. (2003) [YIT03], Zacharias et al. (2004) [ZA04], Zebrun et al. (2001) [ZSW01]

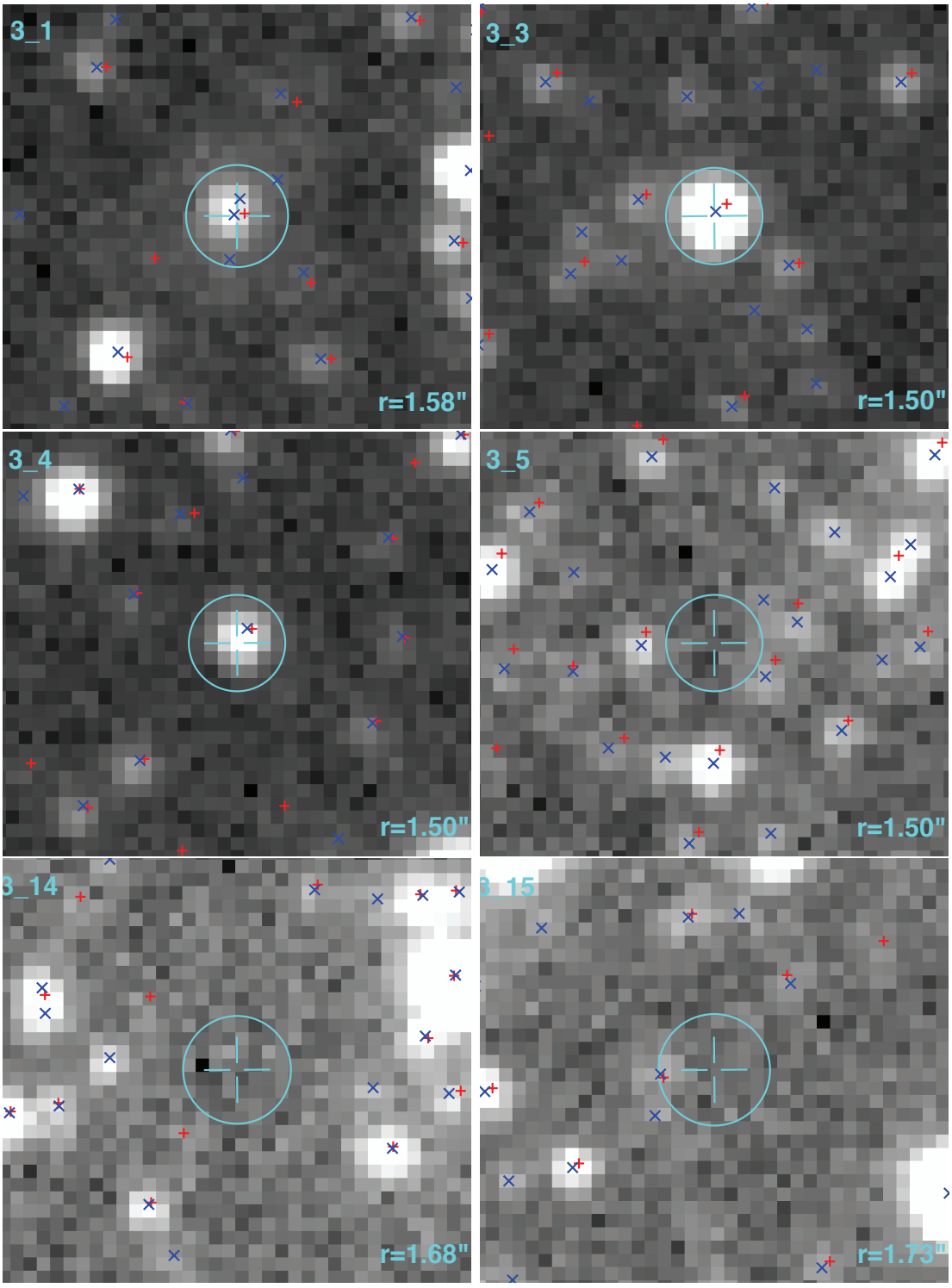

Figure B.1 OGLE *I* band images for Chandra sources in field 3 *This is an electronic Figure.*

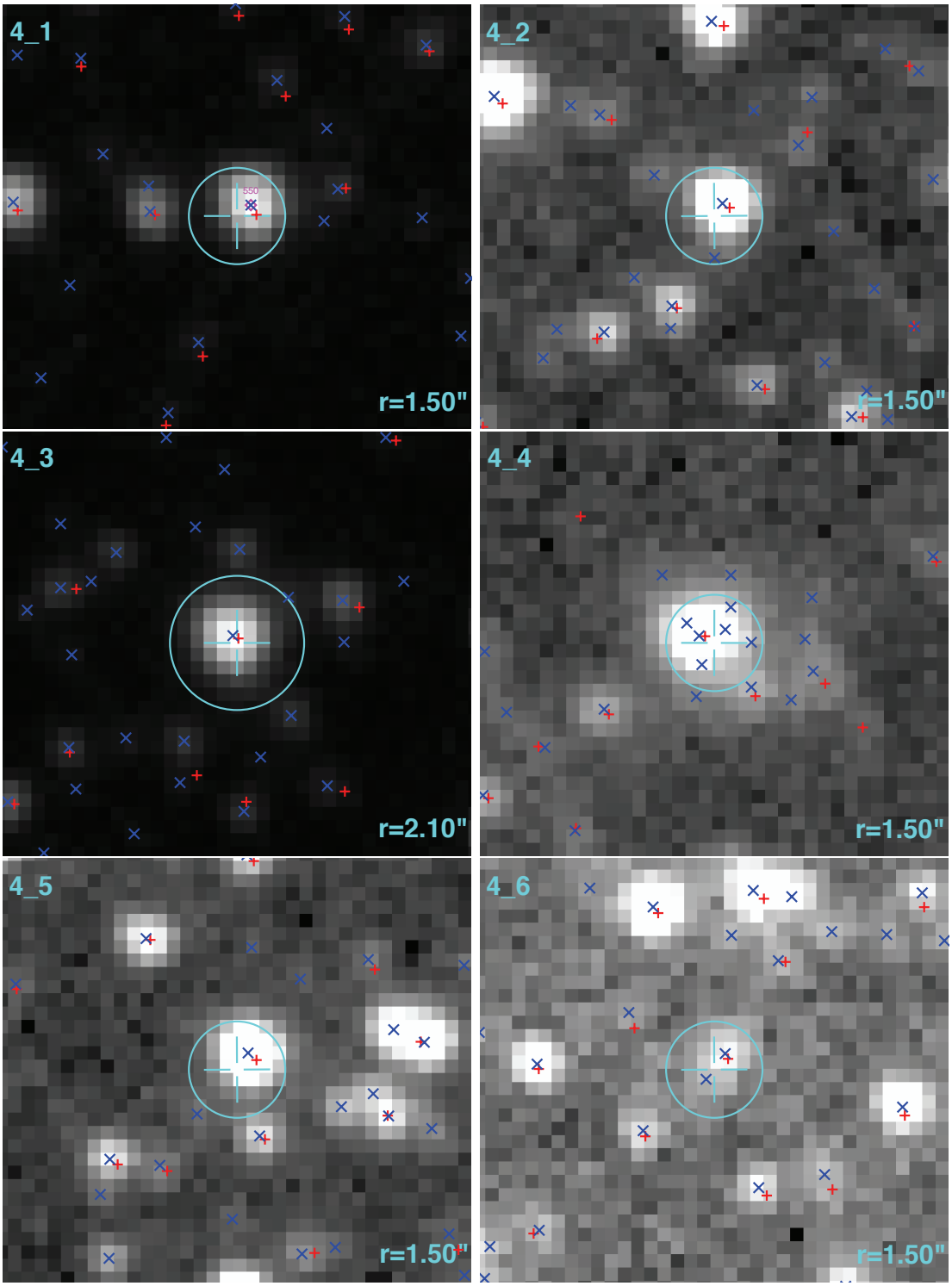

Figure B.2 OGLE *I* band images for Chandra sources in field 4 *This is an electronic Figure.*

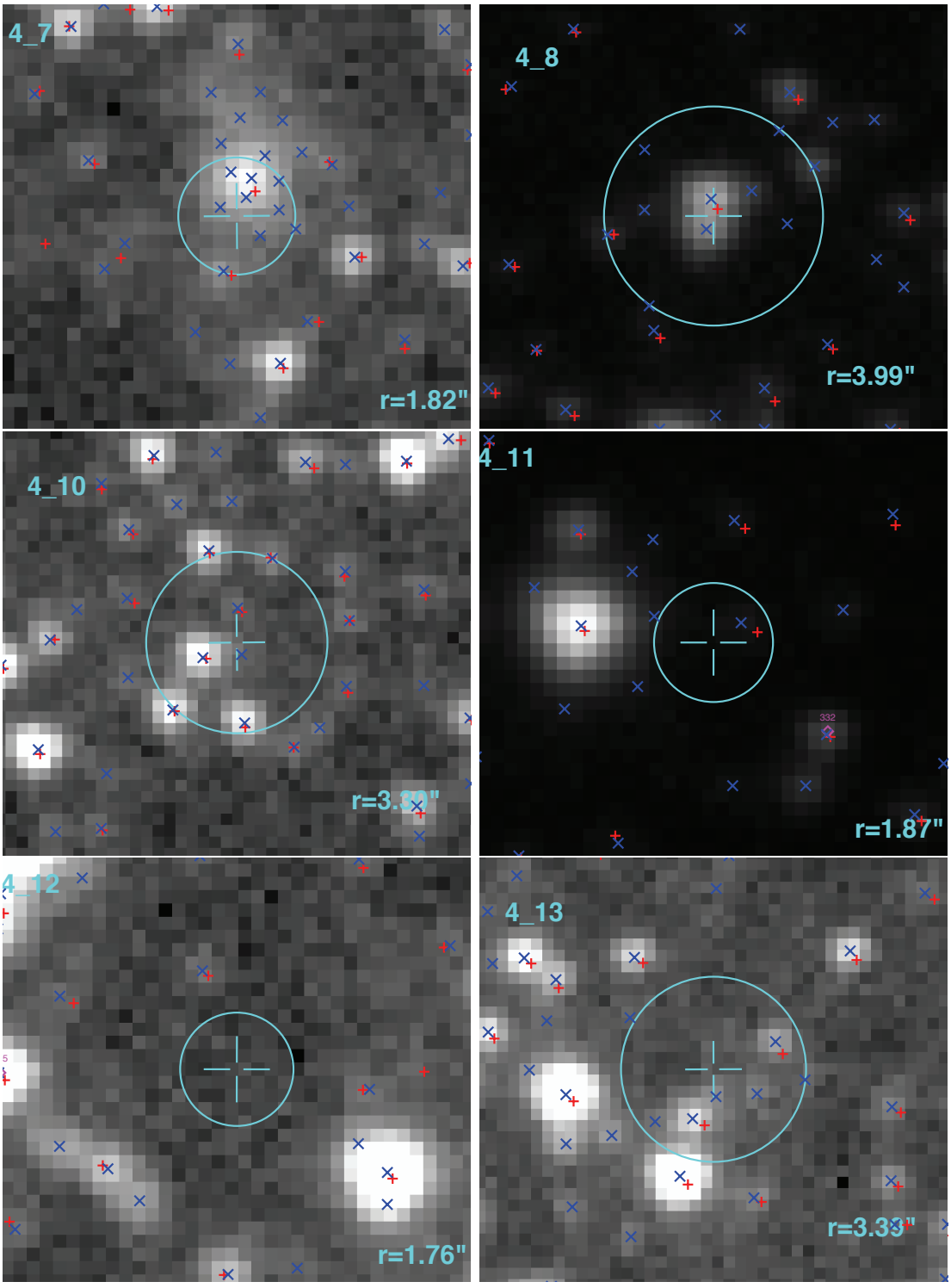
4_7
r=1.82"
4_8
r=3.99"
4_10
r=3.30"
4_11
r=1.87"
4_12
r=1.76"
4_13
r=3.33"

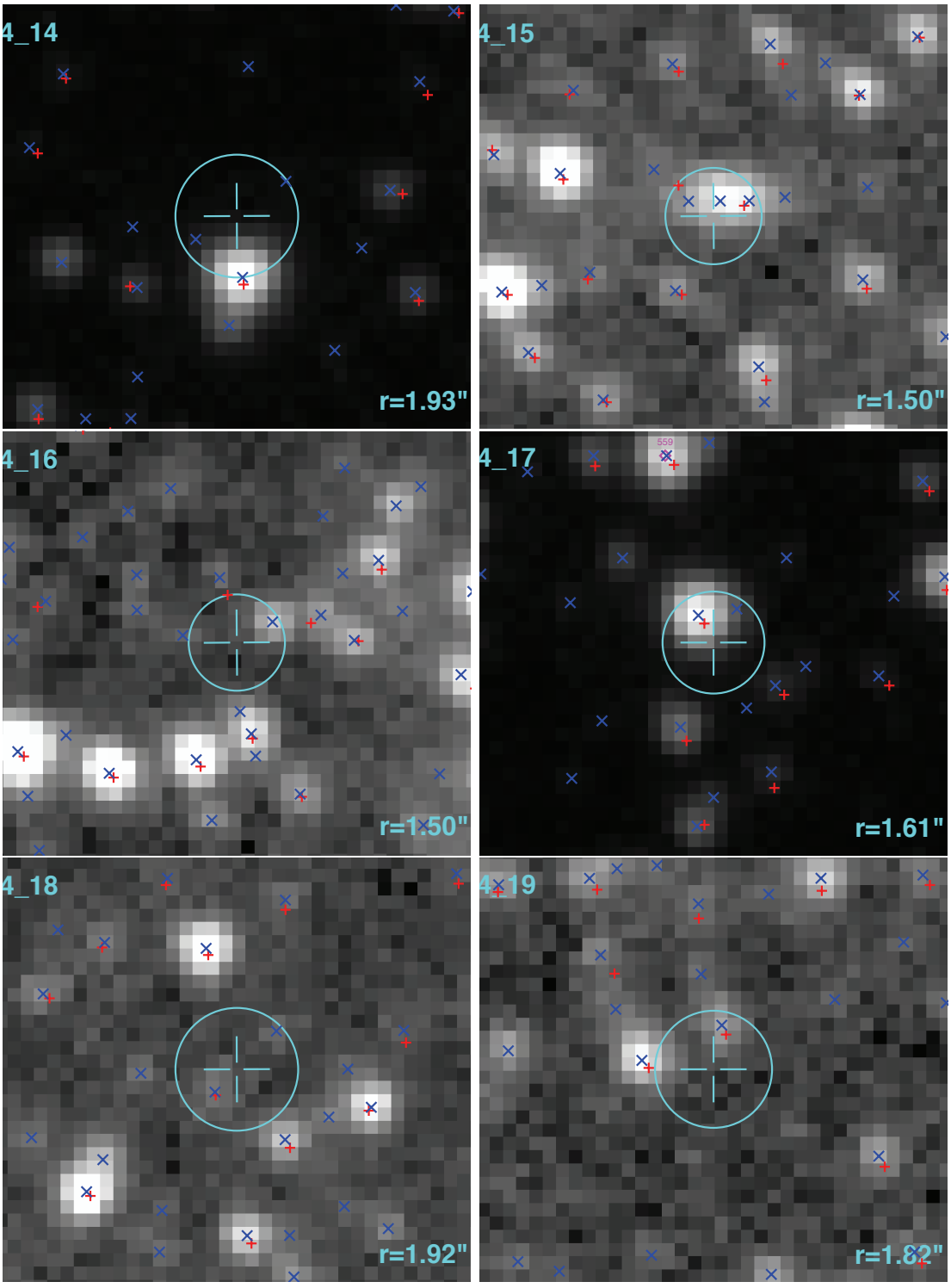
4_14
r=1.93"
4_15
r=1.50"
4_16
r=1.50"
4_17
r=1.61"
4_18
r=1.92"
4_19
r=1.82"

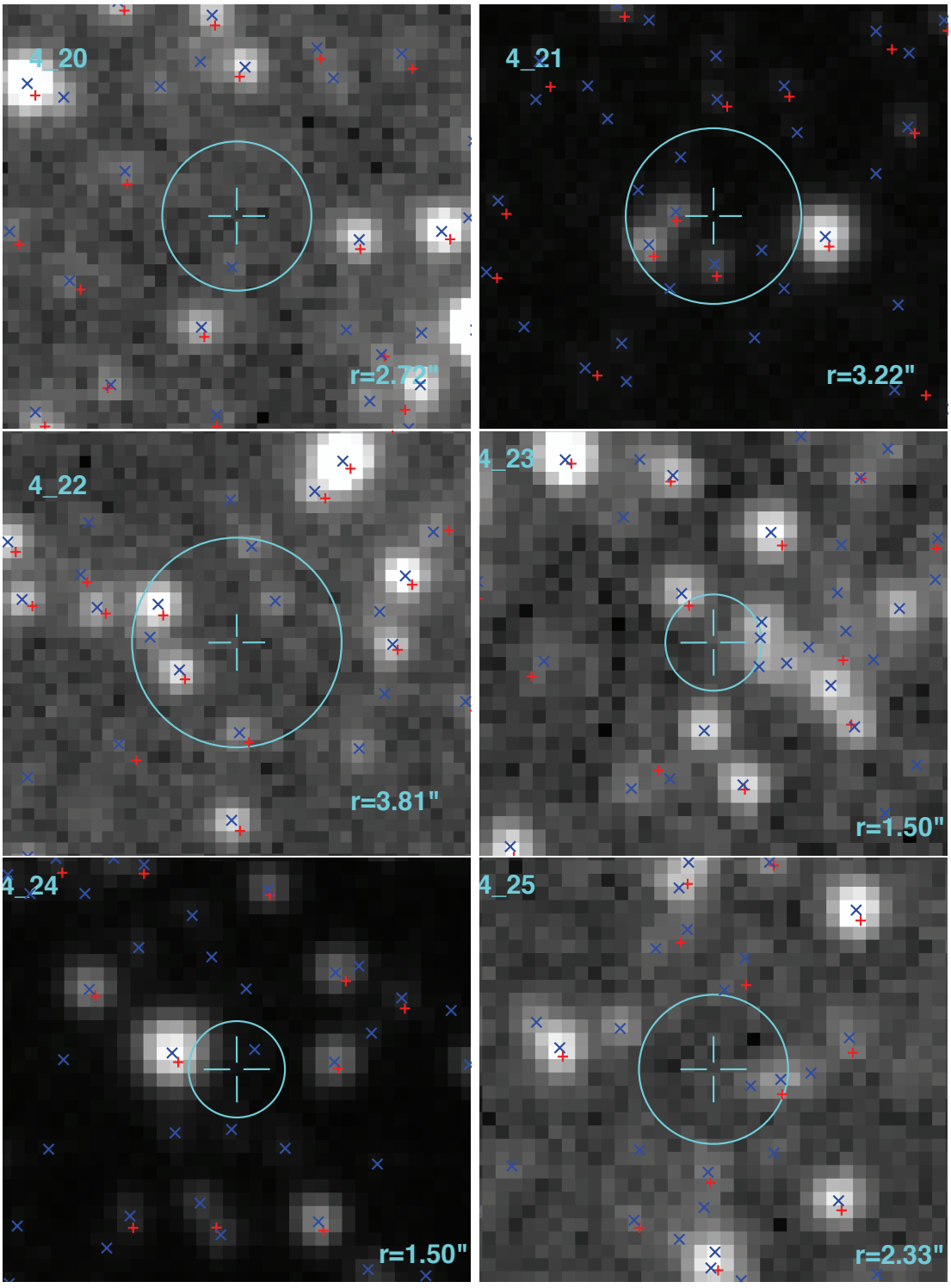
4_20
r=2.72"
4_21
r=3.22"
4_22
r=3.81"
4_23
r=1.50"
4_24
r=1.50"
4_25
r=2.33"

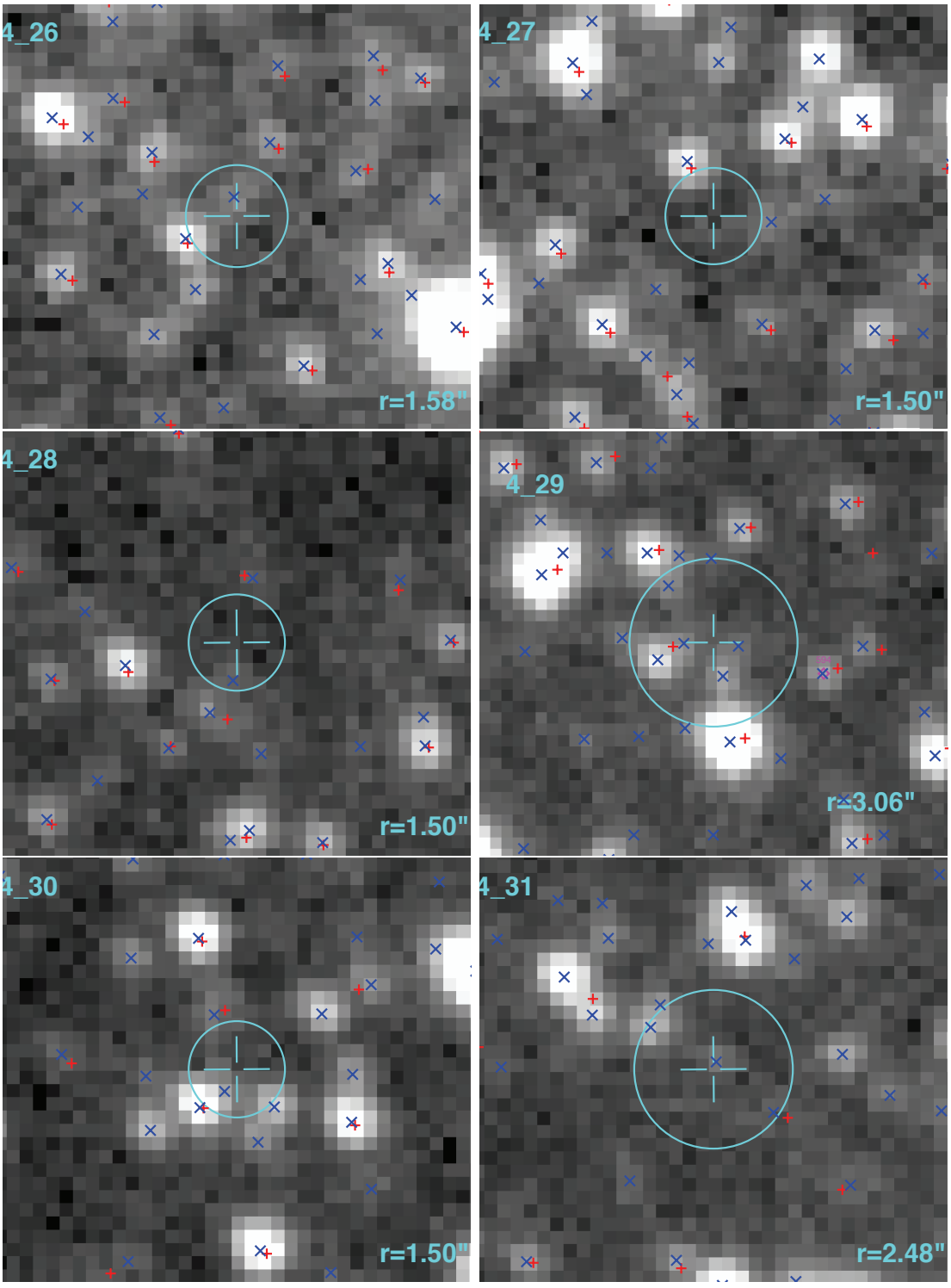
4_26
r=1.58"
4_27
r=1.50"
4_28
r=1.50"
4_29
r=3.06"
4_30
r=1.50"
4_31
r=2.48"

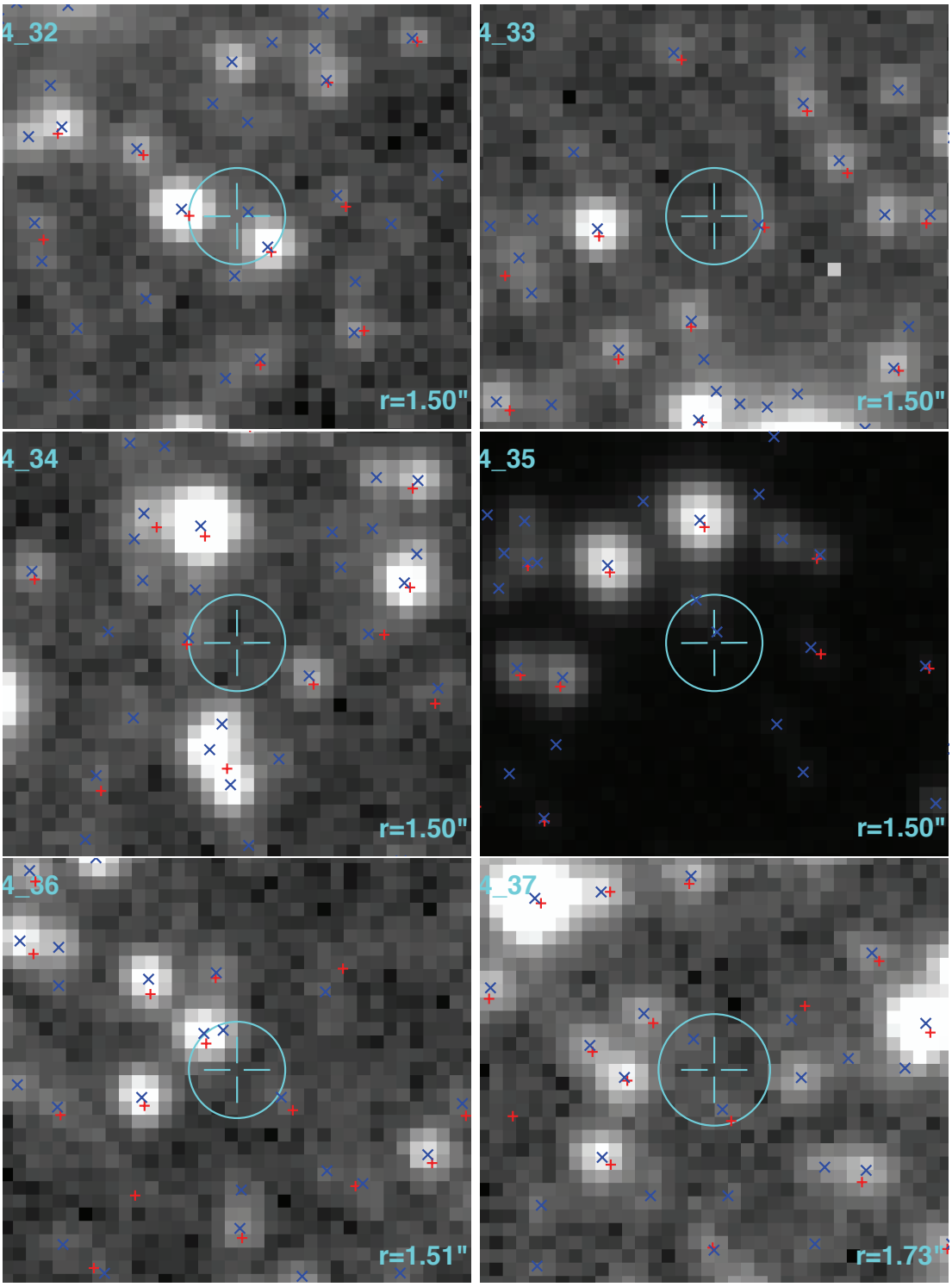
4_32
r=1.50"
4_33
r=1.50"
4_34
r=1.50"
4_35
r=1.50"
4_36
r=1.51"
4_37
r=1.73"

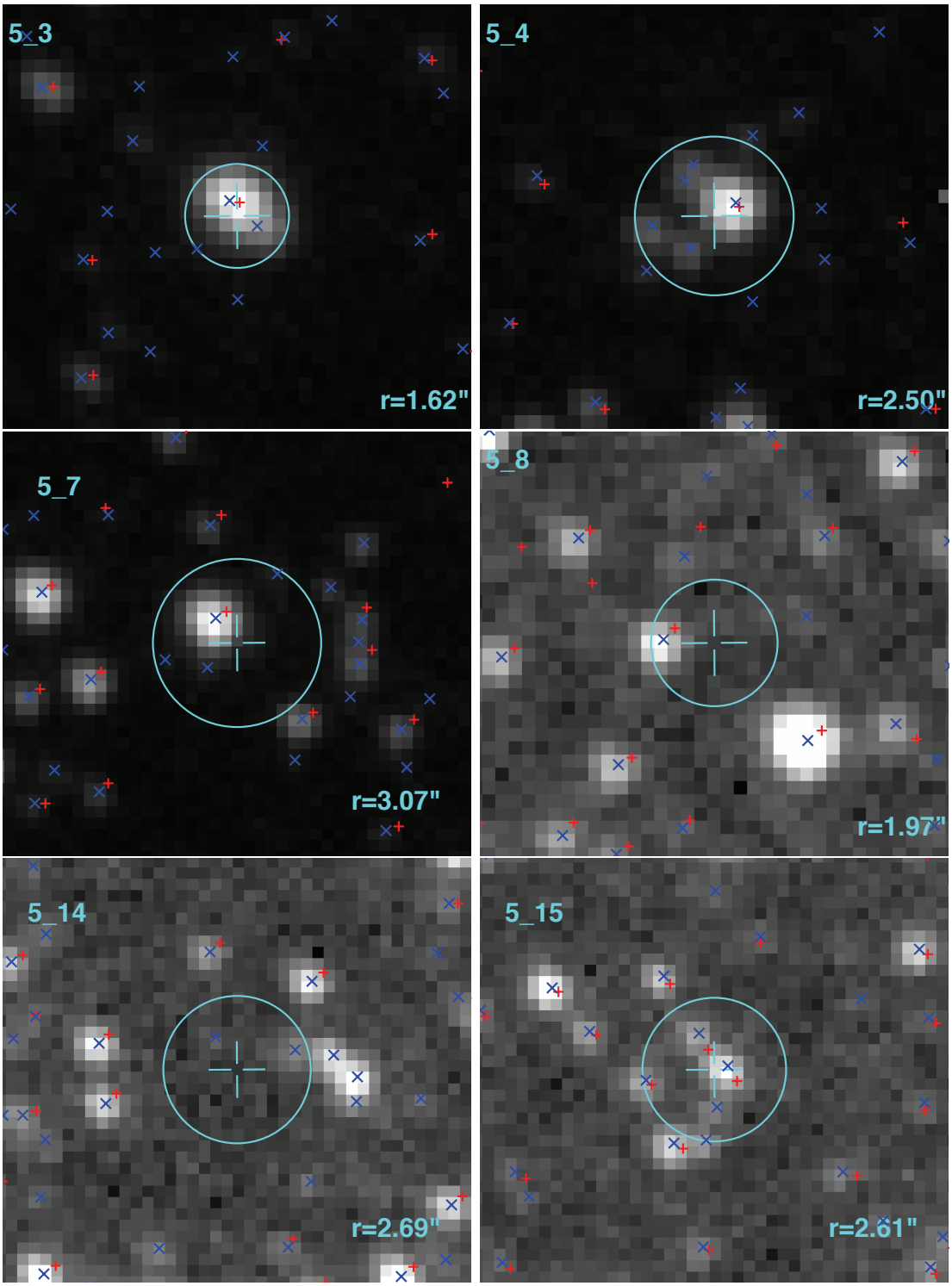

Figure B.3 OGLE *I* band images for Chandra sources in field 5 *This is an electronic Figure.*

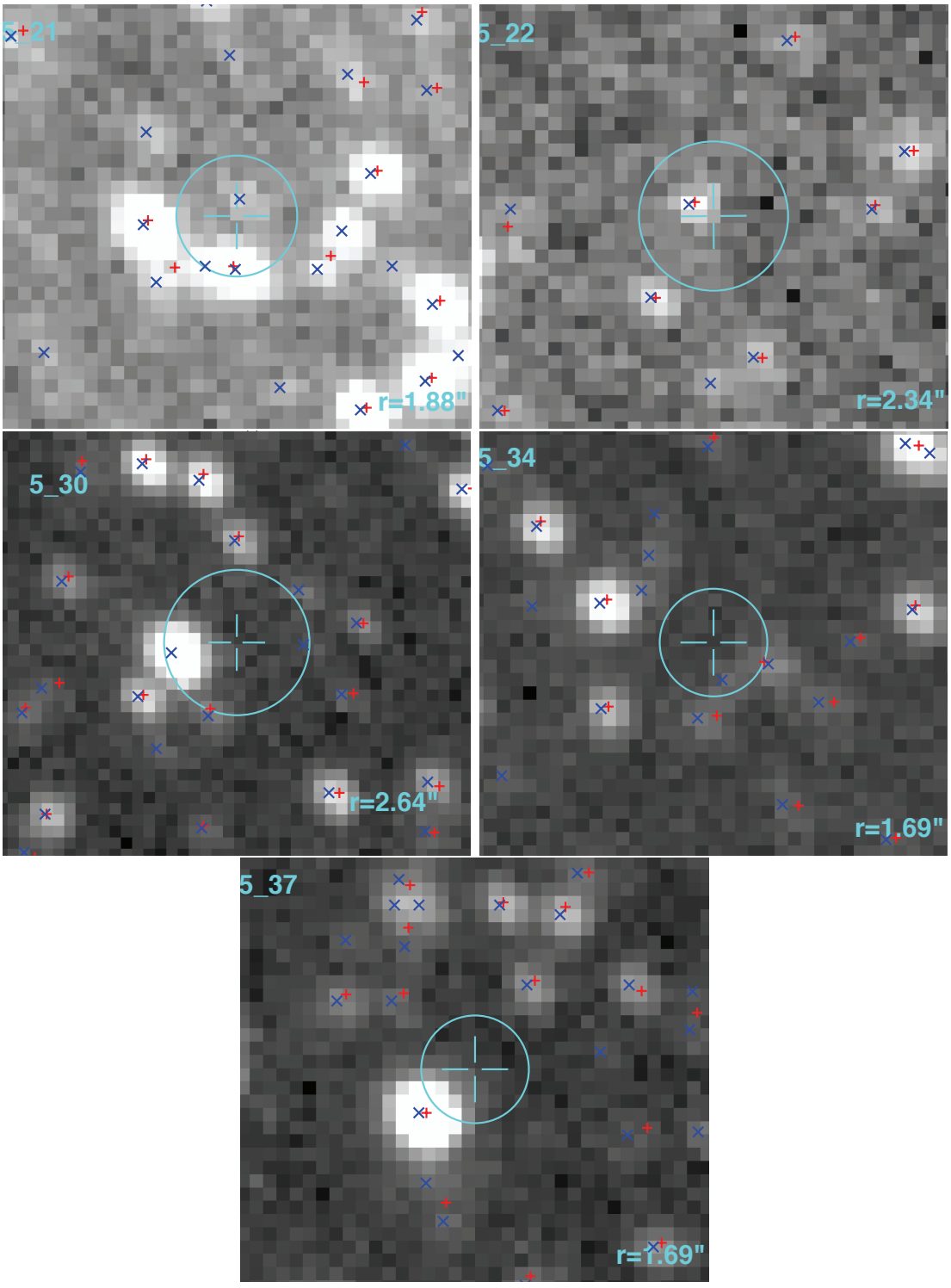
5_21
r=1.88"
5_22
r=2.34"
5_30
r=2.64"
5_34
r=1.69"
5_37
r=1.69"

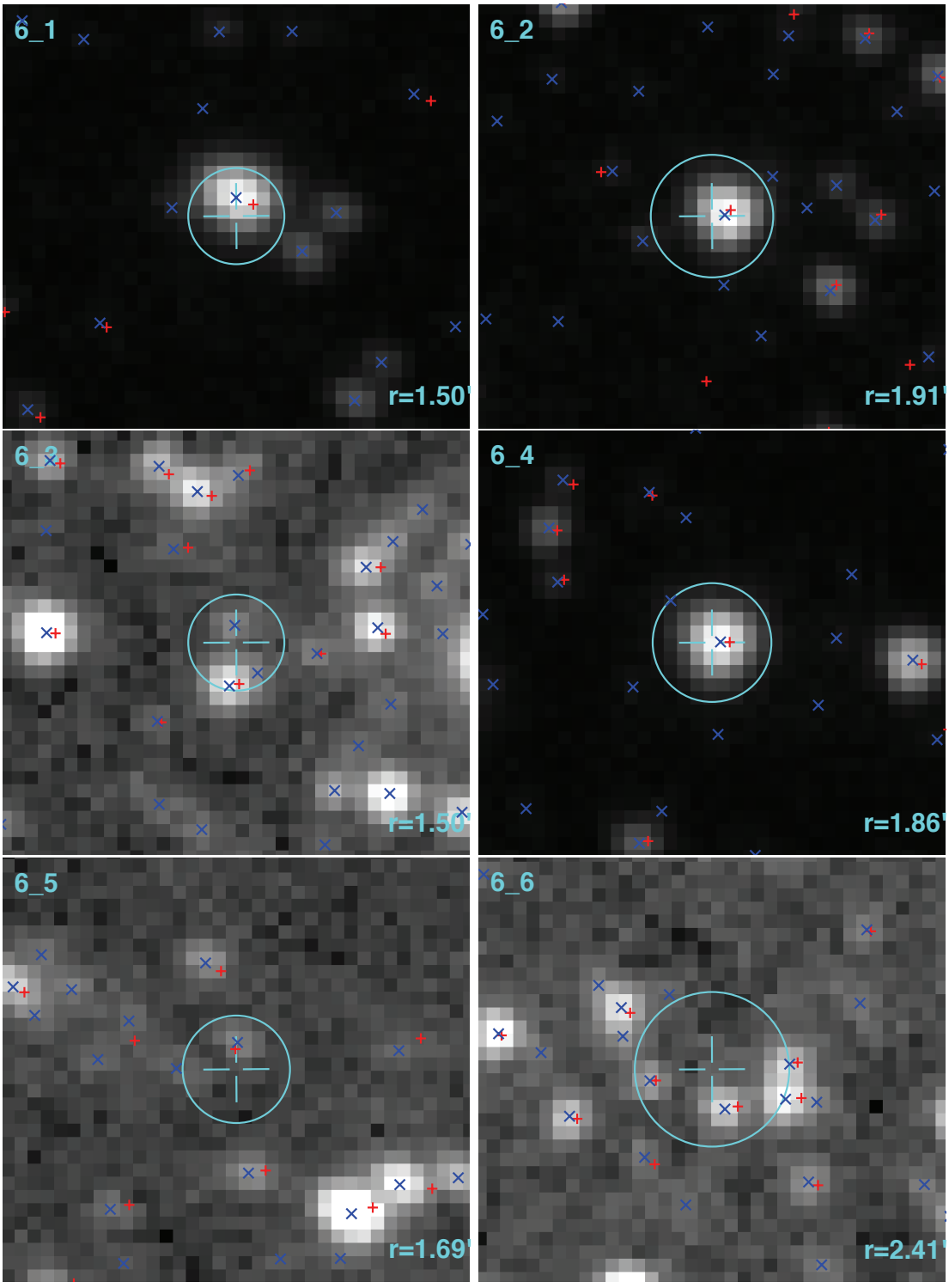

Figure B.4 OGLE *I* band images for Chandra sources in field 6 *This is an electronic Figure.*

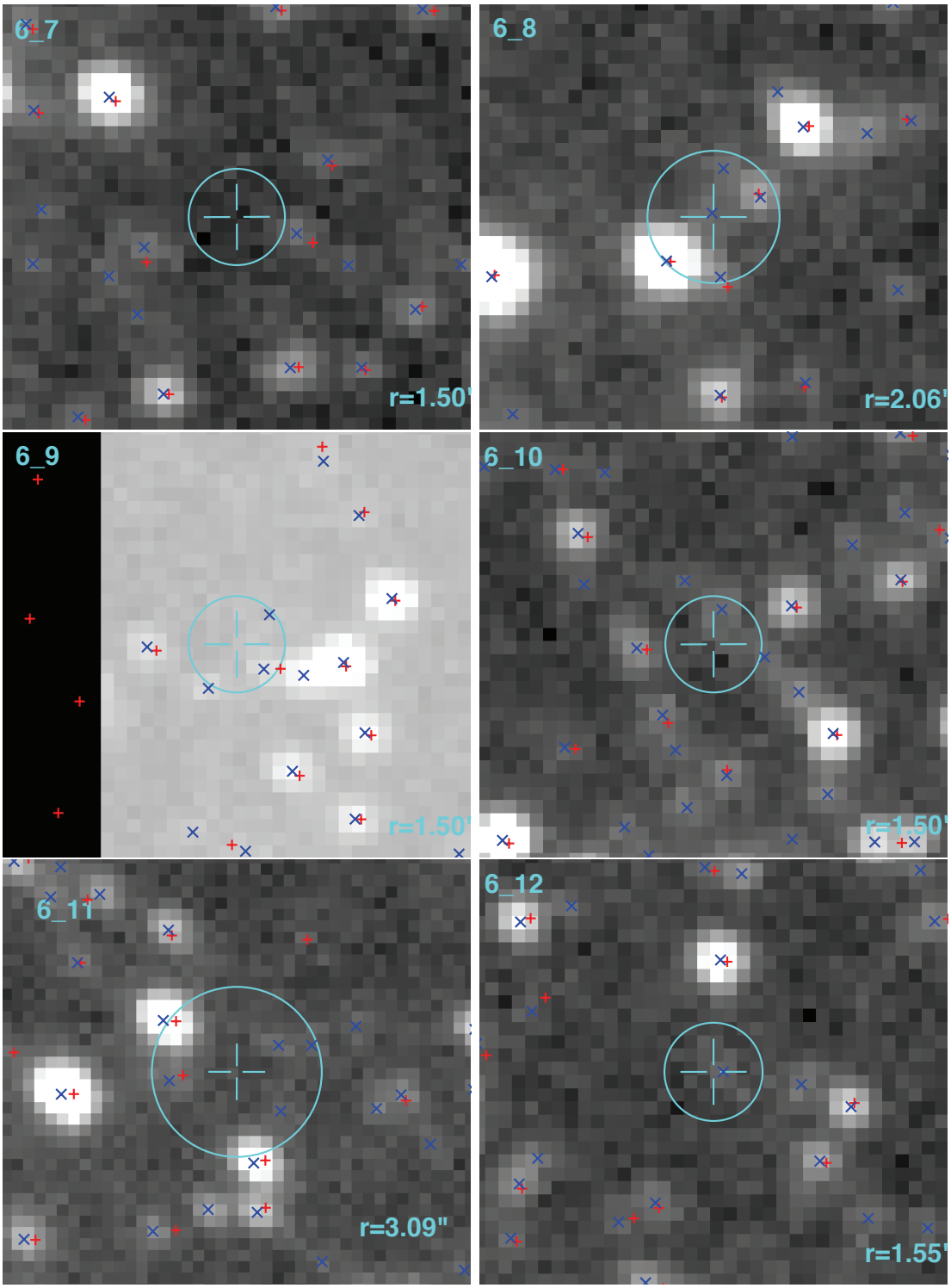
6_7
r=1.50"
6_8
r=2.06"
6_9
r=1.50"
6_10
r=1.50"
6_11
r=3.09"
6_12
r=1.55"

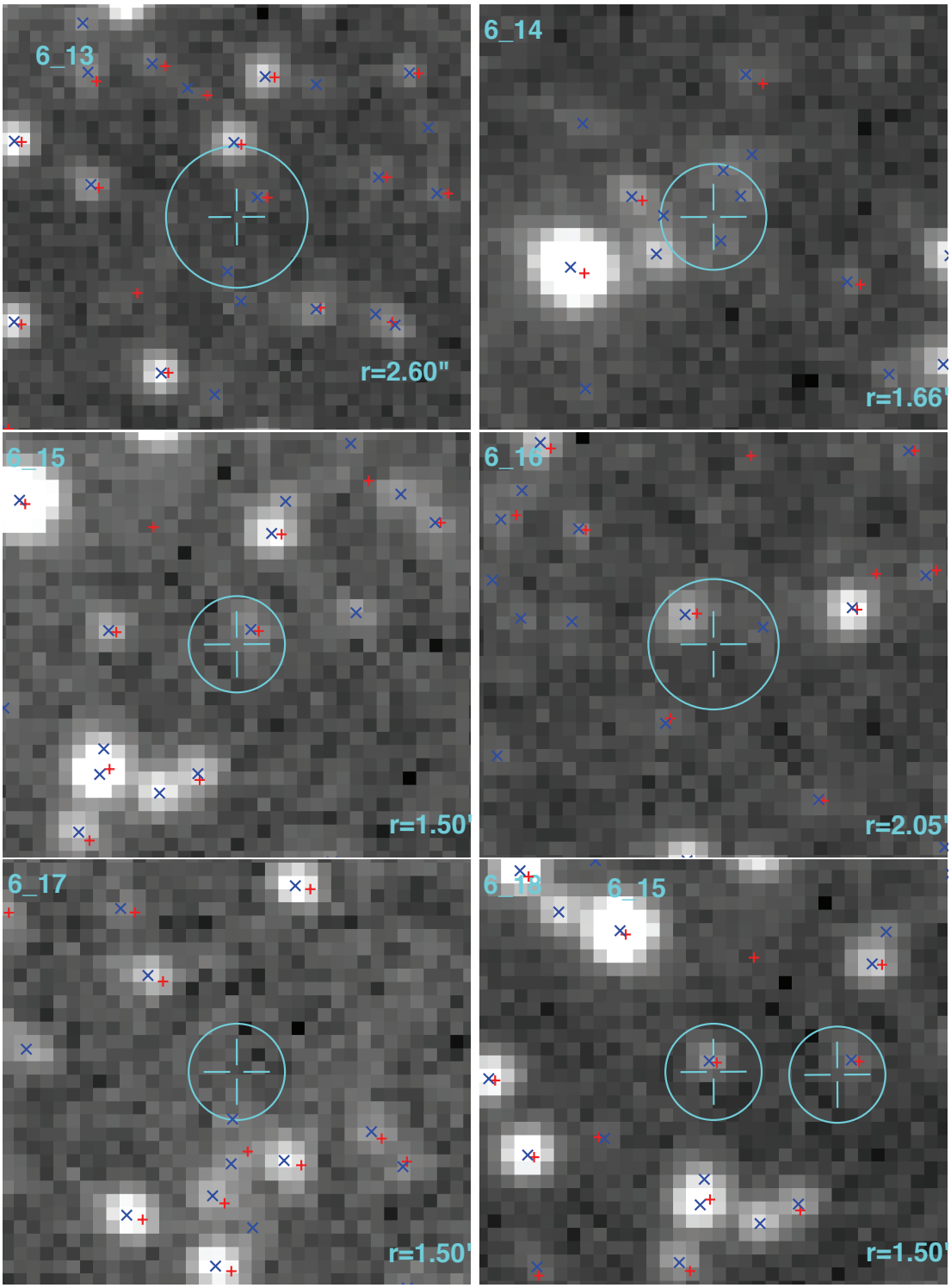
6_13
r=2.60"
6_14
r=1.66"
6_15
r=1.50"
6_16
r=2.05"
6_17
r=1.50"
6_15
r=1.50"

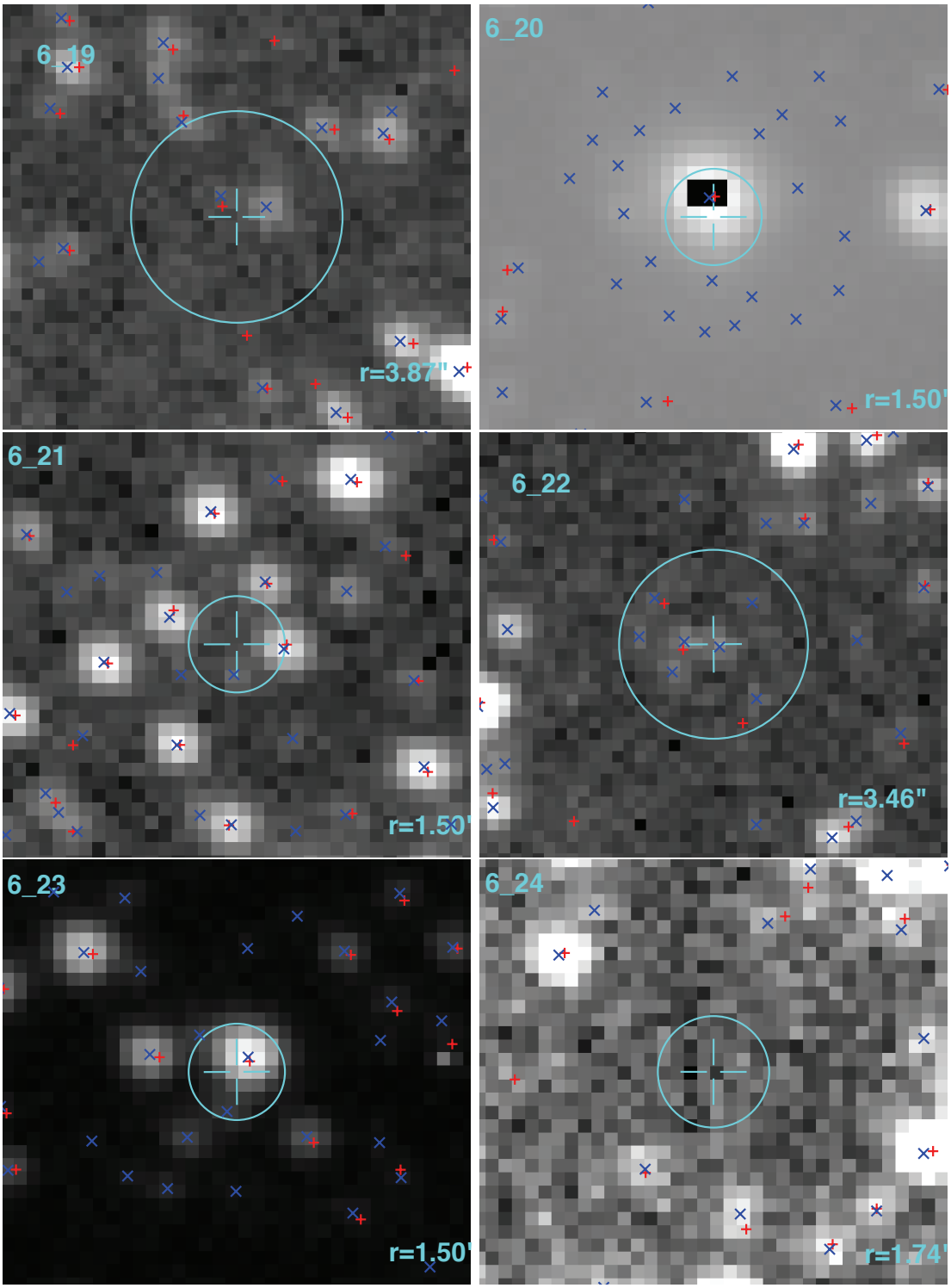
6_19
r=3.87"
6_20
r=1.50"
6_21
r=1.50"
6_22
r=3.46"
6_23
r=1.50"
6_24
r=1.74"

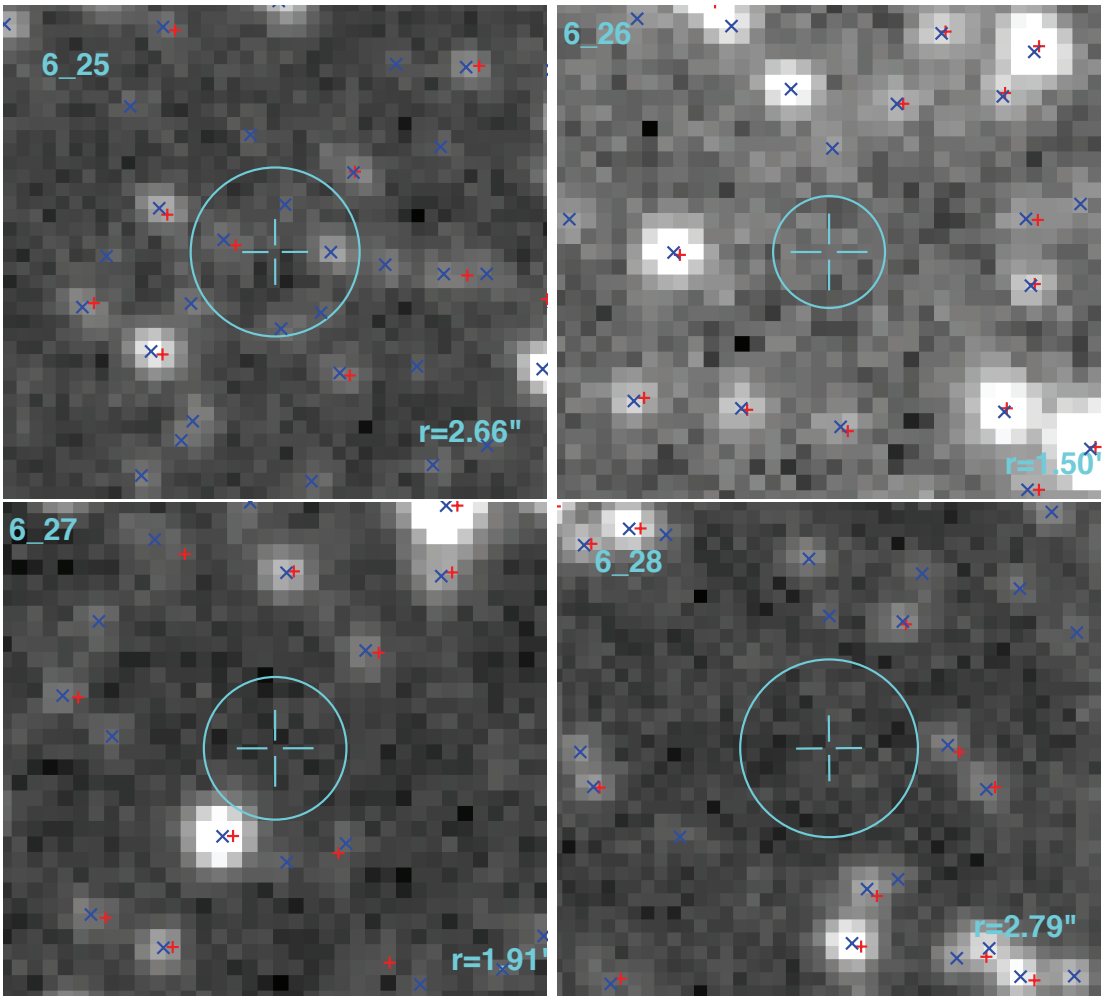
6_25
r=2.66"
6_26
r=1.50"
6_27
r=1.91"
6_28
r=2.79"

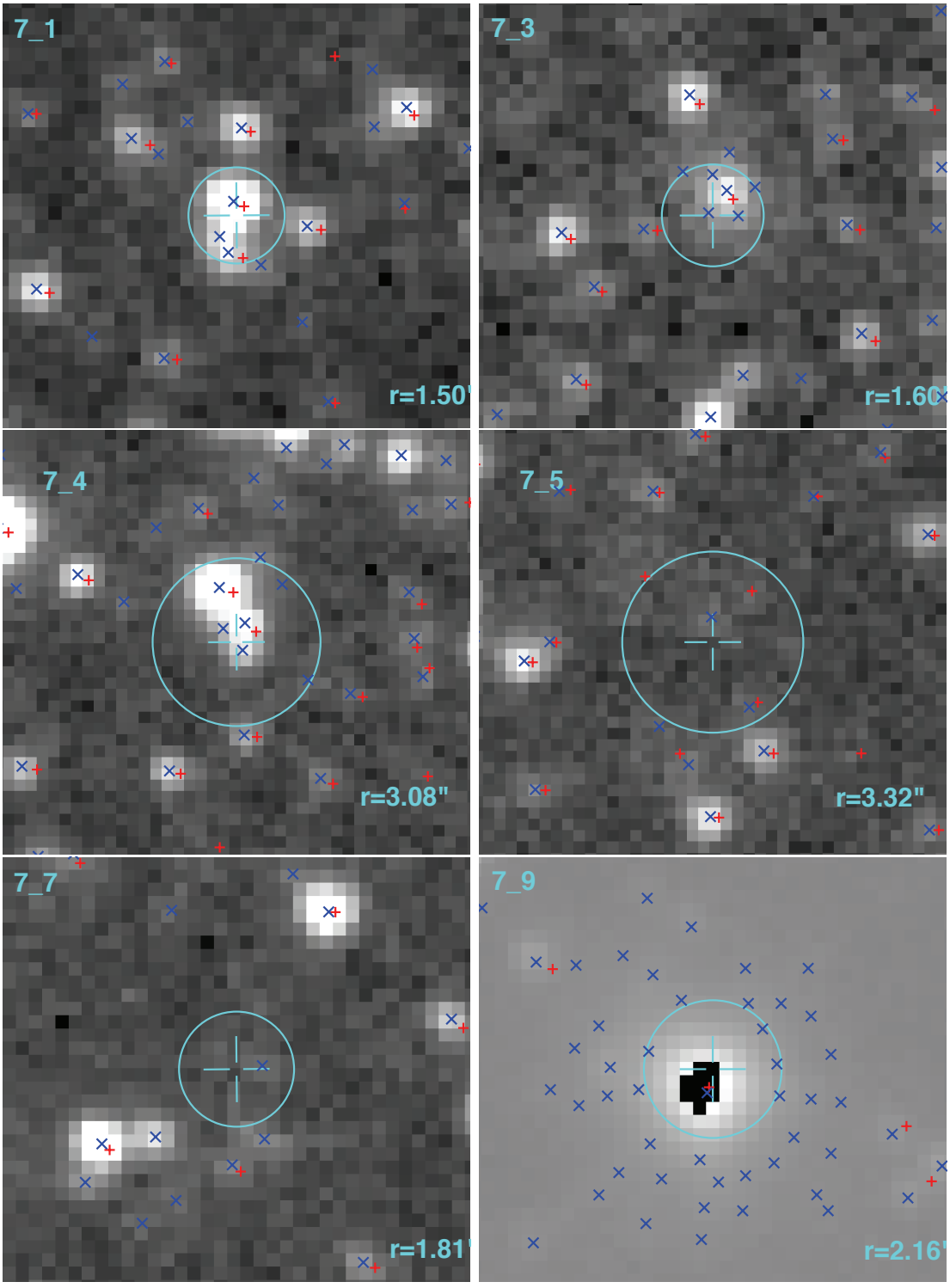

Figure B.5 OGLE *I* band images for Chandra sources in field 7 *This is an electronic Figure.*

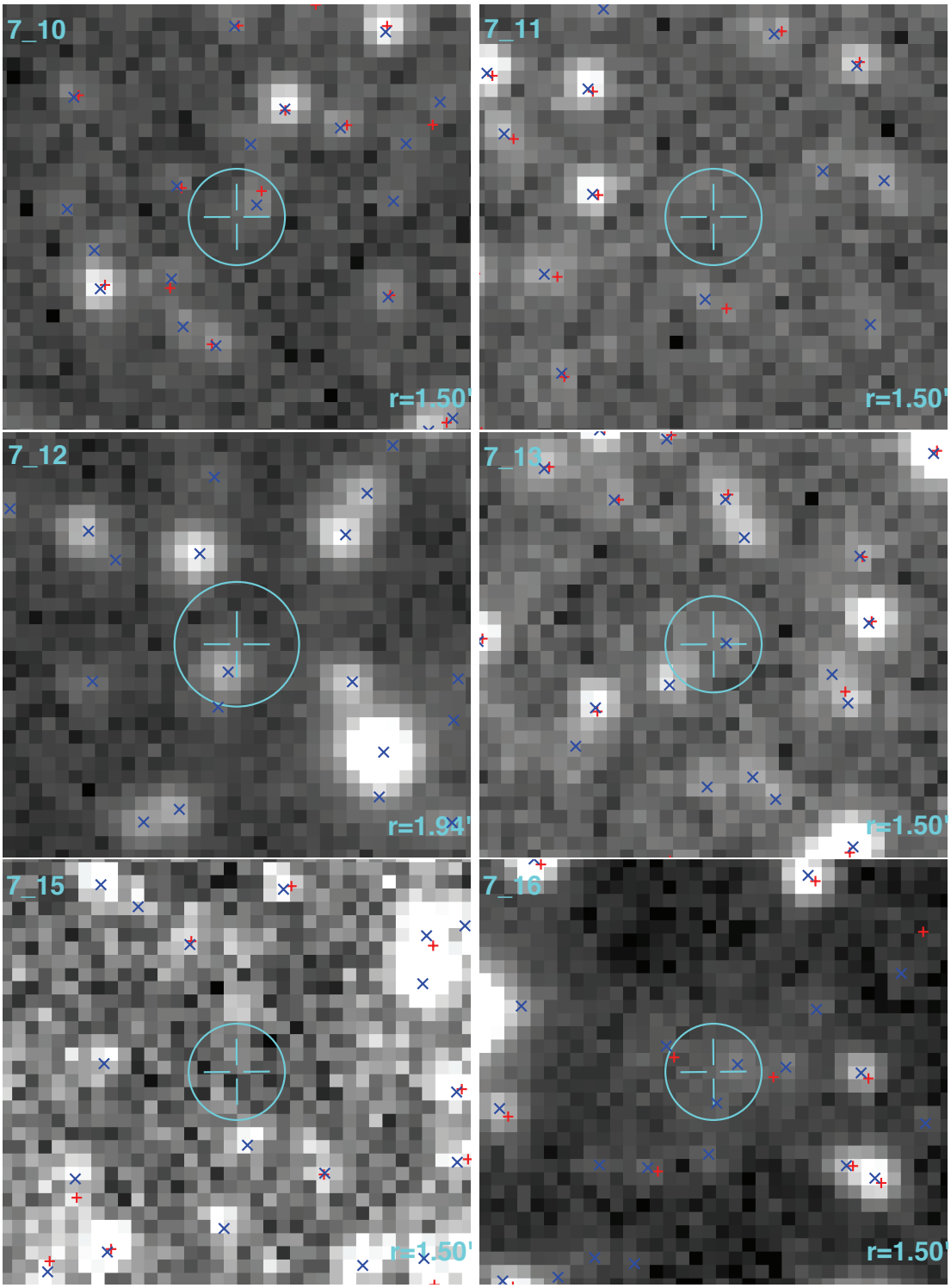
7_10
r=1.50'
7_11
r=1.50'
7_12
r=1.94'
7_13
r=1.50'
7_15
r=1.50'
7_16
r=1.50'

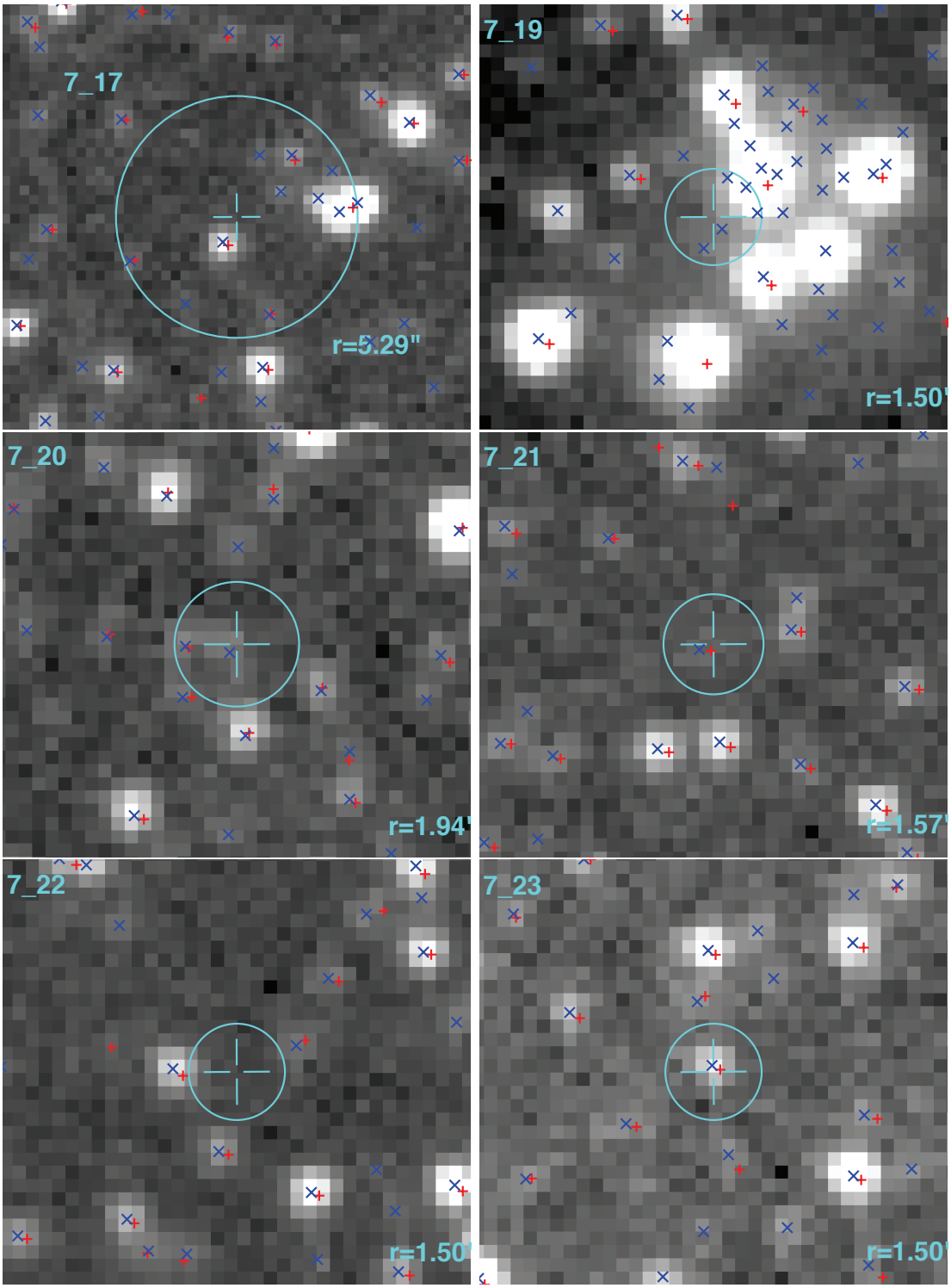
7_17
r=5.29"
7_19
r=1.50"
7_20
r=1.94"
7_21
r=1.57"
7_22
r=1.50"
7_23
r=1.50"

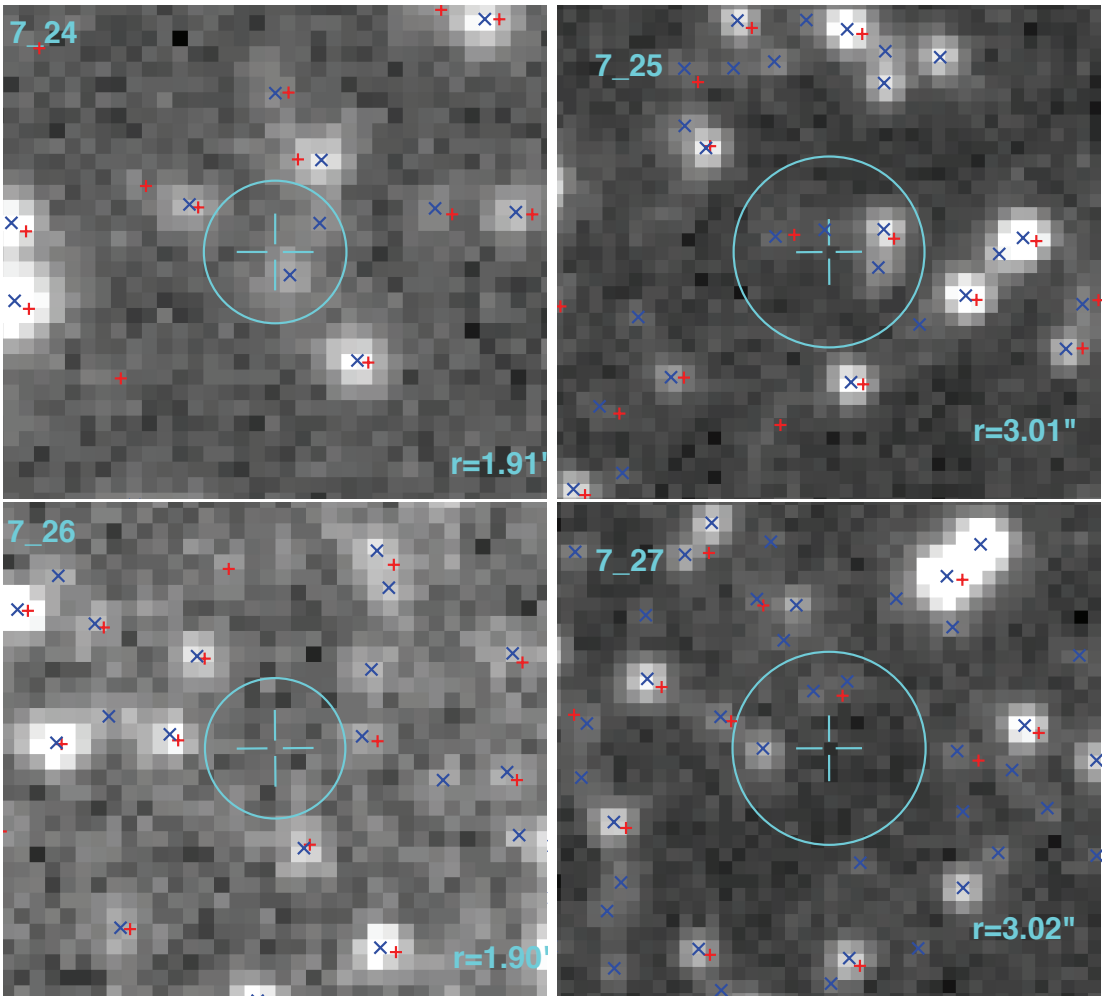
7_24
r=1.91"
7_25
r=3.01"
7_26
r=1.90"
7_27
r=3.02"

Appendix C

SMC HMXBs observed with 2dF

C.1 2dF spectra of 20 HMXBs in the SMC

In this section we present the full wavelength ($\sim 3800 - 8000$Å) 2dF spectra of 20 HMXBs in the SMC (described in Chapter 6).

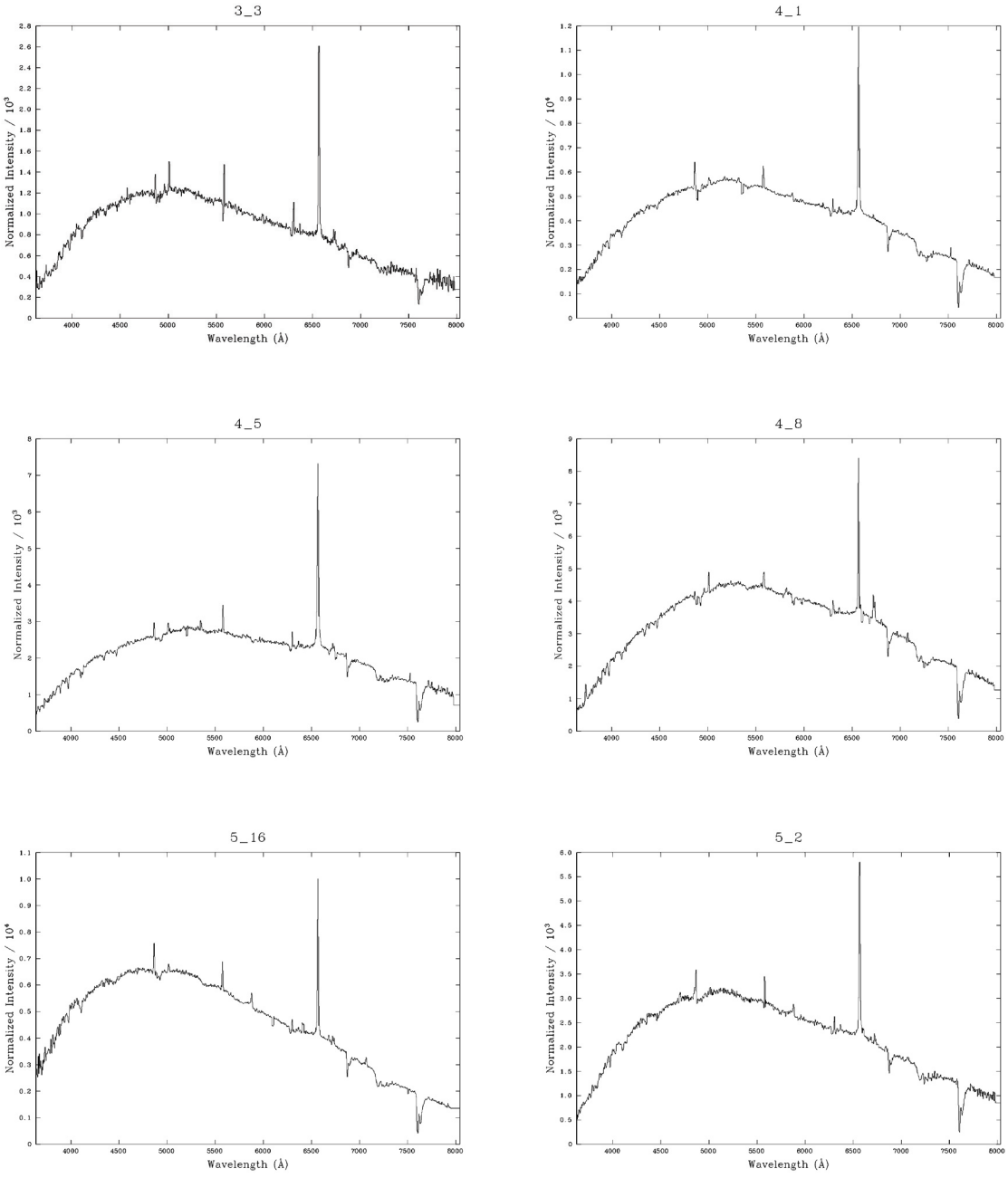

Figure C.1 2dF spectra of 20 HMXBs in the SMC.

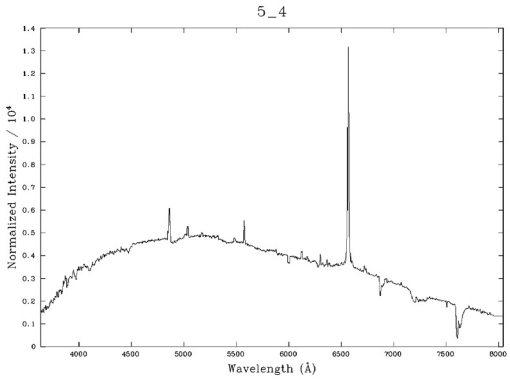
5_4
Normalized Intensity / 10^4
Wavelength (Å)

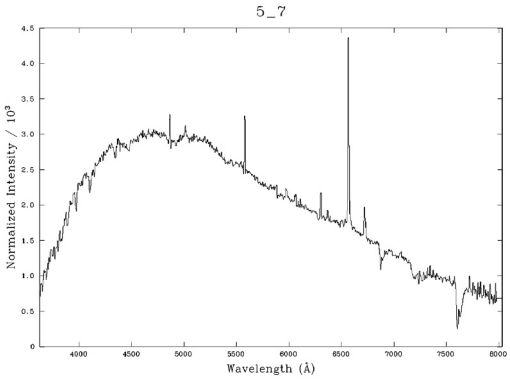
5_7
Normalized Intensity / 10^3
Wavelength (Å)

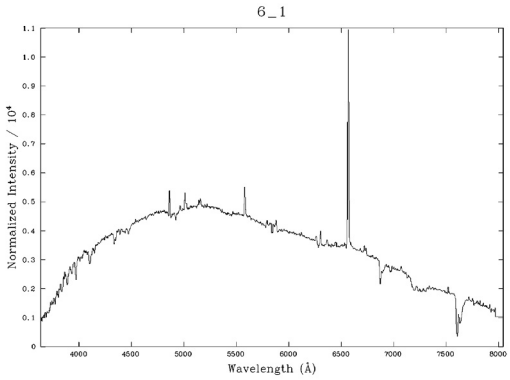
6_1
Normalized Intensity / 10^4
Wavelength (Å)

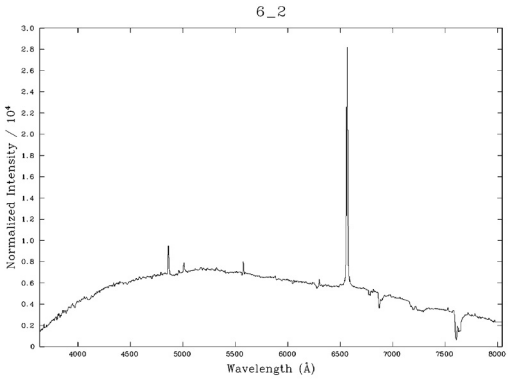
6_2
Normalized Intensity / 10^4
Wavelength (Å)

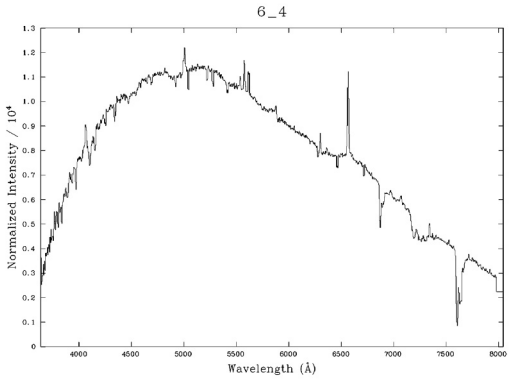
6_4
Normalized Intensity / 10^4
Wavelength (Å)

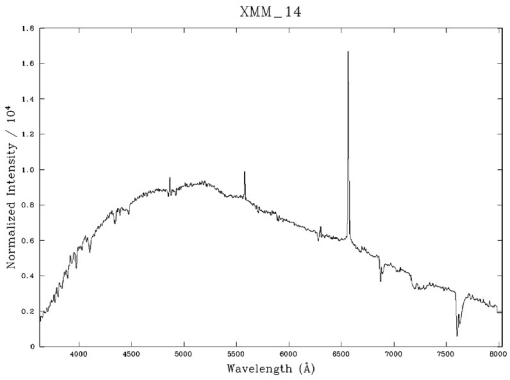
XMM_14
Normalized Intensity / 10^4
Wavelength (Å)

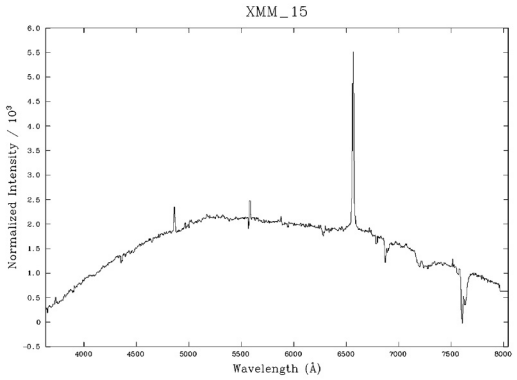
XMM_15
Normalized Intensity / 10^3
Wavelength (Å)

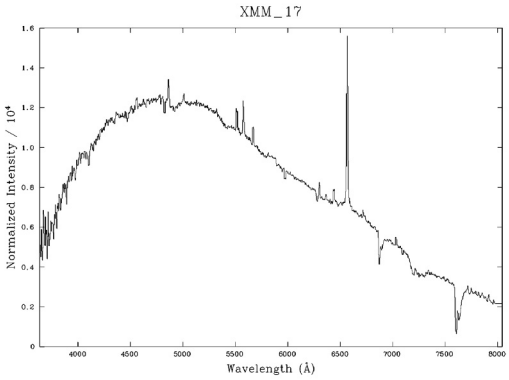
XMM_17
Normalized Intensity / 10^4
Wavelength (Å)

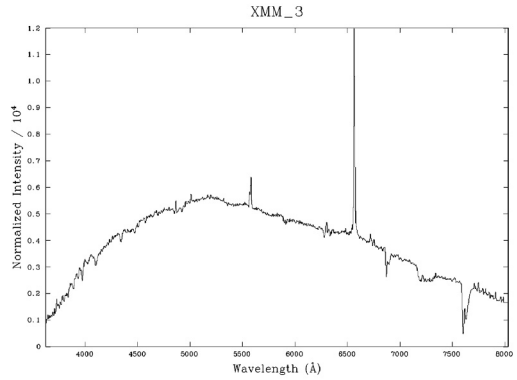
XMM_3
Normalized Intensity / 10^4
Wavelength (Å)

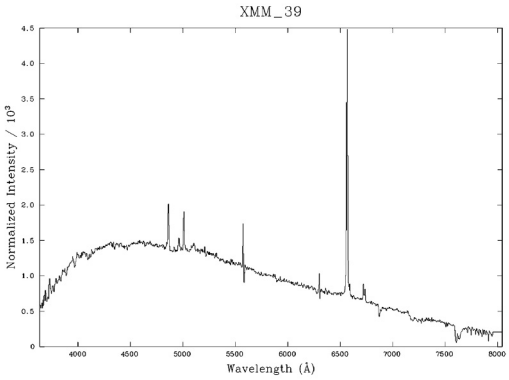
XMM_39
Normalized Intensity / 10^3
Wavelength (Å)

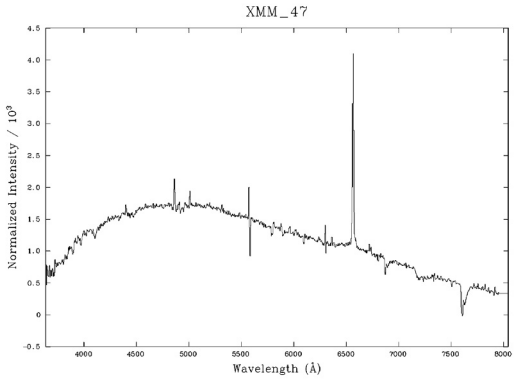
XMM_47
Normalized Intensity / 10^3
Wavelength (Å)

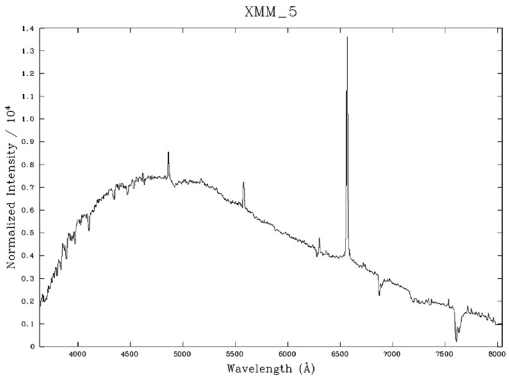
XMM_5
Normalized Intensity / 10^4
Wavelength (Å)

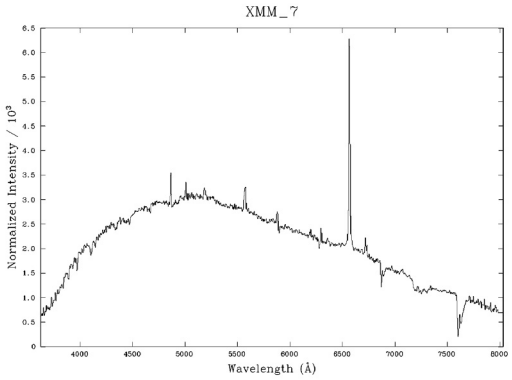
XMM_7
Normalized Intensity / 10^3
Wavelength (Å)

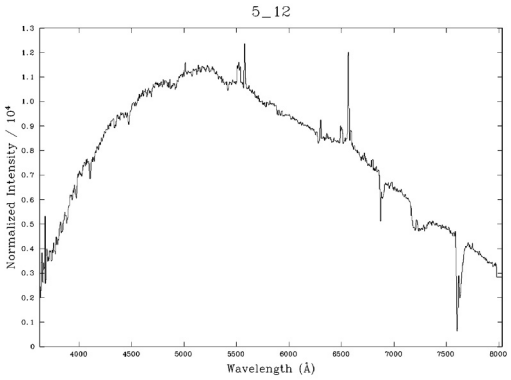
5_12
Normalized Intensity / 10^4
Wavelength (Å)

Appendix D

Light curves of HMXBs with 2dF spectra

We present the I band light curves for sources with 2dF spectra from the OGLE-II database (Figure D.1). The optical ID of each source is given in Chapter 6 (Table 6.4). From top to bottom of this figure for each page we have the following source IDs:

1. *First page* Left column: 3_3, 4_5, 5_4, right column 4_1, 4_8, 5_7
2. *Second page* Left column: 6_1, 6_2, 6_4, right column XMM_14, XMM_17, XMM_3
3. *Third page* Left column: XMM_39, XMM_47, right column XMM_5, XMM_5, XMM_7. Source XMM_5 appears twice because there are two OGLE-II IDs for the same optical source (detected in two neighboring OGLE-II fields).

For 4 sources we identified only MCPS counterparts, since OGLE-II does not have overlap with the regions they are located, and thus we present the MACHO light curves (Figure D.2; without converting the "blue" instrumental magnitude in the standard V band). From top to bottom of this figure we have the following source IDs: 5_16, 5_2, XMM_15, 5_12 (MACHO IDs 207.16202.1726, 207.16202.50, 208.16034.5, and 208.16145.10, respectively).

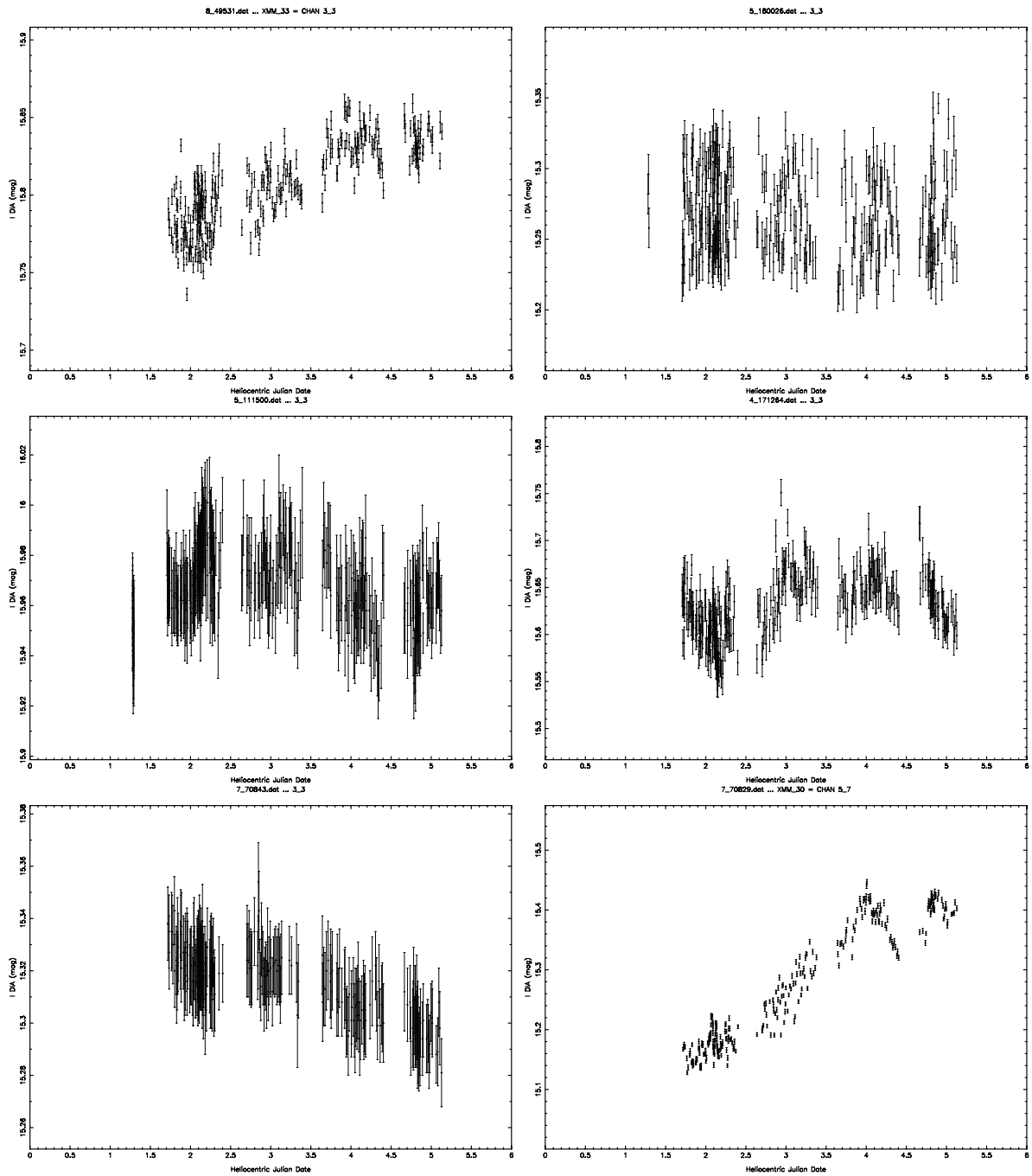

Figure D.1 I band OGLE-II light curves for sources with 2dF spectra. The x-axis gives the time (Julian Date - 2450000) in years, and the y-axis the I band magnitude.

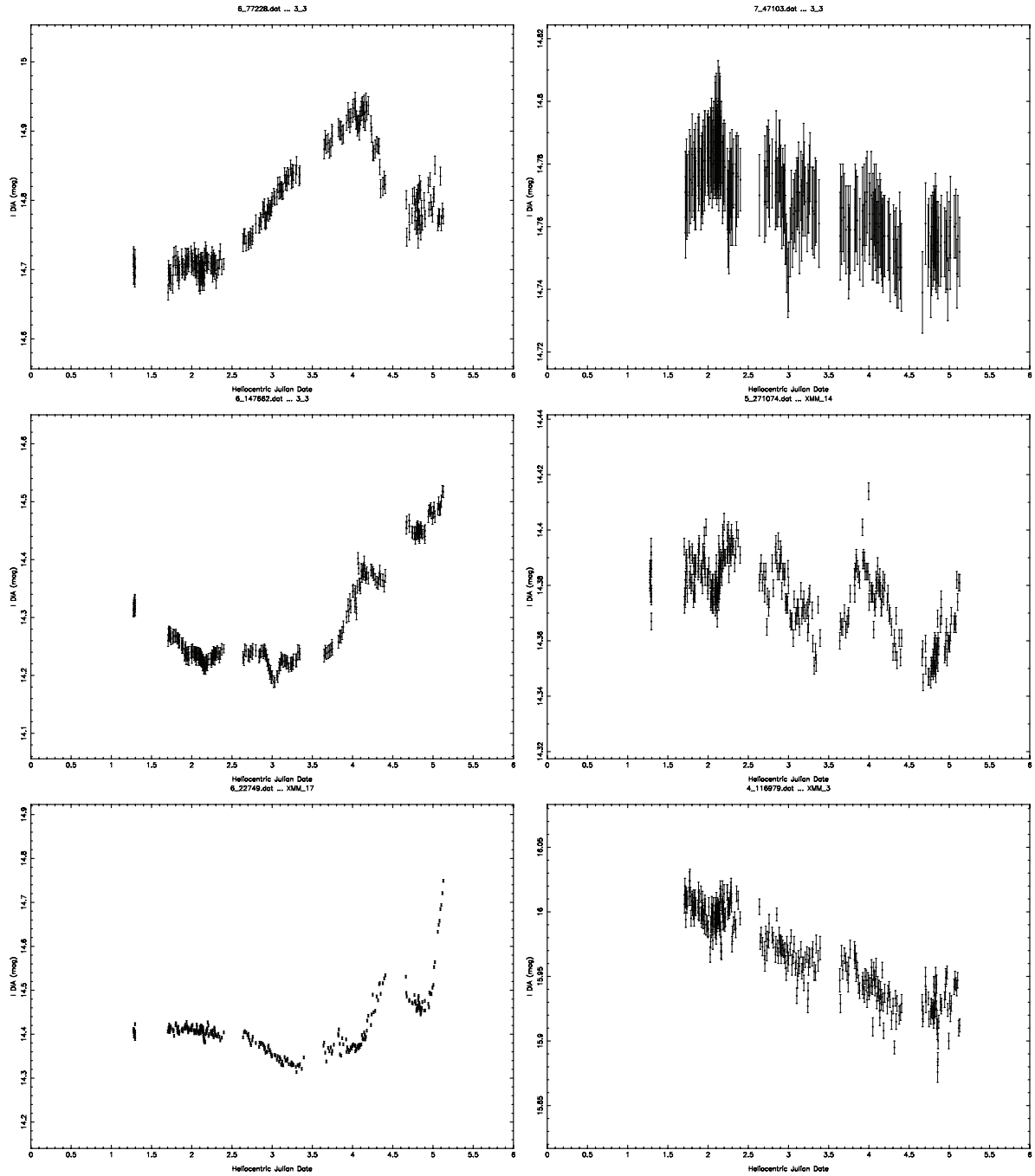
6_77228.dat ... 3_3
I DA (mag)
Heliocentric Julian Date
7_47103.dat ... 3_3
I DA (mag)
Heliocentric Julian Date
6_147662.dat ... 3_3
I DA (mag)
Heliocentric Julian Date
5_271074.dat ... XMM_14
I DA (mag)
Heliocentric Julian Date
6_22749.dat ... XMM_17
I DA (mag)
Heliocentric Julian Date
4_116979.dat ... XMM_3
I DA (mag)
Heliocentric Julian Date

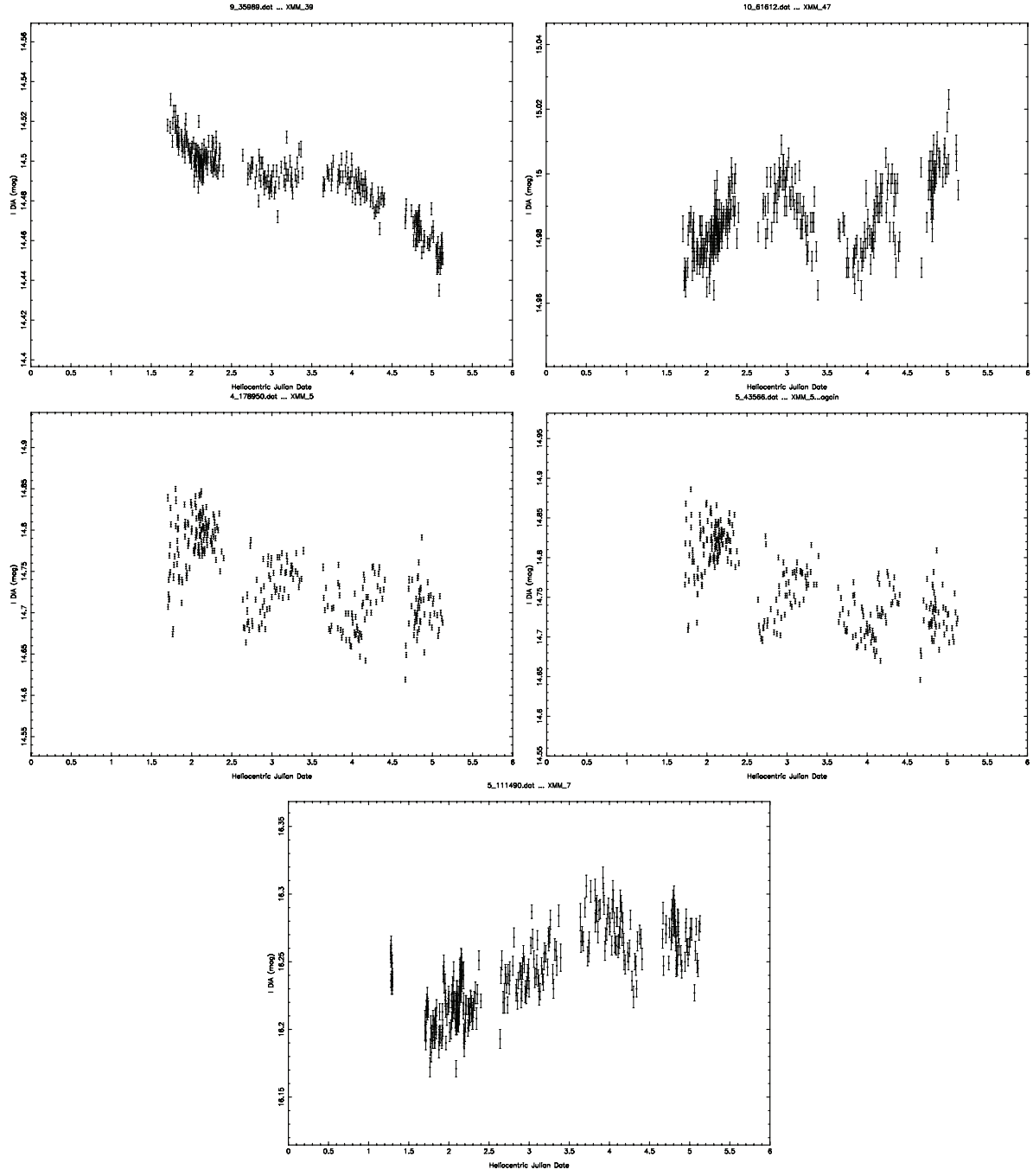
9_35989.dat ... XMM_39
I DIA (mag)
Heliocentric Julian Date
10_61612.dat ... XMM_47
I DIA (mag)
Heliocentric Julian Date
4_178950.dat ... XMM_5
I DIA (mag)
Heliocentric Julian Date
5_43566.dat ... XMM_5...again
I DIA (mag)
Heliocentric Julian Date
5_111490.dat ... XMM_7
I DIA (mag)
Heliocentric Julian Date

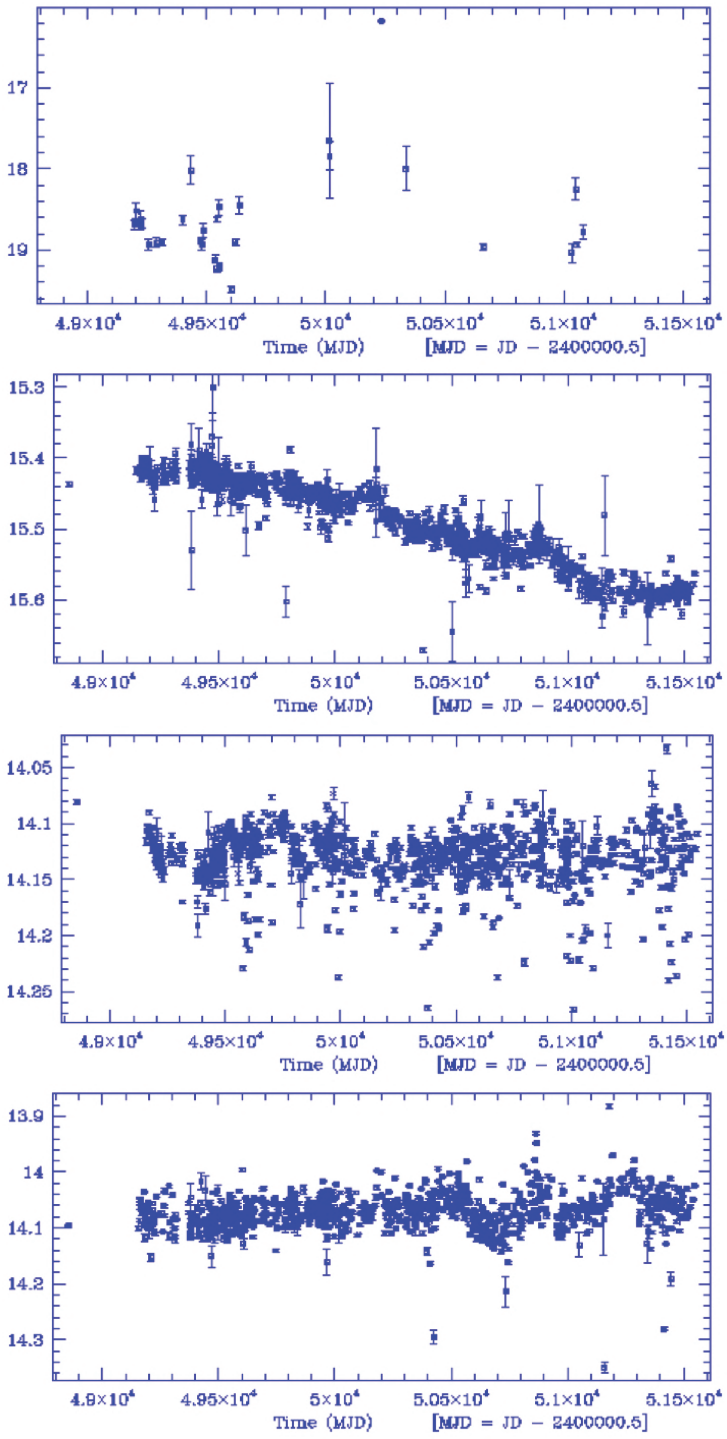

Figure D.2 MACHO light curves for sources with 2dF spectra. The x-axis gives the time (Julian Date - 2400000.5), and the y-axis the "blue" instrumental magnitude.